Universidade de Aveiro Departamento de Química
Ano 2017

Ana Daniela Gonçalves Firmino

Redes Metalo-Orgânicas Baseadas em Ligandos Tetrafosfonato

Metal-Organic Frameworks Based on Tetraphosphonate Linkers

Universidade de Aveiro Departamento de Química
2017

Ana Daniela Gonçalves Firmino

Redes Metalo-Orgnânicas Baseadas em Ligandos Tetrafosfonato

Metal-Organic Frameworks Based on Tetraphosphonate Linkers

Tese apresentada à Universidade de Aveiro para cumprimento dos requisitos necessários à obtenção do grau de Doutor em Química, realizada sob a orientação científica do Doutor Filipe Alexandre Almeida Paz, Investigador Principal do Laboratório Associado CICECO do Departamento de Química da Universidade de Aveiro, e co-orientação do Doutor João Paulo Costa Tomé, Professor Associado do Departamento de Engenharia Química do Instituto Superior Técnico da Universidade de Lisboa.

Apoio financeiro da FCT: SFRH / BD / 84495 / 2012

FCT Fundação para a Ciência e a Tecnologia
MINISTÉRIO DA EDUCAÇÃO E CIÊNCIA

COMPETE 2020 PROGRAMA OPERACIONAL COMPETITIVIDADE E INTERNACIONALIZAÇÃO
PORTUGAL 2020
UNIÃO EUROPEIA Fundo Europeu de Desenvolvimento Regional

Ao meu Pai,
À minha Mãe e à minha Irmã.

o júri

presidente

Prof. Doutor Joaquim Manuel Vieira
Professor Catedrático da Universidade de Aveiro

Prof. Doutor João Carlos Matias Celestino Gomes da Rocha
Crofessor Catedrático da Universidade de Aveiro

Prof. Doutora Susana Graça da Costa
Professora Auxiliar da Universidade do Minho

Doutor Sérgio Manuel Felipe Vilela
Investigador do Instituto IMDEA Energía

Doutor Luís Manuel Cunha Silva
Investigador em Pós-Doutoramento da Universidade do Porto

Doutor Filipe Alexandre Almeida Paz
Investigador Principal da Universidade de Aveiro

agradecimentos

O meu primeiro agradecimento é dirigido à Fundação para a Ciência e a Tecnologia pela bolsa de doutoramento que me atribuíram (com a referência SFRH/BD/84495/2012) conducente à realização desta Dissertação que representa para mim a etapa final da concretização de um objetivo muito ambicionado.

Ao Departamento de Química da Universidade de Aveiro, especialmente ao Laboratório Associado CICECO – Instituto de Materiais de Aveiro e à Unidade de Investigação QOPNA, que me disponibilizaram todas as condições logísticas e materiais necessárias para desenvolver o meu projeto de investigação.

Agradeço também ao Doutor Filipe Paz e ao Doutor João Tomé por terem aceitado ser os meus orientadores e acompanhar-me na concretização deste desafio.

Ao Professor Artur Silva pela disponibilidade que sempre demonstrou e pelos ensinamentos transmitidos durante alguns dos momentos de avaliação no âmbito do Programa Doutoral em Química.

Ao Doutor Duarte Ananias pela sua colaboração no estudo das propriedades fotoluminescentes de alguns materiais que preparei e se encontram descritos nesta Dissertação. Obrigado também à Doutora Anabela Valente e à Doutora Margarida Antunes pela colaboração na investigação da atividade catalítica de alguns compostos sintetizados neste projeto. Ao Doutor Filipe Figueiredo e à Doutora Paula Barbosa agradeço os estudos de condução protónica realizados aos materiais que preparei.

Um grande obrigado ao pessoal técnico do Departamento de Química da Universidade de Aveiro, em especial à Celeste, à Margarete e à Rosário, pelo profissionalismo, disponibilidade e competência que sempre demonstraram e pelos serviços prestados.

Um agradecimento muito especial aos meus colegas do grupo de investigação em MOFs da Universidade de Aveiro pela sua ajuda, disponibilidade e amizade. E a todos os amigos e colegas do CICECO e QOPNA.

E porque os últimos são os primeiros, agradeço à minha família pela paciência e compreensão durante esta etapa da minha vida e por me terem sempre transmitido muita força para seguir adiante!

A todos os meus mais sinceros agradecimentos!

palavras-chave

Redes Metalo-Orgânicas, Fosfonatos, Lantanídeos, Fotoluminescência, Catálise, Condução Protónica.

resumo

Redes Metalo-Orgânicas (MOFs) são materiais híbridos porosos e cristalinos que têm registado um rápido desenvolvimento dadas as suas propriedades excecionais e o grande número de potenciais aplicações, tais como adsorção e separação de gases, catálise, aplicações em biomedicina, dispositivos eletrónicos ou sensores óticos, entre outras, bem como a sua infinita variabilidade química e diversidade topológica sem precedente. Particularmente, MOFs baseadas em lantanídeos e (poli)fosfonatos têm atraído a atenção de investigadores de todas as partes do mundo, principalmente pelos diferentes usos dos ácidos difosfónicos, que são, em geral, facilmente obtidos comercialmente. Para além da sua notável diversidade estrutural, ligandos (poli)fosfonato possuem vantagens relativamente a outros ligandos mais comumente usados, como os carboxilatos (ou aqueles baseados em aminas), contribuindo com a sua notável robustez térmica, mecânica e química para a obtenção de novos materiais.

O grupo de investigação em MOFs da Universidade de Aveiro tem preparado novos materiais a partir da combinação de ligandos orgânicos com grupos fosfonato e, principalmente, lantanídeos. Esta dissertação descreve os resultados mais recentes nesta área envolvendo a síntese de MOFs multidimensionais baseadas em dois ligandos fosfonato tetrapodais. Os ligandos orgânicos usados neste projeto foram desenhados e preparados após seleção e otimização das condições reacionais e métodos de síntese. Reações entre estes ligandos orgânicos e catiões lantanídeo levaram à formação de várias famílias de MOFs 2D e 3D. A preparação destes materiais envolveu o uso de métodos de síntese distintos: síntese hidro(solvo)térmica, evaporação lenta e síntese por irradiação de micro-ondas. A seleção criteriosa dos ligandos orgânicos mostrou ter um papel fundamental na topologia final dos materiais: a presença de um certo grau de flexibilidade por parte do ligando orgânico teve como consequência uma grande variedade estrutural de MOFs obtidas, tanto 2D como 3D. As reações com um outro ligando que apresenta maior rigidez requereram a presença de um segundo ligando (auxiliar) para facilitar a formação da rede. A estrutura cristalina dos materiais foi resolvida através de difração de raios-X de monocristal, técnica usada em conjunto com várias outras técnicas de caracterização de compostos em estado sólido (FT-IR, microscopia eletrónica (SEM e EDS), RMN em estado sólido, análise elementar e termogravimétrica e difração de raios-X de pós). A estabilidade térmica dos materiais reportados foi ainda abordada de forma comparativa, verificando-se que alguns compostos obtidos apresentam robustez e estabilidades térmicas excecionais, num caso particular até cerca dos 800 ºC.

As propriedades intrínsecas de algumas MOFs foram também investigadas. Estudos de fotoluminescência revelaram que o ligando orgânico derivado do bifenilo é um sensibilizador apropriado para catiões Tb^{3+}, levando à formação de materiais emissores de luz verde intensa. Os materiais obtidos também mostraram possuir elevada atividade catalítica, em meio heterogéneo, nomeadamente na reação de abertura do anel epóxido do óxido de estireno e na proteção do benzaldeído pela formação do correspondente acetal (reações na presença de metanol), bem como excelente condução protónica a humidades elevadas, tendo-se registando valores entre os mais elevados para este tipo de materiais híbridos.

keywords

Metal-Organic Frameworks, Phosphonates, Lanthanides, Photoluminescence, Catalysis, Proton Conductivity.

abstract

Metal-Organic Frameworks (MOFs) are hybrid porous crystalline materials which have developed rapidly due to their outstanding properties and myriad of potential applications such as gas storage, separations, catalysis, biomedicine, electronic devices, optical sensors, among several others, as well as their endless chemical variability and unprecedented diversity of pore structure and topology. Particularly, MOFs based on lanthanide (poly)phosphonates have attracted worldwide research attentions, mainly because of the different uses of diphosphonic acid molecules, which are, in general, readily available from commercial sources. Besides their remarkable structural diversity, (poly)phosphonate linkers offer advantages over the more widely used carboxylate (or nitrogen-based) molecules for developing new materials, prompted by their notable chemical, mechanical and thermal robustness.

The MOF research group at the University of Aveiro has prepared MOFs from the combination of phosphonate organic linkers as primary building units (PBUs) with, mainly, lanthanides. This thesis presents the last findings in this area involving the synthesis of multidimensional MOFs based on two tetrapodal phosphonate ligands. The organic PBUs were designed and prepared by selecting and optimizing the best reaction conditions and synthetic routes. The self-assembly between phosphonate PBUs and lanthanide cations led to the formation of several 2D and 3D families of isotypical MOFs. The preparation of these materials was achieved using distinct synthetic approaches: hydro(solvo)thermal, slow evaporation and microwave-assisted synthesis. The selection of the organic PBUs had an important role in the final architectures: a certain degree of flexibility present in the phosphonate ligand afforded a large variety of MOF architectures, both 2D and 3D. The self-assembly using a more rigid organic ligand required an ancillary ligand for the reaction to occur. The crystal structure of these materials was successfully unveiled by single-crystal X-ray diffraction used in tandem with standard solid-state characterization techniques (FT-IR, electron microscopy (SEM and EDS), solid-state NMR, elemental and thermogravimetric analyses and powder X-ray diffraction). Thermal stability of the reported networks was also addressed in a comparative fashion with some MOF materials exhibiting remarkable thermal stabilities and robustness, in one particular case up to *ca.* 800 ºC.

The intrinsic properties of some MOFs were also investigated. Photoluminescence studies revealed that the biphenyl-based organic PBU is a suitable sensitizer of Tb^{3+}, leading to the isolation of intense green-emitting materials. Materials also exhibited high heterogeneous catalytic activity in the ring-opening reaction of styrene oxide and acetalization of benzaldehyde with methanol, as well as excellent protonic conductivity at high humidities, with registered values (in all these studies) among the highest for this type of hybrid materials.

Table of contents

Chapter 3

Chapter 4

Chapter 5

Chapter 8

Abbreviations

^{1}H NMR	proton nuclear magnetic resonance
^{13}C NMR	carbon 13 nuclear magnetic resonance
^{31}P NMR	phosphorous 31 nuclear magnetic resonance
CP MAS	cross-polarization magic-angle spinning
d	doublet
dd	double doublet
DMSO-d_6	deuterated dimethyl sulfoxide
dt	double triplet
EDS	energy dispersive X-ray spectroscopy
ESI	electrospray ionization
FT-IR	Fourier transform infrared
HPDEC	high power decoupling
IUPAC	International Union of Pure and Applied Chemistry
J	coupling constant
Ln	lanthanide
LnOF(s)	Lanthanide-Organic Framework(s)
m	multiplet
MAS	magic-angle spinning
MOF(s)	Metal-Organic Framework(s)
MRI	magnetic resonance imaging
MS	mass spectrometry
MWAS	microwave-assisted synthesis
m/z	mass/charge ratio
$(M + H)^+$	protonated molecular ion
$(M – H)^-$	deprotonated molecular ion
$(M + Na)^+$	sodiated molecular ion
NMR	nuclear magnetic resonance
NO	nitric oxide
PBU(s)	primary building unit(s)
PCPs	porous coordination polymers
ppm	part per million

PXRD	powder X-ray diffraction
RH	relative humidity
s	singlet
SBU(s)	secondary building unit
SEM	scanning electron microscopy
t	triplet
TGA	thermogravimetric analysis
TLC	thin layered chromatography
TOF MS ES	time-of-flight mass spectrometry electrospray
TPM	tetraphenylmethane
VTPXRD	variable-temperature powder X-ray diffraction
δ	chemical shift (in ppm)
wt %	weight percent
ZIFs	zeolitic imidazolate frameworks

Publications Presented in this Thesis

1. *Fast detection of nitroaromatics using phosphonate pyrene motifs as dual chemosensors*
   N. Venkatramaiah, Ana D. G. Firmino, Filipe A. Almeida Paz, João P. C. Tomé
   Chem. Commun., **2014**, *50*, 9683-9686.

2. *Microwave Synthesis of a Photoluminescent Metal-Organic Framework based on a rigid tetraphosphonate linker*
   Ana D. G. Firmino, Ricardo F. Mendes, Duarte Ananias, Sérgio M. F. Vilela, Luís D. Carlos, João P. C. Tomé, João Rocha, Filipe A. Almeida Paz
   Inorg. Chim. Acta, **2017**, *455*, 584-594.

3. *Robust Multifunctional Yttrium-Based Metal-Organic Frameworks with Breathing Effect*
   Ana D. G. Firmino, Ricardo F. Mendes, Margarida M. Antunes, Paula C. Barbosa, Sérgio M. F. Vilela, Anabela A. Valente, Filipe M. L. Figueiredo, João P. C. Tomé, Filipe A. Almeida Paz
   Inorg. Chem., **2017**, *56*, 1193-1208.

4. *Excimer Formation in a Terbium Metal-Organic Framework Assists Luminescence Thermometry*
   Duarte Ananias, Ana D. G. Firmino, Ricardo F. Mendes, Filipe A. Almeida Paz, Mariela Nolasco, Luís D. Carlos, João Rocha
   Chem. Mater., **2017**, *29*, 9547-9554.

5. *Metal-Organic Frameworks assembled from tetraphosphonic ligands and lanthanides*
   Ana D. G. Firmino, Flávio Figueira, João P. C. Tomé, Filipe A. Almeida Paz, João Rocha
   Coord. Chem. Rev., **2018**, *355*, 133-149.

Chapter 1

Metal-Organic Frameworks assembled from tetraphosphonic ligands and lanthanides

1.1. Metal-Organic Frameworks: concepts and challenges

Metal-Organic Frameworks (MOFs) are crystalline microporous compounds and together with Coordination Polymers are coordination networks constructed by the self-assembly of metal ions or clusters (from alkali to transition metals, lanthanides or actinides) with, at least, one organic linker bearing, for example, carboxylic, pyridyl, phosphonic and/or sulfonic acid groups. Strong dative covalent bonds and intermolecular interactions are responsible for the structural stability and variability of these compounds and so they remain in the focus of intense research, mostly driven by both, the interest in finding new and intriguing molecular architectures, and the relevance of developing new or more efficient materials for various applications.[1-9] The main goal in MOFs synthesis is to establish the optimal conditions leading to the formation of stable bridges between the inorganic and organic building blocks, while simultaneously controlling the crystallization kinetics, allowing the nucleation and growth of a desired pure phase.[10] "Design principles" and "predictability" are, thus, recurrent topics in MOF research. In this context, MOFs based on carboxylate or nitrogen-based ligands are most studied because: i) molecules are easily synthesized or are readily available from commercial sources at suitable prices; ii) large-single crystals may be obtained from a wide range of synthetic conditions; iii) "isoreticular design" of frameworks is possible[11] through the rational design of new ligands based on previously reported analogue compounds. Nevertheless, these advantages are shadowed by the well-known poor stability (thermal, mechanical and/or chemical, especially toward hydrolysis) of such MOFs, which ultimately hinders their practical use.[12]

Over the years, a number of research groups working on metal phosphonates chemistry have pioneered the discovery of many interesting framework architectures, including layered and microporous structures based on bi-, tri- or multitopic anionic organic units, such as multipodal phosphonates,[13-16] aminophosphonates[17] and phosphonocarboxylates.[18] Advantages of the phosphonate groups include: i) $C–PO_3$ bond is stable at high temperatures and under a wide range of chemical conditions; ii) three oxygens connected to the phosphorus atom form tetrahedral building units reminiscent of zeolite building blocks.[19] The latter feature ensures bonds to metal centers stronger than the bonds formed by the carboxylate (or nitrogen-based) groups, endowing stability and robustness to the resulting MOFs. However, this feature makes phosphonate coordination less predictable: the richness and variety of coordination modes of these tetrahedral groups

to metal centers is vast, increasing when lanthanides are used (due to their large coordination numbers), ultimately leading to the statistical possibility of a wide variety of secondary building units (SBUs) in solution during the crystallization process.[20] This accounts, to large extent, for the poor solubility of metal phosphonates and their typical isolation as microcrystalline powders. It is, therefore, not surprising that most research in this field has been focused on diphosphonates leading, in most cases, to densely stacked layered structures displaying excellent thermal and mechanical robustness.[21-23] Recently, researchers have focused their attention on tripodal nonlinear phosphonoaromatic ligands, which afford the interesting architectures already reviewed by Taddei and co-workers.[24] Additionally, researchers have also considered advancing and focusing on more complex and larger organic molecules, particularly tetraphosphonic acids, self-assembled with lanthanide cations. It is important to state that these molecules are not common and usually not readily available from commercial suppliers.[25] They have to be individually prepared in good yields and using straightforward reaction procedures.

1.2. Tetrapodal phosphonic acids and LnOFs: general overview

A search in the literature and in the Cambridge Structural Database showed that the most significant and structurally relevant tetrapodal phosphonate-based organic molecules used to date in the preparation of LnOFs are those depicted in Scheme 1.1. For a better comparative purpose, these ligands can immediately be divided into two main families: phosphonoaliphatic and phosphonoaromatic organic linkers, $\mathbf{H_8L^1}$-$\mathbf{H_8L^6}$ and $\mathbf{H_8L^7}$-$\mathbf{H_8L^{10}}$, respectively. Noteworthy, in the former family the ligands are rich in nitrogen atoms, mostly originating from the synthetic routes used to prepare these molecules. Table 1.1 summarizes the various LnOFs prepared and reported using these tetraphosphonic acid linkers.

In the broad field of MOFs, there are two main architectural factors upon which these networks are typically based: secondary building units and organic linkers.[26] Due to the unpredictability of phosphonate groups toward rational design or reticular synthesis of LnOFs, *i.e.*, their usual inability to maintain topological features or form the same secondary building unit, either by extension of the organic ligand or modification of the lanthanide cations, researchers have focused their efforts on the preparation of new (pre-determined) ligands with specific shapes and sizes of the organic motif. Thus, the location

of the C–P bond in the overall organic backbone of the MOF represents an important challenge and in the following section are summarized the principal routes for the synthesis of these molecules, particularly those depicted in Scheme 1.1.

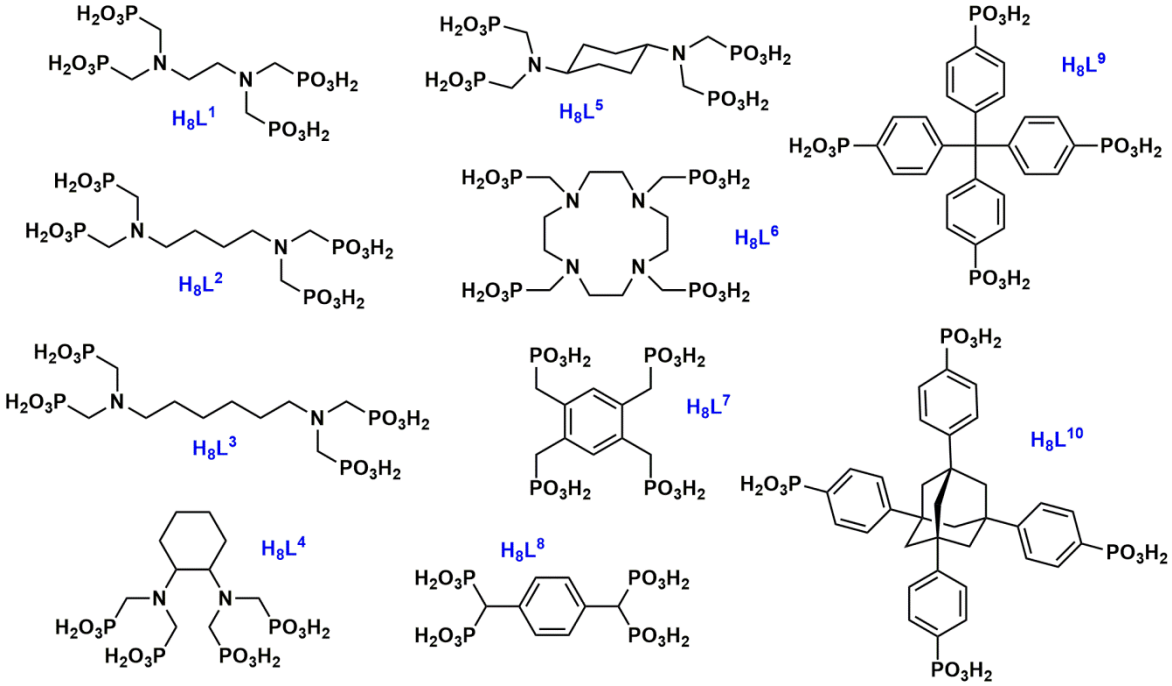

Scheme 1.1. Molecular structure of tretrapodal phosphonic acids employed in the synthesis and characterization of LnOFs:

H_8L^1 – 1,2-Diaminoethane-*N*,*N*,*N'*,*N'*-tetrakis(methylenephosphonic acid)
H_8L^2 – 1,4-Diaminobutane-*N*,*N*,*N'*,*N'*-tetrakis(methylenephosphonic acid)
H_8L^3 – 1,6-Diaminohexane-*N*,*N*,*N'*,*N'*-tetrakis(methylenephosphonic acid)
H_8L^4 – 1,2-Diaminocyclohexane-*N*,*N*,*N'*,*N'*-tetrakis(methylenephosphonic acid)
H_8L^5 – 1,4-Diaminocyclohexane-*N*,*N*,*N'*,*N'*-tetrakis(methylenephosphonic acid)
H_8L^6 – 1,4,7,10-Tetraazacyclododecane-1,4,7,10-tetrakis-(methylenephosphonic acid)
H_8L^7 – 1,2,4,5-Tetrakisphosphonomethylbenzene
H_8L^8 – 1,4-Phenylenebis(methanetriyl)tetraphosphonic acid
H_8L^9 – Tetrakis[4-phosphonophenyl]methane
H_8L^{10} – 1,3,5,7-Tetrakis(4-phosphonophenyl)adamantane

Mono- or di-organophosphonates have a strong propensity to form layered dense structures. Efforts have been made to create porosity using this type of ligands.[27] Some of the strategies used to attempt a disruption of this "too efficient" crystal packing mode are: i) use of polyphosphonate ligands; ii) selection of phosphonate-based molecules with strong nonlinear geometry motifs (mainly because flexible carbon chains tend to align and form pillared structures); iii) increase the networks dimensionality using ancillary linkers. Systematization of all these factors to obtain a pre-designed porous phosphonate-MOF has not yet been accomplished. Phosphonates, as networks primary building units, do not

follow the same "architectural" behavior observed in some families of isoreticular MOFs based on carboxylate or nitrogen-based ligands.[11]

Phosphonate groups may be bonded to metal cations in various ways. Combination of lanthanides and phosphonates constitutes a small group of compounds showing interesting architectures and properties.[28] It has been established that the wide range of coordination numbers shown by these metals constitutes an advantage when they are coordinated to tetrahedral phosphonate-based compounds and their high level of protonation, *i.e.* protons that will be replaced by metals in polyphosphonic acids. This combination of metals with high coordination numbers and tetrapodal ligands having many chelating oxygens proved to be a very successful strategy for the synthesis of robust and stable new MOFs.

Table 1.1. Lanthanide(III) complexes and LnOFs reported using $\mathbf{H_8L^1}$-$\mathbf{H_8L^{10}}$.

Compound	Organic linker	Ancillary linker	Structural features	Ref.
$[C(NH_2)_3]_7[Eu(L^1)(CO_3)]\cdot 10H_2O$	$\mathbf{H_8L^1}$	—	Discrete complex	29
$[C(NH_2)_3]_6[Ln(L^4)(OH)(H_2O)_{1/2}]\cdot 16H_2O$ (Ln = La, Nd, Sm, Eu, Gd, Tb, Ho and Lu)	$\mathbf{H_8L^4}$	—	Discrete complex	30
$[C(NH_2)_3]_7[Tb(L^1)(CO_3)]\cdot 10H_2O$	$\mathbf{H_8L^1}$	—	Discrete complex	31
$[C(NH_2)_3]_7[Nd(L^1)(CO_3)]\cdot 10H_2O$	$\mathbf{H_8L^1}$	—	Discrete complex	32
$K_{17}H_3[Nd_4(L^1)_4]\cdot 36H_2O$	$\mathbf{H_8L^1}$	—	Discrete Tetramer	32
$[Ln(H_7L^6)(H_2O)_2]Cl_2\cdot xH_2O$ (where Ln = La, Nd, Sm, Eu, Gd, and Tb)	$\mathbf{H_8L^6}$	—	1D	33
$[Ln(H_7L^6)(H_2O)_2](ClO_4)_2\cdot xH_2O$ (where Ln = Nd, Sm, Eu, Gd, and Tb)	$\mathbf{H_8L^6}$	—	1D	33
$[Gd(H_5L^2)]\cdot 2H_2O$	$\mathbf{H_8L^2}$	—	2D	34
$[Ln_2(H_6L^2)(ox)_2(H_2O)_2]\cdot 4H_2O$ (Ln = Nd, Eu, Gd)	$\mathbf{H_8L^2}$	H_2ox	3D	35, 36
$[La_2(H_6L^2)(ox)_2]\cdot 2H_2O$	$\mathbf{H_8L^2}$	H_2ox	3D	36
$[Ce_2(H_2O)_6(H_4L^2)(HSO_4)_2]\cdot 4H_2O$	$\mathbf{H_8L^2}$	H_2SO_4	3D	37
$[Ce_2(H_2O)_2(H_4L^2)(HSO_4)_2]\cdot 2H_2O$	$\mathbf{H_8L^2}$	H_2SO_4	3D	37
$[Ce_2(H_2O)_6(H_4L^5)(HSO_4)_2]$	$\mathbf{H_8L^5}$	H_2SO_4	3D	37
$[La(H_5L^3)]\cdot 7H_2O$ (Ln = La, Sm)	$\mathbf{H_8L^3}$	—	3D	38
$[La(H_5L^3)]$	$\mathbf{H_8L^3}$	—	3D	38
$[La(H_5L^3)]\cdot 2H_2O$	$\mathbf{H_8L^3}$	—	3D	38
$[Ln_2(SO_4)_2(H_6L^3)(H_2O)_4]\cdot 10H_2O$ [Ln^{3+}= Eu^{3+}, Sm^{3+} and Gd^{3+}]	$\mathbf{H_8L^3}$	H_2SO_4	3D	39
$[La(H_5L^7)(H_2O)_3]\cdot H_2O$	$\mathbf{H_8L^7}$	—	3D	40
$[Ln(H_5L^8)(H_2O)_2]\cdot 2H_2O$ (Ln = La and Nd)	$\mathbf{H_8L^8}$	—	2D	41
$[Ln(H_5L^8(H_2O)_2)\cdot 2H_2O$ (Ln = La, Nd, Gd and Dy)	$\mathbf{H_8L^8}$	—	2D	41
$[Ln_2(H_2L^8(H_2O)_4)]\cdot 4H_2O$ (Ln = La, Nd, Gd and Dy)	$\mathbf{H_8L^8}$	—	2D	41
$[NaLn(H_4L^8(H_2O)_2)]\cdot 2H_2O$ (Ln = La, Nd, Gd and Dy)	$\mathbf{H_8L^8}$	—	3D	41
$La[C_6H_4PO_{7/4}(OH)_{5/4}]_4C\cdot 4H_2O$	$\mathbf{H_8L^9}$	—	2D	42
$[La_2(H_2O)_6(H_5L^{10})_2]\cdot$Solv	$\mathbf{H_8L^{10}}$	—	3D	43

1.3. Preparation of phosphonic acid linkers

Phosphonate-based compounds find several applications in various research areas and in society such as herbicides,[44] antiviral agents,[45] pharmaceutical/biological active compounds,[46, 47] enzyme inhibitors,[48] flame retardants,[49] corrosion suppressors,[50, 51] heavy metal chelators[52, 53] and organic synthesis reagents.[54] In this context, the preparation of phosphonic acids and their derivatives has been the subject of intensive research that led to a large body of both new and improved methodologies toward the formation of carbon-phosphorus (C–P) bonds.[55]

Some selected methods of phosphonate esters and phosphonic acid synthesis that ultimately resulted in the organic linkers presented in Scheme 1.1 are illustrated and described in the following sub-sections. This summary does not intend to be an exhaustive description of the methods toward the formation of phosphonic acids but, instead, highlights the most common and straightforward ones.

1.3.1. The Michaelis-Arbuzov reaction

This type of reaction for a C–P bond formation is the primary, and the most employed, synthetic route being usually thermally initiated.[56] The product is a dialkylphosphonate proceeding mainly between primary alkyl halides and trialkyl phosphite derivatives (Scheme 1.2).

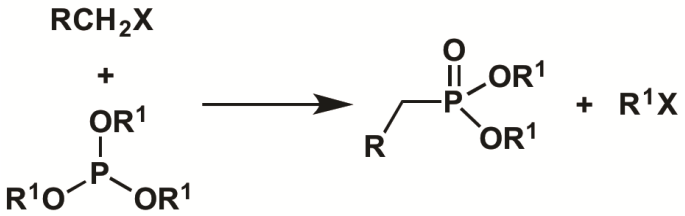

Scheme 1.2. The Michaelis-Arbuzov reaction.

This reaction can be divided into two steps, both consisting of nucleophilic substitutions, generating a phosphonium salt intermediate (Scheme 1.3). Substrates for the Michaelis-Arbuzov reaction can be alkyl halides, mainly alkyl bromides and iodides, due to their higher reactivity. Acyl halides, substituted alkynyl halides[57] and α-bromo esters[58] are also suitable to react with trialkyl phosphite, giving the corresponding phosphonates.

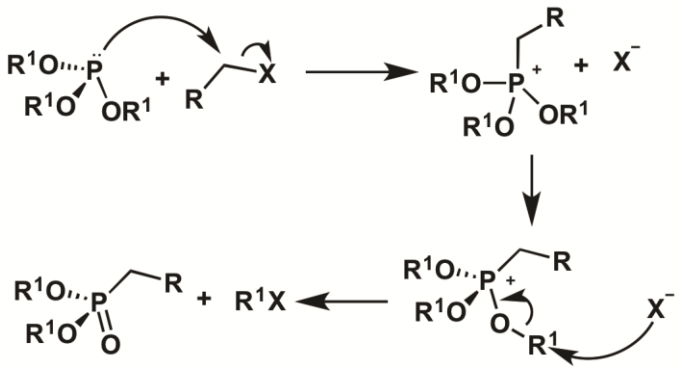

Scheme 1.3. Mechanism of the Michaelis-Arbuzov reaction.

The choice of the trialkyl phosphite is very important because of the generated byproduct, *i.e.*, alkyl halide, at the end of the reaction. The reactivity and volatility of this compound is crucial to achieve high yields of the desired product. The reaction is likely to have a high yield if the byproduct is a less reactive and more volatile halide. Thus, triethyl and triisopropyl phosphite are more often used than trimethyl phosphite because, in the latter case, the methyl halide can compete with the substrate, lowering the overall yield of the desired product.

Recent improvements of the Michaelis-Arbuzov rearrangement involve acceleration of the reaction using microwave-assisted methodologies,[59, 60] trials using ultrasound,[61] Lewis acid catalysts[62] and trimethylsilyl halides[63] in order to perform the reaction in mild conditions. There are also procedures involving ionic liquids.[64]

Plabst and Bein,[41] as well as Taylor and co-workers[40] used the Michaelis-Arbuzov reaction as one of the steps involved in the synthesis of ligands **H_8L^8** and **H_8L^7**, respectively (Scheme 1.4).

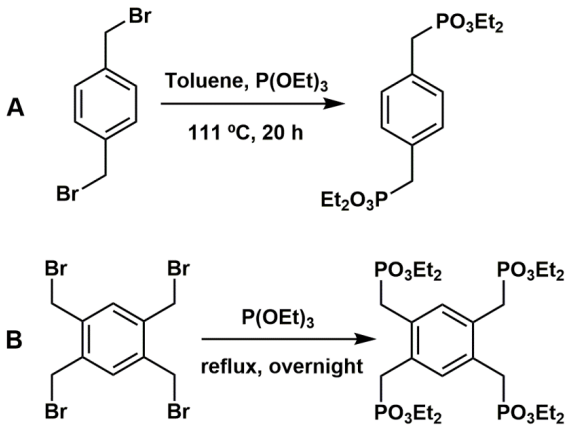

Scheme 1.4. A) Synthesis of tetraethyl-1,4-bis(phosphonomethyl)benzene. Reaction for the synthesis of the organic linker **H_8L^8** developed by Plabst and Bein.[41] B) Synthesis of octaethyl-1,2,4,5-tetrakis(phosphonomethyl)benzene. Precursor of ligand **H_8L^7**.[40]

1.3.2. Catalytic cross-coupling

Due to their usually poor or lack of reactivity with trialkyl phosphite or dialkyl phosphite, aryl and alkenyl halides are not suitable substrates for the Michaelis-Arbuzov reaction or the Michaelis-Becker reaction. The catalytic cross-coupling reaction, like the Michaelis-Arbuzov reaction, is a method of synthesis of dialkyl aryl and alkenylphosphonates from aryl and alkenyl halides and dialkyl, trialkyl or any phosphorus-centered nucleophile with the general formula $RP(OR^1)_2$. The reaction occurs in the presence of a transition metal catalyst as depicted in Scheme 1.5.

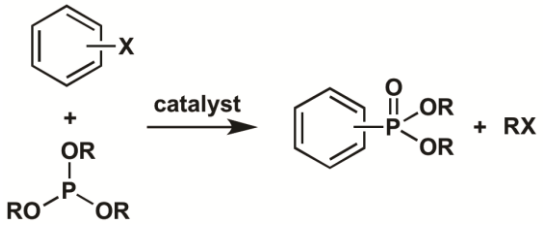

Scheme 1.5. Catalytic cross-coupling reaction.

Using triethylphosphite it was discovered that copper bronze, nickel(II) bromide and nickel(II) chloride can catalyze the reaction with aryl halides, successfully yielding diethyl arylphosphonates. These methodologies are still used though some modifications have been implemented, such as the use of palladium(II) acetate or chloride.[65] To achieve better results in milder conditions, the coupling reaction with dialkyl phosphonates was performed in the presence of a base and a new catalyst was introduced, tetrakis(triphenylphosphine)palladium(0), which made it possible to perform the reaction at lower temperatures (Scheme 1.6).[66, 67] Further modifications, changing the catalyst to a mixture of palladium(II) acetate and 1,1'-bis(diphenylphosphino)ferrocene (dppf) allowed a reduction in the catalyst loadings used in the reaction.[68]

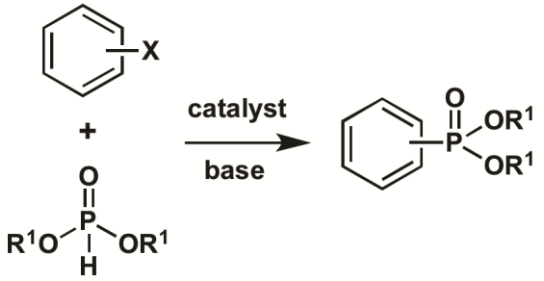

Scheme 1.6. Nickel- or palladium-catalyzed cross-coupling reaction.

For both nickel[69] and palladium cross-coupling reactions there are proposed mechanisms to explain what occurs during each step of the reaction (see sub-section 2.3.1 in Chapter 2 for more details). In a simplistic fashion, the catalysts promote the reaction through an oxidative addition and a reductive elimination process.

Many examples of multifunctional arylphosphonic acids applied as organic linkers in coordination chemistry were obtained using this methodology. An important example concerns the synthesis of the **H_8L^{10}** precursor, which was reported by two different groups using two distinct approaches: Vasylyev *et al.*[70] used a palladium catalyzed cross-coupling reaction, while Jones *et al.*[71] used a nickel-catalyzed cross-coupling reaction (Scheme 1.7).

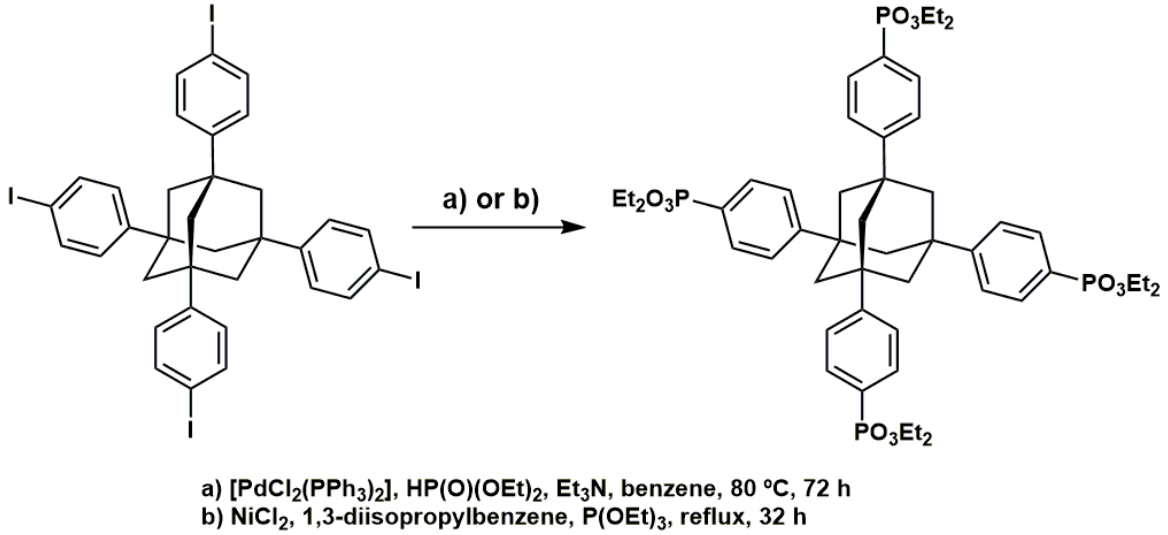

Scheme 1.7. Synthesis of octaethyl-1,3,5,7-tetrakis(4-phosphonophenyl)adamantane. a) Procedure followed by Vasylyev and co-workers[70] with a reported yield of 76%. b) Procedure used by Jones *et al.*[71] with a reported yield of 85%.

In a similar fashion, the preparation of the ester precursor of the phosphonic acid **H_8L^9** was reported by Zareba and co-workers using a procedure optimized to obtain multigram quantities, without the need for chromatographic separation: tetrakis(4-bromophenyl)methane was subjected to nickel-catalyzed cross-coupling with triethyl phosphite, leading to octaethyl-tetrakis(4-phosphonophenyl)methane, with an yield of 61%.[72] An alternative approach was later on proposed by Schütrumpf *et al.*,[20] using tetrakis(triphenylphosphine)palladium(0) as catalyst, in a palladium-catalyzed cross-coupling reaction that originated the corresponding dialkyl phosphonate product with an improved yield of 89% (Scheme 1.8).

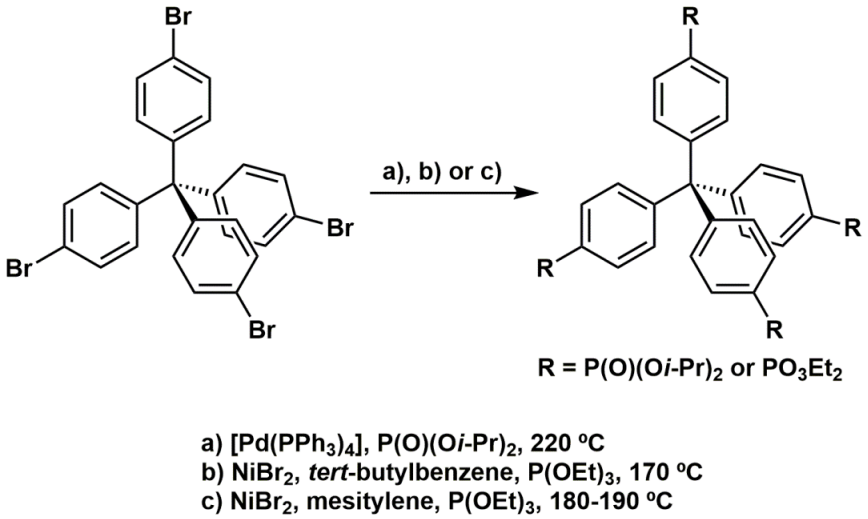

Scheme 1.8. a) Synthesis of octaisopropyl-tetrakis(4-phosphonophenyl)methane. Procedure used by Schütrumpf *et al.*[20] with a reported yield of 89%. b) and c) Synthesis of octaethyl-tetrakis(4-phosphonophenyl)methane. b) Procedure followed by Zareba and co-workers[72] with a reported yield of 61%. c) Procedure followed by Perez *et al.*[42] with a reported yield of 56%.

1.3.3. The Moedritzer-Irani reaction

The Moedritzer-Irani reaction[73] or the Mannich-type condensation (Scheme 1.9) is a simple, economic and common route for the synthesis of *N,N*-disubstituted aminomethylphosphonic acids. This reaction is a special case of Kabachnik-Fields reaction and has the advantage of giving the aminophosphonic acid directly without a hydrolysis step (a discussion about the hydrolysis methodologies of phosphonate esters will be provided in sub-section 1.3.4).

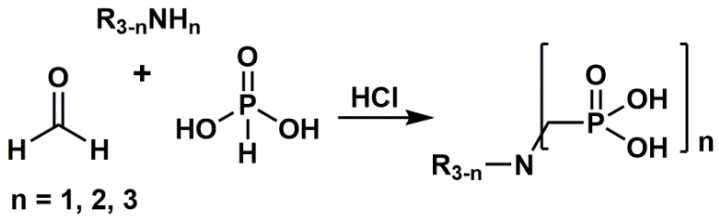

Scheme 1.9. The Moedritzer-Irani reaction.

Although this is a rather inexpensive synthesis, this methodology has the disadvantage of having many byproducts throughout the various steps of the reaction. In some cases, only recrystallization may provide a reasonably pure product. Villemin and co-workers[59] conducted a vast study of this synthetic approach and reported the synthesis of a

series of aminophosphonic acids based on the reaction of various polyamines with phosphorous acid and formaldehyde in water. The selection of microwave as heating source allowed better yields and reduced reaction times comparatively to conventional heating, although the final step of the reaction (recrystallization of the product) can pose some limitations when the acids are very soluble in water. Compounds $\mathbf{H_8L^1}$-$\mathbf{H_8L^5}$ were synthesized using the Moedritzer-Irani reaction.[37, 59]

1.3.4. Transformation of dialkyl phosphonates to phosphonic acids

To obtain the desired phosphonic acid molecules, after functionalization with phosphonate esters a hydrolysis reaction is performed using hydrochloric acid mixtures as depicted in Scheme 1.10.

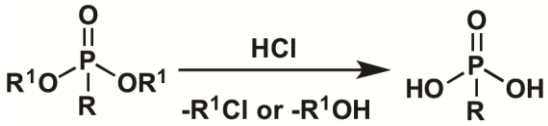

Scheme 1.10. Acidic hydrolysis of dialkyl phosphonates.

In cases where the acidic hydrolysis cannot be performed, either due to degradation of the starting material or other reaction factors, a milder procedure at ambient temperature can be alternatively employed. It considers the transformation of alkyl ester groups into silyl ones by means of trimethylsilyl halides, using mainly bromotrimethylsilane, with the subsequent water hydrolysis or methanolysis (Scheme 1.11).[74-76]

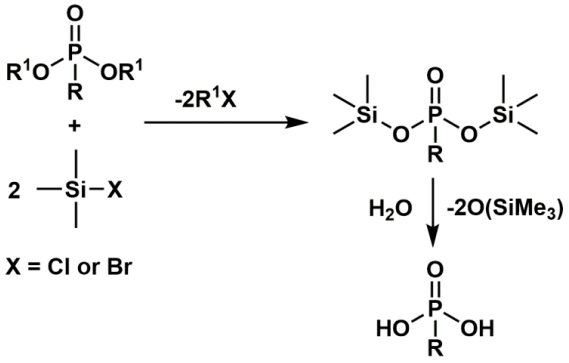

Scheme 1.11. Tandem of transsilylation and hydrolysis of dialkyl phosphonates.

Another hydrolysis approach was reported by Shimizu and co-workers.[77] They developed a synthetic procedure toward a pyrene-tetraphosphonate ester derivative, followed by a "partial hydrolysis" to obtain a tetraphosphonate monoester (Scheme 1.12).

Phosphonate monoesters have, on one hand, the potential to offer carboxylate-like coordination modes to metals and, on the other hand, they act as monoanionic bidentate oxygen donor ligands.[78-80]

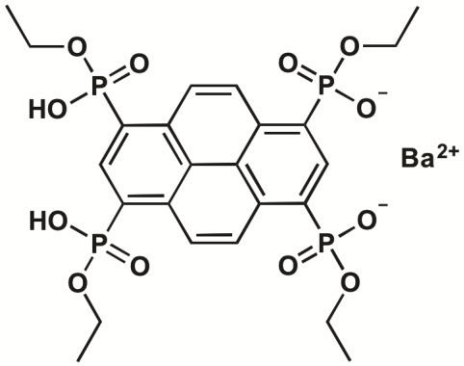

Scheme 1.12. Barium tetraethyl-1,3,6,8-tetrakis(phosphonate)pyrene.

1.4. Lanthanide-tetraphosphonic frameworks

1.4.1. H_8L^1, H_8L^4 and H_8L^6

H_8L^1 is the smallest aminotetraphosphonic ligand illustrated in Scheme 1.1 and has several structural similarities with **H_8L^4**: the proximity of the phosphonic groups, as well as their connectivity through methylene groups to the amine. We note that, to the best of our knowledge, there is not a single MOF-type report using either of these two ligands and lanthanide metals.

Due to the mentioned proximity of phosphonic groups, **H_8L^1** and **H_8L^4** were used successfully by Janicki and co-workers in the synthesis of lanthanide(III) discrete complexes, and their structural and photophysical properties were evaluated.[29-31] The organic ligand acts as a chelate, coordinating through the nitrogen and the oxygen atoms, thus embracing completely the metal centers. Compounds based on polyaminopolyphosphonic acids and lanthanides that form complexes hold great interest, especially due to their application in medicine, *e.g.*, as magnetic resonance imaging (MRI) agents, possible therapeutic pharmaceuticals in bone pain palliation and as strong *in vivo* complexation agents.[81, 82] For one particular case, a cyclic tetrameric Nd-**L^1** based compound,[32] the crystal packing showed that a tunneled structure with an internal diameter of *ca.* 5.2 Å is formed (Figure 1.1). This particular anionic discrete entity, $[Nd_4(\mathbf{L^1})_4]^{20-}$, set apart by being highly negatively charged and with some degree of rigidity, hosts in its cavity water molecules, H^+ and K^+ cations. The K^+ cations not only counter balance the

negative charges of the complexes, but also hold together the tunneled crystal packing due to their positioning in the center of the tetramers. In this way, the structure is stabilized by both hydrogen bonds and electrostatic interactions.

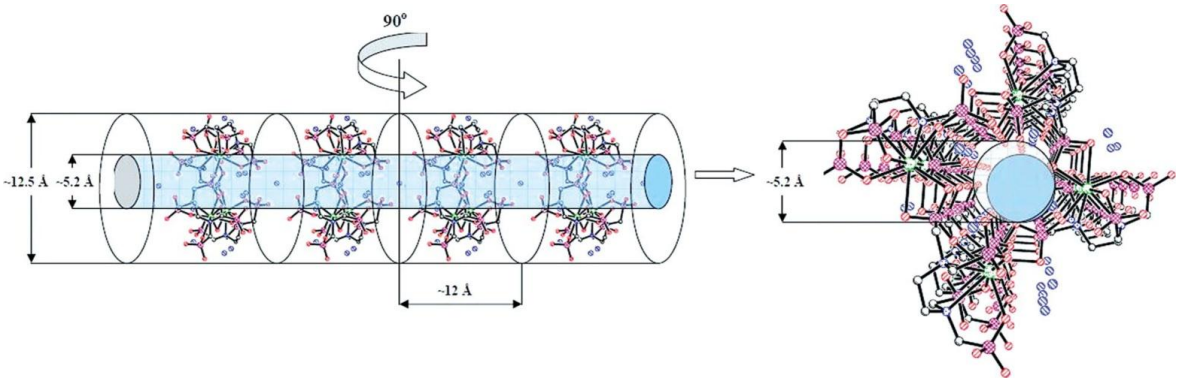

Figure 1.1. Crystal packing of the Nd-**L**[1] tetramer evidencing the rods formed by the close packing of the individual discrete complexes. "Reprinted (adapted) with permission from reference.[32] Copyright (2013) John Wiley & Sons, Inc."

Aiming for the same biological application, Yang *et al.* successfully used **H_8L^6**, a polyazamacrocycle derivative, in the self-assembly of two isotypical families of 1D LnOFs with potential application as contrast agents for magnetic resonance imaging (MRI):[33] $[Ln(H_7L^6)(H_2O)_2]Cl_2{\cdot}xH_2O$ (where Ln = La, Nd, Sm, Eu, Gd, and Tb) and $[Ln(H_7L^6)(H_2O)_2](ClO_4)_2{\cdot}xH_2O$ (where Ln = Nd, Sm, Eu, Gd, and Tb). Reactions were performed in aqueous solutions at low pH, using a slow diffusion methodology. The 1D chained structures feature metal centers doubly bridged by C–PO_3 tetrahedra and, in a similar fashion to the aforementioned Ln(III) discrete complexes, the methylene groups bearing the phosphonate moieties are all turned toward the inorganic metal chains (Figure 1.2).

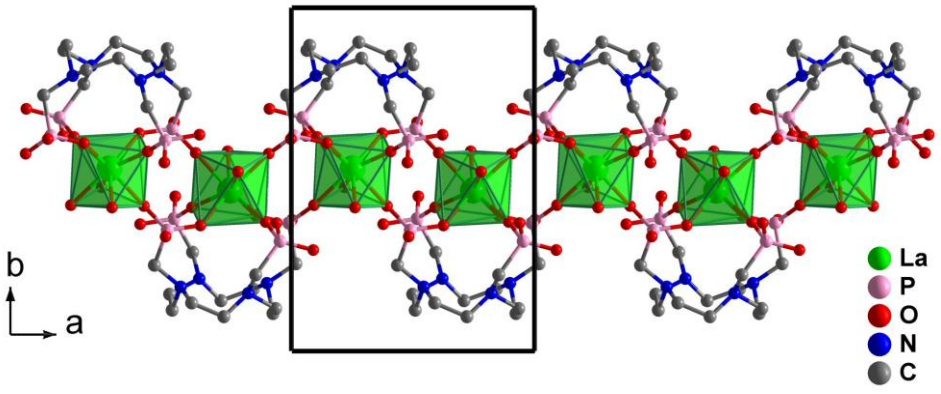

Figure 1.2. Fragment of $[La(H_7L^6)(H_2O)_2]Cl_2{\cdot}xH_2O$, representing the 1D chains found in both families of the reported isotypical families of compounds. For clarity, all crystallization water molecules, H and Cl atoms were omitted.

1.4.2. H_8L^2 and H_8L^5

In 2006 and 2007, Ying and co-workers investigated the coordination ability of **H_8L^2** for the preparation of novel lanthanide polyphosphonates.[34-36] They reported a layered (2D) Gd^{3+} compound and four 3D LnOFs (Ln = La^{3+}, Nd^{3+}, Eu^{3+} and Gd^{3+}) that also contained oxalic acid as ancillary ligand. Oxalic acid has been extensively combined with rare-earth cations. Its anion usually forms direct and close bridges between two metal centers, coordinating the metal through two oxygen atoms from the neighboring carboxyl groups.[83] Because lanthanide phosphonates have low solubilities in water and other organic solvents, being this a significant drawback when growing single-crystals suitable for X-ray structural analysis, the inclusion of a second ligand, such as oxalic acid proved, on one hand, to be a great improvement for both the solubility and crystallinity of lanthanide phosphonates and, on the other hand, it also showed to be a successful synthetic methodology for the design of new architectures.

3D LnOFs, based on Nd^{3+}, Eu^{3+} and Gd^{3+}, are isotypical and formulated as $[Ln_2(H_6L^2)(ox)_2(H_2O)_2]\cdot 4H_2O$. These compounds exhibit a pillared-type structure, that can be described in two different ways: i) metals interconnected by oxalate and $[-NH(CH_2PO_3H)_2]^{2-}$ moieties, with the organic $-CH_2-$ chains acting as pillars; or ii) lanthanide tetraphosphonate layers cross-linked by oxalate anions. On the other hand, the LnOF with La^{3+} is slightly different. $[La_2(H_6L^2)(ox)_2]\cdot 2H_2O$, featuring a 3D framework with tunnels running parallel to the *a*-axis, is built up by the interconnection of metals bridged by $(\mathbf{H_6L^2})^{2-}$ residues. The oxalate anions are located inside the tunnels. The structural differences between these two families of networks, $[Ln_2(H_6L^2)(ox)_2(H_2O)_2]\cdot 4H_2O$ and $[La_2(H_6L^2)(ox)_2]\cdot 2H_2O$, could be mainly explained by the fact that the phosphonate ligands adopt different coordination modes when bound to the metallic centers.[35, 36] In addition, as also pointed out by the authors, the well-known effect coined as "lanthanide contraction" may also be at play, with the smaller (and heavier) lanthanides being more prone to be hydrated.

The 2D compound is based exclusively on Gd^{3+} ions and **H_8L^2** linkers, formulated as $[Gd(H_5L^2)]\cdot 2H_2O$ and prepared using similar hydrothermal conditions as the aforementioned 3D LnOFs. The structure features inorganic metal chains running parallel to the *a*-axis, with neighboring Gd^{3+} cations being connected to each other by two phosphonate groups. Chains are then bridged by $(\mathbf{H_5L^2})^{3-}$ anions, resulting in a 2D layered

structure. Strong hydrogen bonds between non-coordinated phosphonate oxygens interlink the layers into a 3D supramolecular structure.[34]

H_8L^2 and **H_8L^5** were employed in the synthesis of mixed Ce(III) sulfate-tetraphosphonate frameworks reported by Costantino and co-workers (Figure 1.3).[37] Compounds isolated using **H_8L^2**, formulated as $[Ce_2(H_2O)_6(H_4L^2)(HSO_4)_2]\cdot 4H_2O$ and $[Ce_2(H_2O)_2(H_4L^2)(HSO_4)_2]\cdot 2H_2O$, and **$H_8L^5$**, formulated as $[Ce_2(H_2O)_6(H_4L^5)(HSO_4)_2]$, contain sulfate anions acting as bidentate ligands. Their presence increases the dimensionality of the materials to 3D networks because they act as secondary ligands connecting neighboring Ce^{3+} cations, thus, acting as effective bridges, and not only as charge stabilizers.

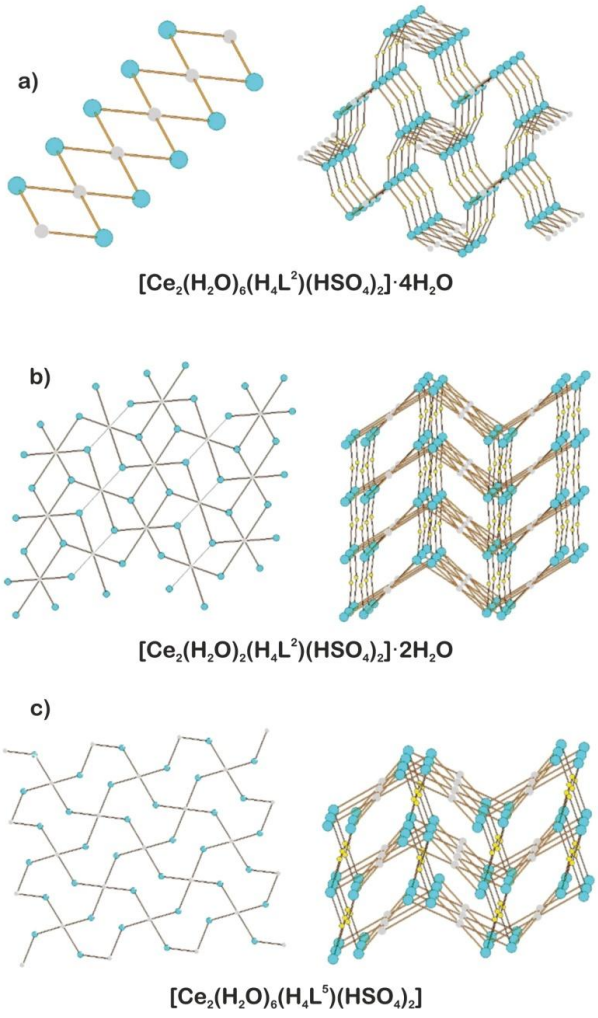

Figure 1.3. *(left)* Topological representation and *(right)* 3D structures of the Ce-phosphonate networks reported by Costantino *et al.*:[37] **a)** $[Ce_2(H_2O)_6(H_4L^2)(HSO_4)_2]\cdot 4H_2O$, **b)** $[Ce_2(H_2O)_2(H_4L^2)(HSO_4)_2]\cdot 2H_2O$ and **c)** $[Ce_2(H_2O)_6(H_4L^5)(HSO_4)_2]$. The pale blue, gray and yellow spheres represent cerium cations, phosphonate ligands and sulfate groups, respectively. "Reprinted (adapted) with permission from reference [37]. Copyright (2010) American Chemical Society."

The two compounds prepared using $\mathbf{H_8L^2}$ are considered pseudo-polymorphic (or solvates) because they essentially only differ in their water content: three water molecules coordinated to the metal center and four crystallization water molecules in $[Ce_2(H_2O)_6(H_4L^2)(HSO_4)_2]\cdot 4H_2O$ and only one water molecule coordinated to the metal and two crystallization water molecules in $[Ce_2(H_2O)_2(H_4L^2)(HSO_4)_2]\cdot 2H_2O$. In the former compound, cerium-phosphonate moieties form 1D columnar pillars parallel to the *a*-axis (Figure 1.3a). The pillars are then connected together by the sulfate groups into a 3D network. In the latter structure, a binodal layer parallel to the *ab* plane is formed by the cerium metals and $(\mathbf{H_4L^2})^{4-}$ ligands. The third dimension is reached thanks to the bridges based on the sulfate anions. In a similar fashion, for the material assembled with $\mathbf{H_8L^5}$, layers parallel to the *bc* plane are also connected by sulfate groups.

The report also described the luminescent properties of the compounds. As expected, two types of emission bands were observed: a strong and narrow band between 300 and 400 nm, attributable to the Ce^{3+} ions emission of UV radiation, and a second broad band registered between 400 and 700 nm assigned to the intraligand transition of the diamino tetraphosphonates. The attribution of this visible band was confirmed by the observation of an analogous behavior in the pure diamino tetraphosphonic acids.

1.4.3. $\mathbf{H_8L^3}$

A flexible microporous family of LnOFs was prepared and reported by Colodrero and co-workers using the diaminophosphonic acid $\mathbf{H_8L^3}$.[38] Although the ambient temperature preparation of the materials presented by the authors takes two months, they were able to obtain 3D open-framework compounds having channels filled with water molecules. Crystallographic studies indicate that the metal centers are exclusively coordinated by oxygen atoms from the terminal tetrahedral phosphonate groups. Furthermore, the incorporation of a ligand possessing an aliphatic chain of six carbons confers to the structure substantial flexibility, which allowed the framework to adjust depending on the number of guest molecules inside the pores. The thermal treatment of the initial $[La(H_5L^3)]\cdot 7H_2O$ compound led to a dehydrated framework with no lattice water molecules, $[La(H_5L^3)]$ (Figure 1.4). This latter compound was not stable when exposed to air at ambient temperature, leading to the immediate incorporation of two water molecules within the framework after just 1 h, thus forming a third framework, $[La(H_5L^3)]\cdot 2H_2O$.

Remarkably, this partially rehydrated network demonstrated much higher ambient temperature stability than the other LnOFs.

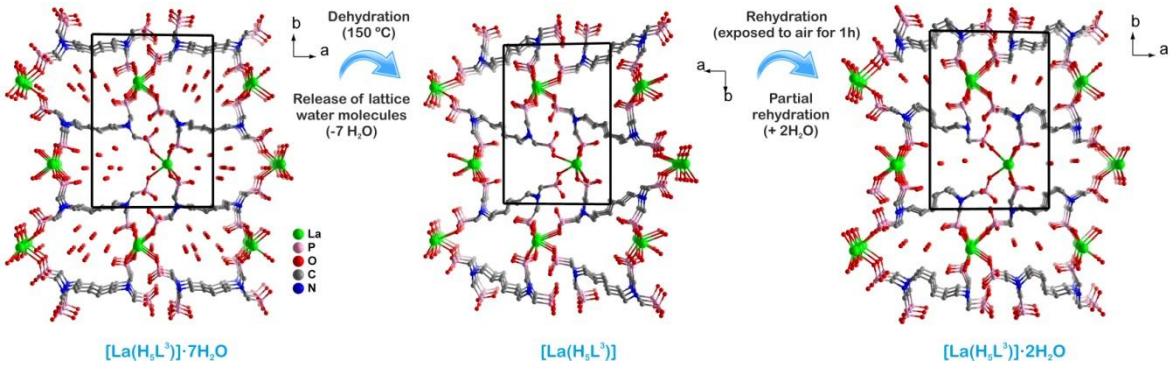

Figure 1.4. Schematic representation of the reversible conversion between the various structures reported by Colodrero and co-workers using the diaminophosphonic acid $\mathbf{H_8L^3}$.[38]

Because of the 1D channels filled with water molecules, the protonic conductivity of $[La(H_5L^3)]\cdot 7H_2O$ was evaluated. Excellent conductivity results were obtained ($\sigma = 8\times10^{-3}$ S cm^{-1}) at 24 ºC and 98 % RH (relative humidity), with an activation energy of 0.25 eV. Outgassing this compound, either under high vacuum at ambient temperature, or at 200 ºC, resulted in the anhydrous material, $[La(H_5L^3)]$. Adsorption-desorption measurements performed using this phase further confirmed the flexibility of this family of compounds, with a particularly interesting result concerning the uptake of NO (nitric oxide): NO adsorption capacity at *ca.* 1 bar was 0.95 mmol g^{-1} (2.85 wt %), comparable to those of some zeolites; however, isotherms are indicative of a strong irreversible adsorption of NO within the pores of the framework, possibly indicating that the NO is bonded to the metal ions.

Our research group has recently improved considerably the reaction times for the synthesis of MOFs assembled using this organic linker. The addition of sulfuric acid to the reaction media led to a new family of LnOFs, formulated as $[Ln_2(SO_4)_2(H_6L^3)(H_2O)_4]\cdot 10H_2O$ [Ln^{3+}= Eu^{3+}, Sm^{3+} and Gd^{3+}], prepared using microwave irradiation at moderate temperatures (80 ºC) and reduced reaction times (15 min). Sulfuric acid proved to be essential in the formation of these materials by delaying the coordination process, *i.e.*, blocking the access of the phosphonic acid groups by coordinating the sulfate anion to the metal centers, leading to the formation of a compact 3D network (Figure 1.5).[39]

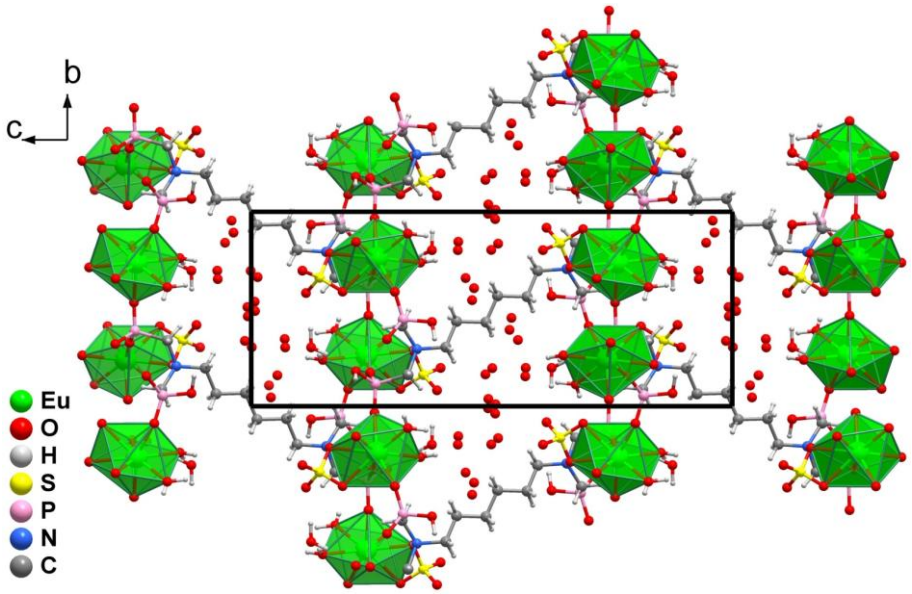

Figure 1.5. Representation of the crystal packing of $[Ln_2(SO_4)_2(H_6L^3)(H_2O)_4]\cdot 10H_2O$ [Ln^{3+}= Eu^{3+}, Sm^{3+} and Gd^{3+}] viewed along the [100] direction.

1.4.4. H_8L^7

The LnOF materials mentioned to this point had their luminescent properties attributed to either the lanthanide ions characteristic emission or to intraligand fluorescent emission. The absence of suitable sensitizers in the organic PBUs (primary building units) typically leads to poor photoluminescent properties of the final materials. To overcome this disadvantage, and potentially boost the emission of the isolated LnOFs, the inclusion of specific groups, such as aromatic rings, into the organic PBUs is required in order to promote the so-called "antenna effect", *i.e.*, ligand-to-metal and/or metal-to-ligand charge transfer. The inclusion of aromatic rigid moieties further enhanced the stability and robustness of materials and promoted an increase in porosity and dimensionality of networks, when compared to materials prepared solely using aliphatic linkers, which usually lead to layered and very compact structures.

Taylor and co-workers used **H_8L^7** to continue their development of new ion conductors and studies of molecular-level transport mechanisms in MOFs.[40] Their aim was to obtain a structurally robust material that is stable in humid environments, resists swelling and, at the same time, has channels filled with crystallographically located water molecules and acidic groups, disposed in such a way that should offer a clear pathway of proton biding sites. Their synthesis strategy included the addition of acid during the self-

assembly of the material. This helped the modulation of crystal growth through protonation of phosphonic moieties, in order to facilitate the exclusion of some metal centers from coordinating with the phosphonate groups, consequently avoiding the formation of a dense and pillared structure. $[La(H_5L^7)(H_2O)_3]\cdot H_2O$ represents the first 3D phosphonate-based LnOF with free diprotic acid groups and adopts a modified pillared-layered motif network, where the hydrophobic part of the ligand pillars hydrophilic 1D La^{3+} phosphonate columns (Figure 1.6). The highly acidic nature of the channels, along with the identification of free water molecules that fill the porous network bridging the phosphonic acid groups through hydrogen bonds, creates a potential hydrogen bond pathway. This factor, allied with the possibility of phosphonate groups to reorient, contributed to the registered proton conductivity values on the order of the best MOF materials: $\sigma = 2.5\times10^{-3}$ S cm^{-1} at 60 ºC and 98 % RH (Figure 1.7).

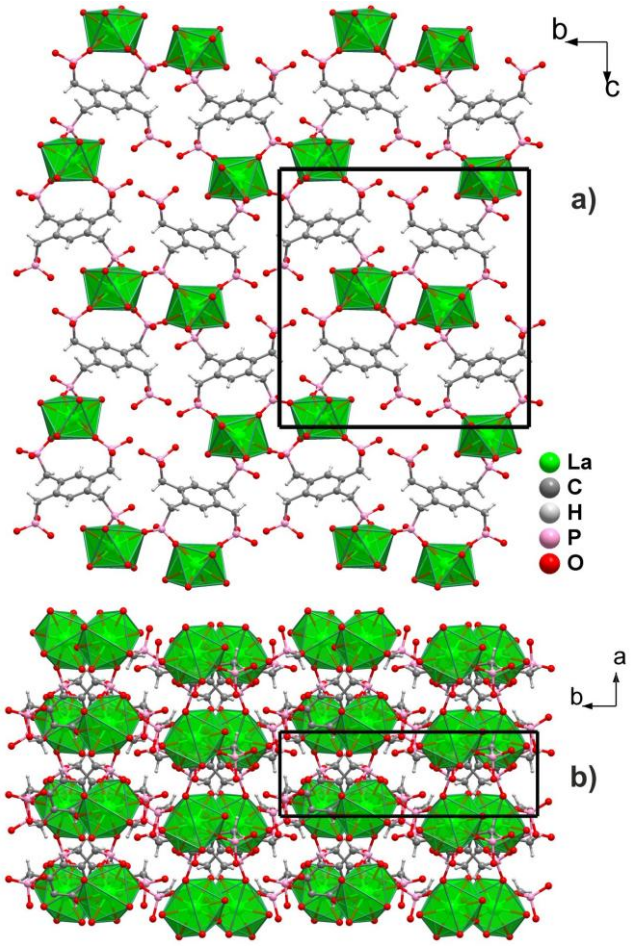

Figure 1.6. Mixed ball-and-stick and polyhedral representation of the crystal packing of $[La(H_5L^7)(H_2O)_3]\cdot H_2O$, reported by Taylor and collaborators,[40] as viewed along the **a)** [100] and **b)** [001] directions of the unit cell. The scheme also emphasizes the hydrophobic portion of the organic linker pillaring hydrophilic lanthanum phosphonate units.

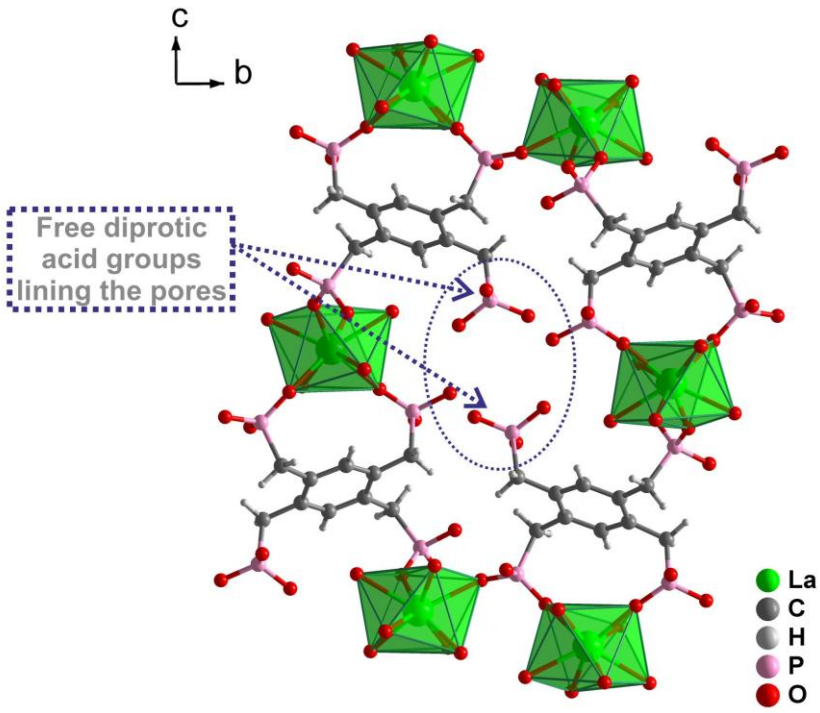

Figure 1.7. Portion of $[La(H_5L^7)(H_2O)_3]\cdot H_2O$, as reported by Taylor and collaborators,[40] emphasizing the presence of uncoordinated phosphonic acid moieties within small channels filled with solvent molecules.

1.4.5. H_8L^8

Plabst and Bein designed and prepared in 2009 the organic linker **H_8L^8** to specifically coordinate lanthanide cations.[41] The molecule has two bisphosphonate groups that can act as bidentate chelating ligands featuring extended and highly variable coordination modes and geometries. The proximity of the phosphonate groups in the linker enables this compound to coordinate to large ions with high coordination numbers, such as lanthanides. A series of high-throughput screening reactions, under hydrothermal conditions, was performed using **H_8L^8** and La^{3+}, Nd^{3+}, Gd^{3+} and Dy^{3+}. Reaction parameters such as time, temperature, pH or ligand/metal/solvent ratios were systematically modified in order to form a library of ninety six samples which were evaluated and compared using powder X-ray diffraction. Fourteen new compounds were obtained that ultimately were systematized into four new LnOF phases.

The most interesting structure emerged when 4 equiv. of NaOH were added to the reaction mixtures with 1 equiv. of metal, leading to the formation of $[NaLa(H_4L^8)(H_2O)_2)]\cdot 2H_2O$ featuring a 3D open framework. The compound showed a well-defined coordination geometry for the lanthanide cations which were coordinated by

bisphosphonate units in an exclusively bidentate fashion. Additionally, compounds from this phase stand out from the remaining ones due to their distinctive and consistent thermal profile (Figure. 1.8).

Later that year, Plabst and co-workers conducted further investigations on the above mentioned 3D material regarding the selectivity of the open-framework toward metal cations.[84] They undertook a combined study of the ion-exchange properties and the framework flexibility. In a first stage, the material was successfully dehydrated after heating for 2 h at 180 ºC (Figure 1.8). Then they proceeded to a series of trials to attempt the replacement of Na^+ cations by alkaline-earth (Mg^{2+}, Ca^{2+}, Sr^{2+}, Ba^{2+}), other alkaline (Li^+, K^+, Rb^+, Cs^+) or selected transition metal ions (Ni^{2+}, Cu^{2+}, Zn^{2+}, Mn^{2+}), using saturated aqueous solutions of the respective salts. Authors concluded that the ionic guests played a crucial role in the chain-forming/breaking mechanism that determined both the flexibility of the framework and the equilibrium between the expanded and the contracted forms, being more than charge equalizers and/or space fillers. The strong response of the framework to guests also led to enhanced selectivity of the material to monovalent cations (Figure 1.9). Divalent cations might reduce the stability and charge balance of the material and, thus, were unequivocally excluded from the open framework, which represented a strikingly interesting result because absolute selectivity is rare in inorganic open-framework ion-exchange materials, and generally relates to the size rather than charge of the guest compounds.

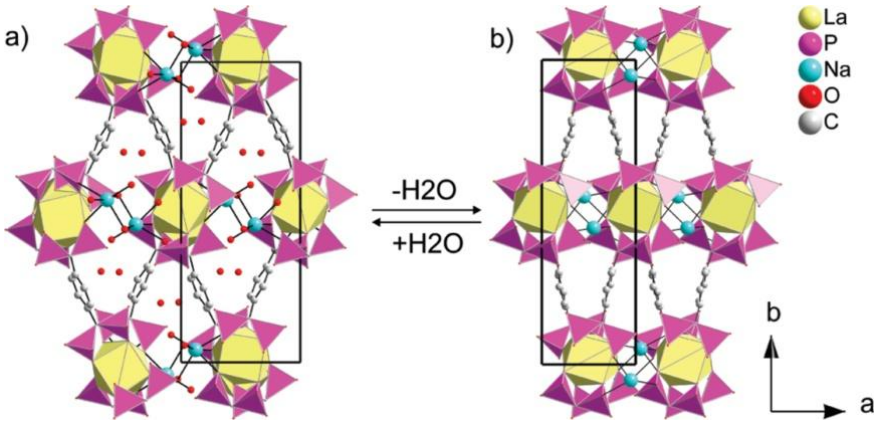

Figure 1.8. Structural representation of the reversible conversion between $[NaLa(H_4L^8)(H_2O)_2)]\cdot 2H_2O$ and $[NaLa(H_4L^8)(H_2O)_2)]$ through the removal, or inclusion, of water molecules. Upon dehydration, the water molecules coordinated to sodium leave the structure. The metal compensates the loss by forming two new bonds with adjacent phosphonate oxygens. "Reprinted (adapted) with permission from reference.[84] Copyright (2009) American Chemical Society."

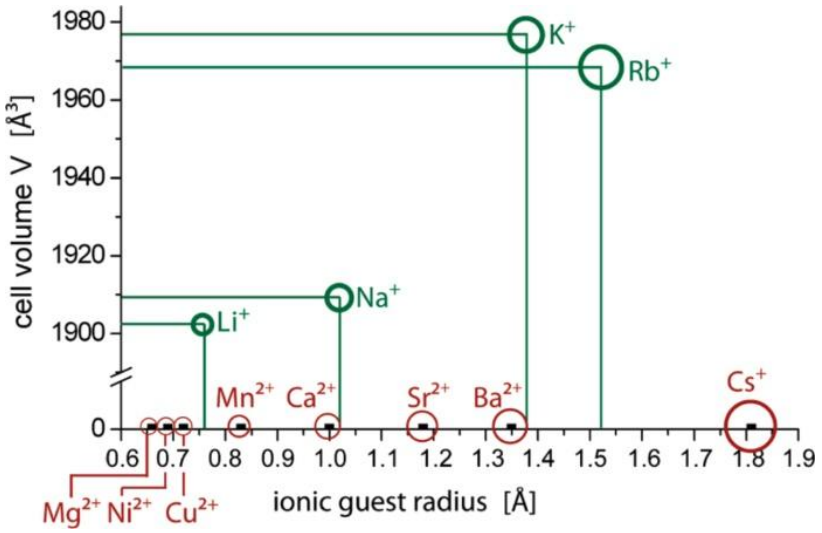

Figure 1.9. Radii of the ions which are taken up (green) or not taken up (red) by [MLa(H_4L^8)] and correlation with the respective cell volume in its highest observed hydrated state: [LiLa(H_4L^8)]·4H_2O dried in air, [NaLa(H_4L^8)]·4H_2O, dried in air; [KLa(H_4L^8)]·(2+*x*)H_2O, humidified; [RbLa(H_4L^8)]·2H_2O humidified or dried in air. "Reprinted (adapted) with permission from reference.[84] Copyright (2009) American Chemical Society."

1.4.6. H_8L^9

A member of the tetraphenylmethane (TPM) family of organic molecules recently reported by Zareba *et al.*[72] is **H_8L^9**. We note that the interest around the central TPM unit resides in its large ("bulky") size and structural rigidity and orientation, which greatly governs the crystal chemistry of the molecule itself and of its derivatives. **H_8L^9** was employed by Perez and co-workers in the preparation of a new lanthanum-phosphonate framework formulated as La[$C_6H_4PO_{7/4}(OH)_{5/4}]_4C$·4$H_2O$ (Figure 1.10).[42] The reported La-phosphonate framework features 2D compact layers, where the metal is coordinated to four different (**H_5L^9**)$^{3-}$ residues. The coordination of the metal to the phosphonate moieties plays a decisive role in the overall stability of the framework, along with the numerous weak hydrogen bonds that exist between the C–PO_3 tetrahedra and the phenyl groups of the adjacent interpenetrated TPM unit.

A remarkable feature of La[$C_6H_4PO_{7/4}(OH)_{5/4}]_4C$·4$H_2O$ is its closely related crystal structure to the corresponding anhydrous tetraphosphonic acid molecule alone, [$C_6H_4PO(OH)_2]_4C$, in addition to the ester precursor, [$C_6H_4PO(OEt)_2]_4C$·H_2O. Considering the tetrahedral nature of the central TPM group and its connection to C–PO_3 moieties, a model for the design of closely related frameworks could then take place. The topochemistry of these compounds can be understood by replacing the TPM [$C_6H_4]_4C$ core

by a large C4 tetrahedron and the C–PO_3 groups by small tetrahedra. The rigid aromatic core and phosphonate groups are preferentially stacked along one direction, forming identical single columns. This 1D pseudocubic stacked body (Figure 1.11) has its stability reinforced by supramolecular interactions involving free and coordination water molecules. In the case of $La[C_6H_4PO_{7/4}(OH)_{5/4}]_4C{\cdot}4H_2O$ the resulting square section columns are interconnected by rows of $LaO_4(H_2O)_4$ bicapped octahedra as depicted in Figure 1.11 (*inset*).

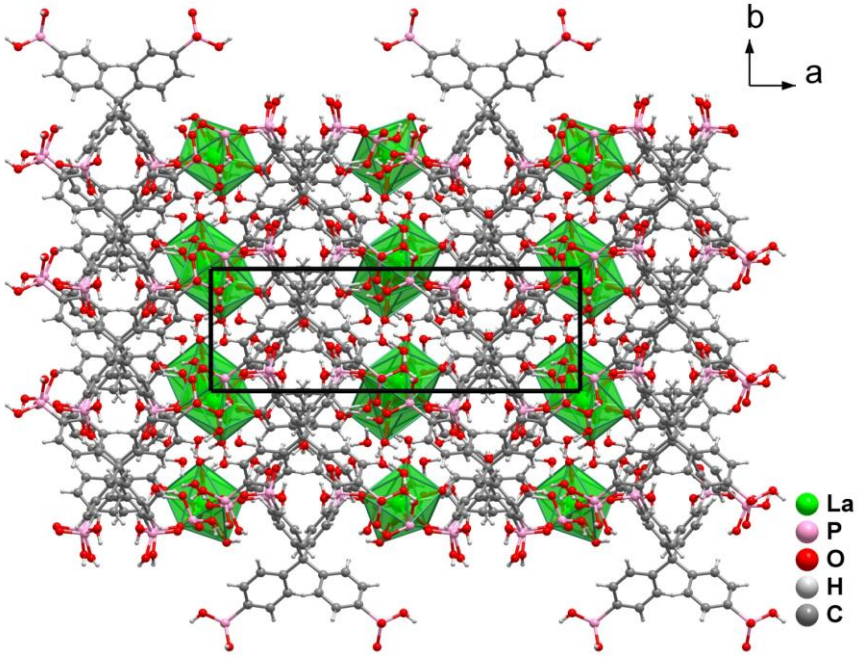

Figure 1.10. Mixed ball-and-stick and polyhedral representation of the crystal structure of $La[C_6H_4PO_{7/4}(OH)_{5/4}]_4C{\cdot}4H_2O$ viewed along the [001] direction.

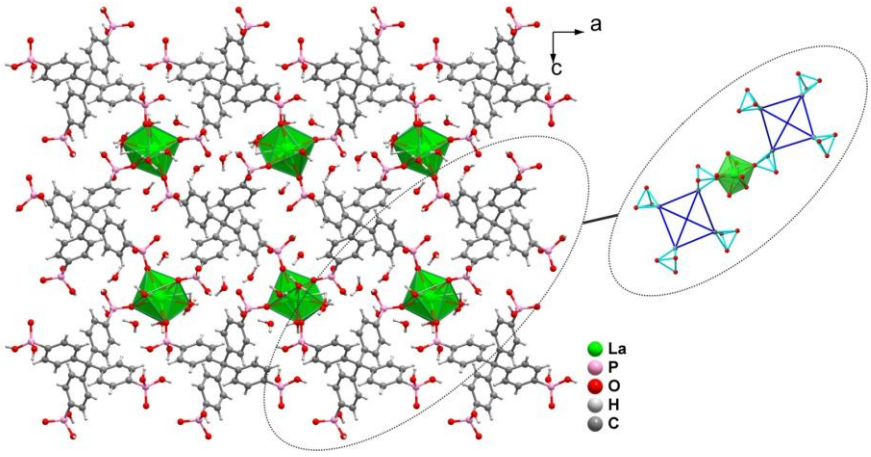

Figure 1.11. Arrangements of the tetraphenylmethane and C–PO_3 tetrahedra units in the crystal structure of $La[C_6H_4PO_{7/4}(OH)_{5/4}]_4C{\cdot}4H_2O$, forming columns parallel to the [010] direction. *Inset* – Schematic representation of the pseudocubic section of the crystal structure.

1.4.7. H_8L^{10}

Boldog and co-workers[43] have investigated the symmetric adamantane-based tetrahedral ligand **H_8L^{10}** in an attempt to increase the porosity and surface area of materials, while preserving the framework robustness. During the screening of the various crystallization conditions using a slow interdiffusion approach, a new crystalline phase was identified as $[La_2(H_2O)_6(H_5L^{10})_2]\cdot$Solv. This compound represented the first MOF of a lanthanide assembled with a truly multifunctional phenylphosphonate linker, *i.e.*, possessing more than two phosphonate moieties in the same organic backbone, thus constituting the starting point for the design of lanthanide-based MOFs of high connectivity based on rigid large phenylphosphonates (Figure 1.12).

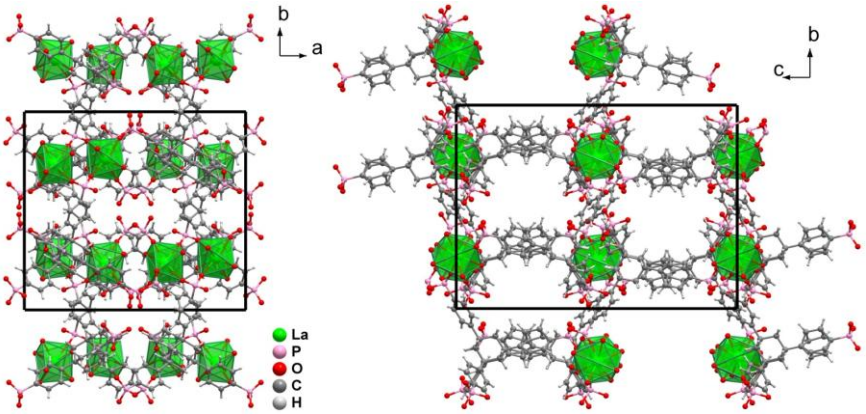

Figure 1.12. Mixed ball-and-stick and polyhedral representation of the crystal structure of $[La_2(H_2O)_6(H_5L^{10})_2]\cdot$Solv viewed along the *(left)* [001] and *(right)* [100] directions of the unit cell, emphasizing the presence of a large open void space (for clarity crystallization solvents in the pores were omitted).

However, the material was not pure. Because of this no quantitative studies regarding the porosity of the open framework could be performed. Nevertheless, single-crystal X-ray diffraction studies showed that the pores are filled by a mixture of disordered water and methanol guest molecules situated in a structure that has its geometry greatly determined by the rigidity of the organic ligand.

1.5. Thermal stability

The majority of LnOF compounds described and discussed in the sub-sections above were developed and prepared by their authors targeting specific properties and

potential applications. This required a multidisciplinary cycle of design, execution and assessment around a key aspect: clear structure-activity relationships. In the field of hybrid materials, structural integrity and stability of the compounds may determine, in many cases, how the material will operate. Taking this factor into account, Table 1.2 summarizes the thermal stability of most of the reviewed LnOFs, determined when an amorphous phase is obtained, either due to instability of the framework (as a consequence of loss of water molecules) or when the organic moiety is decomposed. We note that not all described frameworks are listed in Table 1.2. Several compounds are missing either due to incomplete data in the original papers or due to dubious reported information which could not be verified.

As expected, the increase in dimensionality of frameworks, 1D→2D→3D, seems to contribute to a higher thermal robustness of the LnOFs. An increase in dimensionality is usually associated with an increased metal connectivity and, consequently, to the presence of fewer coordination water molecules. The inclusion of an ancillary linker also seems to promote some thermal stability, especially in the case of compounds possessing oxalate anions. Again, this feature was somehow expected because, as mentioned above, the coordination sphere of cations is completed by oxygens from an anion instead of water molecules that tend to immediately leave the structure when the material is exposed to higher temperatures, leaving naked / unprotected coordination sites. An example that illustrates well how the number of water molecules of coordination could limit the stability of the framework are the two families of compounds assembled using $\mathbf{H_8L^2}$: $[La_2(H_6L^2)(ox)_2]\cdot 2H_2O$ showed a higher thermal stability when compared to $[Ce_2(H_2O)_6(H_4L^2)(HSO_4)_2]\cdot 4H_2O$. The large number of water molecules present in the latter material, concomitantly associated with the presence of a large number of uncoordinated phosphonate groups, is clearly responsible for the overall poor thermal stability. Both these factors explain the enhancement in robustness and stability for the La^{3+} compound.

There is also a clear distinction regarding the thermal stability between the LnOFs assembled using phosphonoaliphatic or phosphonoaromatic organic linkers, $\mathbf{H_8L^1}$-$\mathbf{H_8L^6}$ and $\mathbf{H_8L^7}$-$\mathbf{H_8L^{10}}$, respectively. Besides the structures based on $\mathbf{H_8L^2}$ and ancillary oxalate anions whose thermal stability reaches *ca.* 510 ºC, all the LnOFs based on phosphonoaliphatic ligands are less stable than phosphonoaromatic ones. As mentioned above, the presence of the bridging oxalate anions clearly boosts the overall framework thermal stability, much more than those containing sulfate anions.

Table 2. Decomposition temperature of the LnOFs.

Compound	Organic linker	Ancillary linker	Structural features	Decomposition Temperature (ºC)	Ref.
$[Ln(H_7L^6)(H_2O)_2]Cl_2{\cdot}xH_2O$ (where Ln = La, Nd, Sm, Eu, Gd, and Tb)	$\mathbf{H_8L^6}$	—	1D	*ca.* 300-320	33
$[Ln(H_7L^6)(H_2O)_2](ClO_4)_2{\cdot}xH_2O$ (where Ln = Nd, Sm, Eu, Gd, and Tb)	$\mathbf{H_8L^6}$	—	1D	*ca.* 300-320	33
$[Ln_2(H_6L^2)(ox)_2(H_2O)_2]{\cdot}4H_2O$ (Ln = Nd, Eu, Gd)	$\mathbf{H_8L^2}$	H_2ox	3D	*ca.* 510	35, 36
$[La_2(H_6L^2)(ox)_2]{\cdot}2H_2O$	$\mathbf{H_8L^2}$	H_2ox	3D	*ca.* 510	36
$[Ce_2(H_2O)_6(H_4L^2)(HSO_4)_2]{\cdot}4H_2O$	$\mathbf{H_8L^2}$	H_2SO_4	3D	*ca.* 300-350	37
$[Ce_2(H_2O)_2(H_4L^2)(HSO_4)_2]{\cdot}2H_2O$	$\mathbf{H_8L^2}$	H_2SO_4	3D	*ca.* 300-350	37
$[Ce_2(H_2O)_6(H_4L^5)(HSO_4)_2]$	$\mathbf{H_8L^5}$	H_2SO_4	3D	*ca.* 300-350	37
$[La(H_5L^3)]{\cdot}7H_2O$ (Ln = La, Sm)	$\mathbf{H_8L^3}$	—	3D	*ca.* 250	38
$[Ln_2(SO_4)_2(H_6L^3)(H_2O)_4]{\cdot}10H_2O$ [Ln^{3+}= Eu^{3+}, Sm^{3+} and Gd^{3+}]	$\mathbf{H_8L^3}$	H_2SO_4	3D	*ca.* 100	39
$[La(H_5L^7)(H_2O)_3]{\cdot}H_2O$	$\mathbf{H_8L^7}$	—	3D	*ca.* 300	40
$[Ln(H_5L^8)(H_2O)_2]{\cdot}2H_2O$ (Ln = La and Nd)	$\mathbf{H_8L^8}$	—	2D	*ca.* 600	41
$[Ln(H_5L^8(H_2O)_2){\cdot}2H_2O$ (Ln = La, Nd, Gd and Dy)	$\mathbf{H_8L^8}$	—	2D	*ca.* 600	41
$[Ln_2(H_2L^8(H_2O)_4)]{\cdot}4H_2O$ (Ln = La, Nd, Gd and Dy)	$\mathbf{H_8L^8}$	—	2D	*ca.* 600	41
$[NaLn(H_4L^8(H_2O)_2)]{\cdot}2H_2O$ (Ln = La, Nd, Gd and Dy)	$\mathbf{H_8L^8}$	—	3D	*ca.* 500-600	41

1.6. Outline and Main Objectives of this PhD Thesis

The scope of this PhD project is based on the preparation of functional and multidimensional MOFs from the self-assembly of lanthanides as metallic centers with new tetrapodal phosphonate-based organic ligands, selected and prepared by myself. Therefore, for the first task of this work it is proposed the synthesis of two different organic ligands (Scheme 1.13):

i) [1,1'-biphenyl-3,3',5,5'-tetrayltetrakis(phosphonic acid) (**H_8btp**): a new tetrapodal organic ligand to be used for expanding the family of Metal-Organic Frameworks based on rigid aromatic tetraphosphonic building units;

ii) pyrene-1,3,6,8-tetrayltetrakis(phosphonic acid) (**H_8ptp**): a compound analogue of **H_8btp** but with a pyrene core instead of the biphenyl backbone; to assess the influence of increased rigidity in the organic moieties of the resulting materials;

Based on the literature and previous works describing new and improved methodologies toward the C–P bond formation, it is aimed to prepare all organic molecules using specific synthetic routes. If possible, the strategy will include mild reaction conditions, as well as easy employed purification techniques to successfully isolate both the intermediate phosphonate esters and also the final hydrolyzed phosphonic acids.

Predictably, the synthesis of compounds will be carried out using conventional heating and, if possible, microwave-assisted synthesis (MWAS). The evolution of all reactions will be qualitatively analyzed by thin layer chromatography (TLC) and the purification of intermediate compounds will be carried out either by flash column chromatography or employing crystallization processes using the adequate organic solvents.

All organic compounds will be fully characterized by standard liquid-state techniques (NMR spectroscopy and mass spectrometry) and, if possible, single-crystal X-ray diffraction.

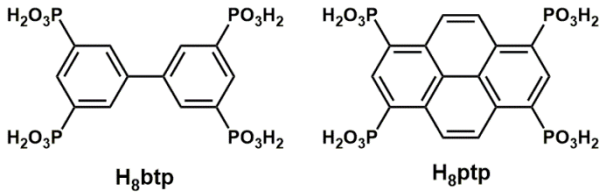

Scheme 1.13. Representation of the molecular structures of the phosphonic acids prepared during the PhD project.

The synthesis of the MOF materials will be based on the use of distinct synthetic methodologies, namely: i) hydro(solvo)thermal synthesis; ii) microwave-assisted synthesis; and iii) "one-pot" synthesis, *i.e.*, a conventional *bench* methodology where the reaction occurs with the help of a magnetic stirrer, optionally with heating. To prepare functional MOFs as phase-pure compounds, preferably with large crystal sizes suitable to be studied by single-crystal X-ray diffraction, it will be necessary to optimize the various reaction parameters (*i.e.*, reaction temperature and time, pH of the reaction medium, solvents or mixtures of solvents, irradiation power, pressure and stirring, for the case of microwave-assisted synthesis, among others). Materials will be characterized using several standard solid-state techniques (powder and single-crystal X-ray diffraction, vibrational spectroscopy (FT-IR and FT-Raman), electron microscopy (SEM and EDS), solid-state

NMR, thermogravimetric and elemental analyses) to determine and investigate the crystalline structure.

Investigations on the intrinsic properties of the resulting MOF materials (*i.e.*, photoluminescence, catalytic behavior and protonic conductivity) may only be possible with the close collaboration with some researchers and group leaders expert in these scientific fields. Thus, the photoluminescent properties of the optically-active MOFs will be analyzed by Dr. Duarte Ananias; the catalytic behavior of the materials will be investigated in Dr. Anabela Valente's research group and the protonic conductivity properties will be investigated in collaboration with the research group led by Dr. Filipe Figueiredo, all Researchers of the Associated Laboratory CICECO (and from the Departments of Chemistry, Physics and Materials & Ceramic Engineering of the University of Aveiro).

Therefore, the main goals to be accomplished using the isolated materials are:

i) analysis of photoluminescent behavior (for materials containing optically-active lanthanide metallic centers);
ii) heterogeneous catalytic behavior, because MOF materials are, usually, stable powdered compounds in several organic solvents. It is proposed the evaluation of catalytic activity of the resulting MOFs in the ring-opening reaction of styrene oxide and the acetalization reaction of benzaldehyde, both in methanol;
iii) protonic conductivity properties evaluation, mainly, for the more stable and robust MOFs, since these studies are performed using variable temperature and humidity conditions.

1.7. References

(1) Horcajada, P.; Gref, R.; Baati, T.; Allan, P. K.; Maurin, G.; Couvreur, P.; Férey, G.; Morris, R. E.; Serre, C.; *Chem. Rev.*, **2012**, *112*, 1232.

(2) Kreno, L. E.; Leong, K.; Farha, O. K.; Allendorf, M.; Van Duyne, R. P.; Hupp, J. T.; *Chem. Rev.*, **2012**, *112*, 1105.

(3) Ramaswamy, P.; Wong, N. E.; Shimizu, G. K. H.; *Chem. Soc. Rev.*, **2014**, *43*, 5913.

(4) Li, J. R.; Kuppler, R. J.; Zhou, H. C.; *Chem. Soc. Rev.*, **2009**, *38*, 1477.

(5) Kurmoo, M.; *Chem. Soc. Rev.*, **2009**, *38*, 1353.

(6) He, Y. B.; Zhou, W.; Krishna, R.; Chen, B. L.; *Chem. Commun.*, **2012**, *48*, 11813.

(7) Chughtai, A. H.; Ahmad, N.; Younus, H. A.; Laypkov, A.; Verpoort, F.; *Chem. Soc. Rev.*, **2015**, *44*, 6804.

(8) Karmakar, A.; Desai, A. V.; Ghosh, S. K.; *Coord. Chem. Rev.*, **2016**, *307*, 313.

(9) Allendorf, M. D.; Bauer, C. A.; Bhakta, R. K.; Houk, R. J. T.; *Chem. Soc. Rev.*, **2009**, *38*, 1330.

(10) Stock, N.; Biswas, S.; *Chem. Rev.*, **2012**, *112*, 933.

(11) Eddaoudi, M.; Kim, J.; Rosi, N.; Vodak, D.; Wachter, J.; O'Keeffe, M.; Yaghi, O. M.; *Science*, **2002**, *295*, 469.

(12) Wang, S. F.; Wang, J. J.; Cheng, W. W.; Yang, X. W.; Zhang, Z. Y.; Xu, Y.; Liu, H. K.; Wu, Y.; Fang, M.; *Dalton Trans.*, **2015**, *44*, 8049.

(13) Distler, A.; Lohse, D. L.; Sevov, S. C.; *J. Chem. Soc.-Dalton Trans.*, **1999**, 1805.

(14) Yang, W. T.; Parker, T. G.; Sun, Z. M.; *Coord. Chem. Rev.*, **2015**, *303*, 86.

(15) Demadis, K. D.; Stavgianoudaki, N. In *Chapter 14 Structural Diversity in Metal Phosphonate Frameworks: Impact on Applications*; The Royal Society of Chemistry, **2012**. pp 438.

(16) Maeda, K.; *Microporous Mesoporous Mat.*, **2004**, *73*, 47.

(17) Drumel, S.; Janvier, P.; Deniaud, D.; Bujoli, B.; *J. Chem. Soc.-Chem. Commun.*, **1995**, 1051.

(18) Tang, S. F.; Song, J. L.; Mao, J. G.; *Eur. J. Inorg. Chem.*, **2006**, 2011.

(19) Zheng, T.; Yang, Z. X.; Gui, D. X.; Liu, Z. Y.; Wang, X. X.; Dai, X.; Liu, S. T.; Zhang, L. J.; Gao, Y.; Chen, L. H.; Sheng, D. P.; Wang, Y. L.; Juan, D. W.; Wang, J. Q.; Zhou, R. H.; Chai, Z. F.; Albrecht-Schmitt, T. E.; Wang, S.; *Nat. Commun.*, **2017**, *8*, 11.

(20) Schutrumpf, A.; Kirpi, E.; Bulut, A.; Morel, F. L.; Ranocchiari, M.; Lork, E.; Zorlu, Y.; Grabowsky, S.; Yucesan, G.; Beckmann, J.; *Cryst. Growth Des.*, **2015**, *15*, 4925.

(21) Shimizu, G. K. H.; Vaidhyanathan, R.; Taylor, J. M.; *Chem. Soc. Rev.*, **2009**, *38*, 1430.

(22) Gagnon, K. J.; Perry, H. P.; Clearfield, A.; *Chem. Rev.*, **2012**, *112*, 1034.

(23) Mahimaidoss, M. B.; Krasnikov, S. A.; Reck, L.; Onet, C. I.; Breen, J. M.; Zhu, N. Y.; Marzec, B.; Shvets, I. V.; Schmitt, W.; *Chem. Commun.*, **2014**, *50*, 2265.

(24) Taddei, M.; Costantino, F.; Vivani, R.; *Eur. J. Inorg. Chem.*, **2016**, 4300.

(25) Paz, F. A. A.; Klinowski, J.; Vilela, S. M. F.; Tome, J. P. C.; Cavaleiro, J. A. S.; Rocha, J.; *Chem. Soc. Rev.*, **2012**, *41*, 1088.

(26) Colodrero, R. M. P.; Angeli, G. K.; Bazaga-Garcia, M.; Olivera-Pastor, P.; Villemin, D.; Losilla, E. R.; Martos, E. Q.; Hix, G. B.; Aranda, M. A. G.; Demadis, K. D.; Cabeza, A.; *Inorg. Chem.*, **2013**, *52*, 8770.

(27) Taylor, J. M.; Mahmoudkhani, A. H.; Shimizu, G. K. H.; *Angew. Chem.-Int. Edit.*, **2007**, *46*, 795.

(28) Clearfield, A.; *J. Alloy. Compd.*, **2006**, *418*, 128.

(29) Mondry, A.; Janicki, R.; *Dalton Trans.*, **2006**, 4702.

(30) Galezowska, J.; Janicki, R.; Mondry, A.; Burgada, R.; Bailly, T.; Lecouvey, M.; Kozlowski, H.; *Dalton Trans.*, **2006**, 4384.

(31) Janicki, R.; Monteil, M.; Lecouvey, M.; Mondry, A.; *Opt. Mater.*, **2013**, *36*, 259.

(32) Janicki, R.; Mondry, A.; *Eur. J. Inorg. Chem.*, **2013**, 3429.

(33) Yang, T. H.; Zhou, K.; Bao, S. S.; Zhu, C. J.; Zheng, L. M.; *Inorg. Chem. Commun.*, **2008**, *11*, 1075.

(34) Ying, S. M.; Zeng, X. R.; Fang, X. N.; Li, X. F.; Liu, D. S.; *Inorg. Chim. Acta*, **2006**, *359*, 1589.

(35) Ying, S. M.; Liu, J. Q.; Cai, S. L.; Zhong, F.; Zhou, G. P.; *Acta Crystallogr. Sect. E.-Struct Rep. Online*, **2007**, *63*, M415.

(36) Ying, S. M.; Mao, J. G.; *Cryst. Growth Des.*, **2006**, *6*, 964.

(37) Costantino, F.; Ienco, A.; Gentili, P. L.; Presciutti, F.; *Cryst. Growth Des.*, **2010**, *10*, 4831.

(38) Colodrero, R. M. P.; Olivera-Pastor, P.; Losilla, E. R.; Aranda, M. A. G.; Leon-Reina, L.; Papadaki, M.; McKinlay, A. C.; Morris, R. E.; Demadis, K. D.; Cabeza, A.; *Dalton Trans.*, **2012**, *41*, 4045.

(39) Mendes, R. F.; Ananias, D.; Carlos, L. D.; Rocha, J.; Paz, F. A. A.; *Cryst. Growth Des.*, **2017**, *17*, 5191.

(40) Taylor, J. M.; Dawson, K. W.; Shimizu, G. K. H.; *J. Am. Chem. Soc.*, **2013**, *135*, 1193.

(41) Plabst, M.; Bein, T.; *Inorg. Chem.*, **2009**, *48*, 4331.

(42) Perez, O.; Bloyet, C.; Rueff, J. M.; Barrier, N.; Caignaert, V.; Jaffres, P. A.; Raveau, B.; *Cryst. Growth Des.*, **2016**, *16*, 6781.

(43) Boldog, I.; Domasevitch, K. V.; Baburin, I. A.; Ott, H.; Gil-Hernandez, B.; Sanchiz, J.; Janiak, C.; *Crystengcomm*, **2013**, *15*, 1235.

(44) Borjesson, E.; Torstensson, L.; *J. Chromatogr. A*, **2000**, *886*, 207.

(45) Rosowsky, A.; Fu, H. N.; Pai, N.; Mellors, J.; Richman, D. D.; Hostetler, K. Y.; *J. Med. Chem.*, **1997**, *40*, 2482.

(46) Alvarez, E.; Marquez, A. G.; Devic, T.; Steunou, N.; Serre, C.; Bonhomme, C.; Gervais, C.; Izquierdo-Barba, I.; Vallet-Regi, M.; Laurencin, D.; Mauri, F.; Horcajada, P.; *Crystengcomm*, **2013**, *15*, 9899.

(47) Berardi, D.; Carlesi, T.; Rossi, F.; Calderini, M.; Volpi, R.; Perfetti, G.; *Int. J. Immunopathol. Pharmacol.*, **2007**, *20*, 455.

(48) Winum, J. Y.; Innocenti, A.; Gagnard, V.; Montero, J. L.; Scozzafava, A.; Vullo, D.; Supuran, C. T.; *Bioorg. Med. Chem. Lett.*, **2005**, *15*, 1683.

(49) Xi, W.; Qian, L. J.; Huang, Z. G.; Cao, Y. F.; Li, L. J.; *Polym. Degrad. Stabil.*, **2016**, *130*, 97.

(50) Chafai, N.; Chafaa, S.; Benbouguerra, K.; Daoud, D.; Hellal, A.; Mehri, M.; *J. Taiwan Inst. Chem. Eng.*, **2017**, *70*, 331.

(51) Gholivand, K.; Yaghoubi, R.; Farrokhi, A.; Khoddami, S.; *J. Solid State Chem.*, **2016**, *243*, 23.

(52) Shaw, M. J.; Nesterenko, P. N.; Dicinoski, G. W.; Haddad, P. R.; *J. Chromatogr. A*, **2003**, *997*, 3.

(53) Park, I. H.; Jung, J. C.; Hwang, S. C.; Joo, J. O.; *Angew. Makromol. Chem.*, **1992**, *197*, 117.

(54) Illy, N.; Fache, M.; Menard, R.; Negrell, C.; Caillol, S.; David, G.; *Polym. Chem.*, **2015**, *6*, 6257.

(55) Zoń, J.; Garczarek, P.; BiaŁek, M. In *Synthesis of Phosphonic Acids and Their Esters as Possible Substrates for Reticular Chemistry*; The Royal Society of Chemistry, **2012**.

(56) Bhattacharya, A. K.; Thyagarajan, G.; *Chem. Rev.*, **1981**, *81*, 415.

(57) Iorga, B.; Eymery, F.; Carmichael, D.; Savignac, P.; *Eur. J. Org. Chem.*, **2000**, 3103.

(58) Ianni, A.; Waldvogel, S. R.; *Synthesis*, **2006**, 2103.

(59) Villemin, D.; Simeon, F.; Decreus, H.; Jaffres, P. A.; *Phosphorus Sulfur Silicon Relat. Elem.*, **1998**, *133*, 209.

(60) Kiddle, J. J.; Gurley, A. F.; *Phosphorus Sulfur Silicon Relat. Elem.*, **2000**, *160*, 195.

(61) Winum, J. Y.; Kamal, M.; Agnaniet, H.; Leydet, A.; Montero, J. L.; *Phosphorus Sulfur Silicon Relat. Elem.*, **1997**, *129*, 83.

(62) Renard, P. Y.; Vayron, P.; Leclerc, E.; Valleix, A.; Mioskowski, C.; *Angew. Chem.-Int. Edit.*, **2003**, *42*, 2389.

(63) Renard, P. Y.; Vayron, P.; Mioskowski, C.; *Org. Lett.*, **2003**, *5*, 1661.

(64) Matveeva, E. V.; Odinets, I. L.; Kozlov, V. A.; Shaplov, A. S.; Mastryukova, T. A.; *Tetrahedron Lett.*, **2006**, *47*, 7645.

(65) Adam, M. S. S.; Kindermann, M. K.; Kockerling, M.; Heinicke, J. W.; *Eur. J. Org. Chem.*, **2009**, 4655.

(66) Hirao, T.; Masunaga, T.; Ohshiro, Y.; Agawa, T.; *Synthesis*, **1981**, 56.

(67) Hirao, T.; Masunaga, T.; Yamada, N.; Ohshiro, Y.; Agawa, T.; *Bull. Chem. Soc. Jpn.*, **1982**, *55*, 909.

(68) Belabassi, Y.; Alzghari, S.; Montchamp, J. L.; *J. Organomet. Chem.*, **2008**, *693*, 3171.

(69) Balthazor, T. M.; Grabiak, R. C.; *J. Org. Chem.*, **1980**, *45*, 5425.

(70) Vasylyev, M. V.; Wachtel, E. J.; Popovitz-Biro, R.; Neumann, R.; *Chem.-Eur. J.*, **2006**, *12*, 3507.

(71) Jones, K. M. E.; Mahmoudkhani, A. H.; Chandler, B. D.; Shimizu, G. K. H.; *Crystengcomm*, **2006**, *8*, 303.

(72) Zareba, J. K.; Bialek, M. J.; Janczak, J.; Zón, J.; Dobosz, A.; *Cryst. Growth Des.*, **2014**, *14*, 6143.

(73) K., M.; Irani, R. R.; *J. Org. Chem.*, **1966**, *31*, 1603.

(74) Rabinowitz, R.; *J. Org. Chem.*, **1963**, *28*, 2975.

(75) McKenna, C. E.; Higa, M. T.; Cheung, N. H.; McKenna, M. C.; *Tetrahedron Lett.*, **1977**, 155.

(76) Morita, T.; Okamoto, Y.; Sakurai, H.; *Bull. Chem. Soc. Jpn.*, **1978**, *51*, 2169.

(77) Taylor, J. M.; Vaidhyanathan, R.; Iremonger, S. S.; Shimizu, G. K. H.; *J. Am. Chem. Soc.*, **2012**, *134*, 14338.

(78) Iremonger, S. S.; Liang, J. M.; Vaidhyanathan, R.; Shimizu, G. K. H.; *Chem. Commun.*, **2011**, *47*, 4430.

(79) Iremonger, S. S.; Liang, J. M.; Vaidhyanathan, R.; Martens, I.; Shimizu, G. K. H.; Thomas, D. D.; Aghaji, M. Z.; Yeganegi, S.; Woo, T. K.; *J. Am. Chem. Soc.*, **2011**, *133*, 20048.

(80) Zhang, J. W.; Zhao, C. C.; Zhao, Y. P.; Xu, H. Q.; Du, Z. Y.; Jiang, H. L.; *Crystengcomm*, **2014**, *16*, 6635.

(81) Finlay, O. G.; Mason, M. D.; Shelley, M.; *Lancet Oncol.*, **2005**, *6*, 392.

(82) Winter, P. M.; Seshan, V.; Makos, J. D.; Sherry, A. D.; Malloy, C. R.; Bansal, N.; *J. Appl. Physiol.*, **1998**, *85*, 1806.

(83) Janicki, R.; Mondry, A.; Starynowicz, P.; *Coord. Chem. Rev.*, **2017**, *340*, 98.

(84) Plabst, M.; McCusker, L. B.; Bein, T.; *J. Am. Chem. Soc.*, **2009**, *131*, 18112.

Chapter 2

Synthesis of Tetrapodal Phosphonate Organic Ligands

2.1. Organophosphorus Chemistry: Historical Survey and General Considerations

The beginning of organophosphorus chemistry was in the early 19th century with the first synthetic chemical study being reported by J. L. Lassaigne in 1820. It consisted of esterification of dehydrated phosphoric acid. Then in 1845, P. Thénard obtained a series of phosphine derivatives and from there progress on the preparation of these compounds has been fairly rapid.

Nowadays, phosphonate based compounds have focused the attention of many research groups around the world due to their many applications not only in biologically active molecules[1] but also their use as herbicide,[2] antiviral agents,[3] and other pharmaceutical applications,[4, 5] corrosion inhibitors,[6] flame retardants,[7] heavy metal chelators[8, 9] and organic synthesis reagents.[10] The described methodologies for the synthesis of phosphonic acids, developed throughout the years, led to an increase in the number of reactions available for the carbon-phosphorus (C–P) bond synthesis, as well as the improvement of the known ones.

This chapter will cover the selected methods and synthesis reactions to obtain the organic ligands used in this thesis for the self-assembly of new MOF materials. In a second stage will be presented and discussed the structural characterization of the newly obtained organic compounds.

2.2. The phosphonic acid group: structure and applications

Organic compounds possessing the general formula R'–P(O)$(OH)_2$ or R'–P(O)$(OR)_2$ (where R and R' = alkyl, aryl groups) are called phosphonic acids or phosphonates. The phosphorus atom presents *sp*^{3} hybridization, and so the geometry of the group is nearly tetrahedral (Scheme. 2.1).

2-Aminoethylphosphonic acid is the naturally-occurring phosphonate first identified in 1959,[11-15] although phosphonates biological role is still poorly understood.[1] Other compounds with bis- or polyphosphonates are not naturally occurring.

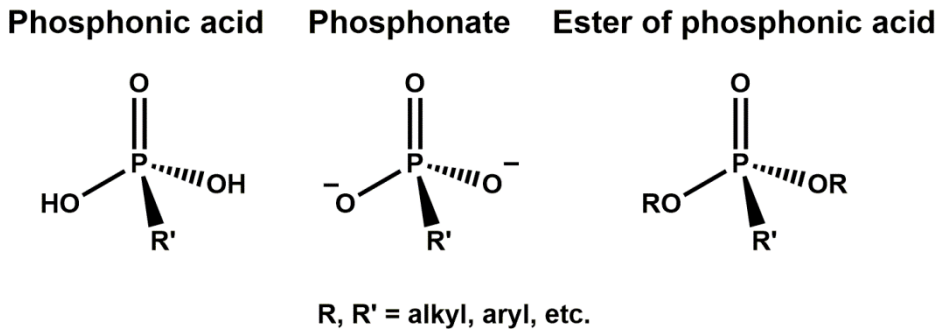

Scheme 2.1. General chemical structure of phosphonic acids, phosphonates and esters of phosphonic acid.

As mentioned above, phosphonates can be used for medical and non-medical applications. In pharmacology they are a class of drugs to treat osteoporosis and similar diseases,[16-18] as well as chelating agents to prevent the formation of insoluble precipitates due to their ability to strongly bind metal ions. Recently, phosphonates were found to serve as carriers for radionuclides in bone cancer treatments.[19, 20] Industrial routines, for example, peroxide bleach stabilizers[21] and desalination systems[22, 23] are some of the applications of this class of compounds through their chelating ability toward metals. Furthermore, due to their binding/chelating properties, phosphonates are also used in detergents and as anchor groups to bind various molecules to surfaces (*e.g.* metal oxide surfaces).[24-26]

2.3. Synthesis and characterization: preparation of phosphonic acid linkers and their phosphonate derivatives

Divalent phosphonic acids ($–PO_3H_2$) physical properties are remarkably different when compared to monovalent carboxylic and sulfonic acids ($–CO_2H$ and $–SO_3H$). Their high melting point and involatility are attributed to their capacity to form hydrogen bonds, enabling these hydrogen bonded networks of phosphonic acid groups to promote, for example, proton transport phenomena, which is a very important found application for proton conductions in fuel cell membranes (Scheme 2.2).[27]

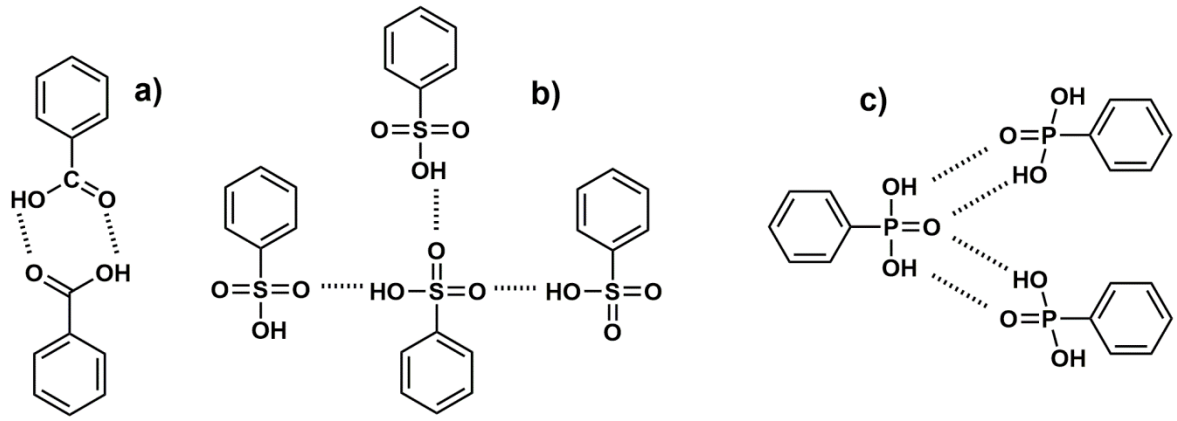

Scheme 2.2. Hydrogen bond schematic illustration in a) phenylcarboxylic acid, b) phenylsulfonic acid and c) phenylphosphonic acid.

Phosphonates many applications have attracted many research groups around the world. Consequently, the synthesis of phosphonic acids and their derivatives has been the subject of intensive research that led to an increase in the number of methodologies for the C–P bond synthesis, as discussed in the previous chapter. In the next sub-sections, it is highlighted and described in more detail the catalytic cross-coupling method, using palladium as catalyst, as well as the transformation of the dialkyl phosphonate intermediates obtained in this work into the final organic phosphonic acids.

2.3.1. Catalytic cross-coupling reaction

Phosphonic acids and their esters form the largest group of compounds containing C–P linkages. Nevertheless, during years prior to 1980, few important new methods for the generation of C–P bonds appeared, the principal being the Michaelis-Arbuzov reaction. With the growing interest in aryl and vinyl phosphonates in medicinal and polymer chemistry, as well as their usefulness as intermediates in organic synthesis, synthetic methodologies toward the functionalization of these compounds with phosphonate groups have attracted much attention.[28]

The first Pd^{II}-catalyzed P-arylation was performed using palladium(II) acetate and the rigid bidentate ligand 2,9-dimethyl-1,10-phenanthroline, without the addition of any base or acid to the reactive mixture. Since then, the Pd^{0}-catalyzed version of this methodology has been widely applied (Scheme 2.3), with the productivity of these reactions being extremely enhanced and the reaction times reduced due to microwave irradiation becoming a common heating method in organic chemistry.[29]

The palladium-catalyzed mechanism, also stated as the Hirao coupling,[30, 31] depends on several factors. It involves in the first step the reduction of the palladium(II) to a palladium(0) complex, if the source contains palladium(II); after that occurs the oxidative addition of the aryl halide to the palladium(0) complex; then ligand exchange is desired so trialkylphosphite is coordinated by the metal center and a nucleophilic substitution of the halide anion also occurs, giving diethyl phosphonate and ethyl halide. Finally the palladium(0) complex is regenerated and a carbon-phosphorus bond is created to form the phosphonate product, diethyl arylphosphonate (Scheme 2.3).[32]

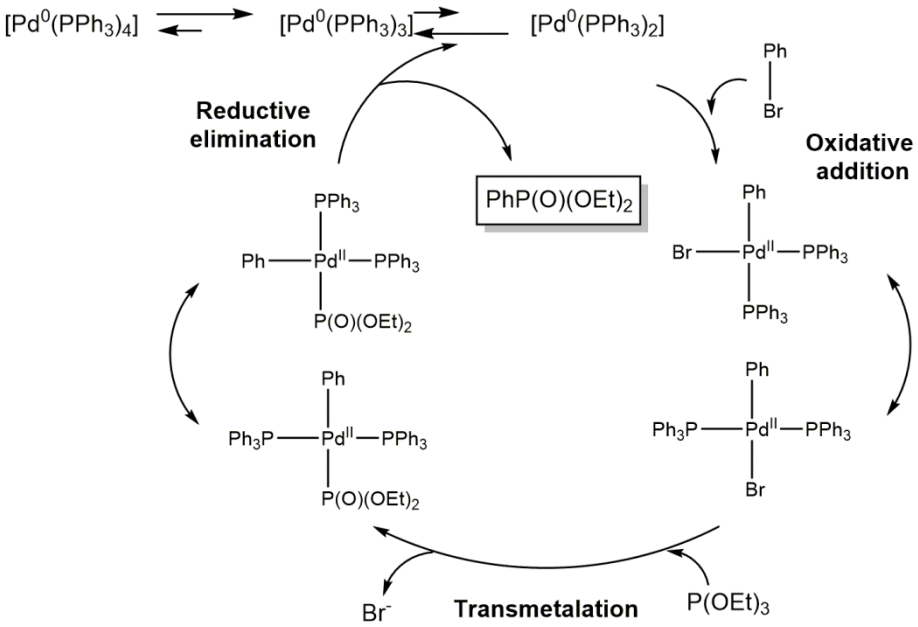

Scheme 2.3. Mechanism of palladium catalyzed cross-coupling reaction.

This chapter only focus the synthesis of two phosphonic organic ligands: i) the tetrapodal biphenyl derivative, [1,1'-biphenyl]-3,3',5,5'-tetrayltetrakis(phosphonic acid) (**H_8btp**); and ii) the tetrapodal pyrene derivative, pyrene-1,3,6,8-tetrayltetrakis(phosphonic acid) (**H_8ptp**) (depicted in Scheme 1.13 in Chapter 1). All synthetic routes, purification processes and characterization (*i.e.* NMR spectroscopy and mass spectrometry) are described in detail.

2.3.2. Strategy

Our research group originally began the quest for new MOF materials self-assembled with highly flexible and aliphatic carboxylate organic molecules that could be

obtained from commercial suppliers.[33-37] Since then, the carboxylate groups have been replaced by phosphonate moieties. Additionally, the rigidity of the linkers was increased in order to improve photoluminescent properties of optically-active materials, as well as their mechanical and thermal robustness.[38-42]

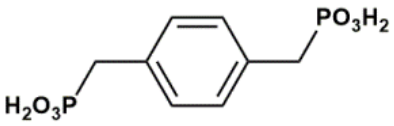

1,4-Phenylenebis(methylene)diphosphonic acid

H_4pmd

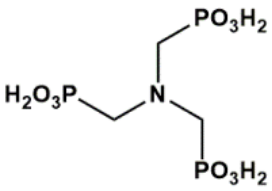

Nitrilotris(methylenephosphonic acid]

H_6nmp

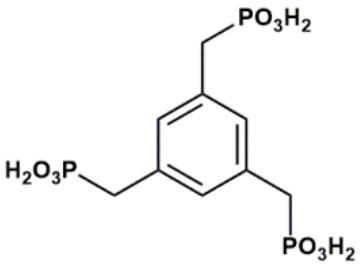

1,3,5-Benzenetrimethylenephosphonic acid

H_6btmp

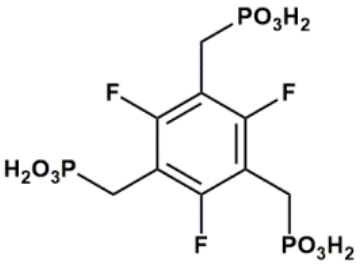

((2,4,6-Trifluorobenzene-1,3,5-triyl)tris(methylene))triphosphonic acid

H_6tftp

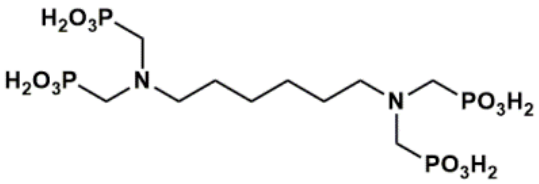

1,6-Diaminohexane-*N*,*N*,*N*′,*N*′-tetrakis(methylenephosphonic acid)

H_8L^3

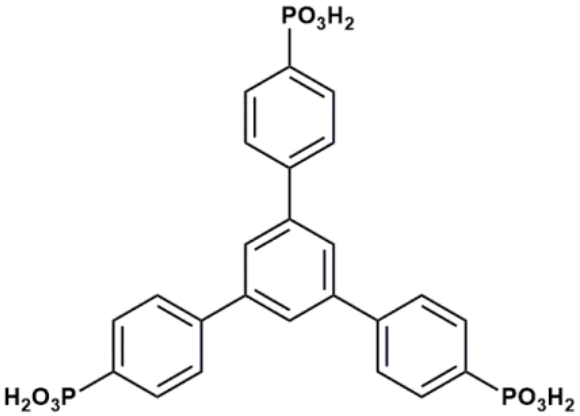

[1,3,5-Tris(4-phosphonophenyl)benzene]

H_6btbp

Scheme 2.4. Phosphonate organic ligands previously used by our research group to prepare MOFs.

From previous studies it was possible to draw some conclusions:

i) The presence of central nitrogen atom, together with methylene groups displayed in a divergent conformation, promotes a high degree of flexibility of the organic molecule and, consequently, supramolecular isomerism. This fact may be related with the preparation of microcrystalline MOF powders, as well as the difficulties that arise when optimizing experimental conditions to obtain phase-pure materials;
ii) One- or two-dimensional MOF materials are usually isolated due to organic PBUs linear conformation. They act as chelating agents instead of branching linkers that connect metal cations in an intricate three-dimensional network;
iii) Previously reported structures possess *f*-block metal cations which are optically-active elements. We observed that the absence of suitable sensitizers in the organic PBUs (*e.g.* aromatic rings), associated with a high number of water molecules present the framework (that promote quenching, *i.e.* non-radiative emission), led to poor photoluminescent properties of final materials. In order to boost the emission of the isolated LnOFs, specific groups have to be included, such as aromatic rings or highly conjugated organic cores, so as to promote an effective *antenna effect*;
iv) Due to the zwitterionic behavior of the nitrogen based organic linkers, in some cases, the synthesized MOF structures possess an additional quencher (or non-radiative supramolecular bond) because the nitrogen atom appears protonated and can establish an extra hydrogen bond interaction within the framework;
v) Highly rigid molecules, such as H_6btbp (Scheme 2.4), should not present a lot of different spacial conformations, which prevents the above mentioned supramolecular isomerism. However, they could be difficult to use for the self-assembly of new materials if the right synthetic conditions are not used (or cannot be achieved and optimized) or the right methodology is not employed.

Comparing carboxylic with phosphonic acid moieties, the latter possess several characteristics that promote the formation of stronger supramolecular arrays for a successful design of crystalline structures: i) phosphonic acids are more acidic than carboxylic acids; ii) they are also non-planar, presenting a tetrahedral geometry with iii) twice the number of protons; iv) their superior cation complexing ability leads to the formation of a vast number of singular metal-phosphonate connectivities, especially when bonded to lanthanide metals that possess high coordination numbers.[43]

Following on the topic and considering all the above mentioned information, we have decided to concentrate efforts on the preparation of tetrapodal aromatic phosphonate-based linkers. With that we prospect the construction of multidimensional LnOF materials with enhanced thermal stability and robustness, as well as improved properties (*e.g.* photoluminescence, catalytic and proton conducting behavior).

2.4. [1,1'-Biphenyl]-3,3',5,5'-tetrakis(phosphonic acid) (H_8btp)

2.4.1. Synthesis

As discussed in Chapter 1, molecular level control of supramolecular structures requires a thorough choice of rigid building units (or PBUs), which then display multiple "adhesive" functional groups disposed in a prefixed directionality of the organic core.[44] The [1,1'-biphenyl]-3,3',5,5'-tetrakis(phosphonic acid) (**H_8btp**) linker was for the first time synthesized and used by our research group for the preparation of LnOFs. The [$Pd(PPh_3)_4$]-catalyzed cross-coupling reaction of 3,3',5,5'-tetrabromobiphenyl (***IL*^{2}**) with triethyl phosphite afforded octaethyl-[1,1'-biphenyl]-3,3',5,5'-tetrayltetrakis(phosphonate) (***IL*^{1}**), a phosphonate ester that produced the respective phosphonic acid (**H_8btp**) after the hydrochloric acid-catalyzed hydrolysis reaction. Usually, the methodology employed to obtain the phosphonate ester derivative is conventional heating at high temperatures on a sand bath during several days. Using microwave-assisted synthesis (MWAS) we were able to significantly reduce the reaction time and the desired compound was obtained from very high to quantitative yields.

Using MWAS we have prepared octaethyl-[1,1'-biphenyl]-3,3',5,5'-tetrayltetrakis(phosphonate) (***IL*^{1}**) in high yields in just 30 minutes. Synthesis started with a Pd^0-catalyzed cross-coupling reaction of 3,3',5,5'-tetrabromo-1,1'-biphenyl with triethyl phosphite. After irradiation, the intermediate compound ***IL*^{1}** was purified by column chromatography and obtained as a colorless oil, with an excellent yield (95%) (Scheme 2.5). Microwave irradiation was the methodology selected for this step of the ligand synthesis because it unequivocally led to higher yields of ***IL*^{1}**, as well as a considerable reduction in the reaction time when compared to conventional heating approaches.[44] The second step is based on a quantitative acid hydrolysis. The intermediate organic molecule ***IL*^{1}** was added to an aqueous solution of concentrated HCl (12 M) and the reaction mixture was refluxed for 24 h. The target compound **H_8btp** was isolated as a white powder in

excellent yields (*ca.* 97%). **H_8btp** and its phosphonate ester intermediate (***IL*^{1}**) were fully characterized by NMR spectroscopy and mass spectrometry (see sub-section 8.3 in the Experimental Section and Figures A.1.1 to A.1.7 in Appendix A.1 for further detailed information).

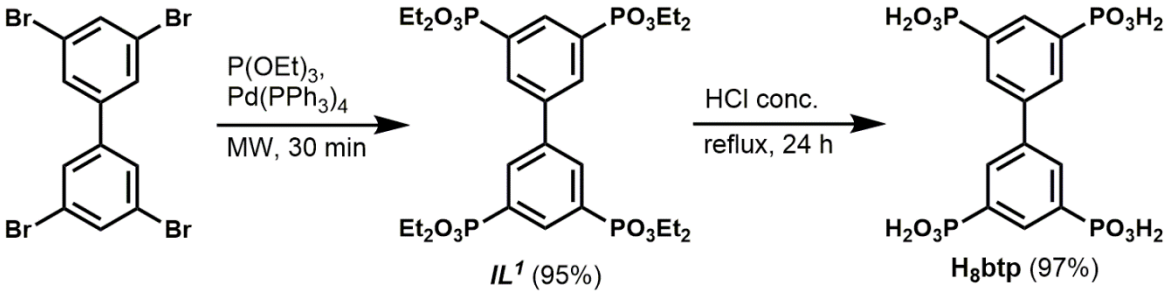

Scheme 2.5. Simplified synthetic procedure to prepare the novel tetrapodal [1,1'-biphenyl]-3,3',5,5'-tetrayltetrakis(phosphonic acid) (**H_8btp**) organic linker.

2.4.2. Structural Elucidation

The intermediate octaethyl-[1,1'-biphenyl]-3,3',5,5'-tetrayltetrakis(phosphonate) (***IL*^{1}**) and the desired [1,1'-biphenyl]-3,3',5,5'-tetrakis(phosphonic acid) (**H_8btp**) organic compounds were both characterized by NMR spectroscopy using $CDCl_3$ and DMSO-d_6, respectively. ***IL*^{1}** and **H_8btp** were also investigated by TOF MS ES^+ and TOF MS ES^- respectively. ^{1}H NMR spectrum of ***IL*^{1}** comprises at δ 1.37 ppm a signal representing one triplet ($J(^1H\text{-}^1H)$ = 6.0 Hz) corresponding to the protons of the methyl ($–CH_3$) group (Figure 2.1). The resonances of the two protons of the $–CH_2–O$ group are located from δ 4.14-4.27 ppm as a multiplet. Regarding the aromatic region of the spectrum, we highlight another multiplet from δ 8.18-8.30 ppm, corresponding to the resonance of the six aromatic protons of the biphenyl backbone of the compound. In the ^{13}C NMR spectrum of ***IL*^{1}**, the resonance of the carbon from the methyl group ($–CH_3$) is located at δ 16.4 ppm. The carbon of the $–CH_2–O$ moiety appears as another singlet at δ 62.7 ppm and the signal comprised in the δ 129.8-131.4 ppm range is attributed to the aromatic carbons directly connected to the phosphorous atoms (identified as C3 in Figure A.1.1 in Appendix A.1). From δ 134.1-134-5 ppm range we highlight the multiplet comprising the resonances of carbons C1, 1', 2, 2', 6 and 6'. At δ 139.9 ppm we can observe a triplet (^2J ($^{13}C\text{-}^{31}P$) = 8.7 Hz) attributed to C4 and C4'. The ^{31}P NMR spectrum of the compound (Figure A.1.2 in Appendix A.1) has a multiplet from δ 16.6-17.2 ppm corresponding to the phosphorous

atoms. In the TOF MS ES^+ spectrum of ***IL*^{1}** (Figure A.1.3 in Appendix A.1) are located two peaks at *m/z* 699.1 $(M + H)^+$ and 721.1 $(M + Na)^+$.

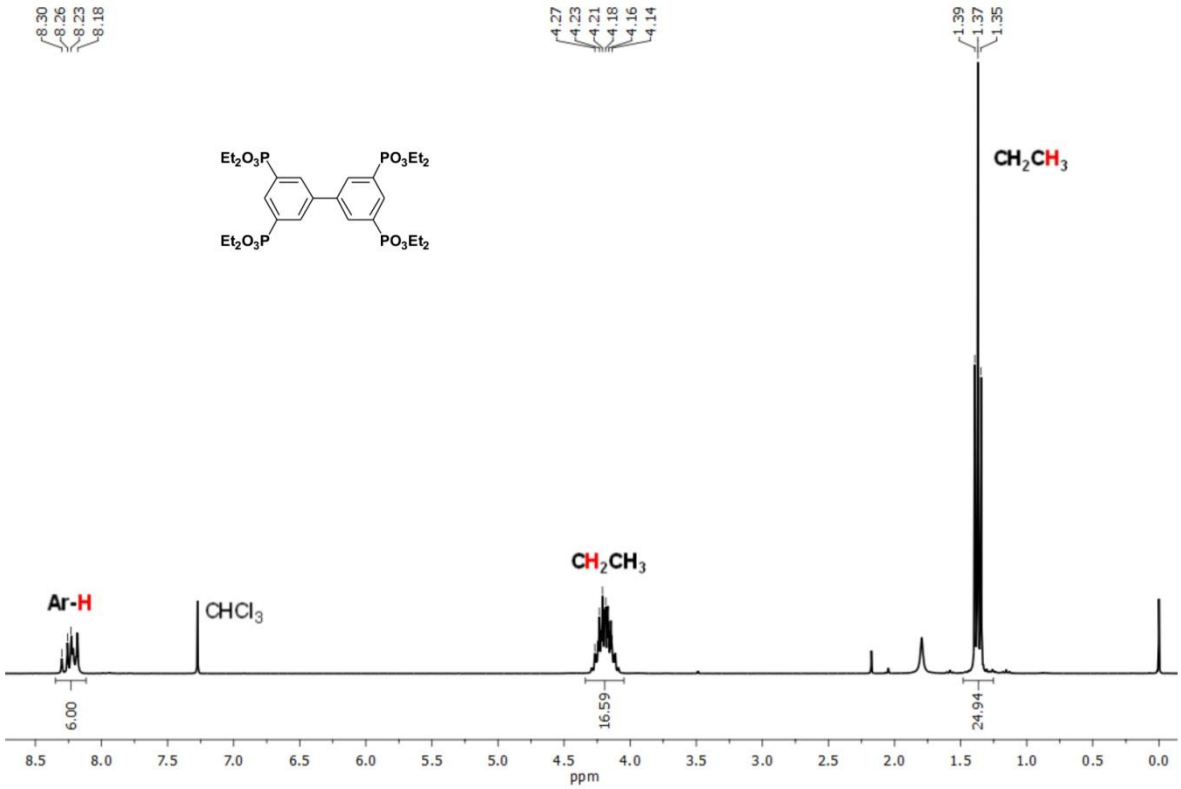

Figure 2.1. ^{1}H NMR spectrum of the intermediate compound octaethyl-[1,1'-biphenyl]-3,3',5,5'-tetrayltetrakis(phosphonate) (***IL*^{1}**) in $CDCl_3$.

The ^{1}H NMR spectrum of **H_8btp** (Figure A.1.4 in Appendix A.1) is composed of a signal at δ 7.98-8.08 ppm, a multiplet attributed to the aromatic protons. The ^{13}C NMR spectrum (Figure A.1.5 in Appendix A.1) presents a multiplet from δ 130.1-130.5 ppm comprising the resonances of carbons C2, 2', 6 and 6'; another multiplet can be observed from δ 132.0-132.2 ppm, attributed to carbons C1 and 1'; the double doublet that appears at δ 135.1 ppm (^{1}J(^{13}C-^{31}P) = 178.5 Hz, ^{3}J (^{13}C-^{31}P) = 13.2 Hz) is attributed to the aromatic carbons directly connected to the phosphorous atoms. Finally, the triplet at δ 137.8 ppm (^{2}J (^{13}C-^{31}P) = 12.5 Hz) corresponds to the resonances of carbons C4 and 4'. The ^{31}P NMR spectrum of the organic ligand **H_8btp** (Figure A.1.6 in Appendix A.1) has a triplet at δ 10.8 ppm (J(^{31}P-^{1}H) = 13.4 Hz), corresponding to the resonance of phosphorous atoms. In the TOF MS ES^- spectrum of **H_8btp** (Figure A.1.7 in Appendix A.1) we highlight one peak at *m/z* 472.9 $(M - H)^-$.

2.5. Pyrene-1,3,6,8-tetrayltetrakis(phosphonic acid) (H_8ptp)

2.5.1. Synthesis

Pyrene-1,3,6,8-tetrayltetrakis(phosphonic acid) (**H_8ptp**) was for the first time used by our group for the preparation of LnOFs. Nevertheless, in 2012 was reported the synthesis of the corresponding phosphonate ester, octaethyl-pyrene-1,3,6,8-tetrayltetrakis(phosphonate) (***IL*^{3}**), by Taylor and co-workers that used a nickel(II) catalyzed cross-coupling reaction to prepare this compound. The synthetic methodology comprised conventional heating at high temperatures and the reaction occurred overnight over a nitrogen atmosphere with a reported yield of 68%.[45]

Using MWAS in a similar approach used for the **H_8btp** linker, our group reported the same compound obtained by Taylor *et al.* in a simple and fast approach, easily prepared in quantitative yields (*ca.* 95%) using a Pd^0-catalyzed cross-coupling reaction under microwave irradiation (at 230 ºC for 45 min). Acid hydrolysis was then carried out, using a 6 M hydrochloric acid solution at 80 ºC during 20 h, which yielded the desired phosphonic acid, **H_8ptp**.[46] The aimed compound was isolated as a light green powder in very good yields (*ca.* 90%) (Scheme 2.6). Both **H_8ptp** and its phosphonate ester intermediate (***IL*^{3}**) were fully characterized by NMR spectroscopy and mass spectrometry (see sub-section 8.4 in the Experimental Section and Figures A.1.8 to A.1.14 in Appendix A.1 for further detailed information).

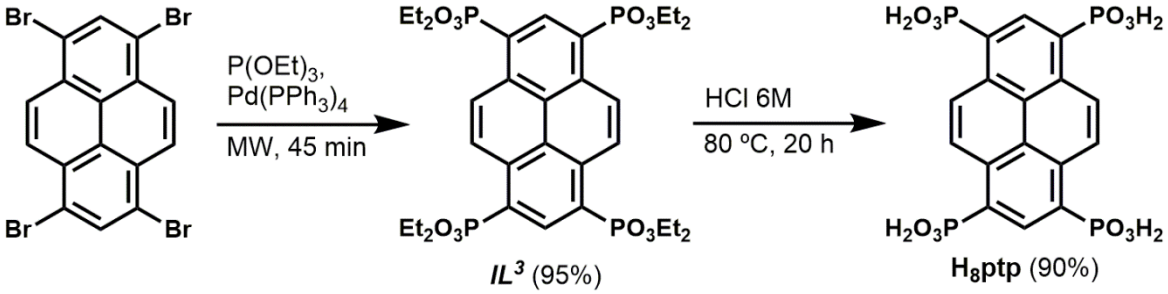

Scheme 2.6. Simplified synthetic procedure to prepare the novel tetrapodal pyrene-1,3,6,8-tetrayltetrakis(phosphonic acid) (**H_8ptp**) organic linker.

2.5.2. Structural Elucidation

The ^{1}H NMR spectrum of ***IL*^{3}** has two signals in the aliphatic region (Figure 2.2): a triplet ($J(^1H\text{-}^1H)$ = 7.5 Hz) situated at δ 1.39 ppm corresponding to the resonance of the –

CH_3 groups and from δ 4.20-4.36 ppm appear the resonances of the protons of the $–CH_2–O$ groups as a multiplet. In the aromatic region of the spectrum, we highlight two other well-defined signals: a singlet at δ 9.19 ppm, corresponding to the resonance of four equivalent aromatic protons of the pyrene core of the compound and a triplet at δ 9.28 ppm (^3J (^{1}H-^{31}P) = 15.0 Hz) corresponding to the remaining two aromatic protons.

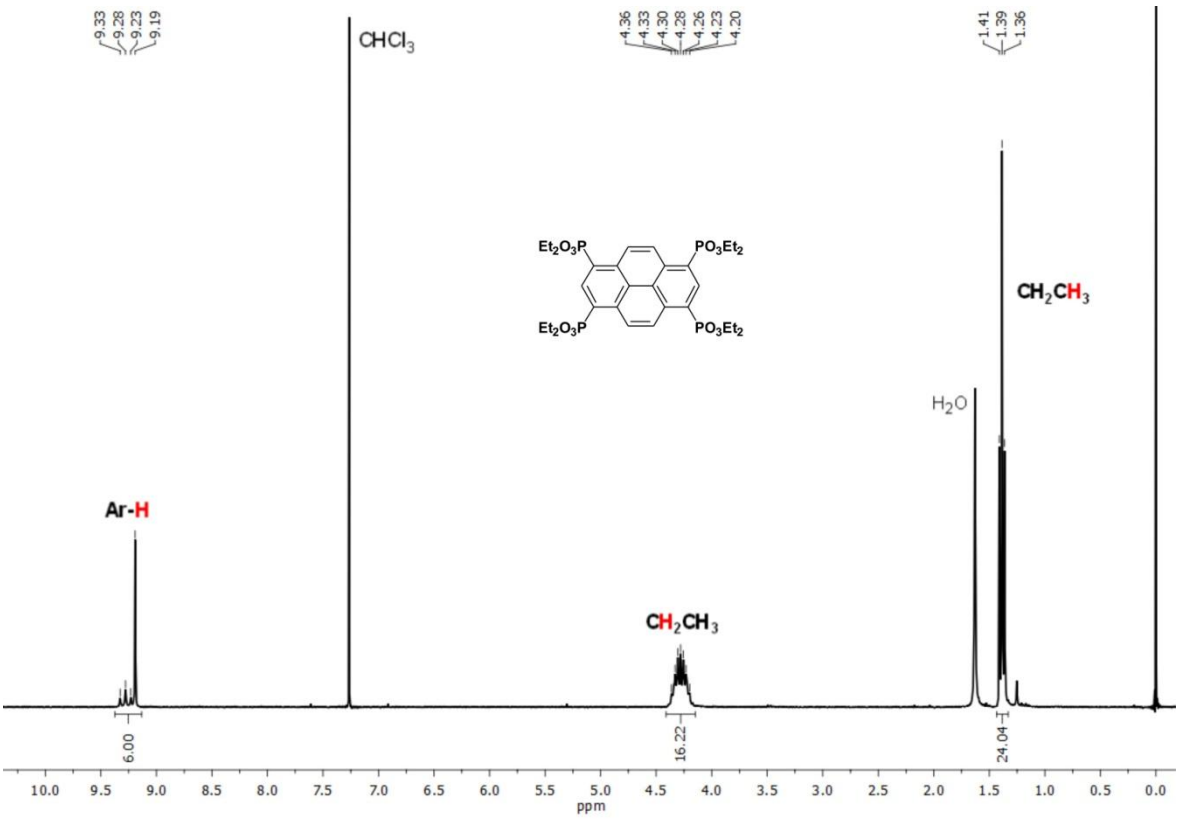

Figure 2.2. ^{1}H NMR spectrum of the intermediate compound octaethyl-pyrene-1,3,6,8-tetrayltetrakis(phosphonate) (***IL*^{3}**) in $CDCl_3$.

In the ^{13}C NMR spectrum of ***IL*^{3}** (Figure A.1.8 in Appendix A.1), the resonance of the carbon from the methyl group ($–CH_3$) is located at δ 16.4 ppm and the carbon of the $–CH_2–O$ moiety appears as another singlet at δ 62.9 ppm. The splitting patterns in the aromatic region helped us in the identification of all aromatic carbons from the pyrene core: the signal at δ 123.8 ppm corresponds to a double doublet (^1J (^{13}C-^{31}P) = 186.4 Hz, ^3J (^{13}C-^{31}P) = 14.3 Hz) and was assigned to the resonances of the carbons directly bonded to the phosphorous atoms (identified in the spectrum as C2); the multiplet from δ 124.2-124.7 ppm comprises the resonances of quaternary carbons, C4 and 4'; the sharp singlet at δ 129.2 ppm corresponds to the four equivalent C–H carbons from the pyrene backbone; from δ 134.8-135.2 ppm the multiplet corresponds to the resonance of four quaternary

carbons (identified in the spectrum as C3); finally, the last signal appears as a triplet at δ 137.1 ppm (^{2}J (^{13}C-^{31}P) = 10.2 Hz) and corresponds to two C–H carbons, C1 and C1'. The ^{31}P NMR spectrum of the compound (Figure A.1.9 in Appendix A.1) has a multiplet from δ 16.8-17.2 ppm corresponding to the phosphorous atoms of the molecule. In the TOF MS ES^{+} spectrum of ***IL³*** (Figure A.1.10 in Appendix A.1) we highlight one peak at *m/z* 746.1 (M^{+}).

From the ^{1}H NMR spectrum of **H_8ptp** (Figure A.1.11 in Appendix A.1) we can identify a multiplet in the aromatic region comprising basically a triplet and a singlet overlapped. These resonances belong to the aromatic protons of the pyrene core. In the ^{13}C NMR spectrum of **H_8ptp** (Figure A.1.12 in Appendix A.1), again the splitting patterns in the aromatic region helped us in the identification of all carbons from the pyrene backbone: the triplet at δ 124.1 ppm (^{3}J (^{13}C-^{31}P) = 7.5 Hz) corresponds to the resonance of quaternary carbons C4 and C4'; the double doublet at δ 128.6 ppm (^{1}J(^{13}C-^{31}P) = 107.9 Hz, ^{3}J (^{13}C-^{31}P) = 7.5 Hz) was assigned to the resonances of the carbons directly bonded to the phosphorous atoms (identified in the spectrum as C2); the sharp singlet at δ 128.6 ppm corresponds to the four equivalent C–H carbons from the pyrene backbone; the multiplet from δ 133.1-133.4 ppm comprises the resonances of four quaternary carbons (identified in the spectrum as C3); finally, the last triplet at δ 135.0 ppm (^{2}J (^{13}C-^{31}P) = 10.2 Hz) corresponds to two C–H carbons, C1 and C1'. The ^{31}P NMR spectrum of the compound (Figure A.1.13 in Appendix A.1) appears as a doublet at δ 11.0 ppm corresponding to the phosphorous atoms of the phosphonic moieties. In the TOF MS ES^{-} spectrum of **H_8ptp** (Figure A.1.14 in Appendix A.1) we highlight one peak at *m/z* 520.9 $(M - H)^{-}$.

2.6. Aerobic homocoupling of arylboronic acids

Efficient homocoupling of arylboronic acids was accomplished by Kirai and co-workers[47] that used the catalytic combination of inexpensive copper salts and 1,10-phenanthroline as a ligand. The homocoupling reaction using the [{(phen)Cu(μ-OH)}$_2$C·3H$_2$O complex proceeds at ambient temperature in atmospheric conditions without the necessity of any additives such as base or oxidants. Another advantage of this methodology is the large variety of substituents on the arylboronic acid, such as halogens, carbonyls or the nitro group. As a result, this methodology was successfully reproduced by

our research group and employed to synthesize the biphenyl reagent 3,3',5,5'-tetrabromobiphenyl, herein referred as ***IL²***.

2.6.1. [1,1'-Biphenyl]-3,3',5,5'-tetrakis(phosphonic acid) (Extended Reaction Strategy)

From readily available 3,5-dibromophenylboronic acid the substituted symmetrical biphenyl ***IL²*** was isolated using an inexpensive and useful methodology under mild reaction conditions: a binuclear (μ-hydroxido)copper complex was used as the catalytically active compound that undergoes efficient transmetalation with the arylboronic acid; the produced dinuclear arylcopper complex is assumed to be essential for the bimetallic reductive elimination of biaryls, as well as the oxidative restoration of the catalyst (Scheme 2.7).

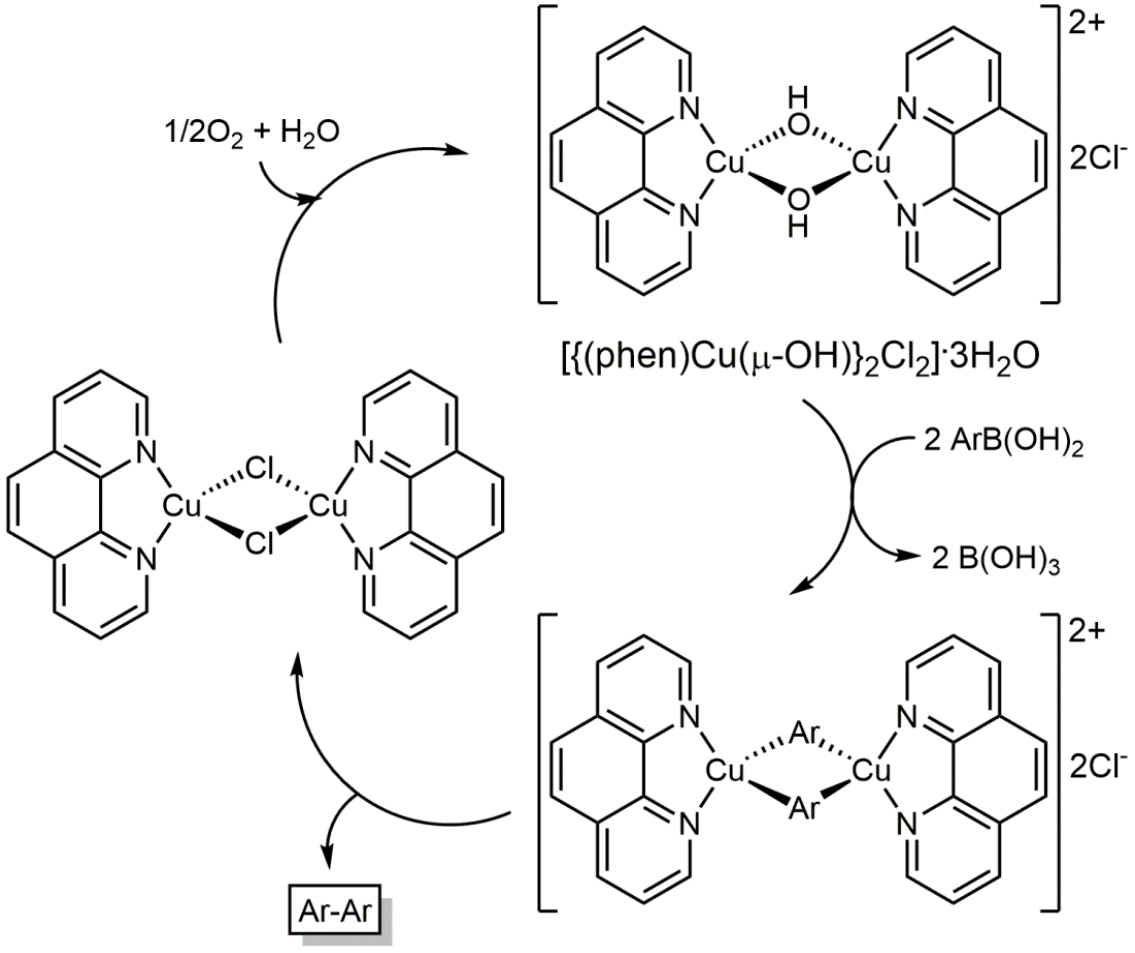

Scheme 2.7. Plausible mechanism of homocoupling catalyzed by [{(phen)Cu(μ-OH)}$_2$Cl$_2$]·3H$_2$O.[47]

[1,1'-Biphenyl-3,3',5,5'-tetrayltetrakis(phosphonic acid) (**H_8btp**) was prepared using the MWAS methodology already reported in the previous section (see sub-section 2.5). Later we decided to extend the synthesis route to the ***IL*^{1}** ligand precursor, because its preparation is, in this way, much less expensive than buying 3,3',5,5'-tetrabromo-1,1'-biphenyl (***IL*^{2}**) from commercial suppliers. Therefore, a novel three-step procedure was developed: the preparation starts with a homocoupling reaction to synthesize the biphenyl backbone of the molecule,[47] followed by the palladium-catalyzed cross-coupling reaction using triethyl phosphite to prepare the corresponding dialkyl arylphosphonate. A hydrolysis reaction was performed using hydrochloric acid to isolate the final polyphosphonic acid (Scheme 2.8).[48, 49]

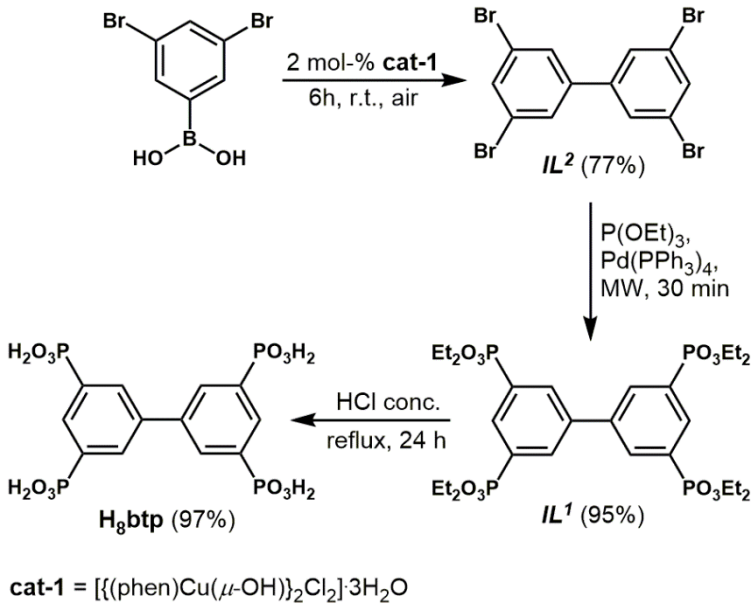

Scheme 2.8. Simplified three-step synthetic procedure to prepare the tetrapodal [1,1'-biphenyl]-3,3',5,5'-tetrayltetrakis(phosphonic acid) (**H_8btp**) organic linker.

Adding a third step for the ligand synthesis procedure represented a great advantage because the costs with ligand synthesis could be significantly reduced, without compromising extensively the global synthesis yield of the final molecule (*ca.* 90%). **H_8btp**, 3,3',5,5'-tetrabromo-1,1'-biphenyl (***IL*^{2}**) and octaethyl-[1,1'-biphenyl]-3,3',5,5'-tetrayltetrakis(phosphonate) (***IL*^{1}**) were all characterized by NMR spectroscopy (see Figure 2.3, sub-section 8.3 and 8.5 in the Experimental Section and Figures A.1.1 to A.1.7 in Appendix A.1 for further detailed information).

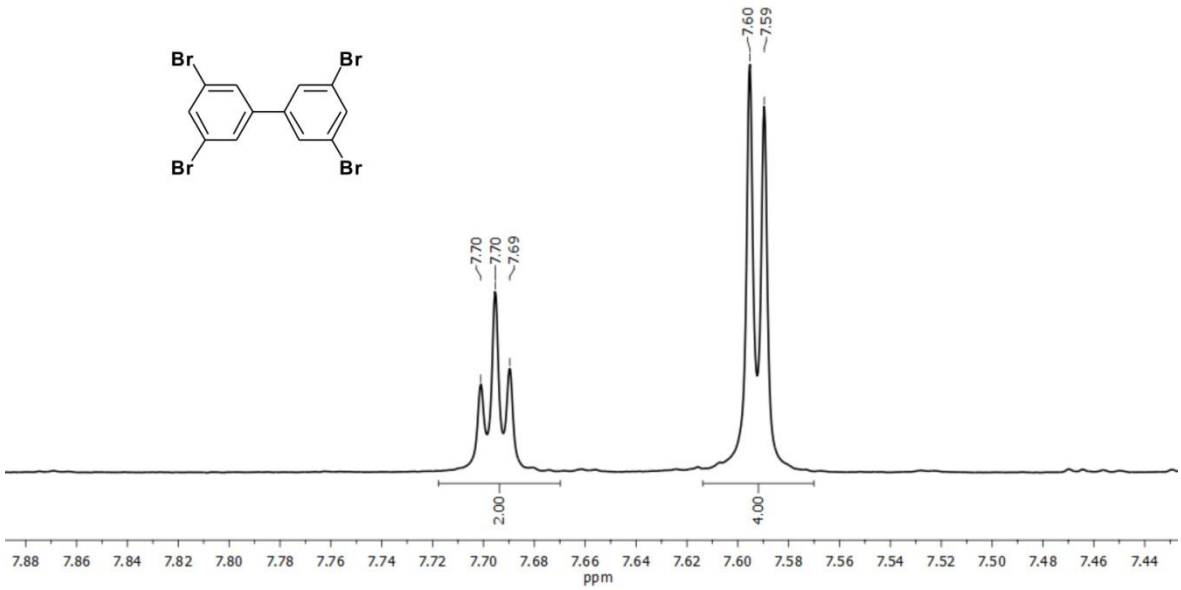

Figure 2.3. ^{1}H NMR spectrum of the intermediate compound 3,3',5,5'-tetrabromo-1,1'-biphenyl (***IL*^{2}) in $CDCl_3$.

2.7. Conclusions

In this chapter was documented in detail the synthetic procedures to prepare two different phosphonic acid organic linkers to be used for the self-assembly of multidimensional MOFs. Both tetrapodal organic linkers, **H$_8$btp** and **H$_8$ptp**, were prepared, in a first step, using a palladium-catalyzed cross-coupling reaction by setting up a reaction mixture containing the respective aryl halide, triethyl phosphite and $[Pd(PPh_3)_4]$. The heating methodology selected to conduct the reaction to obtain the phosphonate esters ***IL*^{1}** and ***IL*^{3}** was a MWAS approach due to its simpler and economical-friendly conditions, higher yields and faster reactions when compared to conventional heating. After the isolation and characterization of ***IL*^{1}** and ***IL*^{3}**, the second step was based on an acid hydrolysis. In this step, the procedure was slightly different for each compound: to carry out the hydrolysis of ***IL*^{1}** was used concentrated HCl (12 M); for the other intermediate ester, ***IL*^{3}**, an aqueous solution of 6 M HCl was used, as well as milder reaction conditions, *i.e.* temperature of 80 ºC instead of reflux of the HCl aqueous solution.

Furthermore, a three-step reaction methodology was developed for the synthesis of **H$_8$btp**: adding a third step to synthesize the corresponding aryl halide (***IL*^{2}**) represented a great reduction regarding the costs to synthesize **H$_8$btp**.

Regarding all the employed synthetic routes reported in this chapter, one can conclude that they are good choices to isolate octaethyl phosphonates and the corresponding phosphonic acids in short periods of time and with high reaction yields:

i) Due to low reactivity, the Michaelis-Arbozov method wasn't directly employed on the aryl halides that were selected as starting reagents. Nevertheless, the Pd^0-catalyzed cross-coupling reaction proved to be a good choice for the reaction between an aryl halide and triethyl phosphite. This methodology has the disadvantage, compared to the Michaelis-Arbuzov reaction, of needing the use of a catalyst to promote the reaction for the synthesis of phosphonate esters, even if only in catalytic amounts;
ii) As our research group concluded before, performing the Pd^0-catalyzed cross-coupling reaction selecting MWAS as the heating methodology proved again to be a very advantageous combination: simpler and less energy-consuming conditions, where the desired phosphonate ester was quickly isolated in high yields and without the generation of any byproducts that could originate difficulties upon purification of compounds and/or lower the yield of the reaction;
iii) Scale-up does not seem to be very difficult for the mentioned reactions: when a bigger reaction vessel (as for instance, with 35 mL of capacity) was used (under constant and restricted control from the equipment of the pressure generated inside the reactor to prevent accidents), it was possible to synthesize the desired compounds in larger quantities;
iv) The use of triethyl phosphite as solvent and reactant at the same time allowed the synthesis of phosphonate intermediates in a fast way, high yields and without any byproducts, as well. This method also contributes to a successful scale-up of the reaction in order to obtain the desired organic molecules in large amounts;
v) Conventional acid hydrolysis proved to be a very efficient approach toward the hydrolysis of large amounts of phosphonate ester intermediates in order to produce the desired phosphonic acid linkers. Performing the reaction under conventional heating was very simple, since it is only needed to mix the intermediate compound with an aqueous solution of HCl. While a 6 M aqueous solution of HCl was enough to hydrolyze the octaethyl phosphonate ***IL*^{3}**, for the other intermediate, ***IL*^{1}**, was required the use of concentrated HCl at higher temperatures.

The structures of all intermediate compounds (***IL*^{1}**, ***IL*^{2}** and ***IL*^{3}**) and the desired organic linkers (**H_8btp** and **H_8ptp**) were unequivocally studied and characterized using standard liquid-state techniques (NMR spectroscopy and mass spectrometry) and, to the best of our knowledge, compounds ***IL*^{1}**, **H_8btp** and **H_8ptp** were reported for the first time by our research group.[46, 48, 49]

2.8. References

(1) Kariotoglou, D. M.; Mastronicolis, S. K.; *Comp. Biochem. Physiol. B-Biochem. Mol. Biol.*, **2003**, *136*, 27.

(2) Borjesson, E.; Torstensson, L.; *J. Chromatogr. A*, **2000**, *886*, 207.

(3) Rosowsky, A.; Fu, H. N.; Pai, N.; Mellors, J.; Richman, D. D.; Hostetler, K. Y.; *J. Med. Chem.*, **1997**, *40*, 2482.

(4) Alvarez, E.; Marquez, A. G.; Devic, T.; Steunou, N.; Serre, C.; Bonhomme, C.; Gervais, C.; Izquierdo-Barba, I.; Vallet-Regi, M.; Laurencin, D.; Mauri, F.; Horcajada, P.; *Crystengcomm*, **2013**, *15*, 9899.

(5) Berardi, D.; Carlesi, T.; Rossi, F.; Calderini, M.; Volpi, R.; Perfetti, G.; *Int. J. Immunopathol. Pharmacol.*, **2007**, *20*, 455.

(6) Winum, J. Y.; Innocenti, A.; Gagnard, V.; Montero, J. L.; Scozzafava, A.; Vullo, D.; Supuran, C. T.; *Bioorg. Med. Chem. Lett.*, **2005**, *15*, 1683.

(7) Xi, W.; Qian, L. J.; Huang, Z. G.; Cao, Y. F.; Li, L. J.; *Polym. Degrad. Stabil.*, **2016**, *130*, 97.

(8) Shaw, M. J.; Nesterenko, P. N.; Dicinoski, G. W.; Haddad, P. R.; *J. Chromatogr. A*, **2003**, *997*, 3.

(9) Park, I. H.; Jung, J. C.; Hwang, S. C.; Joo, J. O.; *Angew. Makromol. Chem.*, **1992**, *197*, 117.

(10) Illy, N.; Fache, M.; Menard, R.; Negrell, C.; Caillol, S.; David, G.; *Polym. Chem.*, **2015**, *6*, 6257.

(11) Horiguchi, M.; Kandatsu, M.; *Nature*, **1959**, *184*, 901.

(12) Kittredge, J. S.; Simonsen, D. G.; Roberts, E.; *Biochemistry*, **1962**, *1*, 624.

(13) Benedict, H. M.; Simons, J. N.; Swidler, R.; *Science*, **1964**, *144*, 1134.

(14) Alhadeff, J. A.; Daves, G. D.; *Biochemistry*, **1970**, *9*, 4866.

(15) Baldwin, M. W.; Braven, J.; *J. Mar. Biol. Assoc. U.K.*, **1968**, *48*, 603.

(16) Brumsen, C.; Hamdy, N. A. T.; Papapoulos, S. E.; *Medicine*, **1997**, *76*, 266.

(17) Watts, N. B.; *Endocrinol. Metabol. Clin. North Amer.*, **1998**, *27*, 419.

(18) Fleisch, H.; *Horm. Metab. Res.*, **1997**, *29*, 145.

(19) Mundy, G. R.; *J. Clin. Oncol.*, **2002**, *20*, 3191.

(20) Bamias, A.; Kastritis, E.; Bamia, C.; Moulopoulos, L. A.; Melakopoulos, L.; Bozas, G.; Koutsoukou, V.; Gika, D.; Anagnostopoulos, A.; Papadimitriou, C.; Terpos, E.; Dimopoulos, M. A.; *J. Clin. Oncol.*, **2005**, *23*, 8580.

(21) Nowack, B.; Stone, A. T.; *Water Res.*, **2006**, *40*, 2201.

(22) Reddy, M. M.; Nancollas, G. H.; *Desalination*, **1973**, *12*, 61.

(23) Gill, J. S.; Varsanik, R. G.; *J. Cryst. Growth*, **1986**, *76*, 57.

(24) Nilsing, M.; Lunell, S.; Persson, P.; Ojamae, L.; *Surf. Sci.*, **2005**, *582*, 49.

(25) Pahnke, J.; Ruhe, J.; *Macromol. Rapid Commun.*, **2004**, *25*, 1396.

(26) Griep-Raming, N.; Karger, M.; Menzel, H.; *Langmuir*, **2004**, *20*, 11811.

(27) Schuster, M.; Rager, T.; Noda, A.; Kreuer, K. D.; Maier, J.; *Fuel Cells*, **2005**, *5*, 355.

(28) Andaloussi, M.; Lindh, J.; Savmarker, J.; Sjoberg, P. J. R.; Larhed, M.; *Chem.-Eur. J.*, **2009**, *15*, 13069.

(29) Villemin, D.; Simeon, F.; Decreus, H.; Jaffres, P. A.; *Phosphorus Sulfur Silicon Relat. Elem.*, **1998**, *133*, 209.

(30) Hirao, T.; Masunaga, T.; Yamada, N.; Ohshiro, Y.; Agawa, T.; *Bull. Chem. Soc. Jpn.*, **1982**, *55*, 909.

(31) Hirao, T.; Masunaga, T.; Ohshiro, Y.; Agawa, T.; *Synthesis*, **1981**, 56.

(32) Zoń, J.; Garczarek, P.; BiaŁek, M. In *Synthesis of Phosphonic Acids and Their Esters as Possible Substrates for Reticular Chemistry*; The Royal Society of Chemistry, **2012**.

(33) Paz, F. A. A.; Klinowski, J.; *J. Phys. Org. Chem.*, **2003**, *16*, 772.

(34) Paz, F. A. A.; Rocha, J.; Klinowski, J.; Trindade, T.; Shi, F. N.; Mafra, L.; *Prog. Solid State Chem.*, **2005**, *33*, 113.

(35) Shi, F. N.; Paz, F. A. A.; Girginova, P.; Rocha, J.; Amaral, V. S.; Klinowski, J.; Trindade, T.; *J. Mol. Struct.*, **2006**, *789*, 200.

(36) Cunha-Silva, L.; Ananias, D.; Carlos, L. D.; Paz, F. A. A.; Rocha, J.; *Z. Kristall.*, **2009**, *224*, 261.

(37) Silva, P.; Vieira, F.; Gomes, A. C.; Ananias, D.; Fernandes, J. A.; Bruno, S. M.; Soares, R.; Valente, A. A.; Rocha, J.; Paz, F. A. A.; *J. Am. Chem. Soc.*, **2011**, *133*, 15120.

(38) Vilela, S. M. F.; Ananias, D.; Gomes, A. C.; Valente, A. A.; Carlos, L. D.; Cavaleiro, J. A. S.; Rocha, J.; Tome, J. P. C.; Paz, F. A. A.; *J. Mater. Chem.*, **2012**, *22*, 18354.

(39) Vilela, S. M. F.; Firmino, A. D. G.; Mendes, R. F.; Fernandes, J. A.; Ananias, D.; Valente, A. A.; Ott, H.; Carlos, L. D.; Rocha, J.; Tome, J. P. C.; Paz, F. A. A.; *Chem. Commun.*, **2013**, *49*, 6400.

(40) Vilela, S. M. F.; Ananias, D.; Fernandes, J. A.; Silva, P.; Gomes, A. C.; Silva, N. J. O.; Rodrigues, M. O.; Tome, J. P. C.; Valente, A. A.; Ribeiro-Claro, P.; Carlos, L. D.; Rocha, J.; Paz, F. A. A.; *J. Mater. Chem. C*, **2014**, *2*, 3311.

(41) Vilela, S. M. F.; Fernandes, J. A.; Ananias, D.; Carlos, L. D.; Rocha, J.; Tome, J. P. C.; Paz, F. A. A.; *Crystengcomm*, **2014**, *16*, 344.

(42) Nolasco, M. M.; Mendes, R. F.; Lima, P. P.; Paz, F. A. A.; Carlos, L. D.; Rocha, J.; *Eur. J. Inorg. Chem.*, **2015**, 1254.

(43) Clearfield, A.; *Curr. Opin. Solid State Mat. Sci.*, **2002**, *6*, 495.

(44) Beckmann, J.; Ruttinger, R.; Schwich, T.; *Cryst. Growth Des.*, **2008**, *8*, 3271.

(45) Taylor, J. M.; Vaidhyanathan, R.; Iremonger, S. S.; Shimizu, G. K. H.; *J. Am. Chem. Soc.*, **2012**, *134*, 14338.

(46) Venkatramaiah, N.; Firmino, A. D. G.; Paz, F. A. A.; Tome, J. P. C.; *Chem. Commun.*, **2014**, *50*, 9683.

(47) Kirai, N.; Yamamoto, Y.; *Eur. J. Org. Chem.*, **2009**, 1864.

(48) Firmino, A. D. G.; Mendes, R. F.; Ananias, D.; Vilela, S. M. F.; Carlos, L. D.; Tome, J. P. C.; Rocha, J.; Paz, F. A. A.; *Inorg. Chim. Acta*, **2017**, *455*, 584.

(49) Firmino, A. D. G.; Mendes, R. F.; Antunes, M. M.; Barbosa, P. C.; Vilela, S. M. F.; Valente, A. A.; Figueiredo, F. M. L.; Tome, J. P. C.; Paz, F. A. A.; *Inorg. Chem.*, **2017**, *56*, 1193.

Chapter 3

Microwave Synthesis of a photoluminescent Metal-Organic Framework based on a rigid tetraphosphonate linker

3.1. Initial Considerations

This chapter gives particular attention to the synthesis of the first series of 2D MOFs obtained using the tetrapodal phosphonate-based organic linker [1,1'-biphenyl]-3,3',5,5'-tetrakis(phosphonic acid) (**H_8btp**).

Microwave-assisted synthesis (MWAS) was used to prepare a new organic building block and a Metal-Organic Framework based on this unit. This synthetic approach is often considered to be an excellent new "green" technique in current organic chemistry. The uniform and efficient irradiation dispersion in the reaction medium accelerates the synthetic processes leading to the synthesis of the targeted molecules in shorter times and in a much cleaner way (when compared with conventional heating methods).[1, 2] This simple and convenient synthetic approach is also exceptional for preparing large amounts of phase-pure MOFs with high reaction yields.[3] Compared with other methods (*e.g.*, slow diffusion, ultrasound-assisted, one-pot and conventional hydro(solvo)thermal synthesis) MWAS is an energy efficient synthetic methodology for the preparation of MOF materials: i) with control of morphology; ii) phase selectivity; iii) homogeneous particle distribution; and iv) close control of several reaction parameters (*i.e.*, temperature, pressure, irradiation power and stirring).[4-12] Additionally, MWAS has also been used to scale-up reactions because the heating process is relatively independent of the reaction volume.[3]

In this chapter it is described how the tetrapodal organic linker **H_8btp** was combined with lanthanide cations to afford the isotypical 2D lanthanide-organic frameworks $[Ln_4(H_6btp)_2(H_4btp)_2(H_8btp)(H_2O)_{16}]\cdot 12H_2O$ [where Ln^{3+} = La^{3+} (**1**), $(La_{0.9}Eu_{0.1})^{3+}$ (**2**) and $(La_{0.9}Tb_{0.1})^{3+}$ (**3**)]. **1** was isolated as large single-crystals and its crystal structure was solved by single-crystal X-ray diffraction. Phase identification of the Eu^{3+}- (**2**) and Tb^{3+}-based (**3**) materials was performed by powder X-ray diffraction. Compound **1** consists of two-dimensional double-deck layers, characterized by an unprecedented tetranodal 2,4,4,4-connected layered network, with total point symbol $\{4\cdot8^5\}_2\{4^2\cdot8^4\}\{4^3\cdot8^2\cdot10\}_4\{4\}_2$. Supramolecular π–π interactions exist both within and between layers. **1-3** were fully characterized in the solid-state by a plethora of techniques [elemental and thermogravimetric analyses, electron microscopy (SEM and EDS), FT-IR spectroscopy and solid-state NMR]. Photoluminescence properties of the optically-active mixed-lanthanide materials **2** and **3** reveal that the employed $H_{8-x}btp^{x-}$ residues are better

suited to sensitize Tb^{3+} than Eu^{3+}, with the measured lifetimes being of 0.83±0.01 and 0.22±0.01 ms, respectively.

3.2. Functional MOFs prepared using a new phosphonate-based organic ligand

3.2.1. Synthetic Strategy of the Ligand and MOFs

Microwave-assisted synthesis (MWAS) is a "green" and sustainable synthetic methodology employed regularly by our research group to prepare both organic linkers and MOF architectures. This methodology can drastically reduce the reaction time when compared to conventional one-pot and hydro(solvo)thermal reactions while, at the same time, increase yields and reduce the formation of secondary products.[12]

Following our motivation in the self-assembly of phosphonic acid-based linkers and lanthanide ions to produce new hybrid crystalline materials with improved features, we envisaged that **H_8btp** could indeed produce novel LnOFs with interesting features. On one hand, the presence of more phosphonic acid chelating moieties and two aromatic rings (when compared with other previously employed phosphonate-based ligands in our group) should enhance structural connectivity ultimately leading to new interesting topological features. On the other hand, these two functional groups could also enhance the properties of the networks, their catalytic activity and photoluminescent properties.[13]

3.2.2. Microwave-assisted synthesis of isotypical $[Ln_4(H_6btp)_2(H_4btp)_2(H_8btp)(H_2O)_{16}]\cdot 12H_2O$ materials

MWAS was further applied for the preparation of the MOFs reported in this chapter. In our group, we have shown that modifying the heating source to microwave irradiation can lead to a significant reduction of the reaction time when compared to conventional one-pot and hydro(solvo)thermal reactions.[14, 15]

The self-assembly under MWAS between the new tetrapodal organic ligand **H_8btp** and lanthanide(III) chloride hydrates afforded a new family of MOF structures composed of three isotypical materials formulated as $[Ln_4(H_6btp)_2(H_4btp)_2(H_8btp)(H_2O)_{16}]\cdot 12H_2O$ [where Ln^{3+} = La^{3+} (**1**), $(La_{0.9}Eu_{0.1})^{3+}$ (**2**) and $(La_{0.9}Tb_{0.1})^{3+}$ (**3**)]. While compound **1** could be isolated as large single-crystals (see Figure B.1.1 in Appendix B.1 showing the presence

of needle-like crystals), phase identification of the mixed-lanthanide materials **2** and **3** as microcrystalline powders was performed using powder X-ray diffraction (Figure B.2.1 in Appendix B.2), unequivocally confirming that all materials share the same crystal structure (even after the performed photoluminescence studies).

Elemental analysis, electron microscopy (Figures in Appendix B.1), solid-state NMR (Figure 3.2) and FT-IR spectroscopy (Figure B.3.1 in Appendix B.3) were used in tandem to evaluate phase purity and homogeneity of the bulk materials.

3.2.3. Crystallographic Description

The aforementioned described MWAS has led to the isolation of a layered double-decked material which was ultimately formulated as $[La_4(H_6btp)_2(H_4btp)_2(H_8btp)(H_2O)_{16}]\cdot 12H_2O$ (**1**) on the basis of single-crystal X-ray diffraction studies. Noteworthy, in order to isolate suitable crystals for these studies, the reactive solution after MW irradiation was left motionless for a period of 7 days so crystals could grow until a desirable and suitable size. The mixed-lanthanide materials **2** and **3** were obtained with a slightly different approach but, as revealed from powder X-ray diffraction studies, they share the same crystal structure with **1**. The following paragraphs will be solely devoted to the description of the crystal features of this latter material.

Compound **1** crystallizes in the tetragonal space group *P*-4*b*2 (Table B.4.1 in Appendix B.4), with the asymmetric unit being composed of one metal center (Figure 3.1 and Figure B.4.1 in Appendix B.4) and fragments from three distinct $H_{8-x}btp^{x-}$ residues (x = 0, 2 and 4), four coordinated and three water molecules of crystallization.

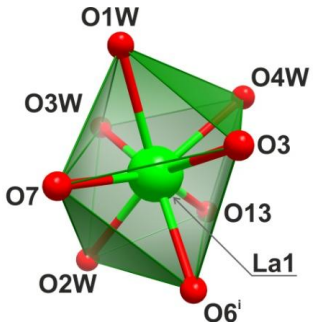

Figure 3.1. Polyhedral representation of the distorted $\{LaO_8\}$ dodecahedral coordination environment present in the crystal structure of $[La_4(H_6btp)_2(H_4btp)_2(H_8btp)(H_2O)_{16}]\cdot 12H_2O$ (**1**). Symmetry transformations used to generate equivalent atoms: (i) $-x+1/2$, $y-1/2$, z. See Table B.4.2 in Appendix B.4 for geometrical details on the represented bond lengths and angles.

The high symmetry tetragonal space group of **1** implies that several organic linkers are overlapped with (and ultimately generated) special positions in the unit cell corresponding to the various symmetry elements.

As depicted in Figure B.4.1 in Appendix B.4, the asymmetric unit contains in total five crystallographically independent phosphonate groups. To further confirm the derived space group of this material, and taking advantage of the presence of diamagnetic La^{3+} metallic centers in **1**, we have used solid-state NMR studies to unequivocally assess the number of crystallographically independent organic chelating units in the bulk material. The HPDEC ^{31}P MAS spectrum shows, in the isotropic region, four well-resolved sharp peaks centered at *ca.* 14.9, 12.5, 10.0 and 4.9 ppm (Figure 3.2). The second peak, centered at 12.5 ppm has a small visible shoulder, which is more noticeable in the spinning sidebands, referring to a 5th resonance centered at *ca.* 11.8 ppm. In summary, the existence of five crystallographically independent phosphorus sites agrees well with the selected space group and the undertaken single-crystal X-ray crystallographic studies.

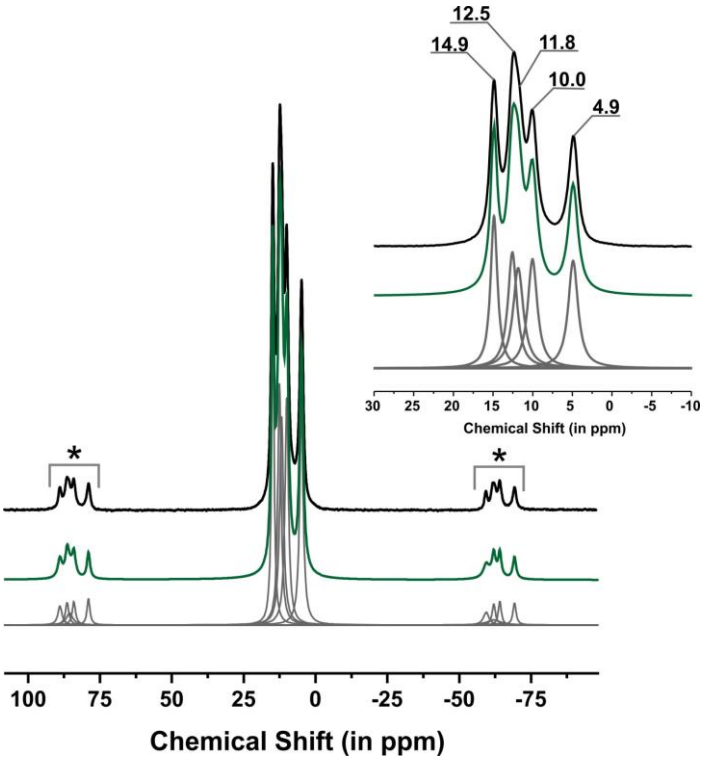

Figure 3.2. ^{31}P HPDEC MAS spectrum of $[La_4(H_6btp)_2(H_4btp)_2(H_8btp)(H_2O)_{16}]\cdot 12H_2O$ (**1**). Spinning sidebands are denoted using an asterisk. Peak deconvolution throughout the entire spectral range (*i.e.*, including the spinning sidebands) with a fixed ratio of *ca.* 1.0 : 1.0 : 1.0 : 1.0 : 1.0 led to fitted isotropic resonances centered at *ca.* 14.9, 12.5, 11.8, 10.0 and 4.9 ppm, respectively. The green line depicts the overall (*i.e.*, sum) data fit while the individual grey lines correspond to the fits of each single peak.

Besides the four coordinated water molecules, the crystallographically independent La^{3+} center is also coordinated to four phosphonate groups, with the eight $\{LaO_8\}$ coordination sphere resembling a distorted dodecahedron as depicted in Figure 3.1. The bond lengths (La–O) and angles (O–La–O) of the coordination polyhedron are comparable to those reported for other Ln^{3+}-based phosphonate compounds (see Table B.4.2 in Appendix B.4 for additional details): while the La–O bond lengths were found in the 2.411(6)- 2.610(8) Å range, the internal O–La–O polyhedral angles were instead refined in the 69.9(2)-151.3(2)º angle range. Of the five crystallographically independent phosphonate groups, only four are bound to the metallic center being coordinated in a typical κ^1-O mode. The groups have, nevertheless, different levels of protonation which, ultimately, influence the coordinating nature of the organic ligands themselves. H_6btp^{2-} and H_8btp both act as tetradentate linkers connecting four symmetry-related metal centers, while H_4btp^{4-} acts as a bidentate organic ligand connecting to two symmetry equivalent metal centers. Noteworthy, this organic moiety is the one bearing the disordered phosphonate group pointing to the inner channels of the network which is not coordinated to any metal center. Indeed, the absence of metal centers in the neighboring of this moiety allows the group to freely rotate (so to establish various hydrogen bonding interactions with the solvent molecules), ultimately explaining the observed disorder (Figure B.4.1 in Appendix B.4 and explanations in the sub-section 8.6 in the Experimental Section dedicated to the crystallographic studies).

The network in **1** is composed of two-dimensional layers placed in the *ab* plane of the unit cell, which are in turn formed by discrete one-dimensional organic cylinders stacked in a typical brick-wall-like fashion with water molecules occupying the free space in-between cylinders (Figure 3.3).

Each of these organic cylinders is comprised of eight symmetry-related metal centers and five organic linkers. The metal centers are distributed in a zigzag fashion along the *ab* plane, while the organic linkers are stacked on top of each other with a rotation angle of about 143º along the *c*-axis, forming double helix like structural motif as depicted in Figure 3.4.

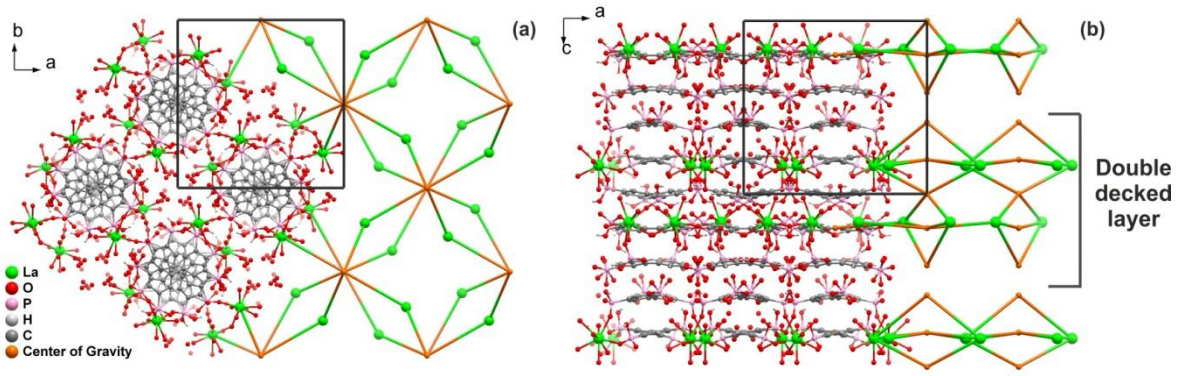

Figure 3.3. Crystal packing of $[La_4(H_6btp)_2(H_4btp)_2(H_8btp)(H_2O)_{16}]\cdot 12H_2O$ (**1**) viewed in perspective along the **(a)** [001] and **(b)** [010] directions of the unit cell. The representations emphasize simultaneously the layered nature of the coordination polymer present in **1** and highlight the 4-nodal topology of the network with total point symbol $\{4\cdot 8^5\}_2\{4^2\cdot 8^4\}\{4^3\cdot 8^2\cdot 10\}_4\{4\}_2$.

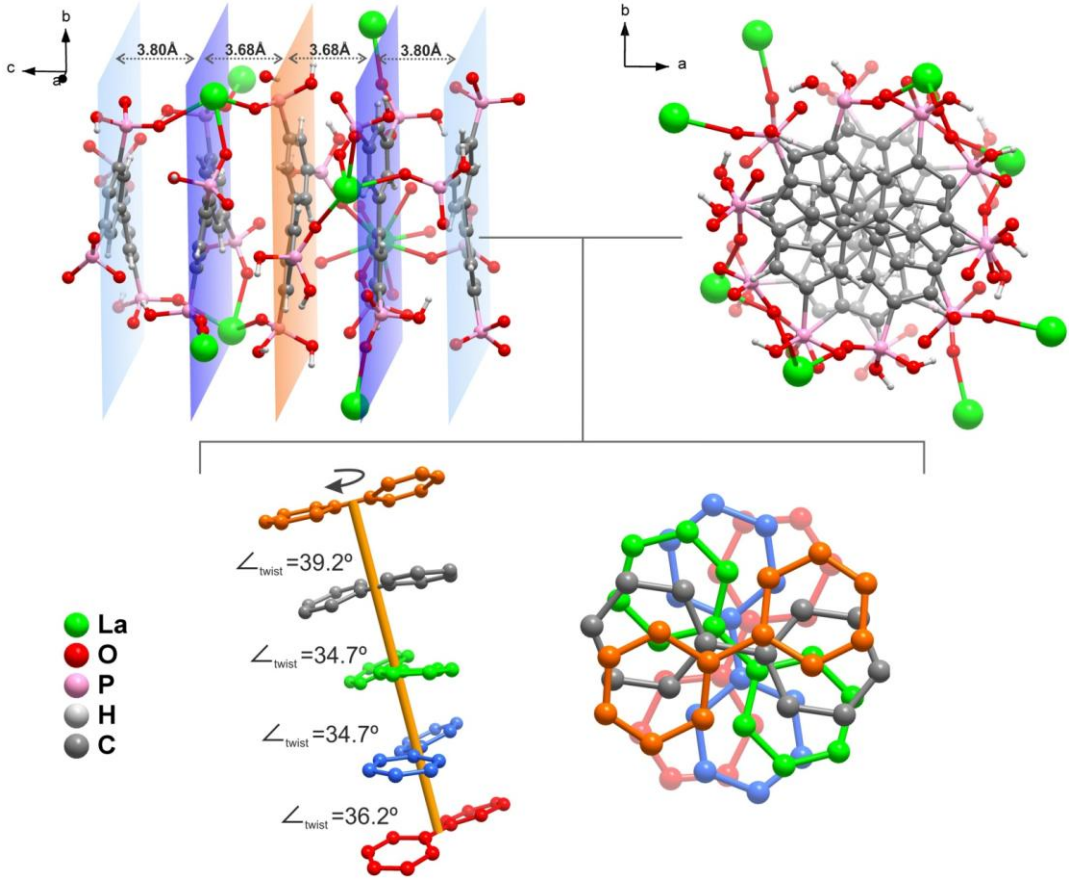

Figure 3.4. Schematic representation of the organic cylinder present in the crystal structure of $[La_4(H_6btp)_2(H_4btp)_2(H_8btp)(H_2O)_{16}]\cdot 12H_2O$ (**1**) viewed along the [100] and [001] directions of the unit cell. The schemes emphasize the close packing nature of the organic linkers, with inter-planar distances ranging between *ca.* 3.68 Å (for the inner ligands of the double deck layer) to *ca.* 3.80 Å (for those located in the outer shell). At the bottom there is a representation of the same organic skeleton in the cylinder emphasizing the rotation along the *c*-axis of the five composing aromatic cores. The average mutual rotations between individual units are also indicated.

The presence and structural importance of these cylinders can be better visualized from a typical topological view of the network itself. Figure 3.3 also depicts the reduction of the network to simple nodes (*i.e.*, the metal centers) and bridges (ensured by the organic linkers). Following the recommendations of Alexandrov *et al.*,[16] who suggested that any moiety (ligand or atoms) connecting more than two metallic centers (μ_n) should be considered as a network node, the network of **1** has three crystallographically distinct nodes for the organic bridges arising from the three independent organic linkers. These nodes share, nevertheless and as calculated using the software package TOPOS, similar internodal connectivity. Compound **1** is, therefore, a tetranodal 2,4,4,4-connected layered network, with total point symbol of $\{4\cdot8^5\}_2\{4^2\cdot8^4\}\{4^3\cdot8^2\cdot10\}_4\{4\}_2$, as revealed by the software package TOPOS.[17] Searches in the *Reticular Chemistry Structure Resource* (RCSR)[18] and in EPINET[19] reveal that this topology has not been, to the best of our knowledge, reported to date. The complex connectivity associated with this new network is also easily visible from the topological representation that, ultimately, simplifies the structure. As clearly observed in Figure 3.3a, organic linkers stack parallel to the *c*-axis being surrounded by metal centers. This connectivity leads to a typical double-decked thick hybrid layer containing two sheets of metal centers embedded in an organic matrix as seen in Figure 3.3b. Within this layer, the organic moieties are further engaged in weak π–π stacking interactions with intercentroid distances ranging between 3.8009(7) Å (for the peripheral ones) and 3.6816(6) Å (registered for the more central interactions). As depicted in Figure 3.3, individual layers stack on top of each other, being also maintained by weak π–π interaction between the rings of adjacent layers [distance of 3.6315(6) Å]. Besides these important weak supramolecular interactions, because the structure is rich in many donor and acceptor atoms capable of establishing strong hydrogen bonds, one observes a number of such connections between the various –POH groups of the phosphonic acid residues and crystallization water molecules (not shown).

3.2.4. Thermogravimetry and thermodiffractometry

The thermal stability of the bulk $[Ln_4(H_6btp)_2(H_4btp)_2(H_8btp)(H_2O)_{16}]\cdot12H_2O$ materials was investigated between ambient temperature and *ca.* 800 ºC, providing additional information on the hydration level of the compounds. As depicted in Figure B.5.1 (in Appendix B.5), the thermograms for the three prepared materials are very similar,

ultimately indicating identical thermal stabilities. Thus, in the following paragraphs discussion will be solely focused on compound **1**.

For **1**, the thermogram does not evidence clear regions in which the mass remains stable. Instead, as depicted in Figure B.5.2 (in Appendix B.5), there is a continuous weight loss (more significant at some specific temperatures) over the entire temperature range, ultimately creating additional difficulties in the individual assignments of temperature ranges *vs*. released residues. Nevertheless, one easily discerns two main weight losses. The first, between ambient temperature and *ca.* 150 ºC, corresponding to 14.9% of the total weight loss, being attributed to a gradual release of a total of 16 coordination and 12 crystallization water molecules (calculated 14.8%). This value agrees well with the water content found from the performed crystallographic studies. At higher temperatures there is a second weight loss, particularly in the temperature range of about 150-800 ºC (32.6%), which is attributed to the decomposition of the organic component. As observed from the thermogram, the weight loss does not stabilize which is an indication that the decomposition occurs with a slow kinetics in this range, with the residue at *ca.* 800 ºC still probably containing a residue of carbon.

Variable-temperature powder X-ray diffraction studies on $[La_4(H_6btp)_2(H_4btp)_2(H_8btp)(H_2O)_{16}]\cdot 12H_2O$ (**1**) further corroborate the aforementioned assumptions concerning the release of the totality of the water molecules with associated phase modifications (Figure B.5.2 in Appendix B.5). Noteworthy, from ambient temperature to *ca.* 300 ºC the crystal structure of **1** changes significantly from a crystalline framework to a complete amorphous phase: structural collapse settles in after *ca.* 60 ºC leading to a fully amorphous compound at just *ca.* 70 ºC.

3.2.5. FT-IR spectroscopic studies

The vibrational FT-IR spectroscopy studies support the structural features unveiled by the X-ray diffraction studies.[20] Figure B.3.1 (in Appendix B.3) compares the FT-IR spectra of $[La_4(H_6btp)_2(H_4btp)_2(H_8btp)(H_2O)_{16}]\cdot 12H_2O$ (**1**), $[La_{3.6}Eu_{0.4}(H_6btp)_2(H_4btp)_2(H_8btp)(H_2O)_{16}]\cdot 12H_2O$ (**2**) and $[La_{3.6}Tb_{0.4}(H_6btp)_2(H_4btp)_2(H_8btp)(H_2O)_{16}]\cdot 12H_2O$ (**3**) in the 4000-350 cm^{-1} spectral region, including assignments for each main observed band. Because the materials are isotypical, only the details for compound **1** are going to be described and discussed.

Compound **1** contains a broad band centered in the *ca.* 3650-2900 cm^{-1} spectral range, which is attributed to both *v*(O–H) stretching vibrational modes from coordination and crystallization water molecules and to the *v*(PO–H) stretching vibration of the phosphonate groups. In the central region of the spectrum, between *ca.* 1830 and 1500 cm^{-1}, it is possible to observe the typical *v*(C=C) stretching vibrational modes arising from the aromatic rings and the deformation stretching of the water molecules. We further observe as well the *v*(P–C) stretching vibrational modes at *ca.* 695 cm^{-1}. Also in this region, the stretching vibrational modes of *v*(P=O) were noticed from *ca.* 1360 to 1020 cm^{-1}, and those of *v*(P–O) from *ca.* 1020 to 800 cm^{-1}.

3.2.6. Photoluminescence

Figure 3.5 displays the excitation spectra of $[La_{3.6}Eu_{0.4}(H_6btp)_2(H_4btp)_2(H_8btp)(H_2O)_{16}]\cdot 12H_2O$ (**2**) at 296 and 15 K, while monitoring the Eu^{3+} emission within the $^5D_0 \rightarrow {}^7F_2$ transition at 612 nm. At the former temperature, the spectrum consists of a pair of UV broad bands (*ca.* 250 - 320 nm and 320 - 380 nm) attributed to π-π* transitions of the organic linkers, and a series of sharp lines assigned to the $^7F_0 \rightarrow {}^5D_{0\text{-}4}$, $^5L_6$ and $^5G_{2\text{-}6}$ Eu^{3+} intra-4*f*^{6} transitions. At 15 K, the higher energy UV broad band increases considerably and dominates the excitation spectrum.

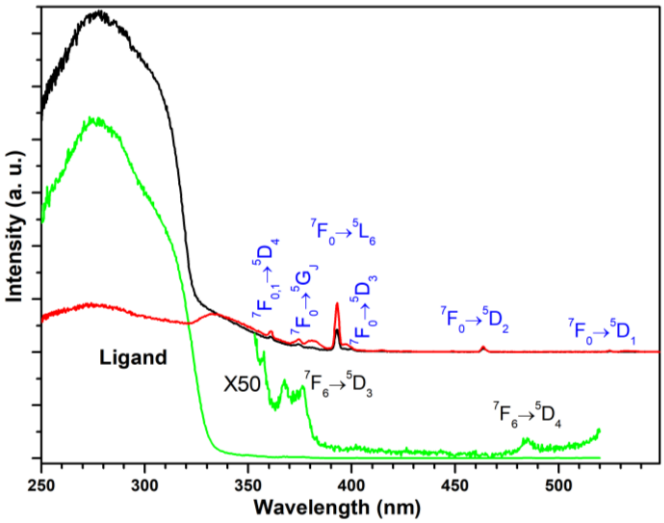

Figure 3.5. Ambient temperature excitation spectra of $[La_{3.6}Eu_{0.4}(H_6btp)_2(H_4btp)_2(H_8btp)(H_2O)_{16}]\cdot 12H_2O$ (**2**) (red line) and $[La_{3.6}Tb_{0.4}(H_6btp)_2(H_4btp)_2(H_8btp)(H_2O)_{16}]\cdot 12H_2O$ (**3**) (green line), while monitoring the emission at 612 and 548 nm, respectively. The excitation spectra of compound **2** acquired at 15 K (black line), with detection at 612 nm, is also provided.

The 296 K excitation spectrum of $[La_{3.6}Tb_{0.4}(H_6btp)_2(H_4btp)_2(H_8btp)(H_2O)_{16}]\cdot 12H_2O$ (**3**) (Figure 3.5) exhibits an intense broad band (*ca.* 250 - 330 nm) peaking at about 278 nm ascribed to the $\pi\rightarrow\pi^*$ electronic transition of the organic moieties. This UV band matches well the excitation profile of the higher energy excitation band of **2**, recorded at 15 K (Figure 3.5). The Tb^{3+} intra-4*f*^{8} transition is noticeably weaker and only observed after magnification. Clearly, the organic linker used in the construction of the networks (**H_8btp**) is more suited to sensitize Tb^{3+} than Eu^{3+}, via a typical energy transfer process, the so-called *antenna effect*. Noteworthy, while at 296 K the Tb^{3+} cations are well activated by the indirect ligand excitation, a direct excitation is more effective for the Eu^{3+} emission.

The emission spectra of **2** show the typical narrow Eu^{3+} $^5D_0\rightarrow{}^7F_{0\text{-}4}$ lines (Figure 3.6). The $^5D_1\rightarrow{}^7F_{0\text{-}2}$ transitions have a residual contribution to the total emission. Particularly for the excitation at 393 and 335 nm, the profiles of the emission spectra are distinct, presenting different Stark components in the $^5D_0\rightarrow{}^7F_{1\text{-}4}$ transitions and two distinct emission lines in the $^5D_0\rightarrow{}^7F_0$ transition region. Thus, photoluminescence detects, at least, two different Eu^{3+} sites, in contrast with the structural characterization techniques described above, which indicate pure crystalline phases with a single Ln^{3+} site. We note, however, that the emission spectrum obtained under direct excitation at 393 nm does not contain any contribution from the additional emission lines present on the 335 nm spectrum. Hence, the spectrum obtained with 335 nm excitation should be attributed to an unidentified impurity phase present at vestigial levels. This phase is, presumably, responsible for the second UV broad band at 335 nm, only prevailing in the 296 K excitation spectrum of **2**. The emission spectra of **3** (Figure 3.6) acquired at 296 K, with excitation at 310 and 280 nm, shows an intense green emission associated with Tb^{3+} $^5D_4\rightarrow{}^7F_{6\text{-}0}$ transitions. The observation of some spectral changes with the selection of distinct excitation wavelengths also indicates the presence of small amounts of impurities. Nevertheless, because of the higher efficiency of the Tb^{3+} emission on the former system, the effect of the contaminating phase for the total emission should be very small.

There is a possible explanation for the presence of small amounts of impurities in compounds **2** and **3**, associated with the synthesis steps used: materials were isolated in large amounts from slow evaporation at ambient temperature, being only obtained after the forced removal of most of the solvent of the reaction mixture (see sub-section 8.11 in the Experimental Section for more details). We will discuss a variant of this methodology on

Chapter 6 that has led to a new phase based on the present organic linker and Eu^{3+} and Gd^{3+} cations (see sub-section 6.1.2 in Chapter 6). We, thus, think that this vestigial phase detected in the photoluminescence studies of **2** and **3** could be a new MOF obtained in a similar reactive system in traceable amounts. Even though this impurity could not be detected from powder X-ray diffraction studies, it is nevertheless detectable in photoluminescence studies.

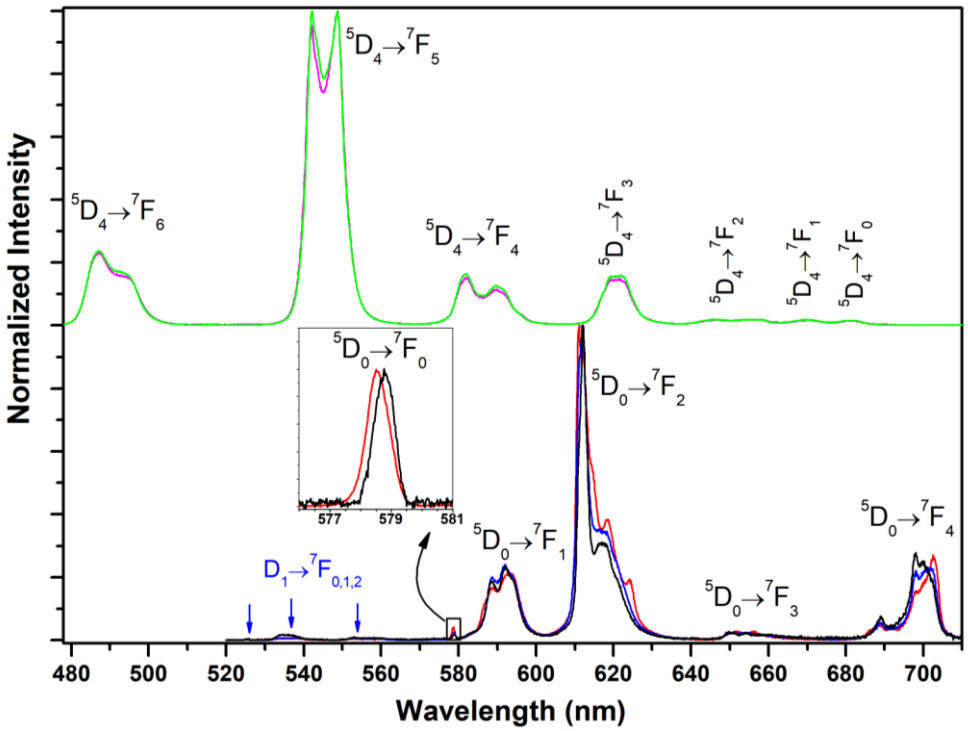

Figure 3.6. Ambient temperature emission spectra of $[La_{3.6}Eu_{0.4}(H_6btp)_2(H_4btp)_2(H_8btp)(H_2O)_{16}]\cdot 12H_2O$ (**2**) with direct excitation at 393 nm (black line) and with ligand excitation at 310 nm (blue line) and at 335 nm (red line). The inset shows a magnification of the $^5D_0\rightarrow{}^7F_0$ transition region. The ambient temperature emission spectra of $[La_{3.6}Tb_{0.4}(H_6btp)_2(H_4btp)_2(H_8btp)(H_2O)_{16}]\cdot 12H_2O$ (**3**) excited at 310 nm (green line) and at 280 nm (magenta line) are depicted on the top.

Additionally, we have also confirmed that in the conditions under which the photoluminescence studies were performed the materials preserved their structural integrity, as observed in previous reports.[21] As depicted in Figure B.2.1 (in Appendix B.2), compounds **2** and **3** retain their crystal structure after the performed studies and, thus, the second Ln environment detected is not due to any *in situ* structural modification induced by low temperature and vacuum.

The ambient temperature $^5D_0$ and $^5D_4$ lifetimes of Eu^{3+} and Tb^{3+} of **2** and **3** were determined by monitoring the emission decay curves within the maximum of the $^5D_0 \rightarrow {}^7F_2$ and $^5D_4 \rightarrow {}^7F_5$ transitions, exciting at 393 and 485 nm, respectively (Figure 3.7).

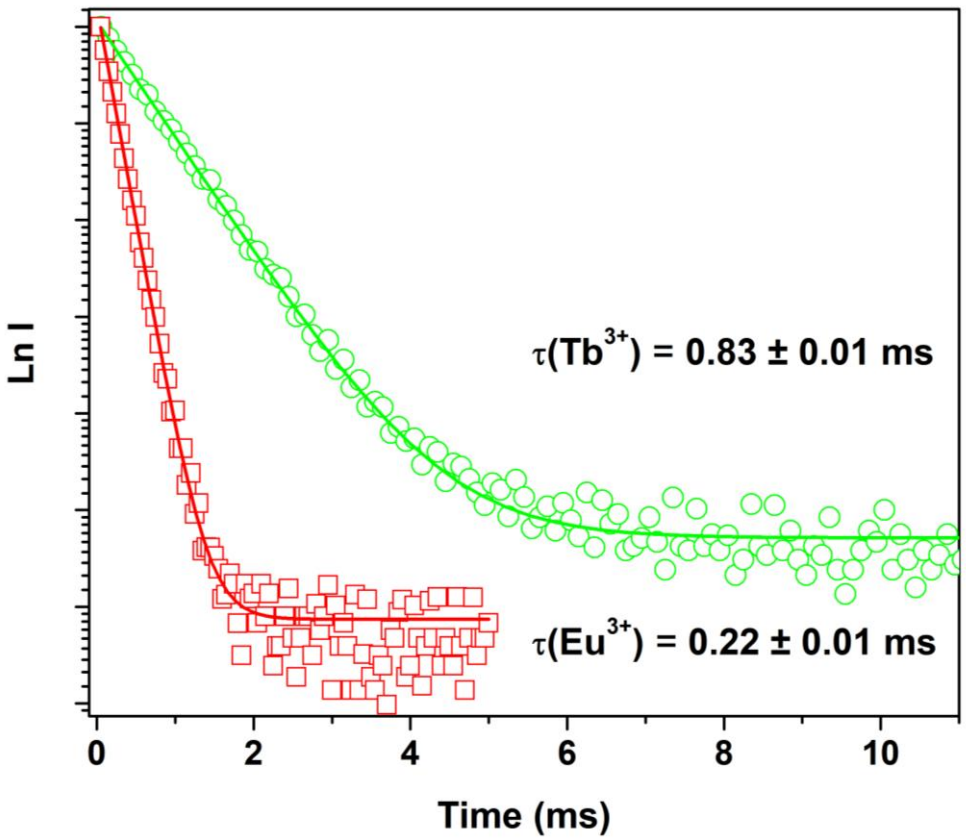

Figure 3.7. $^5D_0$ and $^5D_4$ decay curves of $[La_{3.6}Eu_{0.4}(H_6btp)_2(H_4btp)_2(H_8btp)(H_2O)_{16}]\cdot 12H_2O$ (**2**) (red) and $[La_{3.6}Tb_{0.4}(H_6btp)_2(H_4btp)_2(H_8btp)(H_2O)_{16}]\cdot 12H_2O$ (**3**) (green), acquired at ambient temperature, while monitoring the emission at 612 and 548 nm, respectively, and fitted with single exponential decay functions. The excitation was performed at 393 and 485 nm, respectively.

Decay curves were fitted by single exponential functions, yielding lifetimes of 0.22±0.01 and 0.83±0.01 ms, for **2** and **3**, respectively. This indicates the detection of unique Ln^{3+} crystallographic sites under direct excitation as discussed above for the Eu^{3+} emission.

3.3. Conclusions

A novel tetrapodal polyphosphonic acid linker, [1,1'-biphenyl]-3,3',5,5'-tetrayltetrakis(phosphonic acid) (**H_8btp**), prepared by a simple reaction methodology based

on a "green" and sustainable microwave heating approach was assembled with lanthanide cations to produce a crystalline, layered double-deck MOF formulated as $[Ln_4(H_6btp)_2(H_4btp)_2(H_8btp)(H_2O)_{16}]\cdot 12H_2O$ [where $Ln^{3+} = La^{3+}$ (**1**), $(La_{0.9}Eu_{0.1})^{3+}$ (**2**) and $(La_{0.9}Tb_{0.1})^{3+}$ (**3**)] on the basis of single-crystal X-ray and powder X-ray diffraction. The isolated materials were robust enough to be isotypically modified to engineer photoluminescent compounds, with the process being based on the replacement of La^{3+} by Eu^{3+} and Tb^{3+}. MWAS was the only synthetic approach which could be used to prepare these materials, as under conventional hydro(solvo)thermal conditions the isolated phases were completely different, and essentially mixtures.

The new tetrapodal organic linker seems to have induced the isolation of a highly symmetric network, which crystallizes in a tetragonal space group. Even though the network is based on a single crystallographically independent metal center, the existence of three fragments of linkers has led to a complex tetranodal 2,4,4,4-connected layered network, exhibiting an unprecedented total point symbol of $\{4\cdot 8^5\}_2\{4^2\cdot 8^4\}\{4^3\cdot 8^2\cdot 10\}_4\{4\}_2$. This network has several remarkable structural features, the first concerning the fact that it is a double-deck network in which two sheets of metal centers are embedded within an organic matrix tightly joined together by various weak π–π stacking interactions. The second notable feature concerns the presence of a large number of water molecules inside the various pores and channels of the network. Indeed, as clearly demonstrated by the empirical formulae of the materials, $[Ln_4(H_6btp)_2(H_4btp)_2(H_8btp)(H_2O)_{16}]\cdot 12H_2O$, per lanthanide center there are three of such molecules hosted in the channels. Nevertheless, because the metal centers are located on the periphery of the π–π stacked pillars of linkers, they are also strongly bound to water molecules of coordination, accounting for the poor thermal stability of the materials (at *ca.* 70 ºC the structures loose crystallinity).

The inclusion of optically active lanthanide centers yielded photoluminescent materials. Clearly, the presence of the various water molecules in the structure with the associated O–H luminescence quenchers, accounts for the poor emission of the Eu^{3+}-based material, leading to the relatively small lifetime of 0.22±0.01 ms. Nevertheless, the newly designed organic linker has proven to be effective in transferring energy to Tb^{3+} cations, pumping up the luminescence (lifetime 0.83±0.01 ms).

3.4. References

(1) de la Hoz, A.; Diaz-Ortiz, A.; Moreno, A.; *Chem. Soc. Rev.*, **2005**, *34*, 164.

(2) Lidström, P.; Tierney, J.; Wathey, B.; Westman, J.; *Tetrahedron*, **2001**, *57*, 9225.

(3) Taddei, M.; Dau, P. V.; Cohen, S. M.; Ranocchiari, M.; van Bokhoven, J. A.; Costantino, F.; Sabatini, S.; Vivani, R.; *Dalton Trans.*, **2015**, *44*, 14019.

(4) Phang, W. J.; Lee, W. R.; Yoo, K.; Ryu, D. W.; Kim, B.; Hong, C. S.; *Angew. Chem.-Int. Edit.*, **2014**, *53*, 8383.

(5) Jhung, S. H.; Yoon, J. W.; Hwang, J.-S.; Cheetham, A. K.; Chang, J.-S.; *Chem. Mater.*, **2005**, *17*, 4455.

(6) Hwang, Y. K.; Chang, J.-S.; Park, S.-E.; Kim, D. S.; Kwon, Y.-U.; Jhung, S. H.; Hwang, J.-S.; Park, M. S.; *Angew. Chem.-Int. Edit.*, **2005**, *44*, 556.

(7) Ni, Z.; Masel, R. I.; *J. Am. Chem. Soc.*, **2006**, *128*, 12394.

(8) Sabouni, R.; Kazemian, H.; Rohani, S.; *Chem. Eng. Technol.*, **2012**, *35*, 1085.

(9) Haque, E.; Khan, N. A.; Park, J. H.; Jhung, S. H.; *Chem.-Eur. J.*, **2010**, *16*, 1046.

(10) Liang, W.; D'Alessandro, D. M.; *Chem. Commun.*, **2013**, *49*, 3706.

(11) Liang, W.; Babarao, R.; D'Alessandro, D. M.; *Inorg. Chem.*, **2013**, *52*, 12878.

(12) Klinowski, J.; Almeida Paz, F. A.; Silva, P.; Rocha, J.; *Dalton Trans.*, **2011**, *40*, 321.

(13) Zhang, J.; Zheng, B.; Zhao, T.; Li, G.; Huo, Q.; Liu, Y.; *Cryst. Growth Des.*, **2014**, *14*, 2394.

(14) Vilela, S. M. F.; Ananias, D.; Fernandes, J. A.; Silva, P.; Gomes, A. C.; Silva, N. J. O.; Rodrigues, M. O.; Tome, J. P. C.; Valente, A. A.; Ribeiro-Claro, P.; Carlos, L. D.; Rocha, J.; Almeida Paz, F. A.; *J. Mater. Chem. C*, **2014**, *2*, 3311.

(15) Mendes, R. F.; Silva, P.; Antunes, M. M.; Valente, A. A.; Almeida Paz, F. A.; *Chem. Commun.*, **2015**, *51*, 10807.

(16) Alexandrov, E. V.; Blatov, V. A.; Kochetkov, A. V.; Proserpio, D. M.; *Crystengcomm*, **2011**, *13*, 3947.

(17) Blatov, V. A.; Shevchenko, A. P.; Serezhkin, V. N.; *J. Appl. Crystallogr.*, **2000**, *33*, 1193.

(18) Park, I. H.; Jung, J. C.; Hwang, S. C.; Joo, J. O.; *Angew. Makromol. Chem.*, **1992**, *197*, 117.

(19) Shaw, M. J.; Nesterenko, P. N.; Dicinoski, G. W.; Haddad, P. R.; *J. Chromatogr. A*, **2003**, *997*, 3.

(20) Socrates, G. *Infrared and raman characteristic group frequencies : tables and charts*; John Wiley & Sons, West Sussex, **2007**.

(21) Vilela, S. M. F.; Fernandes, J. A.; Ananias, D.; Carlos, L. D.; Rocha, J.; Tomé, J. P. C.; Almeida Paz, F. A.; *Crystengcomm*, **2014**, *16*, 344.

Chapter 4

Robust Multifunctional Yttrium-Based Metal-Organic Frameworks with Breathing Effect

4.1. Initial Considerations

This chapter describes the synthesis, structural correlations and properties of a family of 3D MOFs prepared by the self-assembly between the tetrapodal phosphonate-based organic linker [1,1'-biphenyl]-3,3',5,5'-tetrakis(phosphonic acid) (**H_8btp**) and yttrium(III) cations as metallic centers.

Phosphonate and yttrium-based MOFs, formulated as [Y(H_5btp)]·5.5H_2O (**4**), [Y(H_5btp)]·2.5H_2O (**5**), (H_3O)[Y_2(H_5btp)(H_4btp)]·H_2O (**6**) and [Y(H_5btp)]·H_2O·0.5(MeOH) (**7**), were prepared using a microwave-assisted synthesis methodology which promoted the self-assembly of the tetraphosphonic organic linker **H_8btp** with yttrium(III) cations. This new family of functional materials, isolated in bulk quantities, exhibits a remarkable breathing effect. Structural flexibility was thoroughly studied by means of X-ray crystallography, thermogravimetry, variable-temperature X-ray diffraction and dehydration and rehydration processes, ultimately evidencing a reversible Single-Crystal to Single-Crystal (SC-SC) transformation solely through the loss and gain of crystallization solvent molecules. Topologically, frameworks remained unaltered throughout this interconversion mechanism, with all compounds being binodal 6,6-connected network with a Schäfli symbol of $\{4^{13}.6^2\}\{4^8.6^6.8\}$.

Results show that this is one of the most stable and thermally robust families of tetraphosphonate-based MOFs synthesized reported to date. Porous materials **5** and **6** were further studied to ascertain their performance as heterogeneous catalysts and proton conductors, respectively, with outstanding results registered for both materials. Compound **5** showed a 94% conversion of benzaldehyde into (dimethoxymethyl)benzene after just 1 h of reaction, amongst the best results registered to date for MOF materials. On the other hand, the protonic conductivity of compound **6** at 98% of relative humidity (2.58×10^{-2} S cm^{-1}) was among the highest registered for MOF materials, with the great advantage of being possible to prepare the material using a simpler and sustainable synthesis methodology, as well as its good stability at ambient conditions (temperature and humidity) over time when compared to others.

4.2. Functional MOFs prepared using yttrium(III) metal centers and the phosphonate-based organic ligand H_8btp

4.2.1. Preparation of MOFs

Following our group previous incursions using di- and triphosphonic linkers,[1-3] we hypothesized that the inclusion of additional aromatic rings and phosphonic acid chelating groups should enhance structural robustness and connectivity, ultimately leading to more structurally and topologically interesting features. On the other hand, the increase in the number of phosphonic acid groups should predictably also enhance the properties of the networks toward future applications, *i.e.*, an expected significant improvement in the catalytic activity and also in the ability to conduct protons.[4]

Reaction between [1,1'-biphenyl]-3,3',5,5'-tetrayltetrakis(phosphonic acid) (**H_8btp**) and yttrium(III) chloride hydrate afforded a new family of structures, [Y(H_5btp)]·5.5H_2O (**4**), [Y(H_5btp)]·2.5H_2O (**5**), and (H_3O)[Y_2(H_5btp)(H_4btp)]·H_2O (**6**), possessing a remarkable breathing effect. The parent material, compound **4**, was obtained under mild and simple microwave irradiation conditions (100 ºC during 1 h). Upon filtration it undergoes a spontaneous single-crystal to single-crystal (SC-SC) transformation, leading to the formation of a new phase-pure material, **5**. Structural studies showed that this transformation was promoted solely by the removal of the solvent, which prompted us to perform more detailed dehydration studies on **5**. As a result, compound **6** was isolated as a pure phase when **5** was dehydrated overnight at 110 ºC. Additionally, we concluded that the dehydration process could not be completely reverted in the presence of water, but only when using methanol: compound **6** in methanol is converted into **7**, which shares the same crystal structure with **5** (see Section 4.2.5 for further details). This selectivity toward methanol happens because the channels of the MOFs are essentially formed by the hydrophobic part of the ligand (benzene rings), thus the higher affinity toward an organic solvent, rather than just water, ultimately promoting a fast reversible effect (see sub-section 8.12 in the Experimental Section for more details).

In order to confirm the phase purity of bulk [Y(H_5btp)]·2.5H_2O (**5**) and (H_3O)[Y_2(H_5btp)(H_4btp)]·H_2O (**6**) materials, powder X-ray diffraction studies were performed at ambient temperature (Figure C.1.1 in Appendix C.1). Elemental analysis, electron microscopy (Figures in Appendix C.2), solid-state NMR (Figure 4.1 and Figures

in Appedix C.3) and FT-IR spectroscopy (Figure C.4.1 in Appendix C.4) were used in tandem to further evaluate phase purity and homogeneity of the bulk materials.

4.2.2. Structural Elucidation

Compounds $[Y(H_5btp)]\cdot 2.5H_2O$ (**5**) and $(H_3O)[Y_2(H_5btp)(H_4btp)]\cdot H_2O$ (**6**) were obtained by single-crystal to single-crystal (SC-SC) transformations, with structural transformations being accompanied by single-crystal X-ray diffraction data. As we compare the empirical formulas of all compounds ($[Y(H_5btp)]\cdot 5.5H_2O$ (**4**), $[Y(H_5btp)]\cdot 2.5H_2O$ (**5**) and $(H_3O)[Y_2(H_5btp)(H_4btp)]\cdot H_2O$ (**6**)) we can immediately infer that the level of protonation and the type of ligand-to-metal coordination is almost the same for all materials. The main difference lies in the crystallization water molecules which are gradually removed (5.5 in **4**, 2.5 in **5** and 2 in **6**), and the presence of a H_3O^+ cation in **6** (formed *in situ* most likely due to proton transfer from a neighboring phosphonic acid group). These SC-SC transformations occur solely by removal of water molecules, without any break or formation of new covalent bonds. The similarity of these three structures can be verified in a topological analysis, which allows us to reduce each network to central nodes and connecting bridges. Compounds are binodal with a 6,6-connected network and a total Schäfli symbol of $\{4^{13}.6^2\}\{4^8.6^6.8\}$ (Figure C.5.1 in Appendix C.5). In fact, the three compounds have similar asymmetric units composed of one metal center and one H_5btp^{3-} residue (four independent phosphonate groups). Taking advantage of the presence of diamagnetic Y^{3+} metallic centers, we have confirmed the number of crystallographic independent phosphonic acid groups through the use of solid-state NMR studies (for the air-stable compounds). The ^{31}P MAS spectrum of **5** shows, in the isotropic region, two well-resolved sharp peaks and a third broad peak, corresponding to two resonances, centered at *ca.* 1.6, 6.8, 11.1 and 12.4 ppm respectively (Figure C.3.1 in Appendix C.3). Peak deconvolution and fitting confirmed that there are four independent phosphorus sites, which correspond to a total of one organic ligand in the asymmetric unit. The same analysis was performed for **6**: the ^{31}P MAS spectrum shows, in the isotropic region, resonances centered at *ca.* 2.6, 9.9, 11.2 and 11.8 ppm (Figure C.3.2 in Appendix C.3). One of the peaks appears as a broad signal due to the overlapping of three resonances, as established after peak deconvolution. In short, the bulk crystalline materials

have four independent phosphorus sites in good agreement with the performed crystallographic studies.

In **6** one of the hydrogen atoms is disordered, leading to the formation of a hydronium ion. This arises from the fact that the hydrogen in O12 "jumps" from this atom to the symmetrically adjacent oxygen, which leads to a negative charge of the network. This negative charge is then balanced by the presence of this hydronium cation. The presence of the hydronium ion was unequivocally confirmed by solid-state ^{1}H NMR studies (Figure 4.1).[5]

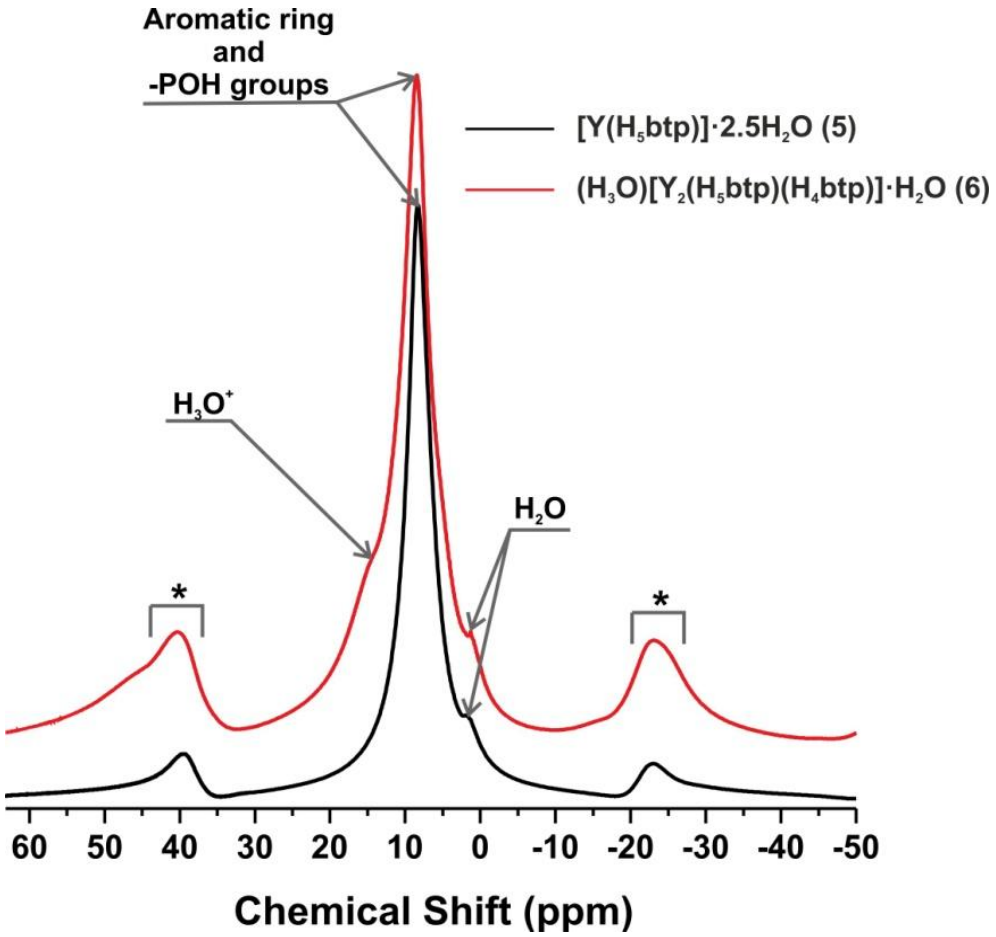

Figure 4.1. ^{1}H MAS spectrum of $[Y(H_5btp)]\cdot 2.5H_2O$ (**5**) and $(H_3O)[Y_2(H_5btp)(H_4btp)]\cdot H_2O$ (**6**). Spinning sidebands are denoted using an asterisk.

The metal centers have the same coordination geometry in all compounds, being hexacoordinated to six distinct phosphonate moieties arising from six symmetry-related organic linker residues: $\{YO_6\}$. The coordination geometry resembles slightly distorted octahedra (Figure 4.2 – *top*). Comparing materials **4**, **5** and **6** we observe a drastic reduction in the overall unit cell volume (from 2710 Å^3 to 2092 Å^3 to 961 Å^3) and also

symmetry change (from monoclinic to triclinic), corresponding mainly to a reduction of the overall solvent-accessible volume (Figure 4.2 – *bottom*). This reduction is a direct consequence of the transition from a more "open" structure to a more compact and closed form.

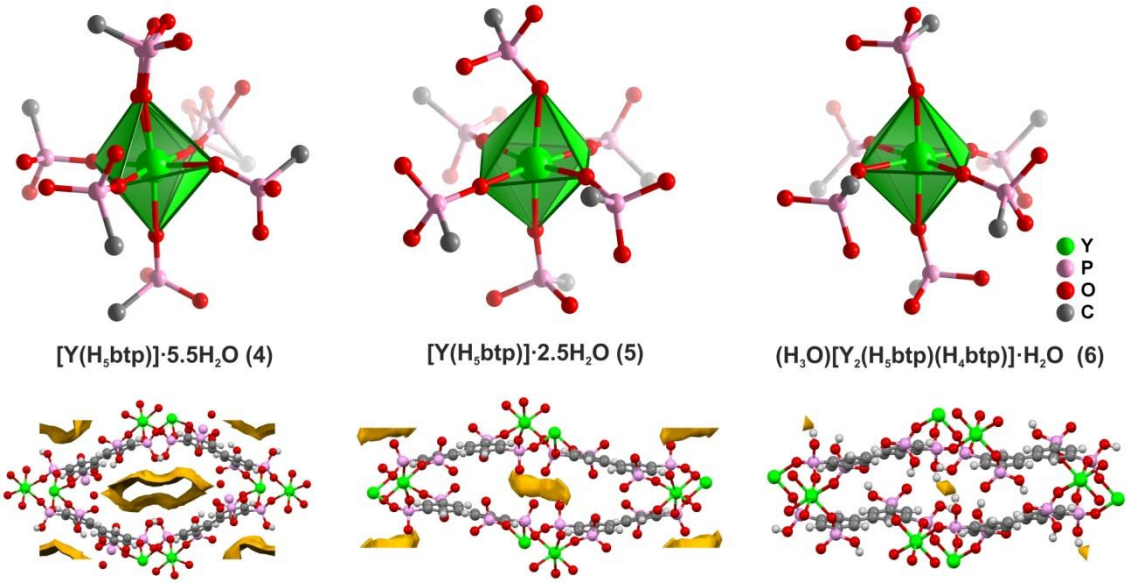

Figure 4.2. *(top)* Distorted octahedral coordination environments of Y^{3+} present in the crystal structures of compounds **4** to **6**. *(bottom)* Channel voids present in frameworks **4** to **6** calculated using Mercury Software (1.2 Å of probe radius and 0.7 Å as grid spacing using the accessible solvent volume algorithm).[6]

The bond lengths and angles of the coordination polyhedra are comparable to those reported by our research group for other Ln^{3+}-based phosphonate compounds. The refined Y–O distances ranges are: 2.190(12)-2.260(5) Å (Δ=0.07 Å) for **4**; 2.200(3)-2.270(3) Å (Δ = 0.5 Å) for **5**; 2.1899(16)-2.2845(15) Å (Δ=0.095 Å) for **6**. The refined Y^{3+} octahedra are all slightly distorted from the perfect geometrical solid, with these distortions changing with the framework transformation. The O–Y–O angles are slightly different from the ideal values (90º and 180º for the *cis* and *trans* angles, respectively). The *cis* and *trans* octahedral angles were found to be, respectively, between 81.6(4) and 95.82(16)º (Δ=14.22º) and 169.7(4) and 175.94(16)º (Δ=6.26º) for **4**, between 81.43(12) and 101.58(11)º (Δ=20.15º) and 164.39(12) and 175.31(12)º (Δ=10.92º) for **5**, and between 84.49(5) and 98.70(6)º (Δ=14.21º) and 171.14(6) and 174.27(5)º (Δ=3.13º) for **6**. These results can already provide some insight of the overall degree of distortion in the octahedra. However, in some cases, discrete values can be misleading. To overcome this

we decided to employ the adaptation of the method proposed by Baur[7] to calculate the distortion index (DI) for bonds and angles:

$$DI_{Bond} = \frac{\sum_{i=1}^{n} | d(Y-O)_i - d(Y-O)_{average} |}{\sum_{i=1}^{n} | d(Y-O)_i |} \quad \text{(Equation 1)}$$

$$DI_{Angle} = \frac{\sum_{i=1}^{n} | \angle(O-Y-O)_i - \angle(O-Y-O)_{ideal} |}{\sum_{i=1}^{n} | \angle(O-Y-O)_i |} \quad \text{(Equation 2)}$$

where *O* corresponds to any coordination site, and the subscripts *i* and average/ideal indicate individual and average/ideal bond lengths and angles. For an octahedron, the values related to the angles should be calculated separately for the *cis* and *trans* angles, which are compared to their ideal values (90 and 180º, respectively). The distortion index (DI) calculated for the three compounds are given in Table 4.1. As one can infer the DI_{bond} does not change significantly for each material. However, the SC-SC transformation from **4** to **5** leads to a higher angle distortion, in particular for the *trans* angles. The loss of three water molecules per asymmetric unit has an effect on the pore size, leading not only to a higher distortion in the coordination sphere of the metal center, but also to a change in the organic linker. As depicted in Figure 4.3 there is an evident slight rotation between the aromatic rings from 7.1º to 12.5º. On the other hand, the SC-SC transformation from **5** to **6** has the contrary effect. With the removal of 1.5 water molecules per asymmetric unit the organic linkers exhibit an identical mutual internal rotation between the aromatic rings as observed in **4** (7.1º for **4** and 7.9º for **6**) (Figure 4.3).

Table 4.1. Distortion index (DI) for bonds and angles (*cis* and *trans*) of the coordination spheres of compounds $[Y(H_5btp)]\cdot 5.5H_2O$ (**4**), $[Y(H_5btp)]\cdot 2.5H_2O$ (**5**) and $(H_3O)[Y_2(H_5btp)(H_4btp)]\cdot H_2O$ (**6**).

	DI_{bond}	DI_{angle} (*cis*)	DI_{angle} (*trans*)
1	0.010	0.045	0.041
2	0.008	0.050	0.058
3	0.009	0.036	0.039

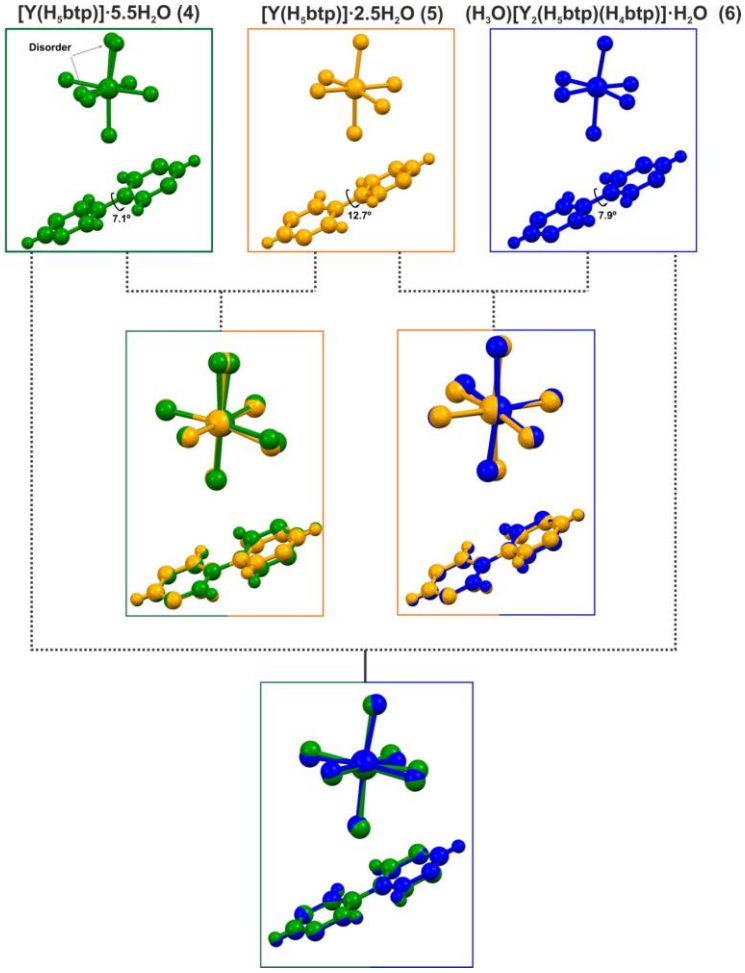

Figure 4.3. *(top)* Schematic representation of the coordination environment and organic linker backbone of compounds **4**-**6** and *(bottom)* overlay between structures **4**-**6**. The overlay was performed using the Mercury Software.[6]

The crystallization water molecules interact with the networks by way of supramolecular contacts (hydrogen interactions) in all compounds. In **4** only hydrogen bonds established between water molecules and the –POH groups of the main structure are present, with a solvent accessible volume calculated of 12.3% per unit cell (calculated using Mercury Software).[6] The high solvent disorder and weak interactions between crystallization water molecules and the –POH groups facilitate the transformation, which, upon filtration, leads to the formation of **5**. The release of some water molecules is accompanied by a reduction of the pore size and a distance decrease between metal centers of opposite sides (Figure 4.4). While in **4** the metal centers are separated by 13.6328(18) and 13.0848(18) Å, in **5** they are closer, separated by 10.5525(10) and 8.9763(9) Å respectively, with a pore size calculated of 1.2% per unit cell. This transformation leads to the formation of a more stable compound, mainly by stronger interactions between water molecules and –POH groups. Not only that, but **5** forms hydrogen bonds between –POH

groups of opposite sides of the channel, leading to a more compact and robust structure (Figure 4.5). With an increase of temperature (by applying a thermal treatment at 110 ºC or higher) some hydrogen bonds are broken and a new SC-SC transformation is observed. This follows the same mechanism as for **5** in which some of the remaining water molecules are removed from the channels of the framework. With only one water molecule per asymmetric unit, **6** is maintained mainly by hydrogen bonds between –POH groups of opposite sides of the channels. As for the previous transformation, there is a visible decrease in solvent accessible volume (reduction to 0.2% per unit cell). However, the metal centers of opposite sides of the channels seem to be slightly farther apart (10.5525(10) and 8.9763(9) Å for **5** and 10.7455(9) and 9.0513(7) Å for **6**) (Figure 4.5). This is due to the spatial distribution of the organic linkers. While in **4** and **5** the ligands form lozenge-based tunnels when connected to the metal centers, in **6** they exhibit a more rectangular shape. This distribution may also explain the lower angle distortion for **6** as discussed previously.

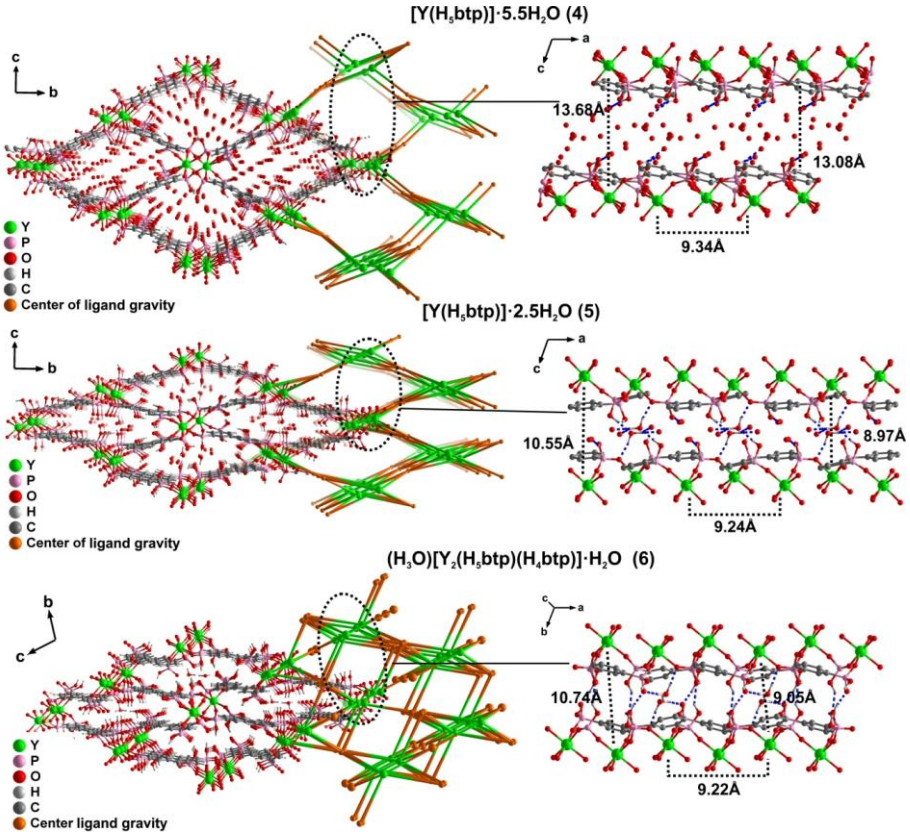

Figure 4.4. *(left)* Schematic representation of the crystal packing of compounds **4**-**6** viewed in perspective along the [100] direction of the unit cell (the 6,6-connected binodal topology is overlapped in all representations). *(right)* Cross-section of the channels viewed along the *a*-axis. The dashed blue lines represent the hydrogen interactions between the water molecules and the POH groups.

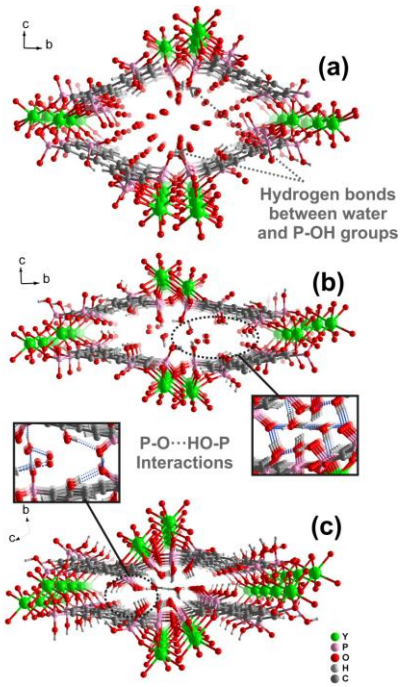

Figure 4.5. Schematic representation of the crystal packing of **(a)** $[Y(H_5btp)]\cdot 5.5H_2O$ (**4**), **(b)** $[Y(H_5btp)]\cdot 2.5H_2O$ (**5**) and **(c)** $(H_3O)[Y_2(H_5btp)(H_4btp)]\cdot H_2O$ (**6**) viewed in perspective along the [100] direction of the unit cell. Supramolecular interactions involving the water molecules and phosphonate groups are emphasized.

4.2.3. Thermogravimetry and thermodiffractometry

The thermal stability of compound $[Y(H_5btp)]\cdot 2.5H_2O$ (**5**) was investigated between ambient temperature and *ca.* 800 ºC (Figure C.6.1 in Appendix C.6), providing additional information on the hydration level of the bulk compound. The crystallinity of the bulk material was further evaluated by employing *in situ* variable-temperature powder X-ray diffraction studies (VTPXRD; Figure C.6.2 in Appendix C.6), in the 25-1200 ºC temperature range.

Between ambient temperature and *ca.* 250 ºC, compound **5** loses approximately 7.5% of mass in two consecutive steps, corresponding to the release of *ca.* 2.5 water molecules of crystallization. This value agrees well with the calculated one (*ca.* 7.4%). A third weight loss, corresponding to 2.7%, occurs between *ca.* 250 and 350 ºC. According to our previous studies[8] the phosphonate groups of the organic ligand in the framework may suffer a rearrangement at this temperature range, leading to the formation of pyrophosphonates with the consequent release of water molecules (in this case the observed 2.7% weight loss is equivalent to one water molecule). In order to evidence this

reorganization, compound **5** was calcined at 350 ºC. The resulting residue was analyzed by FT-IR in order to identify the typical *ν*(P–O–P) stretching vibration, which normally appears in the 930-915 cm^{-1} range (data not shown).[9] Results were inconclusive due to the overlapping of vibrational modes in this spectral region. Nevertheless, considering the amount of phosphonic acid groups, as well as their proximity in the framework, the possibility of their rearrangement toward the formation of pyrophosphonate groups seems to be a plausible possibility.

Variable-temperature powder X-ray diffraction studies on $[Y(H_5btp)]\cdot 2.5H_2O$ (**5**) corroborate the afore mentioned assumptions concerning the release of the water molecules and the concomitant phase modifications (Figure C.6.2 in Appendix C.6): from ambient temperature to *ca.* 350 ºC, the structure of **5** changes, leading to the formation of new crystalline phases. The structure of material **5** starts to collapse from *ca.* 550-600 ºC, becoming almost amorphous at 800 ºC. At *ca.* 1200 ºC, powder X-ray diffraction studies (PDF4+ 2014 release ICDD database) show the formation of a residue composed of yttrium phosphate (YPO_4, ICDD 00-042-0501).

An identical set of studies were performed for $(H_3O)[Y_2(H_5btp)(H_4btp)]\cdot H_2O$ (**6**) (Figures C.6.3 and C.6.4 in Appendix C.6). The first weight loss occurs between ambient temperature and *ca.* 190 ºC, corresponding to the release of two water molecules of crystallization. The experimental value of *ca.* 3.2% agrees well with the calculated one (*ca.* 3.1%). Between *ca.* 190 and 350 ºC is observed a second weight loss (*ca.* 3.4%), also attributed to the release of two water molecules originating from the rearrangement of the phosphonic acid groups in order to, most likely, form pyrophosphonate moieties. After a plateau of approximately 200 ºC (between 350 and 550 ºC) in which the dehydrated material remains stable, the material decomposes. Thermodiffractometry studies show that the structure of **6** remains unaltered up to *ca.* 120 ºC. After this temperature, and up to *ca.* 200 ºC, a new crystalline phase is formed (the dehydrated form of **6**). The possible formation of pyrophosphonates led to a new rearrangement of the framework of **6** (between 200 and 400 ºC). An amorphous residue appears at *ca.* 750 ºC.

4.2.4. FT-IR spectroscopic studies

FT-IR spectroscopy studies clearly support the structural features unveiled by the X-ray diffraction studies. Figure C.4.1 (in Appendix C.4) depicts selected regions in the

spectra of phase-pure compounds **5** and **6**. Relevant differences in some spectral regions are noticeable despite the overall identical profiles. The most striking differences are assigned to vibrational modes of crystallization water molecules, which provide important information concerning the different chemical environments of these moieties in the compounds.

Compound **5** possesses in its pore structure only solvent water molecules. This structural feature is markedly visible in the FT-IR spectra of the compounds, particularly in the 3600-2650 cm^{-1} spectral range that is highly dominated by the O–H vibrational mode of water molecules. While for **5** a broad band includes several vibrations, for **6** more defined vibrational modes are observed in this particular range. A well-defined vibration band centred at 3505 cm^{-1} is attributed to the hydronium cation and confirms a strong hydrogen bond verified previously in the performed single-crystal X-ray studies of **6**.[10] The broad band located at 3375 cm^{-1} is attributed to crystallization water molecules. *ν*(PO–H) and *ν*(C–H) stretching vibrational modes of medium intensity are also observed at 3250 cm^{-1} and 3075 cm^{-1}, respectively.

Below 1860 cm^{-1} the FT-IR spectrum of all materials is very complex, with a large number of medium-to-very strong vibration bands, mainly arising from the organic ligand itself. Based on the literature,[9] the medium intensity bands between 1860 and 1560 cm^{-1} are attributed to the *ν*(C=C) vibration in functionalized benzene rings, as well as the in-plane deformation of water molecules. The peaks at *ca.* 1400 cm^{-1} with medium and weak intensity, respectively, are attributed to the P–C bond's deformation. The *ν*(P=O), *ν*(P–O) and *ν*(P–C) vibration modes appear between 1280 and 600 cm^{-1} (with strong to very strong intensity).

4.2.5. Heterogeneous catalysis

The catalytic performance of $[Y(H_5btp)]\cdot 2.5H_2O$ (**5**) was investigated in the ring-opening reaction of styrene oxide with methanol at 35 ºC. The initial catalytic activity of the MOF was 138 mmol g_{MOF}^{-1} h^{-1} based on conversion at 15 min; 2-methoxy-2-phenylethanol was the sole product formed with 96% yield after 2 h of reaction (catalyst load of 3.3 g L^{-1}). The excellent product selectivity reached with this MOF is a great advantage for applications in the pharmaceutical sector where compounds possessing 1,2-

alkoxy alcohol groups are important intermediates,[11-15] *e.g.*, for the synthesis of tricyclic beta-lactam antibiotics.[16]

For comparative purposes, the ligand and metal precursors of the MOF, namely, **H_8btp** and $YCl_3 \cdot 6H_2O$, were tested as catalysts under similar styrene oxide reaction conditions (**H_8btp** and YCl_3 were used in amounts equivalent to the moles of ligand or metal found in the MOF in standard catalytic tests). Both precursors promoted the conversion of styrene oxide to 2-methoxy-2-phenylethanol with 100% selectivity (Figure C.7.1 in Appendix C.7). The Brönsted acidity of **H_8btp** and, on the other hand, the Lewis acidity of $YCl_3 \cdot 6H_2O$ seems to play an important role in the alcoholysis of the epoxide. For $YCl_3 \cdot 6H_2O$, styrene oxide conversion reached a plateau after 2 h of reaction, suggesting the deactivation of this precursor (it was completely soluble, acting as a homogeneous catalyst). In contrast, **H_8btp** was far more active (100% conversion to 2-methoxy-2-phenylethanol within 15 min of reaction) than $YCl_3 \cdot 6H_2O$ (9%/22% of conversion at 15 min/2 h), suggesting that Brönsted acidity is more favorable for this reaction. Accordingly, the high 2-methoxy-2-phenylethanol yields reached for **5** may be essentially due to Brönsted acid sites.

The lower catalytic activity of **5** in comparison to **H_8btp** may be partly due to differences in the amount of effective active acid sites, because the free organic ligand possesses four phosphonic acid groups per molecule, whereas when it is coordinated in the MOF structure the ligand possesses a smaller number of free OH groups (a fraction of the OH groups are deprotonated and coordinated to the metal centers). On the other hand, **H_8btp** was completely soluble in the reaction medium and, therefore, it acted as a homogeneous acid catalyst, whereas the MOF was completely insoluble and acted as a true heterogeneous catalyst. The heterogeneous nature of the catalytic reaction of styrene oxide over the MOF was, indeed, assessed by leaching tests (see sub-section 8.9 in the Experimental Section for more details). After separating the solid catalyst from the reaction mixtures by membrane filtration at the reaction temperature, the conversion of styrene oxide ceased for the remaining reaction time, indicating the absence of soluble active species desorbed from the MOF (Figure C.7.2 in Appendix C.7). An important advantage of MOF materials over homogeneous catalysts is that the former are easily separated from the reaction mixtures, which can be efficiently carried out by filtration or centrifugation.

To the best of our knowledge there is only one lanthanide-containing MOF, the 1D $[La_2(H_3nmp)_2(H_2O)_4] \cdot 4.5H_2O$, reported by our group, which led to comparable catalytic

results (Table C.7.1 in Appendix C.7).[17] Various transition metal-containing MOFs have been previously tested as catalysts for the methanolysis of styrene oxide (results compared in Table C.7.1 in Appendix C.7).[2, 3, 8, 18-28] Although it is difficult to make clear and fair comparisons due to the different reaction conditions employed between different studies, the catalytic performance of **5** seems to compare favorably to various other MOFs. For example, [Fe(BTC)][19] and MIL-101(HPW)[25] led to 99% styrene oxide conversion in less reaction time than **5**, but the reaction temperature and catalyst loadings were higher, and a lower initial concentration of styrene oxide was used in the case of MIL-101(HPW), which are favorable factors for a faster kinetics.[25] Good catalytic results were reported by Zhou *et al.*[27] but for a MOF with different organic moieties (MIL-101(SO_3H)) which led to 99% conversion at 10 min of reaction, using relatively low initial concentration of styrene oxide.

Compound **5** was further explored in the acid-catalyzed acetalization of benzaldehyde at 35 ºC. Results for this reaction were more thoroughly explored in this work mainly because acetalization reactions are broadly used and very important in organic synthesis. They allow the protection of carbonyl groups of highly functionalized (reactive) molecules, improving the chemical stability toward various reagents such as bases and oxidants.[29] In particular, acetals of benzaldehyde are used in different sectors of the chemical industry, such as the production of perfumes and flavors,[30] pharmaceuticals, plasticizers,[31] cosmetics, food additives, beverages,[30, 32, 33] solvents, and other useful chemicals.[30, 32, 34] Several types of solid acid catalysts have been explored for the acetalization of benzaldehyde, such as zeolites,[10] transition metal mixed oxides,[35] Fe-doped SO_4^{2-}/SnO_2,[36] carbon based catalysts,[37, 38] ion-exchange resins,[39, 40] and MOFs such as MIL-100Fe[41] and SO_3H-MIL-101.[42] The reaction of benzaldehyde with methanol in the presence of **5** at 35 ºC was fast, resulting in (dimethoxymethyl)benzene as the only product formed with 94% yield in 1 h (Figure C.7.3 in Appendix C.7). The catalytic performance of **5** for the acetalization reaction was similar, when compared to the alcoholysis reaction. The acetalization of benzaldehyde involves formation of water as byproduct which can negatively affect the product yield by shifting the equilibrium to the formation of benzaldehyde.[17, 43, 44] Nevertheless, very high conversions were reached for **5**, which may be partly due to favorable surface polarity and competitive adsorption effects. Increasing the catalyst loading from 3.3 $g_{MOF}\ L^{-1}$ to 20 $g_{MOF}\ L^{-1}$ enhanced the reaction rate, and the (dimethoxymethyl)benzene yields at 30 min increased from 49% to 89%, respectively (Figure C.7.3 in Appendix C.7). These results are outstanding in comparison to those for

the 1D MOF $[La_2(H_3nmp)_2(H_2O)_4]\cdot 4.5H_2O$ tested under identical benzaldehyde reaction conditions, which led to 94% (dimethoxymethyl)benzene yield only after 20 h (catalyst loading of 20 g_{MOF} L^{-1}) (Table C.7.2 in Appendix C.7).[17] The superior catalytic performance of **5** compared to various MOFs investigated for this reaction is clearly demonstrated in Table C.7.2 (in Appendix C.7)[17, 19, 43, 45-49] In order to gain mechanistic insights into the acetalization reaction, precursors **H_8btp** and $YCl_3\cdot 6H_2O$ were also tested for the benzaldehyde conversion (the precursors were used in amounts equivalent to the moles of MOF added in catalytic tests using 3.3 g_{MOF} L^{-1}). **H_8btp** and $YCl_3\cdot 6H_2O$ led to extremely fast conversion of benzaldehyde to (dimethoxymethyl)benzene, which was formed with 91% and 96% yield at 15 min of reaction, respectively (Figure C.7.3 in Appendix C.7). Hence, Brönsted and Lewis acidity can be highly favorable for the acetalization reaction. Comparably high product yields were reached after 2 h reaction in the presence of **5**, which may be due to Lewis (*e.g.*, defect Y-sites) and/or Brönsted acid sites (phosphonic acid groups). On the other hand, it is possible that Lewis acid Y-sites induce Brönsted acidity by polarizing water molecules which are formed as byproduct of the acetalization reaction. The Brönsted acid-catalyzed reaction of benzaldehyde may take place via protonation of the carbonyl group and reaction with methanol to give a hemiacetal intermediate, which further reacts with another methanol molecule to give the acetal product, (dimethoxymethyl)benzene (Scheme C.7.1 in Appendix C.7).[46] While the Lewis acid catalyzed mechanism may be similar to that proposed by Janiak *et al.*,[46] involving coordination of the alcohol and aldehyde reactants to Lewis acid sites leading to chelating intermediates, which are converted to the acetal and water (Scheme C.7.2 in Appendix C.7).

The recyclability of the MOF was investigated by carrying out four consecutive batch runs of benzaldehyde conversion (20 g_{MOF} L^{-1}, at 35 ºC; Figure 4.6). Differences in the initial catalytic activity were observed between runs, which may be partly due to some fragmentation of the particles of the catalyst. Nevertheless, for the investigated material, very high benzaldehyde conversions were reached for four consecutive batch runs (93-98% at 1 h reaction), with (dimethoxymethyl)benzene being always the sole reaction product (100% selectivity). Material **5** retained its structural integrity during subsequent runs, which was confirmed by PXRD (Figure C.7.4 in Appendix C.7) and FT-IR spectroscopy (Figure C.7.5 in Appendix C.7) of the used solids.

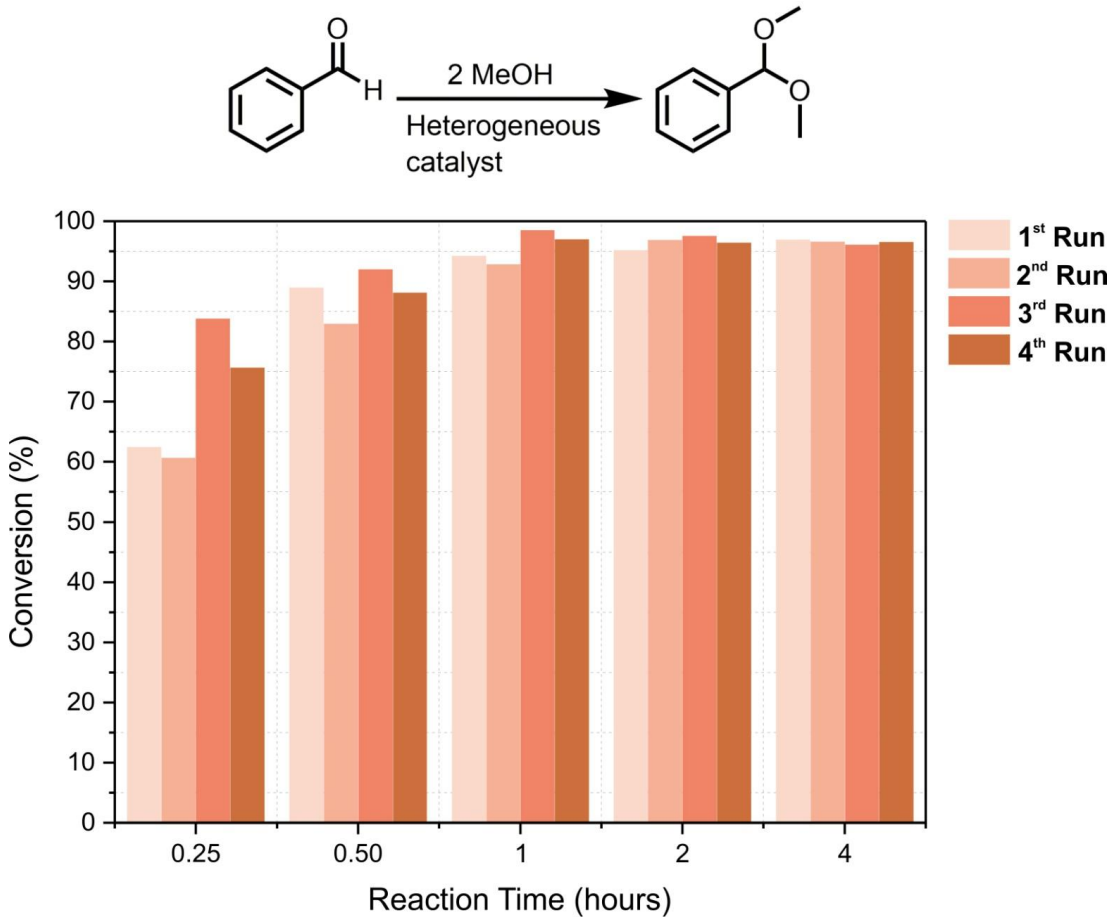

Figure 4.6. Reaction of benzaldehyde with methanol to afford (dimethoxymethyl)benzene in the presence of the heterogeneous catalyst $[Y(H_5btp)]\cdot 2.5H_2O$ (**5**) in four consecutive batch runs. Reaction conditions: 35 ºC, 4 h, catalyst load = 20 g_{MOF} L^{-1}. (Dimethoxymethyl)benzene was formed with 100% selectivity.

The same studies for the alcoholysis of styrene oxide and acetalization of benzaldehyde were performed using $(H_3O)[Y_2(H_5btp)(H_4btp)]\cdot H_2O$ (**6**). It was observed that during the first batch run of the catalytic studies compound **6** was converted into $[Y(H_5btp)]\cdot H_2O\cdot 0.5(MeOH)$ (**7**). This compound shares the same crystalline phase with **5** as ascertained by PXRD (Figure C.7.6 in Appendix C.7) and FT-IR spectroscopy (Figure C.7.7 in Appendix C.7).

Methanol uptake by compound **6**, and a subsequent phase transition to **7**, was further corroborated by thermogravimetry (Figure C.7.8 in Appendix C.7). Compound **7** loses 2.6% (calculated *ca.* 2.7%) of its weight between ambient temperature and *ca.* 70 ºC, corresponding to the release of 0.5 molecules of methanol. As expected, after the release of the methanol molecules, the thermal behavior of compound **7** is very much identical to that of **6** (Figure C.6.3 in Appendix C.6).

4.2.6. Protonic conductivity

Proton conducting materials have gained a lot of interest in recent years due to their many applications, especially for hydrogen fuel cells. Metal-organic frameworks are some of those materials. Structure-defined MOFs possess several supramolecular interactions with guest solvents, and so they have been studied due to the high protonic conductivity they exhibit. Yet the relationship between the hydrogen-bonding pathways and proton conductivity is not always sufficiently investigated. The exact network of the confined guests in the pores is often not determined because of structural disorder, even when the framework structure is clear. In this work, the possibility to determine the MOF architectures for the breathing system using single-crystal X-Ray diffraction proved to be an advantage because of the opportunity to visualize the potential ion transfer pathways within the network. The 1D channels with surface non-coordinated –POH groups of the MOFs herein studied have an obvious potential to enable high levels of protonic conductivity by accommodating a variable amount of water molecules. To clarify this relationship between conductivity and structure pathways we tried to illustrate the hydrogen-bonding networks between acidic species and guest water molecules in materials **4**, **5** and **6** (Figure 4.4 – *right*). We were interested in the analysis of viable proton conduction pathways throughout the structure of the synthesized materials and verified that the hydrogen bonding networks of acidic species and guest molecules was extremely well-ordered for material **6**, although the water molecules embedded in the narrow pores were separated by a considerable distance. This problem, however, was not occurring in the remaining materials (**4** and **5**): even though not all hydrogen bonds could be distinguished due to the high disorder, the guest molecules are much more dispersed throughout the channels, contributing to a much more intricate arrangement of hydrogen bonds that could facilitate the proton conducting mechanism.[50] In addition, **6** arose as a very promising material due to the natural proton transfer occurring during the desolvation process, leading to the presence of H_3O^+ species in the material. Taking all this into account, conductivity studies under variable relative humidity (RH) have been carried out for the composition with the least water content $(H_3O)[Y_2(H_5btp)(H_4btp)]\cdot H_2O$ (**6**) MOF, with the expectation that the material can effectively absorb further water molecules leading to enhanced proton transport, possibly associated with a phase transition to the more hydrated phases, $[Y(H_5btp)]\cdot 2.5H_2O$ (**5**) or even $[Y(H_5btp)]\cdot 5.5H_2O$ (**4**).

Measurements were conducted on two $(H_3O)[Y_2(H_5btp)(H_4btp)]\cdot H_2O$ (**6**) samples, one corresponding to the as-prepared material, hereafter referred to "as-prepared", and another that was previously dried at 120 ºC overnight, which is identified as "predried". The powder could be easily pressed into disk-shaped pellets, free from major defects and retaining its crystallinity, as well as structural integrity. In agreement with our expectations, the impedance spectra for both samples display a tremendous influence regarding relative humidity. At RH of 80% and lower, the spectra are dominated by one single semicircle and one capacitive tail at low frequency, corresponding to the bulk resistance of the pellet and the electrode relaxation, respectively (Figures C.8.1 and C.8.2 in Appendix C.8). Increasing RH reduces the amplitude of the semicircle which is indicative of the lowering of the ohmic resistance of the sample (*R*). We additionally observe an increase of the frequency at the top of the semicircle (f_{peak}), which is a measure of the relaxation frequency of the ionic polarization. Assuming that a simple description of the ionic relaxation by the usual parallel *RC* equivalent circuit with the peak frequency is given by $f_{peak} = (2\pi RC)^{-1}$, one concludes that the capacitance *C* remains constant, or even increases, in agreement with a slight increase of the dielectric constant expected for a material with higher water content. Under saturated conditions (98% RH), the magnitude of decrease of *R* is such that f_{peak} increases beyond the measuring range of the LCR meter (2MHz) and only the electrode impedance is observed. In this case, *R* is given by *Z'* at the high frequency intercepted with the real axis of the Nyquist plot.

Figure 4.7 shows the conductivity data for both the "as-prepared" and "predried" samples in Arrhenius plots coordinated for variable RH conditions. The figure confirms that the large increase in conductivity with increasing humidity registered for **6** is most likely a result of the induced absorption of water by the material. At and below 80% RH, the temperature dependence of the conductivity displays the typical linear Arrhenius trend, with activation energy in the range 0.26-0.48 eV, with somewhat lower values for the predried sample, and especially the as-prepared sample at 20% RH (0.26 eV) (Table 4.2). The latter may be explained by kinetic reasons dictated by the larger water content in this sample which responds differently when exposed to the initial dry 20% RH environment (the measurements were carried out with increasing temperature, at each RH). Nevertheless, the range of activation energies is in line with those reported for other MOFs,[51] and suggests the structural diffusion of protons (along the water domains formed in the vicinity of the acidic phosphonate groups) as the dominating charge transport mechanism in these materials. Unfortunately, the amount of absorbed water should be

rather low in this humidity range (≤80% RH) and, as a result, the magnitude of the conductivity is rather low, only marginally exceeding 10^{-5} S cm^{-1} at 94 ºC and 80% RH.

Table 4.2. Activation Energy in eV for the Protonic Conductivity Measured under Variable Relative Humidity.

	activation energy (eV)			
	20[a]	**40[a]**	**60[a]**	**80[a]**
Predried pellet	0.35	0.37	0.44	0.40
As-prepared pellet	0.26	0.40	0.48	0.46

[a]RH (%)

At 98% RH, Figure 4.7 demonstrates, however, a spectacular enhancement of the conductivity from 7.70×10^{-5} to 1.94×10^{-2} S cm^{-1} between 60 and 80 ºC, which further increases to 0.03 S cm^{-1} at 94 ºC. In these conditions the hydrogen bonds maintaining the structure are weakened and a higher quantity of water flows though the pores of **6**, which eventually transforms into the more hydrated $[Y(H_5btp)]\cdot2.5H_2O$ (**5**) phase. This was confirmed by the PXRD pattern collected from the pellet after impedance measurements at 98% RH / 94 ºC, which shows clear evidence of formation of **5** (Figure C.8.3 in Appendix C.8, blue pattern). This X-ray powder pattern collected at ambient temperature contains reflections of both compounds **6** and **5**, probably due to the reversibility of the **6**→**5** phase transition below 80 ºC. It should be noticed that the same partial phase transformation is observed by rehydrating freshly synthesized material **6** under more drastic hydrothermal conditions (Figure C.8.3 in Appendix C.8, green pattern). The additional water molecules present in **5**, as well as the higher mobility due to the increase in pore size, allow the transport of a higher amount of protons.[52] This abrupt increase has been reported in the past. Tominaka[53] and collaborators have reported a rapid raise in conductivity from 5.0×10^{-9} to 3.9×10^{-5} S cm^{-1} due to the increase of RH from 50% RH to 67% for $((CH_3)_2NH_2)[Li_2Zr(C_2O_4)_4]$ at 17 ºC. Bazaga-García and co-workers[54] have reported a similar abrupt increase at 98% RH visible with the increase of the temperature: Ca-PiPhtA-I $(Ca_2[(HO_3PC_6H_3COOH)_2]_2[(HO_3PC_6H_3(COO)_2H)(H_2O)_2]\cdot5H_2O)$ shows an increase in conductivity from 5.7×10^{-4} to 1.3×10^{-3} S cm^{-1} between 24 and 40 ºC. The water content remains unaltered before and after the change in temperature; consequently the increase of conductivity is attributed to a thermal activation mechanism which led to a small structural and/or textural change.

Compound **6** shows similar conductivity values at low temperatures (40 and 60 ºC) when compared with several MOFs.[55] On the other hand, it also shows an excellent conductivity at 98% RH (2.58×10^{-2} S cm^{-1}), being one of the best results reported for these kind of materials. It is comparable to PCMOF21/2,[56] with 2.1×10^{-2} S cm^{-1} at 85 ºC and 90% RH, and only surpassed by $\{[(Me_2NH_2)_3(SO_4)]_2[Zn_2(ox)_3]\}_n$,[57] ($4.2\times10^{-2}$ S cm^{-1}, ambient temperature and 98% RH) and H_2SO_4@MIL-101[58] (6.0×10^{-2} S cm^{-1} at 80 ºC and 20% RH), the latter actually being a mixture of sulfuric acid and a MOF. When we compare, however, the synthesis and properties of all materials, both **6** and **5** arise as the more stable compounds which can be obtained using simple methodologies, with no need for demanding storage conditions (when compared to PCMOF21/2), using faster and more sustainable reaction conditions (compared to $\{[(Me_2NH_2)_3(SO_4)]_2[Zn_2(ox)_3]\}_n$) and with no need of several synthetic steps or high temperature conditions (which was the case of MIL-101 and the subsequent H_2SO_4@MIL-101).

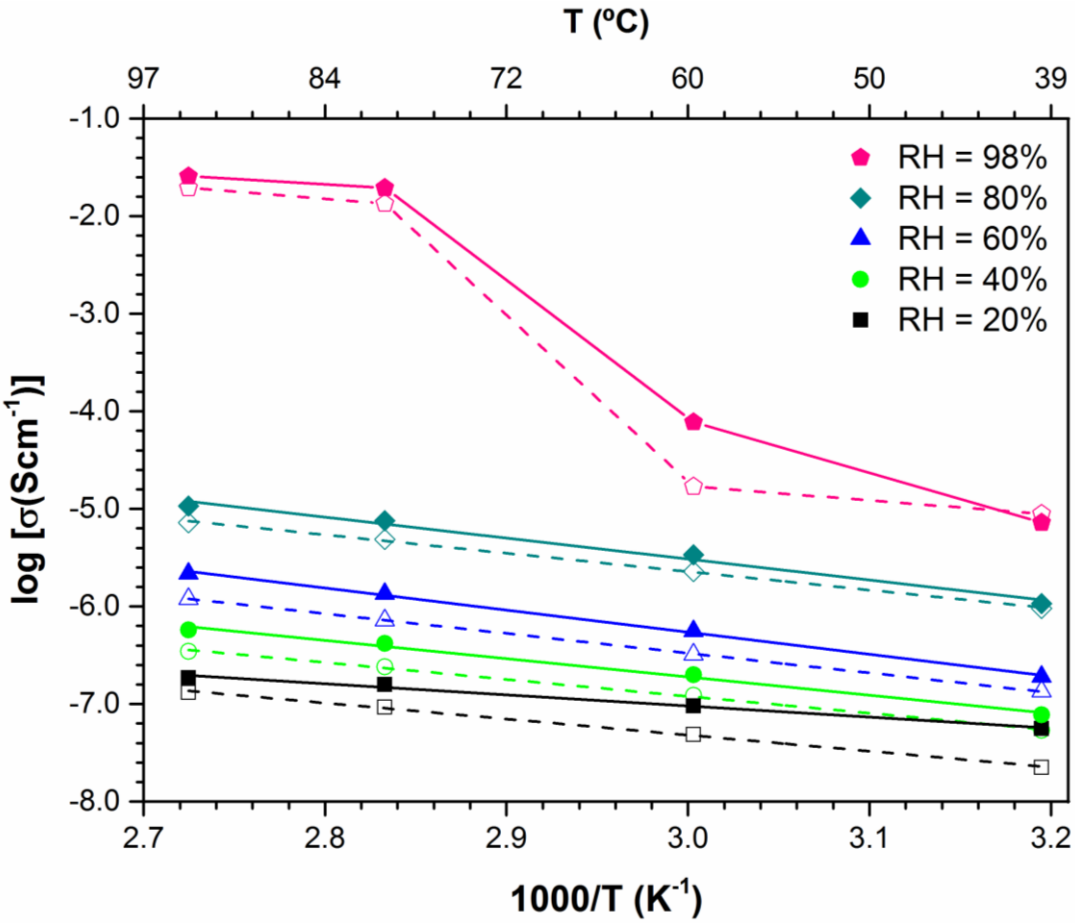

Figure 4.7. Arrhenius plots of the protonic conductivity of $(H_3O)[Y_2(H_5btp)(H_4btp)]\cdot H_2O$ (**6**) samples (predried pellet – open symbols; as-prepared pellet – solid symbols). The lines for RH 80% and lower humidity are fits to the Arrhenius equation, and a simple guide for the eye for 98% RH.

4.3. Conclusions

A new family of materials exhibiting unique multifunctionality was prepared using a methodology based on microwave-assisted synthesis (MWAS). The three novel open-framework phase-pure MOFs, $[Y(H_5btp)]\cdot 5.5H_2O$ (**4**), $[Y(H_5btp)]\cdot 2.5H_2O$ (**5**), and $(H_3O)[Y_2(H_5btp)(H_4btp)]\cdot H_2O$ (**6**), were obtained in bulk quantities. **4** was isolated using a simple, fast and high yield synthetic process, when compared to more conventional methodologies, while **5** and **6** were obtained by single-crystal to single-crystal (SC-SC) transformations: **5** is formed after filtration of **4** and **6** is prepared by heating **5** at 110 ºC overnight. The structural relationships between the three networks and their breathing effect were thoroughly studied. It was verified that after the removal of lattice water molecules at moderate temperatures, the crystalline three-dimensional framework is maintained. Single-crystal X-ray diffraction showed that the three structures are virtually the same, a binodal 6,6-connected network with a total Schäfli symbol of $\{4^{13}.6^2\}\{4^8.6^6.8\}$, with the sole difference being the number of crystallization water molecules. The present study further indicated that the yttrium coordination environment is composed exclusively by phosphonate oxygens, *i.e.* there are no water molecules coordinated to the metal centers. This structural feature clearly contributes to the observed mechanical robustness and thermal stability of the materials, particularly evident for material **6** which showed an outstanding thermal stability up to *ca.* 600 ºC. A detailed and exhaustive literature search[39, 59-68] revealed that **6** is indeed one of the most stable reported MOFs based on a tetraphosphonic organic linker concerning exposure to humidity and mechanical and thermal robustness.

After full characterization in the solid state, properties envisaging possible applications of the materials were investigated: usage in heterogeneous catalysis and protonic conductivity (for **5** and **6**, respectively). Outstanding performance results were observed for both applications. **5** showed excellent catalytic activity in two distinct acid-catalyzed reactions: ring-opening reaction of styrene oxide with methanol at 35 ºC, with the formation of 2-methoxy-2-phenylethanol as the sole product with 96% yield at 2 h of reaction; in the acetalization of benzaldehyde with 94% conversion into (dimethoxymethyl)benzene at 1 h of reaction. To the best of our knowledge, this latter result is amongst the best results registered to date of all those reported in the literature for

a MOF material. For the ring-opening reaction, the present material compares very well with one of our previous best reported materials, $[La_2(H_3nmp)_2(H_2O)_4]\cdot 4.5H_2O$.[17]

Concerning the protonic conductivity properties of **6**, it was verified a tremendous influence regarding relative humidity (RH). Although the conductivity marginally exceeds the 10^{-5} S cm^{-1} up to 94 ºC and 80% RH, when exposed to 98% RH, a great increase was observed. At this value of humidity, an increase of conductivity between 60 and 80 ºC (from 7.70×10^{-5} to 1.94×10^{-2} S cm^{-1}) was registered, which further increased to 0.03 S cm^{-1} at 94 ºC. **6** is, therefore, one of the best performing MOFs reported to date concerning proton conductivity, with conductivities in the same magnitude of only two other reported materials in the literature. We note, however, that an important advantage of **6** in comparison to these other materials resides with its inherent stability at ambient conditions (temperature and humidity), as well as its sustainable, simple and easy to perform synthesis methodology.

A further study on material **6** to confirm the flexibility of the framework showed the high affinity of the material toward methanol, leading to the formation of $[Y(H_5btp)]\cdot H_2O\cdot 0.5(MeOH)$ (**7**), an isotypical network with **5**. Remarkably, the same behavior was not observed when **6** was simply exposed to water, even at high temperatures, with only a partial rehydration being observed. The reasons for such remain unknown to date.

4.4. References

(1) Vilela, S. M. F.; Ananias, D.; Fernandes, J. A.; Silva, P.; Gomes, A. C.; Silva, N. J. O.; Rodrigues, M. O.; Tome, J. P. C.; Valente, A. A.; Ribeiro-Claro, P.; Carlos, L. D.; Rocha, J.; Paz, F. A. A.; *J. Mater. Chem. C*, **2014**, *2*, 3311.

(2) Vilela, S. M. F.; Ananias, D.; Gomes, A. C.; Valente, A. A.; Carlos, L. D.; Cavaleiro, J. A. S.; Rocha, J.; Tome, J. P. C.; Paz, F. A. A.; *J. Mater. Chem.*, **2012**, *22*, 18354.

(3) Vilela, S. M. F.; Firmino, A. D. G.; Mendes, R. F.; Fernandes, J. A.; Ananias, D.; Valente, A. A.; Ott, H.; Carlos, L. D.; Rocha, J.; Tome, J. P. C.; Paz, F. A. A.; *Chem. Commun.*, **2013**, *49*, 6400.

(4) Firmino, A. D. G.; Mendes, R. F.; Ananias, D.; Vilela, S. M. F.; Carlos, L. D.; Tome, J. P. C.; Rocha, J.; Paz, F. A. A.; *Inorg. Chim. Acta*, **2017**, *455*, 584.

(5) Colodrero, R. M. P.; Papathanasiou, K. E.; Stavgianoudaki, N.; Olivera-Pastor, P.; Losilla, E. R.; Aranda, M. A. G.; Leon-Reina, L.; Sanz, J.; Sobrados, I.;

Choquesillo-Lazarte, D.; Garcia-Ruiz, J. M.; Atienzar, P.; Rey, F.; Demadis, K. D.; Cabeza, A.; *Chem. Mat.*, **2012**, *24*, 3780.

(6) Macrae, C. F.; Edgington, P. R., McCabe, P., ; Pidcock, E.; Shields, G. P.; Taylor, R.; Towler, M. v. d. S., J.; *J. Appl. Cryst.*, **2006**, *39*, 453.

(7) Baur, W.; *Acta Cryst. B*, **1974**, *30*, 1195.

(8) Silva, P.; Vieira, F.; Gomes, A. C.; Ananias, D.; Fernandes, J. A.; Bruno, S. M.; Soares, R.; Valente, A. A.; Rocha, J.; Paz, F. A. A.; *J. Am. Chem. Soc.*, **2011**, *133*, 15120.

(9) Socrates, G. *Infrared and raman characteristic group frequencies : tables and charts*, **2007**.

(10) Zhang, J.; Zheng, B.; Zhao, T. T.; Li, G. H.; Huo, Q. S.; Liu, Y. L.; *Cryst. Growth Des.*, **2014**, *14*, 2394.

(11) Conolly, M. E.; Kersting, F.; Dollery, C. T.; *Prog. Cardiovasc. Dis.*, **1976**, *19*, 203.

(12) Decree, J.; Geukens, H.; Leempoels, J.; Verhaegen, H.; *Drug Dev. Res.*, **1986**, *8*, 109.

(13) Jacobsen, E. N.; *Accounts Chem. Res.*, **2000**, *33*, 421.

(14) Joossens, J.; Van der Veken, P.; Lambeir, A. M.; Augustyns, K.; Haemers, A.; *J. Med. Chem.*, **2004**, *47*, 2411.

(15) Young, R. R.; Growdon, J. H.; Shahani, B. T.; *N. Engl. J. Med.*, **1975**, *293*, 950.

(16) Stead, P.; Marley, H.; Mahmoudian, M.; Webb, G.; Noble, D.; Ip, Y. T.; Piga, E.; Rossi, T.; Roberts, S.; Dawson, M. J.; *Tetrahedron: Asymmetry*, **1996**, *7*, 2247.

(17) Mendes, R. F.; Silva, P.; Antunes, M. M.; Valente, A. A.; Paz, F. A. A.; *Chem. Commun.*, **2015**, *51*, 10807.

(18) Vilela, S. M. F.; Ananias, D.; Fernandes, J. A.; Silva, P.; Gomes, A. C.; Silva, N. J. O.; Rodrigues, M. O.; Tomé, J. P. C.; Valente, A. A.; Ribeiro-Claro, P.; Carlos, L. D.; Rocha, J.; Paz, F. A. A.; *J. Mater. Chem. C*, **2014**, *2*, 3311.

(19) Biswas, S.; Maes, M.; Dhakshinamoorthy, A.; Feyand, M.; De Vos, D. E.; Garcia, H.; Stock, N.; *J. Mater. Chem.*, **2012**, *22*, 10200.

(20) Dhakshinamoorthy, A.; Alvaro, M.; Garcia, H.; *Chem. Eur. J.*, **2010**, *16*, 8530.

(21) Jiang, D.; Mallat, T.; Krumeich, F.; Baiker, A.; *J. Catal.*, **2008**, *257*, 390.

(22) Jiang, D. M.; Urakawa, A.; Yulikov, M.; Mallat, T.; Jeschke, G.; Baiker, A.; *Chem. Eur. J.*, **2009**, *15*, 12255.

(23) Silva, P.; Ananias, D.; Bruno, S. M.; Valente, A. A.; Carlos, L. D.; Rocha, J.; Paz, F. A. A.; *Eur. J. Inorg. Chem.*, **2013**, *2013*, 5576.

(24) Tanaka, K.; Otani, K.; *New J. Chem.*, **2010**, *34*, 2389.

(25) Wee, L. H.; Bonino, F.; Lamberti, C.; Bordiga, S.; Martens, J. A.; *Green Chem.*, **2014**, *16*, 1351.

(26) Wee, L. H.; Lohe, M. R.; Janssens, N.; Kaskel, S.; Martens, J. A.; *J. Mater. Chem.*, **2012**, *22*, 13742.

(27) Zhou, Y. X.; Chen, Y. Z.; Hu, Y. L.; Huang, G.; Yu, S. H.; Jiang, H. L.; *Chem. Eur. J.*, **2014**, *20*, 14976.

(28) Zu, D. D.; Lu, L.; Liu, X. Q.; Zhang, D. Y.; Sun, L. B.; *J. Phys. Chem.: C*, **2014**, *118*, 19910.

(29) Wiles, C.; Watts, P.; Haswell, S. J.; *Tetrahedron*, **2005**, *61*, 5209.

(30) Ajaikumar, S.; Pandurangan, A.; *J. Mol. Catal. A: Chem.*, **2008**, *290*, 35.

(31) Elliot, A. J. *1,3-dioxalane polymers in comprehensive heterocyclic polymers*, **1984**.

(32) Bauer, K.; Garbe, D.; Surburg, H. *Common fragrances and flavour materials: Preparation and uses*, New York, USA, **2001**.

(33) Wu, S. S.; Dai, W. L.; Yin, S. F.; Li, W. S.; Au, C. T.; *Catal. Lett.*, **2008**, *124*, 127.

(34) Clode, D. M.; *Chem. Rev.*, **1979**, *79*, 491.

(35) Sudarsanam, P.; Mallesham, B.; Prasad, A. N.; Reddy, P. S.; Reddy, B. M.; *Fuel Process. Technol.*, **2013**, *106*, 539.

(36) Yang, Z. W.; Chen, L. N.; Hong, W.; Kang, R. X.; Wang, J.; Jia, N.; Zhao, L.; Ma, H. C.; *Acta Phys.-Chim. Sin.*, **2012**, *28*, 2148.

(37) Liu, L.; Zhao, Y. C.; Gan, S.; Liang, X. Z.; Yang, J. G.; He, M. Y.; *J. Nat. Gas Chem.*, **2008**, *17*, 149.

(38) Gao, S.; Liang, X. Z.; Wang, W. J.; Cheng, W. P.; Yang, J. G.; *Chin. Sci. Bull.*, **2007**, *52*, 2892.

(39) Patwardhan, S. A.; Dev, S.; *Synthesis (Stuttg)*, **1974**, 348.

(40) Stenberg, V. I.; Kubik, D. A.; *J. Org. Chem.*, **1974**, *39*, 2815.

(41) Zhang, F. M.; Shi, J.; Jin, Y.; Fu, Y. H.; Zhong, Y. J.; Zhu, W. D.; *Chem. Eng. J.*, **2015**, *259*, 183.

(42) Jin, Y.; Shi, J.; Zhang, F. M.; Zhong, Y. J.; Zhu, W. D.; *J. Mol. Catal. A-Chem.*, **2014**, *383*, 167.

(43) Ren, Y. W.; Liang, J. X.; Lu, J. X.; Cai, B. W.; Shi, D. B.; Qi, C. R.; Jiang, H. F.; Chen, J.; Zheng, D.; *Eur. J. Inorg. Chem.*, **2011**, 4369.

(44) Dikhtiarenko, A.; Khainakov, S. A.; de Pedro, I.; Blanco, J. A.; Garcia, J. R.; Gimeno, J.; *Inorg. Chem.*, **2013**, *52*, 3933.

(45) Bromberg, L.; Hatton, T. A.; *ACS Appl. Mater. Interfaces*, **2011**, *3*, 4756.

(46) Herbst, A.; Khutia, A.; Janiak, C.; *Inorg. Chem.*, **2014**, *53*, 7319.

(47) Timofeeva, M. N.; Panchenko, V. N.; Jun, J. W.; Hasan, Z.; Matrosova, M. M.; Jhung, S. H.; *Appl. Catal., A*, **2014**, *471*, 91.

(48) Wang, P.; Li, H.; Gao, Q.; Li, P. Z.; Yao, X.; Bai, L. Y.; Nguyen, K. T.; Zou, R. Q.; Zhao, Y. L.; *J. Mater. Chem. A*, **2014**, *2*, 18731.

(49) Dhakshinamoorthy, A.; Alvaro, M.; Garcia, H.; *Adv. Synth. Catal.*, **2010**, *352*, 3022.

(50) Bao, S. S.; Li, N. Z.; Taylor, J. M.; Shen, Y.; Kitagawa, H.; Zheng, L. M.; *Chem. Mat.*, **2015**, *27*, 8116.

(51) Tang, J.; Oka, T.; *Journal of Molecular Spectroscopy*, **1999**, *196*, 120.

(52) Bhattacharya, S.; Gnanavel, M.; Bhattacharyya, A. J.; Natarajan, S.; *Cryst. Growth Des.*, **2014**, *14*, 310.

(53) Tominaka, S.; Coudert, F. X.; Dao, T. D.; Nagao, T.; Cheetham, A. K.; *J. Am. Chem. Soc.*, **2015**, *137*, 6428.

(54) Bazaga-Garcia, M.; Colodrero, R. M. P.; Papadaki, M.; Garczarek, P.; Zon, J.; Olivera-Pastor, P.; Losilla, E. R.; Leon-Reina, L.; Aranda, M. A. G.; Choquesillo-Lazarte, D.; Demadis, K. D.; Cabeza, A.; *J. Am. Chem. Soc.*, **2014**, *136*, 5731.

(55) Ramaswamy, P.; Wong, N. E.; Shimizu, G. K. H.; *Chem. Soc. Rev.*, **2014**, *43*, 5913.

(56) Kim, S.; Dawson, K. W.; Gelfand, B. S.; Taylor, J. M.; Shimizu, G. K. H.; *J. Am. Chem. Soc.*, **2013**, *135*, 963.

(57) Nagarkar, S. S.; Unni, S. M.; Sharma, A.; Kurungot, S.; Ghosh, S. K.; *Angew. Chem. Int. Ed.*, **2014**, *53*, 2638.

(58) Ponomareva, V. G.; Kovalenko, K. A.; Chupakhin, A. P.; Dybtsev, D. N.; Shutova, E. S.; Fedin, V. P.; *J. Am. Chem. Soc.*, **2012**, *134*, 15640.

(59) Yoon, M.; Suh, K.; Natarajan, S.; Kim, K.; *Angew. Chem. Int. Ed.*, **2013**, *52*, 2688.

(60) Boldog, I.; Domasevitch, K. V.; Baburin, I. A.; Ott, H.; Gil-Hernandez, B.; Sanchiz, J.; Janiak, C.; *Crystengcomm*, **2013**, *15*, 1235.

(61) Plabst, M.; Bein, T.; *Inorg. Chem.*, **2009**, *48*, 4331.

(62) Taylor, J. M.; Dawson, K. W.; Shimizu, G. K. H.; *J. Am. Chem. Soc.*, **2013**, *135*, 1193.

(63) Taylor, J. M.; Mahmoudkhani, A. H.; Shimizu, G. K. H.; *Angew. Chem. Int. Ed.*, **2007**, *46*, 795.

(64) Vasylyev, M. V.; Wachtel, E. J.; Popovitz-Biro, R.; Neumann, R.; *Chem. Eur. J.*, **2006**, *12*, 3507.

(65) Ying, S. M.; Mao, J. G.; *Cryst. Growth Des.*, **2006**, *6*, 964.

(66) Janicki, R.; Mondry, A.; *Eur. J. Inorg. Chem.*, **2013**, 3429.

(67) Janicki, R.; Monteil, M.; Lecouvey, M.; Mondry, A.; *Opt. Mater.*, **2013**, *36*, 259.

(68) Costantino, F.; Donnadio, A.; Casciola, M.; *Inorg. Chem.*, **2012**, *51*, 6992.

Chapter 5

Exceptional Thermal Stability of a new series of isotypical Lanthanide-Organic Frameworks

5.1. Initial Considerations

The hydrothermal self-assembly reaction between lanthanide chloride salts and the tetrapodal organic ligand [1,1'-biphenyl]-3,3',5,5'-tetrayltetrakis(phosphonic acid)] (**H_8btp**) promoted the formation of a new series of isotypical 3D lanthanide-organic frameworks (LnOFs), formulated as $[Ln(H_5btp)]\cdot 2H_2O$ [where Ln^{3+} = Gd^{3+} (**8**), Tb^{3+} (**9**), Dy^{3+} (**10**), Ho^{3+} (**11**), Er^{3+} (**12**) and Tm^{3+} (**13**)].[1] Compounds are isostructural and possess a tubular 3D supramolecular framework built up in a similar fashion as compounds **4**, **5** and **6** (discussed in the previous chapter). Single-crystal X-ray diffraction studies that were performed on compound **9** also showed the local environments around phosphonate groups: hydrogen bonds along the *a*-axis are established between crystallization water molecules and phosphonate groups; the network has lozenge-shaped tubular channels with intermolecular interactions between adjacent organic ligand molecules forming a strong microporous framework. Furthermore, a single-crystal to single-crystal transformation is also reported. $[Ln(H_5btp)]\cdot 2H_2O$ can be transformed into $[Ln(L)_2]$ (where $L^{3/2-}$ = $[-(PO_2H)(C_6H_3)(PO_2)O-]_n^{3/2n-}$), the latter showing an outstanding thermal stability, with the material maintaining its crystallinity and structural features up to *ca.* 800 ºC, thus being the most thermally robust and stable MOF material reported to date. This extraordinary thermal stability is attributed to the close compact 3D network maintained especially by strong pyrophosphonate bridges. This family of materials also represents the first example of robust 100% lanthanide-containing 3D networks assembled from tetrapodal $H_{8-x}btp^{x-}$ residues.

5.2. LnOFs prepared using lanthanide chloride salts and the phosphonate-based organic ligand H_8btp

5.2.1. Hydrothermal Synthesis

The reaction between **H_8btp** and different lanthanide chloride salts (from $GdCl_3\cdot 6H_2O$ to $TmCl_3\cdot 6H_2O$) under hydrothermal conditions (5 day heating program) allowed the preparation of a new series of isotypical materials (see sub-section 8.13 in the Experimental Section for more details). The same synthetic conditions were used in all cases and led to the formation of needle-like crystals with sizes ranging from 100 to 2 μm, as observed in Figure 5.1 (see Figures in Appendix D.1, Figure D.2.1 in Appendix D.2 and

Figures in Appendix D.3 for additional characterization of compounds). The average particle sizes seem to follow an interesting trend. Lanthanides with higher ionic radius tend to form larger crystals, with a progressive decrease in particle size observed for the smaller metals [Gd(**8**) > Tb(**9**) > Dy(**10**) > Ho(**11**) > Er(**12**) > Tm (**13**)]. Larger lanthanides (Gd^{3+} and Tb^{3+}) also have higher particle distribution, with needles ranging from 30 to 100 μm, while smaller ones (Er^{3+} and Tm^{3+}) present a smaller but more homogeneous crystal size. This type of size distribution behavior depending on the metal center is not usual for LnOF materials and to the best of our knowledge was only reported in our group for the $[Ln_2(H_3bmt)_2]\cdot H_2O$ materials: the metallic center exhibits a rare octahedral coordination environment (that we also observed for our compounds), which might induce a progressive reduction in crystal size with the decrease of the metallic ionic radii.[2]

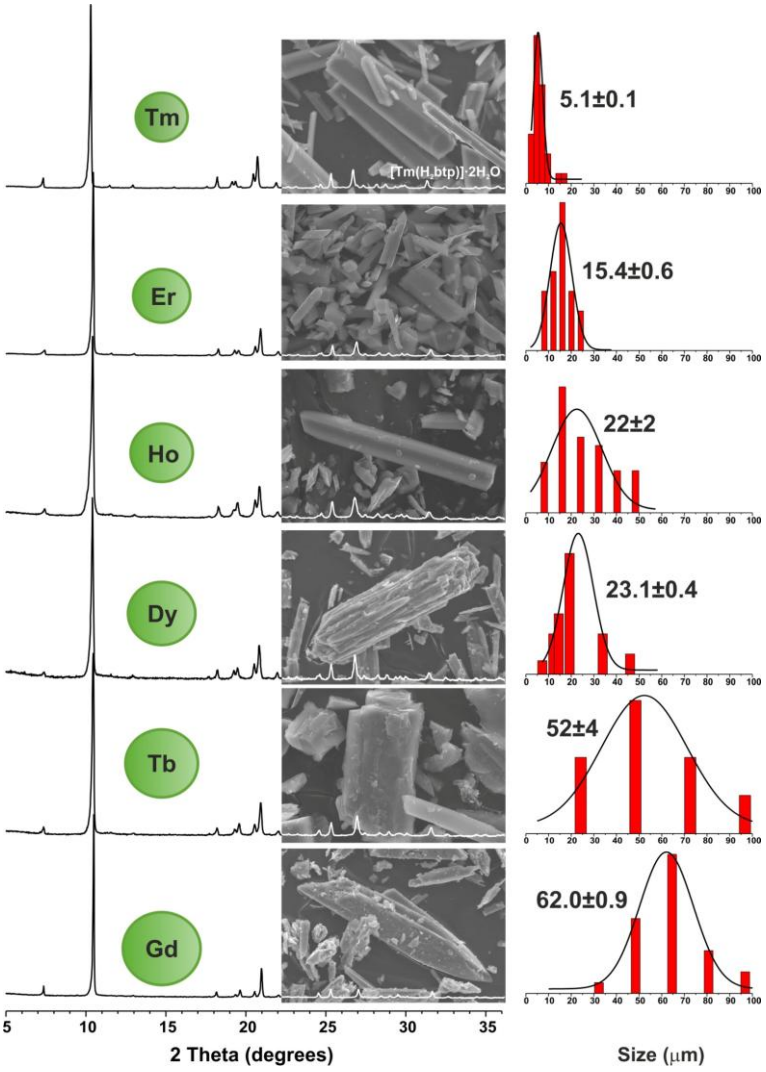

Figure 5.1. Powder X-ray diffraction, scanning electron microscopy images and particle size distribution of $[Ln(H_5btp)]\cdot 2H_2O$ [where Ln^{3+} = Gd^{3+} (**8**), Tb^{3+} (**9**), Dy^{3+} (**10**), Ho^{3+} (**11**), Er^{3+} (**12**) and Tm^{3+} (**13**)]. Average particle size was calculated using a Gaussian function and are presented in μm.

As expected, hydro(solvo)thermal conditions originate particles with bigger lengths than those obtained using microwave-assisted synthesis (MWAS) and discussed in the previous chapter.[3] On the other hand, the size of these particles obtained using hydro(solvo)thermal conditions is comparable to compound $[La_4(H_6btp)(H_4btp)(H_8btp)(H_2O)_{16}]\cdot 12H_2O$ (**1**) (Chapter 3), that we synthesized using microwave irradiation, followed by a seven day period of slow evaporation.[4] We can, thus, conclude that the reaction time is definitely an important parameter that determines particle size for the synthesized materials in this chapter. Because temperature, and consequently autogenous pressure inside the autoclave, as well as metal centers for the self-assembly, were parameters that we changed (relatively to previous reactions) in order to isolate these phase-pure compounds, it seems that these parameters do not have a significant role in the final particle size and morphology.

5.2.2. Crystal Structure Elucidation of $[Tb(H_5btp)]\cdot 2H_2O$ (9)

Due to a better crystal diffraction quality, compound **9** was chosen to be studied using single-crystal X-ray diffraction. Formulated as $[Tb(H_5btp)]\cdot 2H_2O$, **9** crystallizes in the monoclinic space group *C*2/*c*. The asymmetric unit is composed of half metal center and half H_6btp^{2-} residue with only one disordered crystallization water molecule. The coordination environment shares remarkable similarity with the family of MOF materials discussed in the previous chapter, namely $[Y(H_5btp)]\cdot 5.5H_2O$ (**4**), $[Y(H_5btp)]\cdot 2.5H_2O$ (**5**) and $(H_3O)[Y_2(H_5btp)(H_4btp)]\cdot H_2O)$ (**6**).[3] All metals are coordinated to six different phosphonate moieties arising from six symmetry-related H_6btp^{2-} residues, resembling a slight distorted octahedron, a coordination mode not usual for LnOF materials (with coordination numbers normally between seven and nine). In fact, **9** shares other similarities with the yttrium family of MOFs previously discussed: the 3D network is constructed by terbium phosphonate chains in a zigzag conformation extending along the *c*-axis, being connected by the organic linker (Figure 5.2). This allowed the formation of a microporous material with an arrangement resembling a lozenge shaped tubular structure. The similarity is also transposed in a topological view, with all materials forming a binodal net, with a 6,6 connection net and a point symbol of $\{4^{13}.6^2\}\{4^8.6^6.8\}$. In case of **9** the planar rearrangement of the organic linker in the structure, with no torsion angle between the two aromatic rings, allowed the formation of weak π-π interactions [distance between rings =

3.856(6) Å], alongside with the normal hydrogen interactions between crystallization water molecules and the phosphonic acid groups (see Figure 5.2 and Tables in Appendix D.4 for further details).

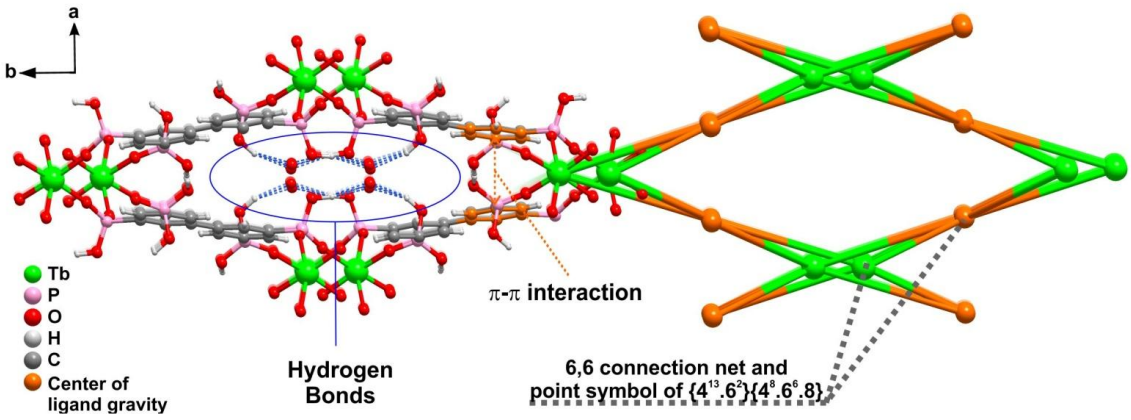

Figure 5.2. Schematic representation of the crystal packing and topological view of the [Tb(H_5btp)]·2H_2O (**9**) network, emphasizing the intramolecular interactions present in the structure.

5.2.3. Structural transformation of [Tb(H_5btp)]·H_2O (9) into [Tb($L)_2$] (14) and thermal stability

In the previous chapter, we have studied the stability and single-crystal to single-crystal (SC-SC) transformation of a similar family of MOF materials: [Y(H_5btp)]·5.5H_2O (**4**) is transformed into [Y(H_5btp)]·2.5H_2O (**5**) by simple removal of the solid from the mother solution (filtration) while the latter can be further dehydrated and consequently transformed into (H_3O)[Y_2(H_5btp)(H_4btp)]·H_2O (**6**) by heating overnight at 110 ºC. These transformations were possible by sole removal of crystallization water molecules from the framework, with no major changes to the coordination backbone of the MOFs structure. Taking into account the structural similarities between the materials **8-13** (discussed in this chapter) and the previous yttrium based compounds, we decided to test the thermal stability of compound **9**. After heating **9** overnight at 400 ºC, we observed a SC-SC transformation to a new MOF material by single-crystal X-ray diffraction analysis. The thermal stability of [Tb(H_5btp)]·2H_2O (**9**) was then investigated between ambient temperature and *ca.* 1200ºC (Figure 5.3 – *bottom*). In addition, and in order to evaluate the effect of increasing temperature to the crystal structure, *in situ* variable-temperature powder X-ray diffraction studies (Figure 5.3 – *top*) have been performed for compound **9**,

in the temperature range of 25–1200 ºC, providing additional information on the hydration level of the compounds (the same studies were performed for the remaining materials as well, see Figures in Appendix D3). As depicted in Figure 5.3, between ambient temperature and *ca.* 250 ºC the crystallization water molecules are removed from the structure, leading to a decrease of approximately 4.8% in mass, corresponding to the release of the two water molecules (calculated as *ca.* 5.4%). This release is accompanied by a shift of the second reflection to higher 2θ, *i.e.* on the [110] plane. This shift points to a reduction of the unit cell dimensions, in particular in the [100] and [010] directions, which indicated a proximity between the terbium-phosphonate chains. The second weight loss, corresponding to 6.1%, occurs between *ca.* 250 and 650 ºC. According to our previous studies at this temperature range the phosphonate groups of the organic ligand in the framework suffer a rearrangement, leading to the formation of pyrophosphonates[5] (Figure D.2.2 in Appendix D.2) with the consequent release of water molecules (in this case the observed weight loss is equivalent to approximately two water molecules). Again, this behavior is accompanied by another shift of the second reflection to higher 2θ, leading to the formation of a new crystalline phase.

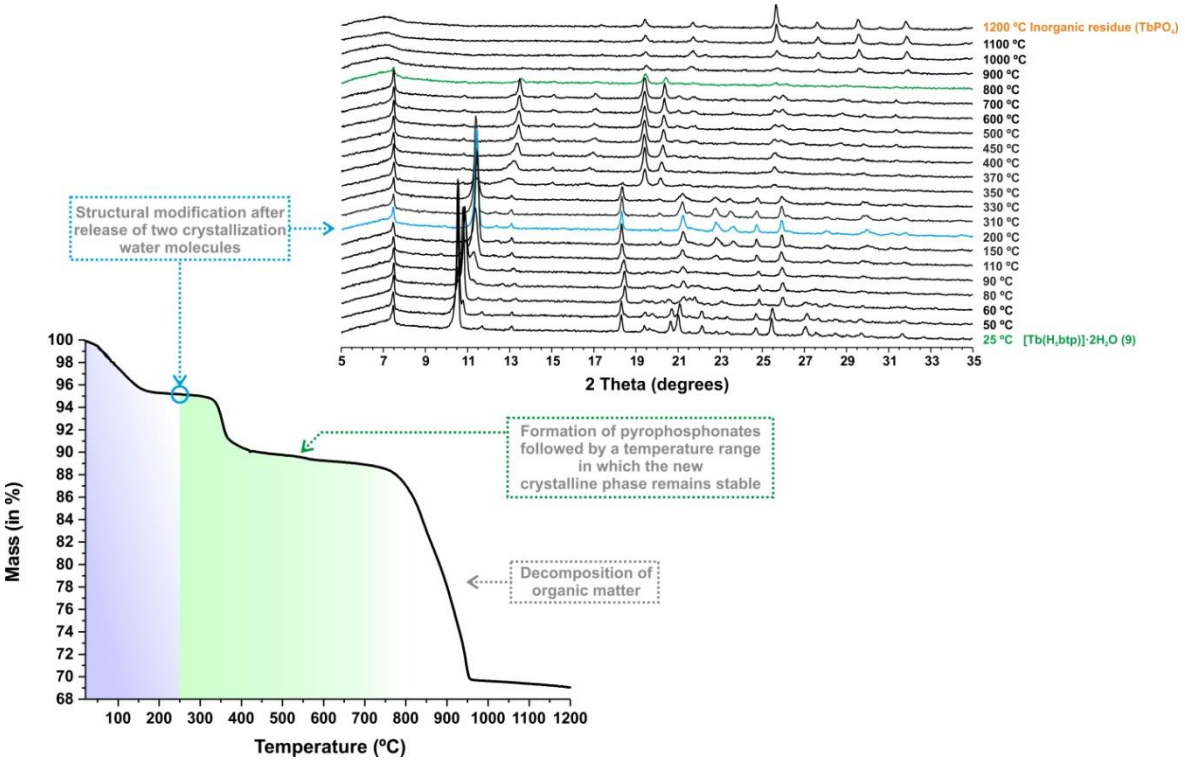

Figure 5.3. (*bottom*) Thermogram and (*top*) variable-temperature powder X-ray diffraction studies of [Tb(H_5btp)]·2H_2O (**9**) collected between ambient temperature and *ca.* 1200 ºC.

This new crystalline phase was unveiled by single-crystal X-ray diffraction and formulated as $[Tb(L)_2]$ (where $L^{3/2-}$ = $[–(PO_2H)(C_6H_3)(PO_2)O–]_n^{3/2n-}$). The structure crystallizes in the centrosymmetric space group $P2_1/n$, and agrees well with the performed thermogravimetric and thermodiffractometric studies. $[Tb(L)_2]$ (**14**) is composed by the same terbium phosphonate chains along the [101] plane as the parent material, compound **9**, connected by the organic linkers (Figure 5.4). While **9** maintains a coplanar arrangement of the aromatic rings, *i.e.* no torsion of the biphenyl core, **14** has higher distortion, as shown by its slightly distorted octahedral coordination sphere (Figure 5.5a). The SC-SC transformation of **9** into **14** can therefore be described in two steps: in the first step the crystallization water molecules are removed from the network, which is accompanied with a decrease of the Tb···Tb distances of the terbium-phosphonate chains, ultimately bringing the phosphonic acid groups closer to each other; the second step is the formation of the pyrophosphonate bridges with the release of two water molecules per formula unit, resulting in a final distance of metal centers of 7.660(3) Å (Figure 5.5b).

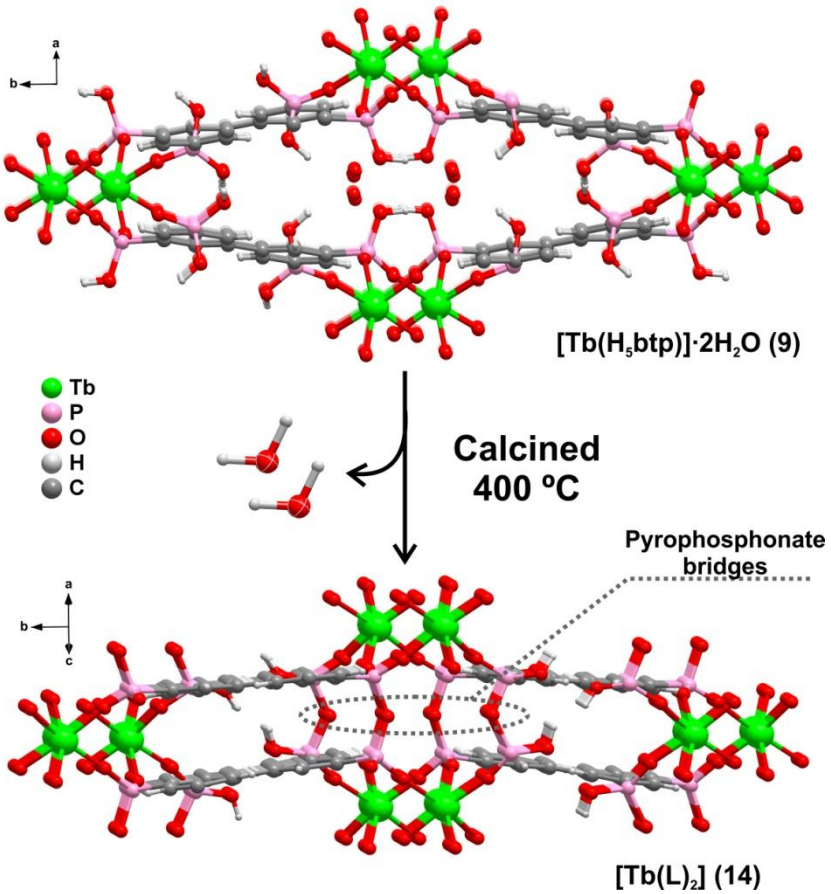

Figure 5.4. Schematic representation of the single-crystal to single-crystal transformation of $[Tb(H_5btp)]·2H_2O$ (**9**) into $[Tb(L)_2]$ (**14**) at 400 ºC with emphasis on the formation of the pyrophosphonate bridges.

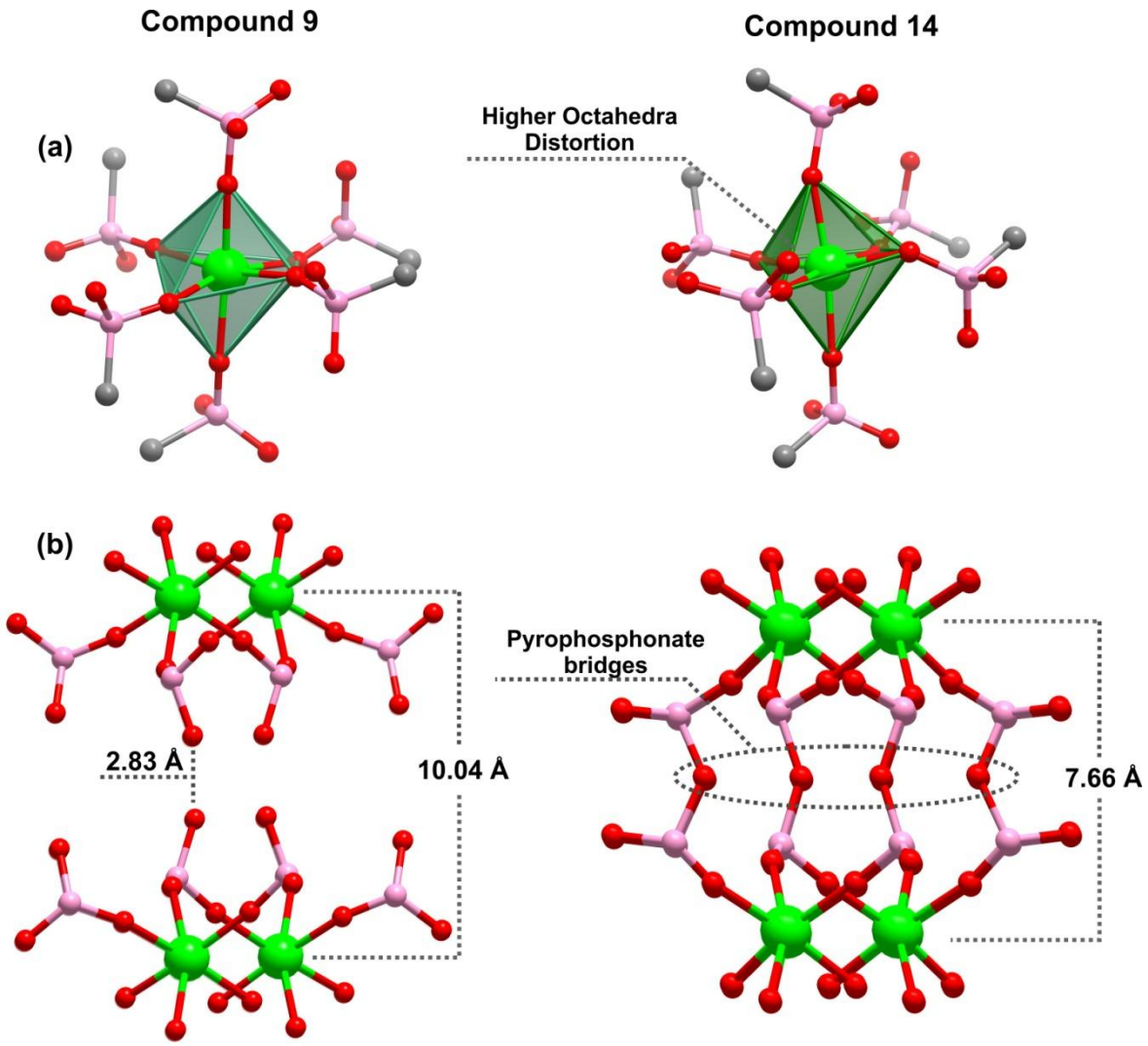

Figure 5.5. (**a**) Coordination environment of $[Tb(H_5btp)]\cdot 2H_2O$ (**9**) and $[Tb(L)_2]$ (**14**); (**b**) schematic representation of the decrease in Tb···Tb distances during the single-crystal to single-crystal transformation as well as the formation of the pyrophosphonate bridges.

These pyrophosphonate bridges combined with newly established hydrogen bonds and π-π interactions [distance of 3.5697(15) Å between aromatic rings] confer to this phase of the material high thermal stability. In fact, this new MOF is stable up to *ca.* 800 ºC (Figure 5.3 and 5.6), temperature at which it starts decomposing into the inorganic residue $TbPO_4$. This corresponds to the highest thermal stability reported to date for this class of hybrid materials.

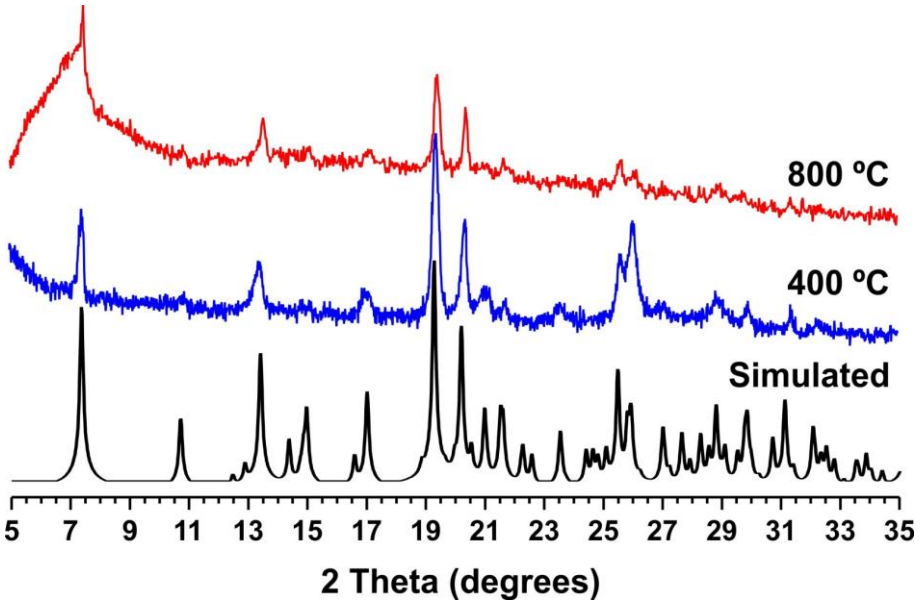

Figure 5.6. Comparison between the simulated (black line), dehydrated at 400 ºC (blue line) and 800 ºC (red line) powder X-ray diffraction patterns of $[Tb(L)_2]$ (**14**).

5.3. Conclusions

In this chapter we reported the preparation of new porous 3D LnOFs, a family of materials formulated as $[Ln(H_5btp)]\cdot 2H_2O$ [where Ln^{3+} = Gd^{3+} (**8**), Tb^{3+} (**9**), Dy^{3+} (**10**), Ho^{3+} (**11**), Er^{3+} (**12**) and Tm^{3+} (**13**)] from the reaction between lanthanide chloride hydrated salts with the organic ligand [1,1'-biphenyl]-3,3',5,5'-tetrayltetrakis(phosphonic acid) (**H_8btp**) under hydrothermal conditions. The materials were isolated as phase-pure large single crystals and characterized using in tandem several standard solid-state techniques.

Motivated by our successful previous work, we decided to do further investigations on the coordination ability of the organic ligand **H_8btp** using different conditions to promote the self-assembly of crystalline materials, in a new series of reactions. Since all previous reported compounds involved the use of microwave irradiation as the heating methodology for the self-assembly of new compounds, in this chapter we decided that typical hydro(solvo)thermal conditions, a more conventional heating source for the MOFs synthesis, should be tested. The results were large amounts of a novel microporous phase-pure MOF family, assembled using lanthanide metal centers, from Gd^{3+} to Tm^{3+}, presenting a structure only possible to be obtained using this synthetic approach. While this is a different structure, $[Ln(H_5btp)]\cdot 2H_2O$ materials were found to be three-dimensional

LnOFs very similar to our previously discussed family of yttrium-based compounds: a comparable lozenge shaped network, with only crystallization water molecules present in the channels of the framework and a coordination geometry of the metals that resembles slightly distorted octahedra.[3]

This family of compounds has shown outstanding thermal stability (*ca.* 800 ºC) due to an interesting SC-SC transformation that occurs in these materials as a consequence of increasing temperature. The three-dimensional framework is maintained after removal of lattice water molecules; yet, continuous heating above *ca.* 350 ºC triggers a SC-SC transformation to a new phase of the material that we were able to identify and study using single-crystal X-ray diffraction. It was verified that the loss of lattice water molecules promoted the proximity of phosphonate groups that ultimately rearranged into four pyrophosphonate bridges located within each pore of the microcrystalline network. These bridges, allied to the stability of the C–PO_3 bond, as well as the remaining molecular interactions in this structure, contributed to the registered high decomposition temperature of these materials. These results highlight the advantages of using phosphonate-based molecules for the self-assembly of new MOF materials; they also open the possibility of using MOFs in new fields of research where they were previously not considered due to lack of stability or robustness.

5.4. References

(1) Ananias, D.; Firmino, A. D. G.; Mendes, R. F.; Paz, F. A. A.; Nolasco, M.; Carlos, L. D.; Rocha, J.; *Chem. Mater.*, **2017**, *29*, 9547.

(2) Paz, F. A. A.; Vilela, S. M. F.; Tome, J. P. C.; *Cryst. Growth Des.*, **2014**, *14*, 4873.

(3) Firmino, A. D. G.; Mendes, R. F.; Antunes, M. M.; Barbosa, P. C.; Vilela, S. M. F.; Valente, A. A.; Figueiredo, F. M. L.; Tome, J. P. C.; Paz, F. A. A.; *Inorg. Chem.*, **2017**, *56*, 1193.

(4) Firmino, A. D. G.; Mendes, R. F.; Ananias, D.; Vilela, S. M. F.; Carlos, L. D.; Tome, J. P. C.; Rocha, J.; Paz, F. A. A.; *Inorg. Chim. Acta*, **2017**, *455*, 584.

(5) Silva, P.; Vieira, F.; Gomes, A. C.; Ananias, D.; Fernandes, J. A.; Bruno, S. M.; Soares, R.; Valente, A. A.; Rocha, J.; Paz, F. A. A.; *J. Am. Chem. Soc.*, **2011**, *133*, 15120.

Chapter 6

New isotypical families of LnOFs

6.1. From 2D to 3D Functional MOFs based on [1,1'-biphenyl]-3,3',5,5'-tetrayltetrakis(phosphonic acid) (H_8btp)

6.1.1. Initial Considerations

To recognize the potential role of metal-organic frameworks (MOFs) or porous coordination polymers (PCPs) in a specific topic or practical application, researchers always establish comparisons between new materials with previously synthesized equivalent compounds or, in the case of applications, a comparative study of performance and appliance is always presented in order to validate the relevance of the newly synthesized compounds. Among the assorted reasons why there are so many reports in the area of MOFs and PCPs and why they remain an attractive topic of research, we can point out, for example, their tunable chemical structure and/or their multifunctional properties. Research focused on these factors led, over time, toward materials with significant improvements for specific applications. We can, thus, conclude that there is a general key concept which encircles all major reports and discussions regarding MOFs and PCPs synthesis and characterization: functional engineering.[1] This is a concept intrinsic in many studies and reports regarding MOF materials because researchers aim to connect the physicochemical properties of the compounds to their future practical employment. And if the objective, which is the foreseeable practical application of the compound, is not achieved, efforts resume in order to synthesize the next compound which will fulfill the required realistic parameters.

The next section will illustrate (as mentioned above) specific examples of how it was possible to improve properties, such as chemical and thermal stability (*e.g.* through modification of the pore size or dimensionality of the framework), in order to obtain an alternative material with enhanced properties, and yet, at the same time, attempt to maintain a similar topology of the framework, *i.e.* without undergoing a major structural recombination of metal centers and ligands to assemble the framework.

In Chapter 3 we presented a new series of MOF materials self-assembled from the organic ligand [1,1'-biphenyl]-3,3',5,5'-tetrakis(phosphonic acid) (**H_8btp**) and La^{3+} cations (or mixtures of lanthanides), which then showed, not only fascinating structural features, but interesting photoluminescent properties as well. However, we also registered that these materials presented a significant drawback (which might also be seen as a disadvantage

regarding a future practical application): their thermal stability was very low with the framework being only stable between ambient temperature and *ca.* 70 ºC.

In order to try to overcome this disadvantage, in this section is described how the **H_8btp** linker afforded another isotypical 2D LnOF family of materials, $[Ln_7(H_5btp)_5(H_6btp)_3(H_2O)_{12}]\cdot 23.5H_2O\cdot MeOH$ [where Ln^{3+} = Eu^{3+} (**15**) and Gd^{3+} (**16**)], isolated using the same self-assembly methodology previously reported for materials in Chapter 3 (*i.e.*, microwave-irradiation followed by slow evaporation).

Furthermore, a third series of LnOFs, formulated as $[Ln_4(H_3btp)(H_4btp)(H_5btp)(H_2O)_8]\cdot 3H_2O$ [where Ln^{3+} = Ce^{3+} (**17**), Pr^{3+} (**18**), and Nd^{3+} (**19**)], was also synthesized, but, in this case, these 3D materials were prepared under conventional hydro(solvo)thermal conditions.

The crystal structures of both isotypical families of 2D and 3D compounds were unveiled by single-crystal X-ray diffraction studies. All materials were fully characterized by standard solid-state techniques [FT-IR, electron microscopy (SEM and EDS), thermogravimetric and elemental analyses].

6.1.2. Microwave-assisted synthesis of isotypical $[Ln_7(H_5btp)_5(H_6btp)_3(H_2O)_{12}]\cdot 23.5H_2O\cdot MeOH$ materials

Previously we discussed how MWAS followed by slow evaporation successfully led to the preparation of a new family of MOF structures composed of three isotypical materials formulated as $[Ln_4(H_6btp)_2(H_4btp)_2(H_8btp)(H_2O)_{16}]\cdot 12H_2O$ [where Ln^{3+} = La^{3+} (**1**), $(La_{0.9}Eu_{0.1})^{3+}$ (**2**) and $(La_{0.9}Tb_{0.1})^{3+}$ (**3**)]. Using basically the same synthetic approach, a new family of compounds, $[Ln_7(H_5btp)_5(H_6btp)_3(H_2O)_{12}]\cdot 23.5H_2O\cdot MeOH$ [where Ln^{3+} = Eu^{3+} (**15**) and Gd^{3+} (**16**)], was isolated by simple change in metal precursor.

Initially, the main goal of these reactions was to expand the series of materials synthesized to the remaining lanthanide centers. In spite of the different structural phase of the material, compounds **15** and **16** share many similarities with compounds **1**-**3**. For an identical composition of reactive mixtures, changing only the metal centers (see sub-section 8.11 in the Experimental Section for further detailed information), this second 2D family of MOFs could be isolated as large single-crystals (see Figure 6.1 and Figures E.1.1 and E.1.2 in Appendix E.1 showing the presence of needle-like crystals). Phase identification of the synthesized LnOFs was performed using powder X-ray diffraction

(Figure 6.1), showing that materials share the same crystal structure. Further structural details were confirmed using elemental analysis, electron microscopy (Figures E.1.1 and E.1.2 in Appendix E.1), FT-IR spectroscopy (Figure 6.6) and thermogravimetric analysis (Figure 6.5) in order to evaluate phase purity and homogeneity of the bulk materials.

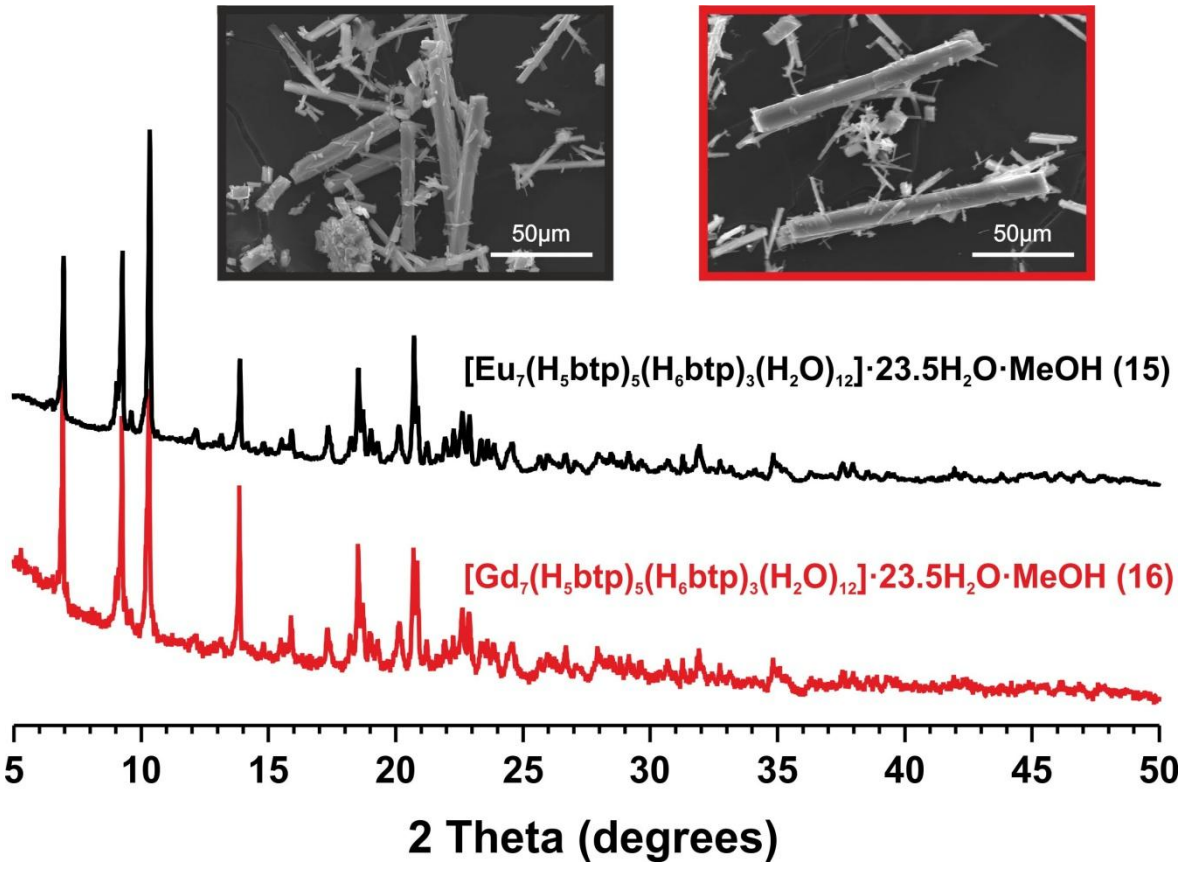

Figure 6.1. Powder X-ray diffraction patterns and SEM images of bulk materials $[Ln_7(H_5btp)_5(H_6btp)_3(H_2O)_{12}]\cdot 23.5H_2O\cdot MeOH$ [where Ln^{3+} = Eu^{3+} (**15**) and Gd^{3+} (**16**)]. As expected, applying the same synthetic conditions originated particles with comparable size and morphology as compounds **1-3**.

6.1.3. Crystal Structure Elucidation of $[Eu_7(H_5btp)_5(H_6btp)_3(H_2O)_{12}]\cdot 23.5H_2O\cdot MeOH$ (15)

Compound **15** was formulated as $[Eu_7(H_5btp)_5(H_6btp)_3(H_2O)_{12}]\cdot 23.5H_2O\cdot MeOH$ by single-crystal X-ray diffraction data, crystallizing in the monoclinic space group $P2_1/c$. The asymmetric unit is quite complex (Figure 6.2) composed of three and half metal centers and four different $H_{8-x}btp^{x-}$ residues (x = 2 and 3). The structure is maintained by hydrogen interactions between the phosphonate groups and the 17.75 water molecules and half of a methanol molecule.

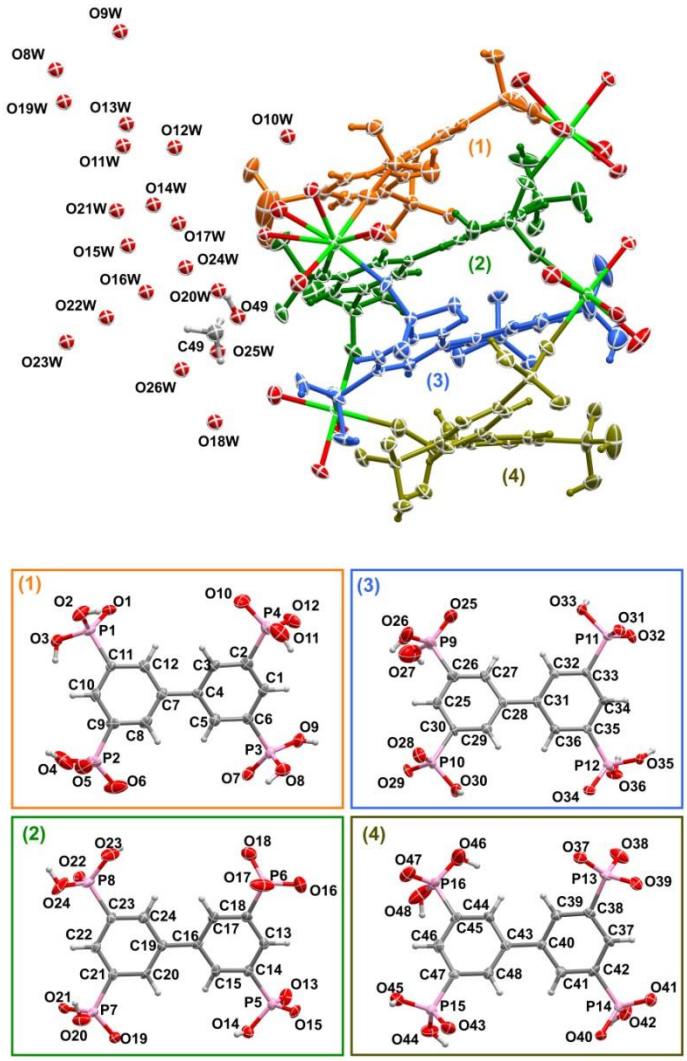

Figure 6.2. Asymmetric unit of $[Eu_7(H_5btp)_5(H_6btp)_3(H_2O)_{12}]\cdot 23.5H_2O\cdot MeOH$ (**15**) showing all non hydrogen atoms represented as thermal ellipsoids drawn at 50% probability level and hydrogen atoms as small spheres with arbitrary radius.

The four metal centers have different coordination numbers. Eu1 is a point of inversion, being hexacoordinated to six different phosphonate groups, while Eu2 is octocoordinated to five different phosphonate groups and three coordination water molecules. The remaining two metal centers, Eu3 and Eu4 are both heptacoordinated to two coordination water molecules and five phosphonate groups each. For the first two cases, the phosphonate groups coordinate with the metal centers with the same κ^1-O mode of coordination while for the last two, besides this mode of coordination, two phosphonate groups have a μ-*O,O* coordination mode. The Eu–O bond lengths were found in the 2.221(7)–2.535(16) Å range, comparable to those reported for other Ln^{3+}-based

phosphonate compounds, and the internal O–La–O polyhedral angles are in the 69.5(4)–180.0(2)º range.

The phosphonic groups have two different protonation degrees, 5 or 6, arising from the disordered hydrogen atom in two adjacent phosphonate groups. All of them connect to a different number of metal centers: two organic linker residues act as a tri and tetradentate linkers connecting three and four metal centers each, while the other residue acts as a hexadentate linker, connected to six metal centers. The last organic residue acts as a pentadentate linker connected to five metal centers. For this last residue one of the hydrogen atoms of a phosphonate group (O23) is disordered, with the hydrogen jumping from this atom to the adjacent phosphonate group (O30), balancing the net charge and maintaining the neutrality of **15**.

Regarding its configuration, **15** is also composed of 2D layers (as compound **1**) placed in the *ac* plane of the unit cell, which are formed by discrete 1D organic cylinders stacked in a typical brick-wall-like fashion, with water molecules occupying the free space in-between cylinders (Figure 6.3).

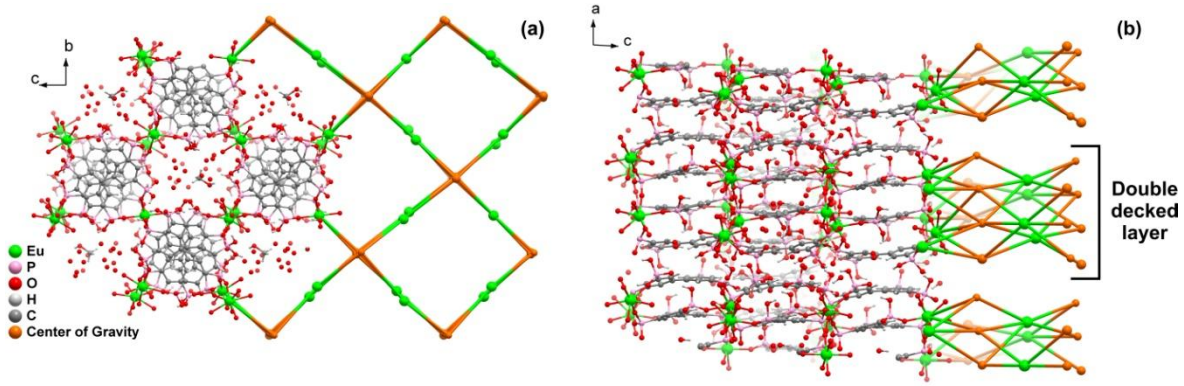

Figure 6.3. Crystal packing of $[Eu_7(H_5btp)_5(H_6btp)_3(H_2O)_{12}]\cdot 23.5H_2O\cdot MeOH$ (**15**) viewed in perspective along the **(a)** [100] and (**b**) [010] directions of the unit cell. The representations emphasize simultaneously the layered nature of the coordination polymer present in **15** and highlight the 4-nodal topology of the network with total point symbol $\{4^{13}.6^2\}_2\{4^3\}_2\{4^5.6^3.8^2\}_6\{4^6.8^8.10\}\{4^6\}_2\{4^9.6\}$.

Each of these cylinders is comprised of one asymmetric unit: the metal centers have the same zig-zag conformation along the *bc* plane, and the organic linkers are stacked on top of each other with a rotation angle of 136º along the *a* axis, forming double helix like structural motif, as depicted in Figure 6.4. This lower rotation of the organic component in comparison to **1** (where the rotation was of 143º) leads to a slight change in terms of

topology, with **15** being a octanodal net, with a 3,4,5,5,5,5,6,6 connection net and the point group $\{4^{13}.6^2\}E_2\{4^3\}_2\{4^5.6^3.8^2\}_6\{4^6.8^8.10\}\{4^6\}_2\{4^9.6\}$. Besides the connection between the organic linkers with the metal center, they form weak π–π interactions, with distances ranging between 3.11 and 3.37 Å. These 2D layers are then stacked on top of each other and are also maintained by weak π–π interactions between the rings of adjacent layers (distance of 3.982(6)Å). Although it was not shown, hydrogen bonds between –POH groups of the phosphonic acid residues and the crystallization water molecules are also observed which have great effect on the thermal stability of **15**, as discussed in the next section (see Tables E.2.1 and E.2.2 in Appendix E.2 for further detailed information).

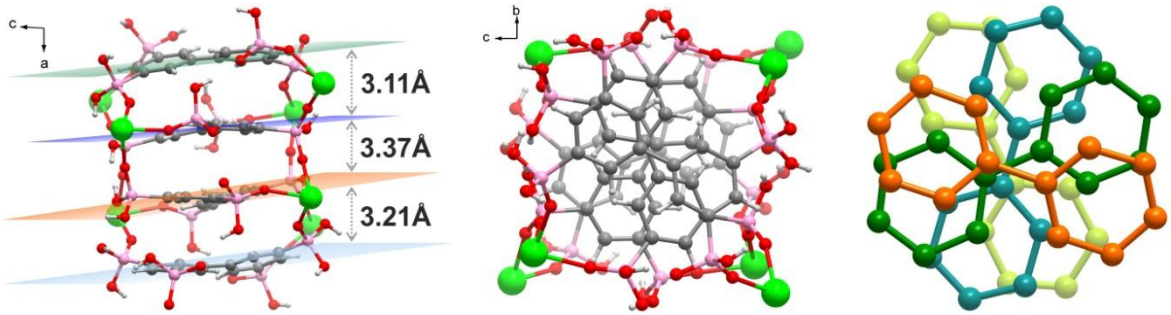

Figure 6.4. Schematic representation of the organic cylinder present in the crystal structure of $[Eu_7(H_5btp)_5(H_6btp)_3(H_2O)_{12}]\cdot 23.5H_2O\cdot MeOH$ (**15**) viewed along the [010] and [100] directions of the unit cell. The schemes emphasize the close packing of the organic linkers, with inter-planar distances ranging between *ca.* 3.11 Å to *ca.* 3.37 Å. On the right there is a representation of the same organic skeleton in the cylinder emphasizing the close packing and rotation along the *a*-axis of the four composing aromatic cores.

6.1.4. Thermogravimetry

The thermal stability of compound $[Gd_7(H_5btp)_5(H_6btp)_3(H_2O)_{12}]\cdot 23.5H_2O\cdot MeOH$ (**16**) was investigated between ambient temperature and *ca.* 800 ºC, providing additional information on the hydration level of this family isostructural compounds. As depicted in Figure 6.5, the thermogram for compound **16** shares many similarities with compounds **1**-**3** (see Figures in Appendix B.5), ultimately indicating comparable thermal behavior between these compounds. This fact is not surprising since both families share many structural similarities, consequently it is predictable that their thermal stability is, more or less, identical.

For compound **16**, the thermogram does not evidence clear regions in which the mass remains stable. Instead, there is a continuous weight loss (more significant at some

specific temperatures) over the entire temperature range. This behavior creates some difficulties for individual assignments of temperature range *vs.* released residues, although it was foreseeable that this should happen, due to the large number of coordination and crystallization solvents present in the structure. Nevertheless, one easily discerns three main weight losses. The first, between ambient temperature and *ca.* 135 ºC, corresponding to 8.6% of the total weight loss, being attributed to the release of all crystallization solvents from the structure (calculated 8.27%), *i.e.* 23.5 water molecules and one methanol molecule. This value agrees well with the water content found from the performed crystallographic studies. Above this temperature, there is an immediate second weight loss until *ca.* 420 ºC. In this temperature range, coordination water molecules are leaving the structure, which then results in the following and final step corresponding to the decomposition of the organic component until 800 ºC. As observed from the thermogram, the weight loss does not stabilize which might indicate that at *ca.* 800 ºC the residue still contains residual carbon/organic components. Due to the lack of MOF sample, thermodiffractometry studies were not performed for compound **16**, however, considering the structural similarities between **16** and **1**, it is predictable that the large number of water molecules released upon heating will be associated with a structural change of the material to an amorphous phase at low temperatures as well.

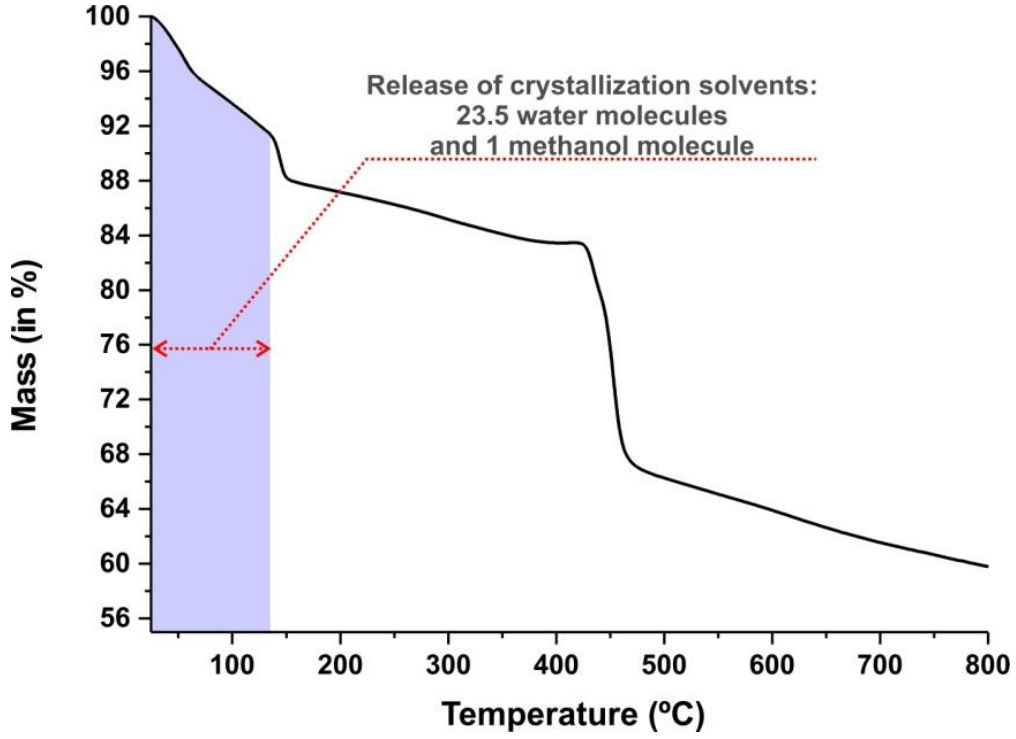

Figure 6.5. Thermogram of $[Gd_7(H_5btp)_5(H_6btp)_3(H_2O)_{12}]\cdot 23.5H_2O\cdot MeOH$ (**16**) collected between ambient temperature and *ca.* 800 ºC.

6.1.5. FT-IR spectroscopic studies

The vibrational FT-IR spectroscopy studies support the structural features unveiled by the X-ray diffraction studies.[2] Figure 6.6 shows the FT-IR spectra of $[Gd_7(H_5btp)_5(H_6btp)_3(H_2O)_{12}]\cdot 23.5H_2O\cdot MeOH$ (**16**) in the 3650-350 cm^{-1} spectral region, including assignments for each main observed band. Because materials **15** and **16** are isotypical, only the details for compound **16** are going to be described and discussed. Compound **16** contains a broad band centered in the *ca.* 3600-2800 cm^{-1} spectral range, which is attributed to both *ν*(O–H) stretching vibrational modes from coordination and crystallization water molecules and to the *ν*(PO–H) stretching vibration of the phosphonate groups. In the central region of the spectrum, between *ca.* 1745 and 1560 cm^{-1}, it is possible to observe the typical *ν*(C=C) stretching vibrational modes arising from the aromatic rings and the deformation stretching of the water molecules. We further observe as well a sharp vibrational mode at *ca*. 695 cm^{-1}, corresponding to the *ν*(P–C) stretching vibration. Also in this region, the stretching vibrational modes of *ν*(P=O) were noticed from *ca*. 1300 to 1070 cm^{-1}, and those of *ν*(P–O) from *ca*. 1070 to 830 cm^{-1}.

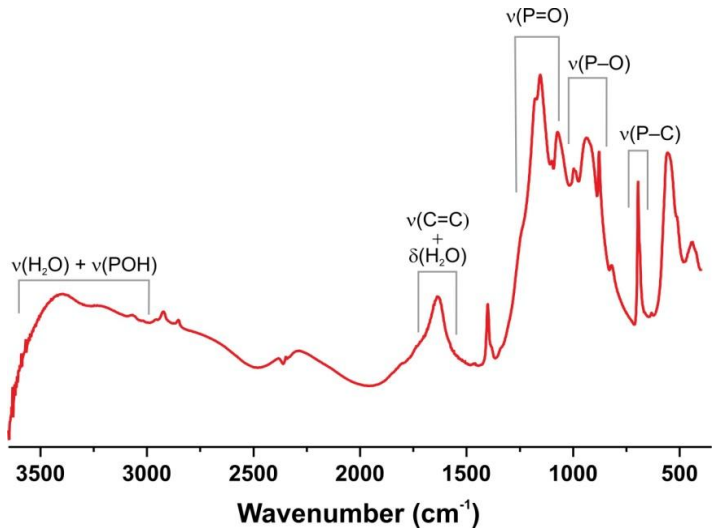

Figure 6.6. FT-IR spectra (in absorbance, arbitrary units) of $[Gd_7(H_5btp)_5(H_6btp)_3(H_2O)_{12}]\cdot 23.5H_2O\cdot MeOH$ (**16**).

6.1.6. Hydro(solvo)thermal synthesis of isotypical $[Ln_4(H_3btp)(H_4btp)(H_5btp)(H_2O)_8]\cdot 3H_2O$ materials

Microwave-assisted synthesis, slow diffusion and hydro(solvo)thermal synthesis are synthetic methodologies with distinct principles. As a result, when applied individually

for the self-assembly of MOFs, inevitably they lead to great structural diversity of synthesized compounds.

In this context, a new series of LnOFs was synthesized using identical compositions of reactive mixtures as compounds **1**-**3**, **15** and **16**, with two major differences: i) different metal centers were used for the self-assembly reactions; ii) the heating source was altered from microwave irradiation to conventional hydro(solvo)thermal synthesis (see sub-section 8.13 in the Experimental Section for further detailed information).

Altering the heating conditions successfully led to a new family of 3D compounds formulated as $[Ln_4(H_3btp)(H_4btp)(H_5btp)(H_2O)_8]\cdot 3H_2O$ [where Ln^{3+} = Ce^{3+} (**17**), Pr^{3+} (**18**), and Nd^{3+} (**19**)]. Compounds were isolated as large single-crystals (see Figures E.1.3 to E.1.5 in Appendix E.1 showing the presence of needle-like crystals). Phase identification of the synthesized LnOFs was performed using powder X-ray diffraction (Figure 6.7), showing that materials share the same crystal structure. Further structural details were confirmed using in tandem elemental analysis, thermodiffractometry (Figure 6.9) electron microscopy (Figures E.1.3 to E.1.5 in Appendix E.1), FT-IR spectroscopy (Figure E.3.1 in Appendix E.3) and thermogravimetric analyses (Figure E.4.1 in Appendix E.4) in order to evaluate phase purity and homogeneity of the bulk materials.

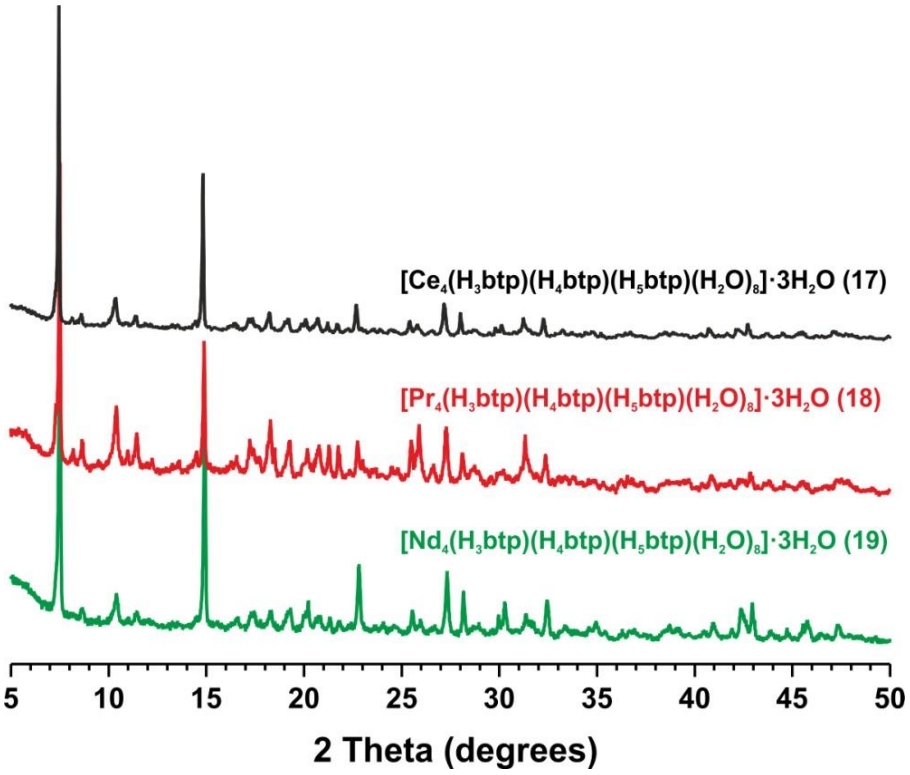

Figure 6.7. Powder X-ray diffraction patterns of bulk materials $[Ln_4(H_3btp)(H_4btp)(H_5btp)(H_2O)_8]\cdot 3H_2O$ materials [where Ln^{3+} = Ce^{3+} (**17**), Pr^{3+} (**18**) and Nd^{3+} (**19**)].

In previous chapters we reported new families of compounds assembled using hydro(solvo)thermal conditions and demonstrated, as well, that varying the reaction conditions and/or methodologies afforded new structures. Based on these results, compounds **17**-**19** arise as a new family of LnOF materials featuring a 3D open framework with a lot of structural similarities as compounds **1** and **15** (Figure 6.8).

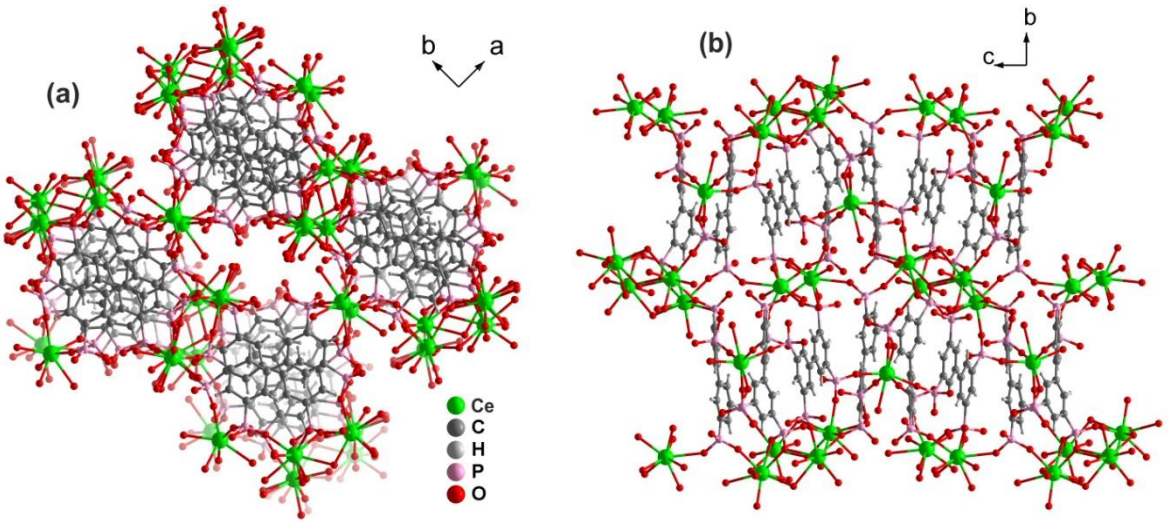

Figure 6.8. Crystal packing of $[Ce_4(H_3btp)(H_4btp)(H_5btp)(H_2O)_8]\cdot 3H_2O$ (**17**) viewed in perspective along the **(a)** [001] and (**b**) [100] directions of the unit cell. The representations emphasize simultaneously the 3D network of the coordination polymer present in **17** and highlight the close packing of the organic linkers and structural similarities between 2D compounds **1**-**3**, **15** and **16** and 3D materials **17**-**19** (see Tables E.2.3 and E.2.4 in Appendix E.2 for further detailed information). Water molecules of crystallization were omitted for clarity.

6.1.7. Structural comparison and thermal stability of $[Ln_4(H_3btp)(H_4btp)(H_5btp)(H_2O)_8]\cdot 3H_2O$ materials

Changing the metal source on one hand, and the experimental methodology on the other led to the preparation of two distinct new materials. While **15** and **16** were obtained using a combination of microwave-assisted synthesis with slow evaporation, **17**-**19** were self-assembled in less time using conventional hydro(solvo)thermal synthesis. Regarding the structural features of both materials, they possess significant differences: although both crystallize in the centrosymmetric space group $P2_1/c$ and have a cylinder shaped structure with organic ligands stacked on top of each other in a brick-wall fashion (see Figure 6.3 and 6.8), compounds **15** and **16** are 2D layered polymers, while **17**-**19** crystallize as 3D

networks. The precipitation by slow evaporation approach used to obtain the former family of compounds allowed the allocation of a superior number of solvent molecules in the structure in comparison to materials **17**-**19** (*i.e.* **17**-**19** present almost half the water molecules per metal center). Most water molecules in **15** and **16** can be found dispersed in the interstitial space between layers along the *bc* plane, maintained by several hydrogen interactions. For compounds **17**-**19**, on the other hand, the absence of these crystallization water molecules allowed the coordination of the organic residues in every direction of the unit cell, forming a more compact and ordered 3D network. This feature has significant meaning regarding the thermal stability of materials, as discussed next.

The thermal behavior of the bulk $[Ln_4(H_3btp)(H_4btp)(H_5btp)(H_2O)_8]\cdot 3H_2O$ (**17**-**19**) materials was investigated between ambient temperature and *ca.* 800 ºC, providing additional information on the thermal stability and hydration level of this family isostructural compounds. As depicted in Figure E.4.1 (in Appendix E.4), the thermograms for the three prepared materials are very similar, ultimately indicating identical thermal stabilities. Thus, in the following paragraphs discussion will be solely focused on compound **17** (Figure 6.9 – *bottom*).

For compound **17**, one easily discerns four main weight losses in the thermogram. The first, between ambient temperature and *ca.* 100 ºC, corresponding to 2.2% of the total weight loss, being attributed to the release of all crystallization solvents from the structure (calculated 2.5%), *i.e.* three water molecules. This value agrees well with the water content found from the performed crystallographic studies. Above this temperature, there is a second weight loss until *ca.* 300 ºC. In this temperature range, coordination water molecules are leaving the structure (in this case the observed 7.3% weight loss is equivalent to eight water molecules). Between 300 and 400 ºC the resulting residue suffers a third weight loss of 1.9%, a value that agrees well with the possibility of rearrangement and formation of pyrophosphonate groups (as observed for previously discussed compounds), with the resultant loss of two water molecules. Finally, the following and final step corresponds to the decomposition of the organic content until 800 ºC. As observed from the thermogram, the weight loss does not stabilize which might indicate that at *ca.* 800 ºC the residue still contains residual carbon/organic components.

Variable-temperature powder X-ray diffraction studies on $[Ce_4(H_3btp)(H_4btp)(H_5btp)(H_2O)_8]\cdot 3H_2O$ (**17**) further corroborate the aforementioned assumptions concerning the release of water molecules and phase modifications (Figure 6.9 – *top*): from ambient temperature to *ca.* 300 ºC, the structure of **17** changes, leading to

the formation of a new crystalline phase as a consequence of the release of crystallization and coordination water molecules. The structure of **17** starts to collapse above this temperature becoming almost fully amorphous at 550 ºC.

While they share many structural similarities, 3D compounds **17**-**19** show superior framework stability when compared to previously discussed $[Ln_4(H_6btp)_2(H_4btp)_2(H_8btp)(H_2O)_{16}]\cdot 12H_2O$ (**1**-**3**) and $[Ln_7(H_5btp)_5(H_6btp)_3(H_2O)_{12}]\cdot 23.5H_2O\cdot MeOH$ (**15** and **16**) materials that became amorphous at low temperatures. This feature can be explained by the enhanced connectivity between metal ions and organic linkers in materials **17**-**19**: they present better stability due to the 3D network in comparison to the 2D layered structures of LnOFs **1**-**3**, **15** and **16**, as well as, less water molecules coordinated to metal centers that tend to leave the structure when the material is exposed to higher temperatures, leaving naked/unprotected coordination sites that destabilize the framework.

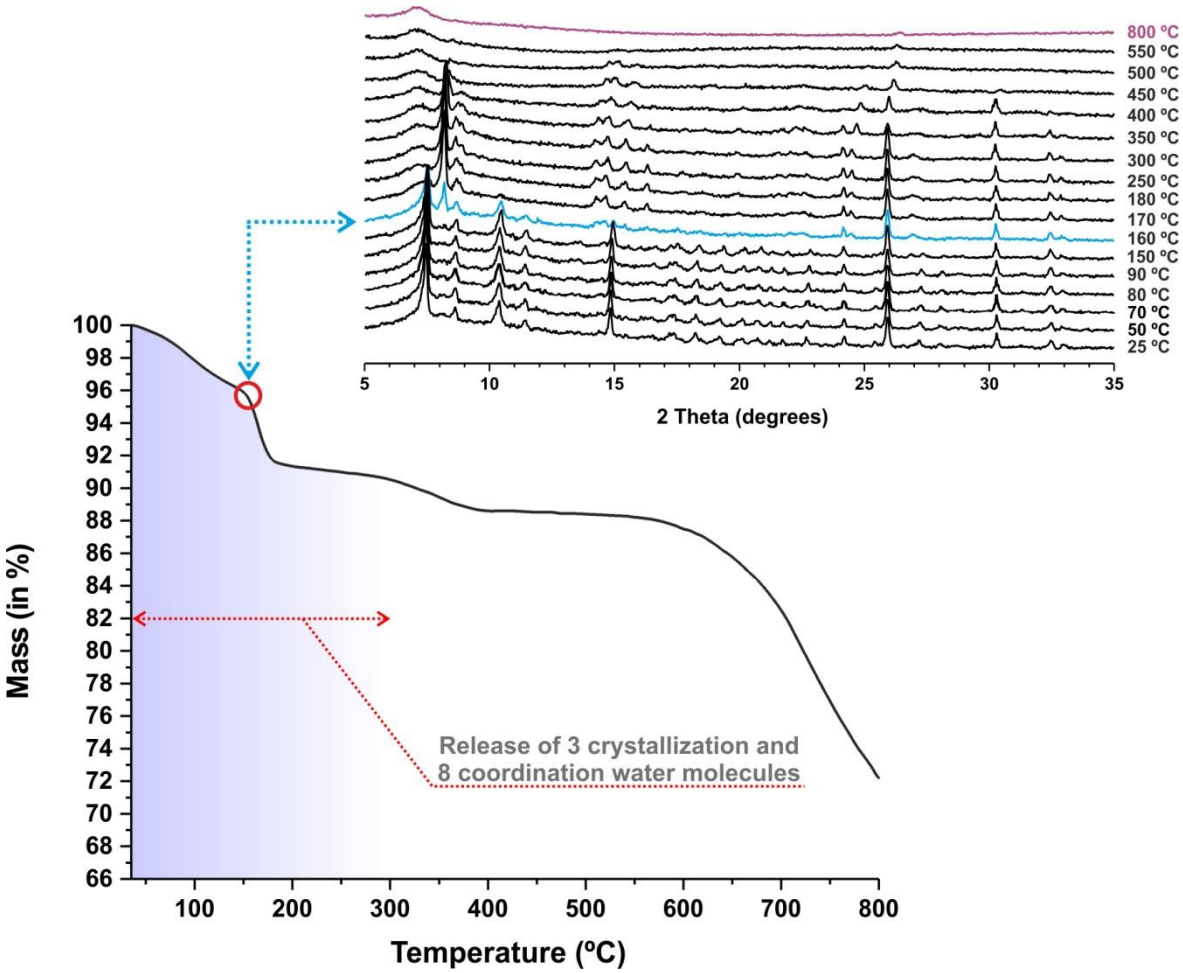

Figure 6.9. (*bottom*) Thermogram and (*top*) variable-temperature powder X-ray diffraction studies of $[Ce_4(H_3btp)(H_4btp)(H_5btp)(H_2O)_8]\cdot 3H_2O$ (**17**) collected between ambient temperature and *ca.* 800 ºC.

6.2. Introducing a second ligand: new route to multifunctional metal-organic frameworks assembled from two linkers

6.2.1. Initial Considerations and Synthetic Strategy

Pyrene is a fascinating core to construct fluorescent-conjugated light emitting compounds and, because of its extensive π-electron delocalization and electron-accepting nature, has been extensively studied as fluorescent probe in many applications.[3-7] Flat aromatic molecules and linear π-conjugated systems possess, however, a major well-known drawback: their emission in the solid state is effectively suppressed due to the formation of dimmers and/or excimers via π–π staking.[6] Although this structural feature seems to constitute a definite disadvantage for the use of this compound for the fabrication of fluorescent devices (that materials chemists have been incessantly trying to overcome), we envisaged that functionalizing the pyrene core with phosphonate groups and using this linker for the self-assembly of MOFs could produce highly crystalline porous compounds due to the inherent ability of pyrene to form well organized structures.[8] On the other hand, materials assembled using this rigid molecule should possess, in theory, enhanced thermal stability, as well as appealing photoluminescent properties to be explored.

In this section we report high-throughput hydrothermal syntheses of two new series of LnOFs obtained using pyrene-1,3,6,8-tetrayltetrakis(phosphonic acid) (**H_8ptp**) as the organic linker. Compounds $[Ln_2(H_4ptp)(ox)(H_2O)_6]\cdot 5H_2O$ [where Ln^{3+} = Ce^{3+} (**20**), Pr^{3+} (**21**), Nd^{3+} (**22**), Sm^{3+} (**23**), Eu^{3+} (**24**), Gd^{3+} (**25**), Tb^{3+} (**26**) and Dy^{3+} (**27**)] and $[Ln_2(H_4ptp)(ox)(H_2O)_6]\cdot H_2O$ [where Ln^{3+} = Ho^{3+} (**28**), Er^{3+} (**29**), Tm^{3+} (**30**), Yb^{3+} (**31**), Lu^{3+} (**32**) and Y^{3+} (**33**)] were isolated as microcrystalline powders. As a consequence, for only one of the families were we able to solve the crystal structure by single-crystal X-ray diffraction. Nevertheless, full characterization in the solid state of all compounds prompted us to propose an empirical formula for the second series of compounds as well.

6.2.2. Hydrothermal syntheses of isotypical $[Ln_2(H_4ptp)(ox)(H_2O)_6]\cdot 5H_2O$ and $[Ln_2(H_4ptp)(ox)(H_2O)_6]\cdot H_2O$ materials

Conventional hydrothermal synthesis was applied for the preparation of LnOFs based on the newly synthesized organic linker **H_8ptp**. This highly rigid and strongly fluorescent molecule functionalized in the 1-, 3-, 6-, and 8-positions with phosphonic acid

groups afforded two new families of microporous LnOFs when combined with lanthanide metal centers and oxalic acid as ancillary linker. As we discussed previously, the size, structural rigidity and orientation will unequivocally govern the crystal chemistry of the linker itself and, in the case of the pyrene derivative **H_8ptp**, early studies led us to conclude that lanthanide phosphonates based on this linker had low solubilities. Oxalic acid (H_2ox) was thus used as a second ligand to fulfill two main objectives: improve the solubility of lanthanide phosphonates and create bridges between metal centers.

To prepare compounds $[Ln_2(H_4ptp)(ox)(H_2O)_6]\cdot 5H_2O$ (**20**-**27**) and $[Ln_2(H_4ptp)(ox)(H_2O)_6]\cdot H_2O$ (**28**-**33**) solutions of the respective lanthanide chloride salts in distilled water were added to a mixture composed of **H_8ptp** and H_2ox in distilled water. The resulting reactive mixtures were kept in the oven according to the following temperature programs:

- For compounds **20**-**27**, 48 h (from ambient temperature to 140 ºC), 24 h (isothermal at 140 ºC) and 48 h (cooling to ambient temperature);
- For compounds **28**-**33**, 5 days at 140 ºC (pre-heated oven). The vessels were then removed from the oven and allowed to cool at ambient temperature (see sub-section 8.13 in the Experimental Section for further details).

All compounds were isolated as microcrystalline pale green powders in good yields. Phase identification of all materials was performed using powder X-ray diffraction (Figures 6.10 and 6.11).

Concerning morphology, one observes that compounds **20**-**27** do not seem to share the same crystal habit (see Figures E.1.6 to E.1.13 in Appendix E.1). Although all eight materials share the same crystalline phase and the same synthetic conditions were used in all cases (with the exception of metal centers), two of them, **24** and **27** respectively, possess feather-like crystals with bigger sizes than the remaining compounds.

For compounds **28**-**33**, an interesting crystal morphology was observed (see Figures E.1.14 to E.1.19 in Appendix E.1). SEM images of this family of compounds evidenced a curious and unusual morphology: cross-like crystallites with sizes ranging from 5 to 30 μm.

Bulk materials **20**-**33** were then fully characterized using standard solid-state techniques: structural details were confirmed using in tandem elemental analysis, thermodiffractometry (Figures 6.14, 6.15) electron microscopy (Figures E.1.6 to E.1.19 in

Appendix E.1), FT-IR spectroscopy (Figures E.3.2 and E.3.3 in Appendix E.3), thermogravimetric analyses (E.4.2 and E.4.3 in Appendix E.4) and solid-state NMR (Figure 6.13) in order to evaluate phase purity and homogeneity of all compounds and propose a possible empirical formula for compounds **28**-**33**.

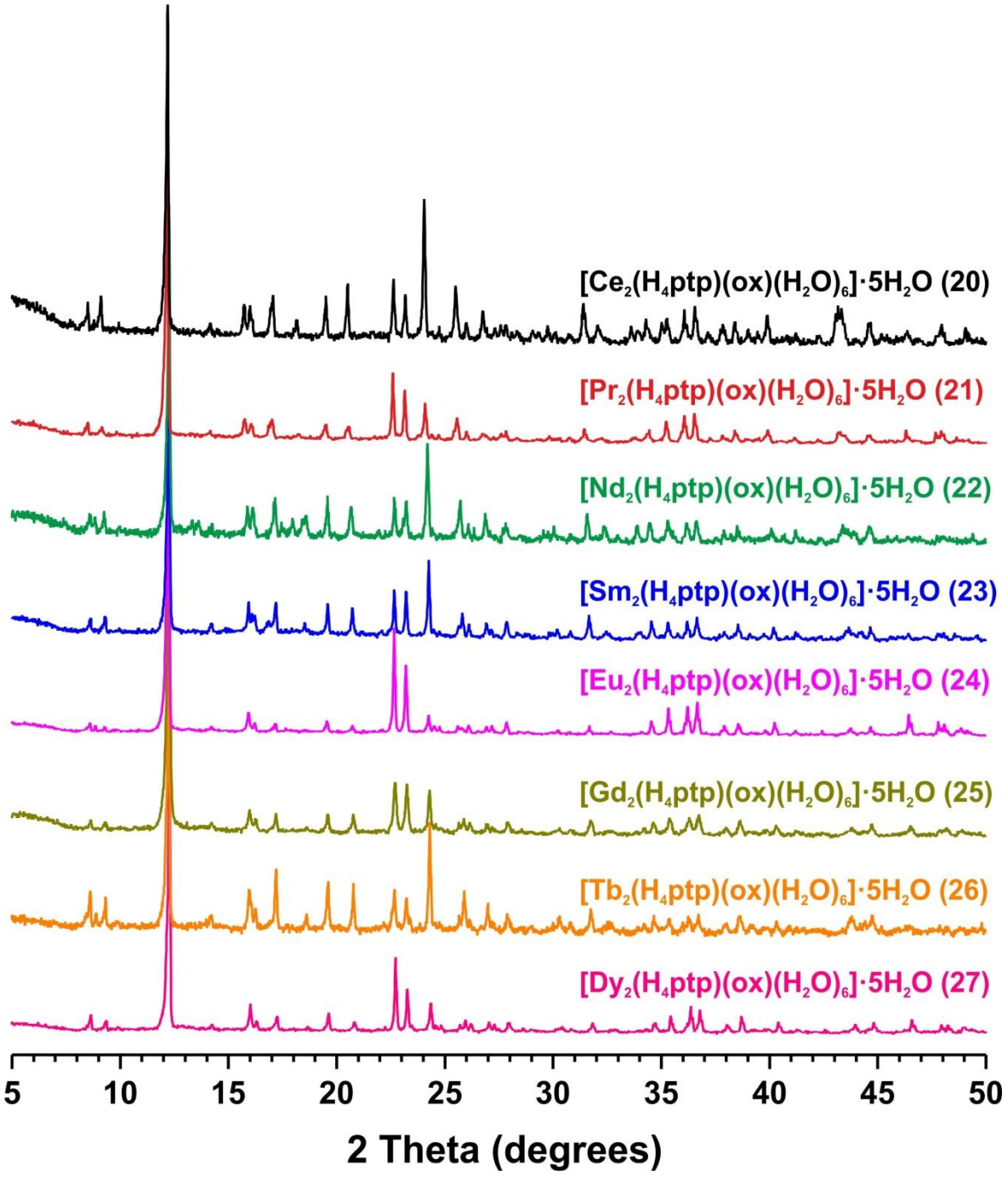

Figure 6.10. Powder X-ray diffraction patterns of bulk materials $[Ln_2(H_4ptp)(ox)(H_2O)_6]\cdot 5H_2O$ [where Ln^{3+} = Ce^{3+} (**20**), Pr^{3+} (**21**), Nd^{3+} (**22**), Sm^{3+} (**23**), Eu^{3+} (**24**), Gd^{3+} (**25**), Tb^{3+} (**26**) and Dy^{3+} (**27**)].

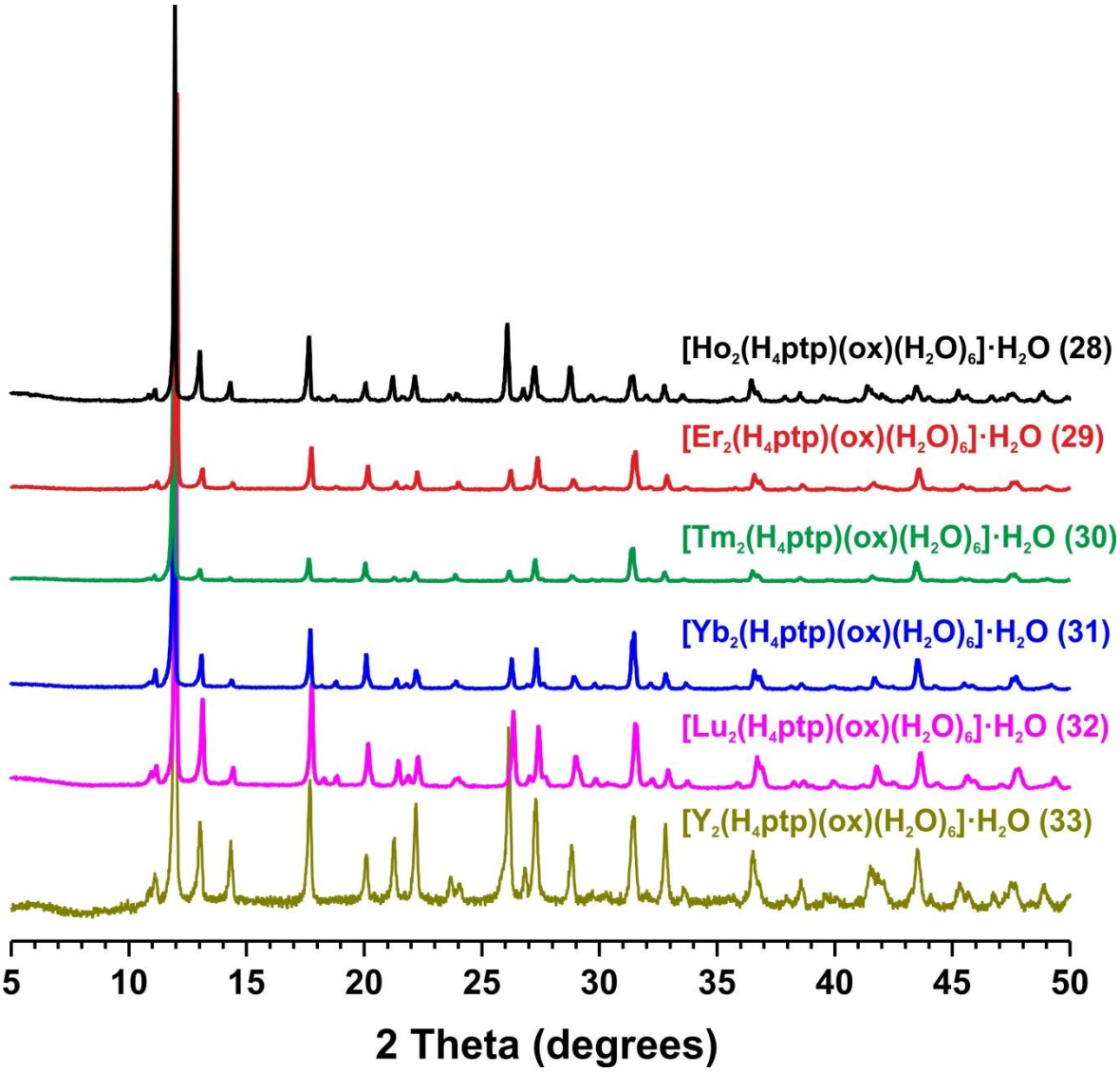

Figure 6.11. Powder X-ray diffraction patterns of bulk materials $[Ln_2(H_4ptp)(ox)(H_2O)_6]\cdot H_2O$ [where Ln^{3+} = Ho^{3+} (**28**), Er^{3+} (**29**), Tm^{3+} (**30**), Yb^{3+} (**31**), Lu^{3+} (**32**) and Y^{3+} (**33**)].

The crystalline structure of material **21** was unveiled by single-crystal X-ray diffraction (Figure 6.12). The compound was formulated as $[Pr_2(H_4ptp)(ox)(H_2O)_6]\cdot 5H_2O$ and crystallizes in the centrosymmetric space group *I*2/*a*, with an asymmetric unit comprising one metal center, half H_2ptp organic linker and half of an oxalic acid molecule. Adding oxalic acid to the reactive mixture proved to be crucial for the self-assembly of **21**, being responsible for assisting the phosphonic groups to maintain the inorganic chains formed in the [100] direction (Figure 6.12c). These chains are then connected by H_4ptp residues along the *c*-axis (Figure 6.12a) forming a tunnel-shaped porous 3D network, with several coordination and crystallization water molecules trapped inside.

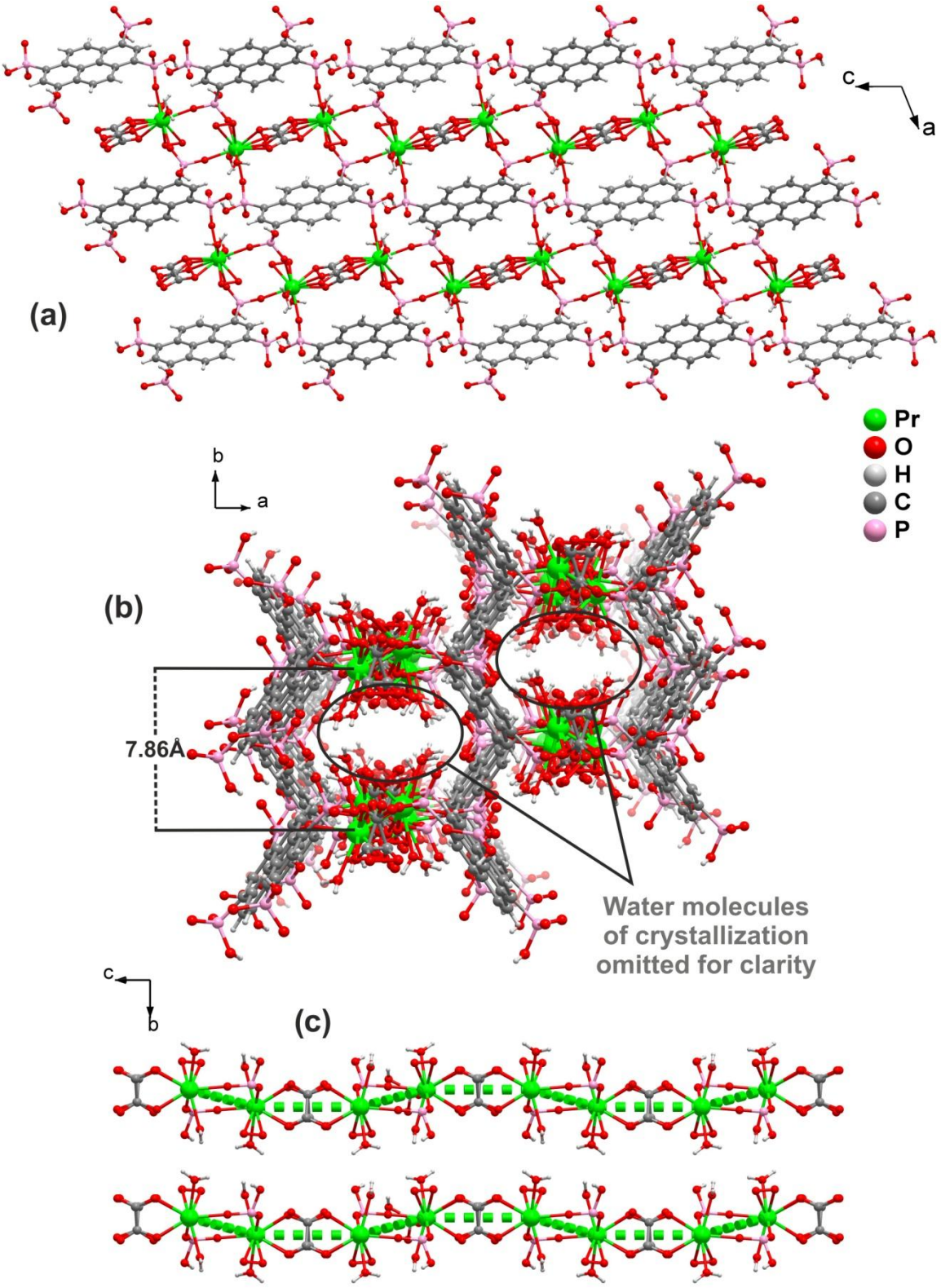

Figure 6.12. Crystal packing of $[Pr_2(H_4ptp)(ox)(H_2O)_6]\cdot 5H_2O$ (**21**) viewed in perspective along the **(a)** [010] and (**b**) [001] directions of the unit cell. The representations emphasize the porous 3D network of the coordination polymer present in **21** and highlight the role of oxalic acid bridging metal centers. Water molecules of crystallization were omitted for clarity. **(c)** Representation of the layer along the *bc* plane of $[Pr_2(H_4ptp)(ox)(H_2O)_6]\cdot 5H_2O$ (**21**) depicting the coordination mode of oxalic acid to the metal centers.

Unfortunately, the same single-crystal crystallographic interpretation was not possible for the second series of compounds, due to the size of the crystals. Nevertheless, taking advantage of the presence of diamagnetic Y^{3+} metallic centers in material **33**, we were able to confirm the probable number of crystallographic independent phosphonic acid groups in the asymmetric unit of this material through the use of solid-state NMR studies. The ^{31}P CP MAS spectrum of **33** shows, in the isotropic region, a sharp peak corresponding to the overlapping of two resonances, centered at *ca.* 2.2 and 2.7 ppm (Figure 6.13). Peak deconvolution and fitting confirmed that there are two independent phosphorus sites, which may correspond to a total of half of an organic ligand residue present in the asymmetric unit of this material. Due to the rigidity of the organic ligand **H_8ptp**, it is not expected that a lot of different spacial conformations will arise from the self-assembly of MOFs using this molecule. This aspect, allied with the fact that the same heating methodology was employed for the synthesis of all these pyrene-based materials, *i.e.* hydrothermal conditions, leads to the possibility that an analogous structure of materials **20**-**27** was obtained here, given that the performed crystallographic studies on material **21** also indicate two independent phosphorus sites in the asymmetric unit.

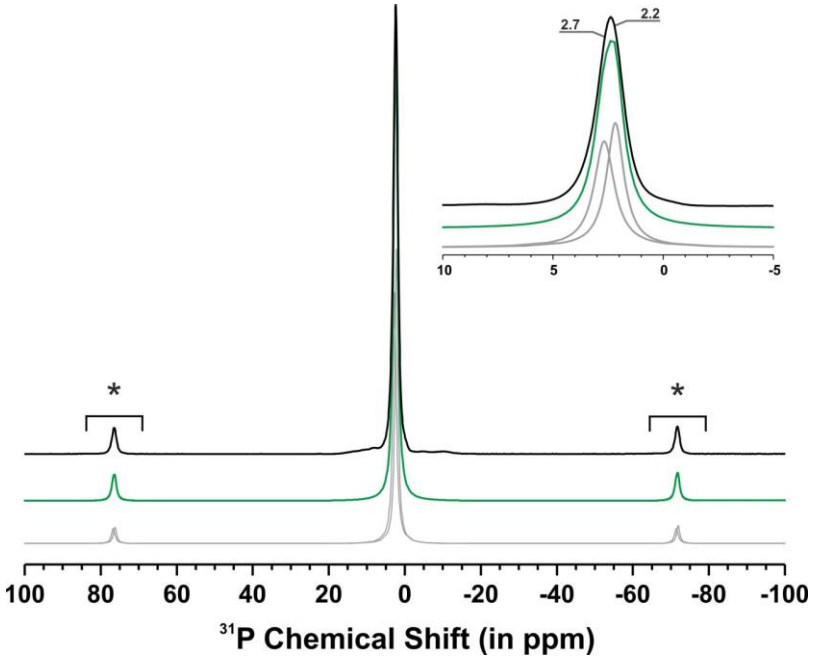

Figure 6.13. ^{31}P CP MAS spectrum of $[Y_2(H_4ptp)(ox)(H_2O)_6]\cdot H_2O$ (**33**) (black line). Spinning sidebands are denoted using an asterisk. Peak deconvolution and integration throughout the entire spectral range (*i.e.*, including the spinning sidebands) gives a ratio of *ca.* 1.0 : 1.0 for the isotropic resonances centered at *ca.* 2.2 and 2.7 ppm respectively. The green line depicts the overall (*i.e.*, sum) data fit, while the individual light grey lines correspond to the fits of each single peak.

6.2.3. Thermogravimetry and thermodiffractometry

The thermal stability of the bulk $[Ln_2(H_4ptp)(ox)(H_2O)_6]\cdot 5H_2O$ and $[Ln_2(H_4ptp)(ox)(H_2O)_6]\cdot H_2O$ materials was investigated between ambient temperature and *ca.* 800 ºC, providing additional information on the hydration level of all compounds. As depicted in Figures E.4.2 and E.4.3 (in Appendix E.4), the thermograms for the two prepared series of materials are very similar for the respective family of compounds, ultimately indicating the same thermal stabilities between compounds **20** to **27** and **28** to **33**. Thus, in the following paragraphs discussion will be solely focused on one compound from each series.

The thermal stability of compound $[Eu_2(H_4ptp)(ox)(H_2O)_6]\cdot 5H_2O$ (**24**) was investigated between ambient temperature and *ca.* 800 ºC. The crystallinity of the bulk material was further evaluated by employing *in situ* variable temperature powder X-ray diffraction studies, in the 25-200 ºC temperature range (Figure 6.14).

Between ambient temperature and *ca.* 90 ºC, compound **24** loses approximately 3.0% of mass, corresponding to the release of two water molecules of crystallization. This value agrees well with the calculated one (*ca.* 3.3%). Above this temperature, there are two consecutive weight losses between 100 and 170 ºC. In this temperature range, the remaining crystallization water molecules are released from the structure, as well as five coordination water molecules (in this case the observed 12.7% weight loss is equivalent to eight water molecules). Above this temperature the weight loss does not stabilize until 800 ºC, which indicates that the residue suffers additional rearrangements and still contains residual carbon/organic components at the end of measurements.

Variable-temperature powder X-ray diffraction studies on the same compound further corroborate the aforementioned assumptions concerning the release of water molecules and phase modifications: at *ca.* 100 ºC, the structure of **24** changed to a new crystalline phase as a consequence of the release of two crystallization water molecules, as calculated above. The two consecutive weight losses between 100 and 170 ºC destabilize and promote the amorphization of the structure at 170 ºC.

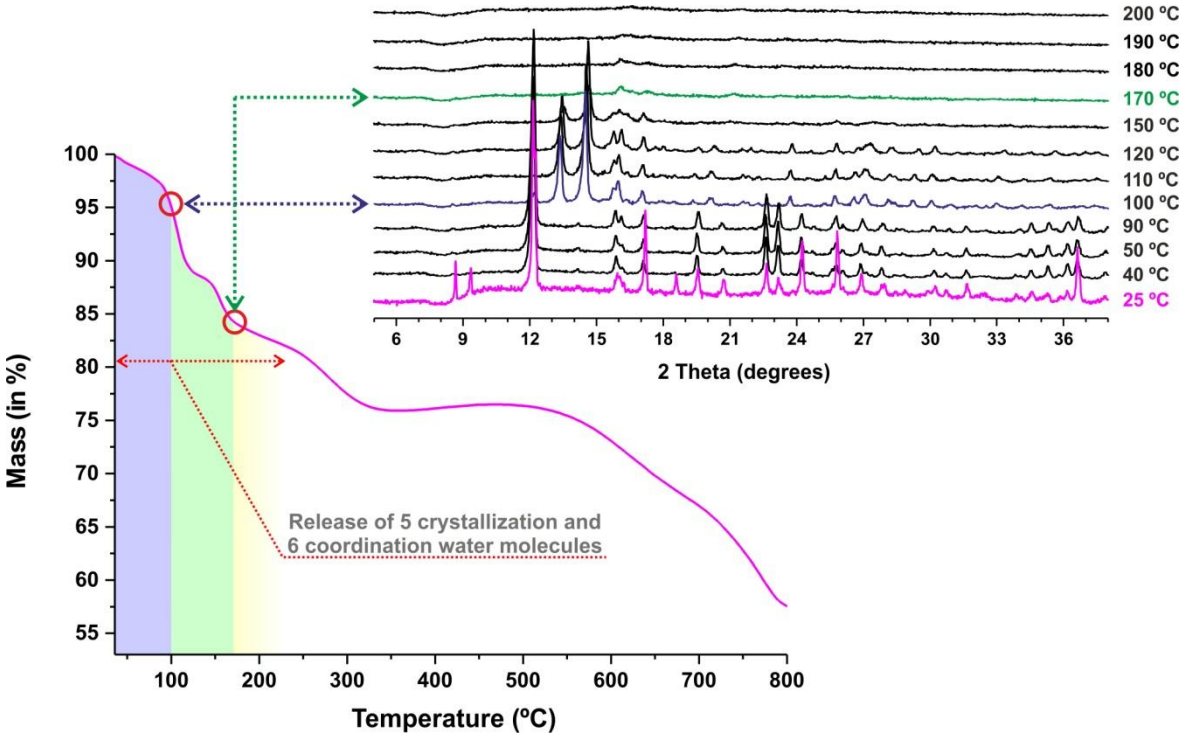

Figure 6.14. (*bottom*) Thermogram and (*top*) variable-temperature powder X-ray diffraction studies of $[Eu_2(H_4ptp)(ox)(H_2O)_6]\cdot 5H_2O$ (**24**) collected between ambient temperature and *ca.* 800 ºC.

An identical set of studies were performed for $[Ho_2(H_4ptp)(ox)(H_2O)_6]\cdot H_2O$ (**28**) that provided information to understand additional structural features of materials **28**-**33** (Figure 6.15).

The first weight loss occurs between ambient temperature and *ca.* 100 ºC, corresponding to the release of one water molecule of crystallization. The experimental value of *ca.* 1.9% agrees well with the calculated one (*ca.* 1.7%). A second and very intense weight loss of *ca.* 9.0% occurs almost immediately, between 100 ºC and *ca.* 175 ºC, and corresponds to a weight loss equivalent to six water molecules. After a plateau of approximately 125 ºC (between 175 and 300 ºC) in which the dehydrated material remains stable, the organic moiety starts decomposing. Thermodiffractometry studies validate the assumptions concerning the release of water molecules and phase modifications of compound **28**: at *ca.* 100 ºC, the structure changed to a new crystalline phase as a consequence of the release of one crystallization water molecule. The framework of **28** remains unaltered between 100 and *ca.* 300 ºC, which indicates that the weight loss that occurs in this temperature range does not affect the crystalline phase of the material. After 300 ºC the organic component of the material starts decomposing with the consequent collapse of the framework.

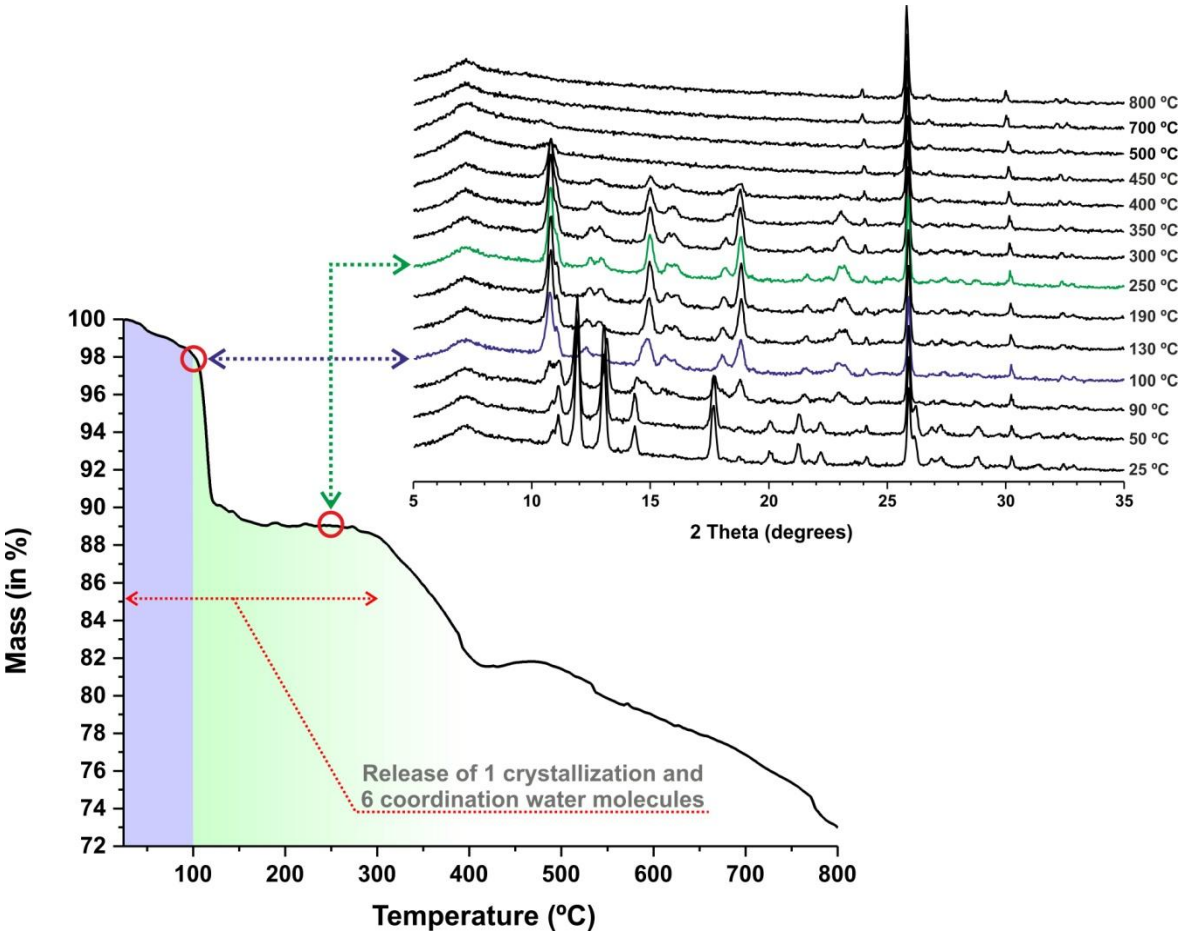

Figure 6.15. (*bottom*) Thermogram and (*top*) variable-temperature powder X-ray diffraction studies of $[Ho_2(H_4ptp)(ox)(H_2O)_6]\cdot H_2O$ (**28**) collected between ambient temperature and *ca.* 800 ºC.

6.2.4. FT-IR spectroscopic studies

The vibrational FT-IR spectroscopy studies support the structural features unveiled by the X-ray diffraction studies.[2] Figure E.3.2 and E.3.3 (in Appendix E.3) compare the FT-IR spectra of $[Ln_2(H_4ptp)(ox)(H_2O)_6]\cdot 5H_2O$ (**20**-**27**) and $[Ln_2(H_4ptp)(ox)(H_2O)_6]\cdot H_2O$ (**28**-**33**) materials in the 3650-350 cm^{-1} spectral region. Because materials **20**-**27** and **28**-**33** are isotypical, only the details for compounds **20** (Figure 6.16) and **28** (Figure 6.17) are going to be described and discussed next.

Compound **20** contains a broad band centered in the *ca.* 3600-3050 cm^{-1} spectral range, which is attributed to both ν(O–H) stretching vibrational modes from coordination and crystallization water molecules and to the ν(PO–H) stretching vibration of the phosphonate groups of the organic ligand $\mathbf{H_8ptp}$. In the central region of the spectrum, between *ca.* 1700 and 1570 cm^{-1}, it is possible to observe a sharp signal comprising the

typical *v*(C=C) stretching vibrational modes arising from the aromatic rings, the *v*(C=O) vibration from the oxalic acid, and the deformation stretching of the water molecules. We further observe as well a sharp vibrational mode at *ca*. 740 cm^{-1}, corresponding to the *v*(P–C) stretching vibration. Also in this region, the stretching vibrational modes of *v*(P=O) were noticed from *ca*. 1280 to 1110 cm^{-1}, and those of *v*(P–O) from *ca*. 1040 to 880 cm^{-1}. Finally, the *v*($–CO_2^-$) stretching vibration from the presence of oxalic acid in the structure appears between 635 and 475 cm^{-1}, supporting the previously performed crystallographic studies on compound **21**.

The assignment of the observed bands in compound **28** is basically the same as compound **20**. Nevertheless, it is possible to notice one main difference between compounds **20**-**27** and **28**-**33**: the *v*(O–H) stretching vibrational modes from coordination and crystallization water molecules and –POH groups are more defined for the latter family of compounds in this particular range. In Chapter 4, a well-defined vibration band centred at 3505 cm^{-1} was attributed to the hydronium cation from material $(H_3O)[Y_2(H_5btp)(H_4btp)]\cdot H_2O$ (**6**) and confirmed a strong hydrogen bond identified in the performed single-crystal X-ray studies of this compound. We are not able to confirm that the same is occurring for materials **28**-**33**, however a similar vibration is present at *ca.* 3590 cm^{-1} for this family of materials. These results point towards the presence strong hydrogen interactions in the network of these materials.

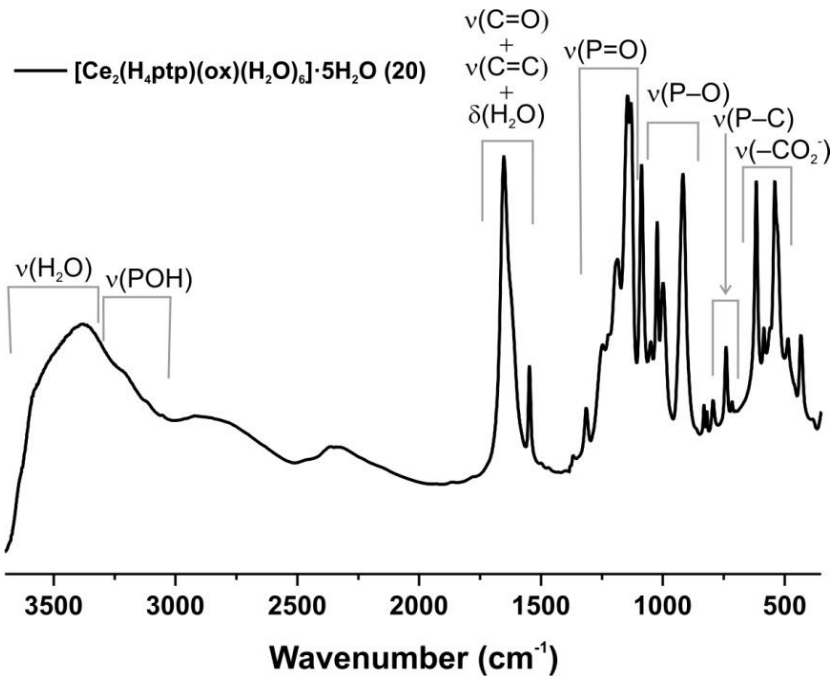

Figure 6.16. FT-IR spectra (in absorbance, arbitrary units) of $[Ce_2(H_4ptp)(ox)(H_2O)_6]\cdot 5H_2O$ (**20**).

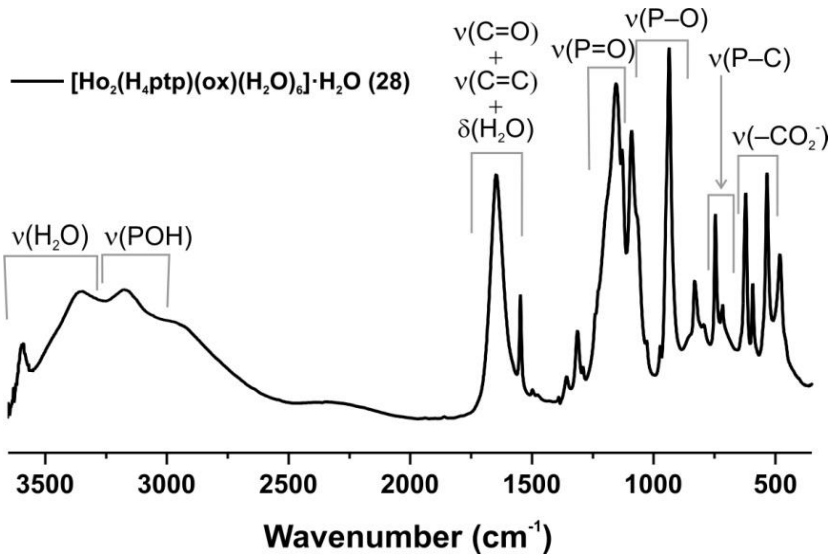

Figure 6.17. FT-IR spectra (in absorbance, arbitrary units) of $[Ho_2(H_4ptp)(ox)(H_2O)_6]\cdot H_2O$ (**28**).

6.3. Conclusions

In this chapter we reported the preparation of four new series of porous LnOFs: a family of two 2D materials formulated as $[Ln_7(H_5btp)_5(H_6btp)_3(H_2O)_{12}]\cdot 23.5H_2O\cdot MeOH$ [where Ln^{3+} = Eu^{3+} (**15**) and Gd^{3+} (**16**)]; a second 3D family based on the same organic linker (**H_8btp**) formulated as $[Ln_4(H_3btp)(H_4btp)(H_5btp)(H_2O)_8]\cdot 3H_2O$ [where Ln^{3+} = Ce^{3+} (**17**), Pr^{3+} (**18**), and Nd^{3+} (**19**)]; from the reaction between lanthanide chloride hydrated salts with the organic ligand pyrene-1,3,6,8-tetrayltetrakis(phosphonic acid) (**H_8ptp**), under hydrothermal conditions, two families were obtained, $[Ln_2(H_4ptp)(ox)(H_2O)_6]\cdot 5H_2O$ [where Ln^{3+} = Ce^{3+} (**20**), Pr^{3+} (**21**), Nd^{3+} (**22**), Sm^{3+} (**23**), Eu^{3+} (**24**), Gd^{3+} (**25**), Tb^{3+} (**26**) and Dy^{3+} (**27**)] and $[Ln_2(H_4ptp)(ox)(H_2O)_6]\cdot H_2O$ [where Ln^{3+} = Ho^{3+} (**28**), Er^{3+} (**29**), Tm^{3+} (**30**), Yb^{3+} (**31**), Lu^{3+} (**32**) and Y^{3+} (**33**)].

Regarding the isolated compounds using **H_8btp**, studies have been focused on the self-assembly of structures envisaging a drastic reduction of the required reaction time when compared to compounds $[Ln_4(H_6btp)_2(H_4btp)_2(H_8btp)(H_2O)_{16}]\cdot 12H_2O$ [where Ln^{3+} = La^{3+} (**1**), $(La_{0.9}Eu_{0.1})^{3+}$ (**2**) and $(La_{0.9}Tb_{0.1})^{3+}$ (**3**)] (from Chapter 3). Hence, we successfully obtained materials **17**-**19**, using hydro(solvo)thermal synthesis, as a new family of compounds comprising a lot of structural features comparable to compounds **1**-**3**, as well as, **15** and **16**. We were also able to significantly improve the thermal stability of these structures characterized by their supramolecular stacked arrangement of organic linkers due to the enhanced connectivity and dimensionality present in the 3D networks.

The use of conventional hydrothermal synthesis with the same synthetic conditions (temperature, 140 ºC; time, 5 days) used for 3D LnOFs $[Ln(H_5btp)]\cdot 2H_2O$ [where Ln^{3+} = Gd^{3+} (**8**), Tb^{3+} (**9**), Dy^{3+} (**10**), Ho^{3+} (**11**), Er^{3+} (**12**) and Tm^{3+} (**13**)] (from Chapter 5), successfully led to the isolation of a series of eight new LnOFs based on the organic ligand **H_8ptp** and oxalic acid (used as ancillary ligand). Materials formulated as $[Ln_2(H_4ptp)(ox)(H_2O)_6]\cdot 5H_2O$ [where Ln^{3+} = Ce^{3+} (**20**), Pr^{3+} (**21**), Nd^{3+} (**22**), Sm^{3+} (**23**), Eu^{3+} (**24**), Gd^{3+} (**25**), Tb^{3+} (**26**) and Dy^{3+} (**27**)] were fully characterized using standard solid-state techniques and their crystalline structure was unveiled by single-crystal X-ray diffraction studies. Further studies conducted using the remaining lanthanide chloride salts and Y^{3+} led to the isolation of a second series of six compounds, formulated as $[Ln_2(H_4ptp)(ox)(H_2O)_6]\cdot H_2O$ [where Ln^{3+} = Ho^{3+} (**28**), Er^{3+} (**29**), Tm^{3+} (**30**), Yb^{3+} (**31**), Lu^{3+} (**32**) and Y^{3+} (**33**)], with a particular crystallite morphology unusual for this kind of hybrid materials.

The two series of materials based on **H_8ptp** reported in this chapter constitute the first examples of synthesized MOFs based on this organic ligand. However, one of the main objectives of this work was not achieved: due to the particular morphology and small crystal sizes of compounds **28**-**33**, single-crystal X-ray diffraction studies were not possible to be performed, thus the crystalline framework of these compounds remains unknown.

6.4. References

(1) Kumar, P.; Kim, K. H.; Kwon, E. E.; Szulejko, J. E.; *J. Mater. Chem. A*, **2016**, *4*, 345.

(2) Socrates, G. *Infrared and raman characteristic group frequencies : tables and charts*; John Wiley & Sons, West Sussex, **2007**.

(3) Figueira-Duarte, T. M.; Mullen, K.; *Chem. Rev.*, **2011**, *111*, 7260.

(4) Feng, X.; Hu, J. Y.; Tomiyasu, H.; Seto, N.; Redshaw, C.; Elsegood, M. R. J.; Yamato, T.; *Org. Biomol. Chem.*, **2013**, *11*, 8366.

(5) de Halleux, V.; Calbert, J. P.; Brocorens, P.; Cornil, J.; Declercq, J. P.; Bredas, J. L.; Geerts, Y.; *Adv. Funct. Mater.*, **2004**, *14*, 649.

(6) Moorthy, J. N.; Natarajan, P.; Venkatakrishnan, P.; Huang, D. F.; Chow, T. J.; *Org. Lett.*, **2007**, *9*, 5215.

(7) Sase, M.; Yamaguchi, S.; Sagara, Y.; Yoshikawa, I.; Mutai, T.; Araki, K.; *J. Mater. Chem.*, **2011**, *21*, 8347.

(8) Stylianou, K. C.; Heck, R.; Chong, S. Y.; Bacsa, J.; Jones, J. T. A.; Khimyak, Y. Z.; Bradshaw, D.; Rosseinsky, M. J.; *J. Am. Chem. Soc.*, **2010**, *132*, 4119.

Chapter 7

General Conclusions

For this PhD project it was proposed as the main objective the preparation of porous functional and multidimensional MOF materials from the self-assembly of lanthanide cations with new tetrapodal phosphonate-based organic ligands designed and isolated in large amounts. Efforts were directed and focused toward the optimization of ideal reaction conditions, as well as achieve the best synthetic approaches to obtain both organic linkers and multidimensional MOFs in high yields and, at the same time, high levels of purity.

In the vast body of structural knowledge available on Metal-Organic Frameworks, compounds built up of tetraphosphonic acid linkers and lanthanides are still a poorly explored sub-field. This is presumably due, to a large extent, to the lack of commercially available organic linkers with these chelating units. Thus, research groups working in the field have ameliorated a number of synthetic strategies to produce, in good yields, and in a fast, cost-effective and simple way, suitable amounts of these molecules. In this PhD project we also meant to fulfill this objective when we developed synthetic routes to prepare tetrapodal phosphonate-based organic ligands **H_8btp** and **H_8ptp** to be used in the self-assembly of new MOF materials.

Tetraphosphonic acid molecules (particularly the phosphonoaromatic ligands) form, in general, rather robust, thermally stable networks. A number of structural features are at the genesis of this: on one hand, an increased connectivity by the ligand to metal centers is usually accompanied by an increase in the networks dimensionality and, consequently, the presence of fewer coordination water molecules which promote low-temperature MOF degradation, *e.g.* large number of molecules are associated with decomposition temperatures around or below 100 ºC, as clearly demonstrated by compounds $[Ln_4(H_6btp)_2(H_4btp)_2(H_8btp)(H_2O)_{16}]\cdot 12H_2O$ [where Ln^{3+} = La^{3+} (**1**), $(La_{0.9}Eu_{0.1})^{3+}$ (**2**) and $(La_{0.9}Tb_{0.1})^{3+}$ (**3**)] and $[Ln_7(H_5btp)_5(H_6btp)_3(H_2O)_{12}]\cdot 23.5H_2O\cdot MeOH$ [where Ln^{3+} = Eu^{3+} (**15**) and Gd^{3+} (**16**)]; on the other hand, the usage of ancillary ligands, such as oxalate, seem to promote lanthanide-phosphonates solubility, better thermal stability, as well as, improve structural connectivity.

The presence of a large number of phosphonic acid groups in the organic linkers also seems to endorse interesting properties. For example, the use of tetrapodal phosphonic acids leads to a large number of uncoordinated framework –POH groups, promoting good results concerning proton conductivity and heterogeneous catalysis. These linkers further induce a rich structural diversity, with structures spanning from discrete complexes to MOF-type architectures (1D, 2D or 3D). In this realm, it is a notable fact that flexible

frameworks exhibiting a "breathing effect" can be isolated and characterized at various hydration stages. For this PhD project we highlight the yttrium-based MOFs, formulated as $[Y(H_5btp)]\cdot 5.5H_2O$ (**4**), $[Y(H_5btp)]\cdot 2.5H_2O$ (**5**), $(H_3O)[Y_2(H_5btp)(H_4btp)]\cdot H_2O$ (**6**) and $[Y(H_5btp)]\cdot H_2O\cdot 0.5(MeOH)$ (**7**), that definitely illustrated this specific feature.

In summary, the universe of lanthanide-tetraphosphonic frameworks is still limited but the few examples herein described clearly showed two main aspects. Firstly, this type of compounds may have very high thermal stability and potential applications not attainable by other MOFs (*e.g.* those based on carboxylates). Secondly, these tetraphosphonate-based networks bear a large number of uncoordinated –POH groups. This, allied with the presence of water channels, can boost proton conductivity, a property of great interest in current materials research.

Previous investigations carried out by our research group led us to use synthetic approaches based on microwave irradiation for the preparation of the phosphonate esters ***IL*^{1}** and ***IL*^{3}**, precursors of the organic ligands **H_8btp** and **H_8ptp**. A strict optimization of several reaction conditions (*e.g.* reaction time, temperature and solvents) permitted the use of MWAS, employed as a straightforward reaction methodology and characterized, essentially, by the drastic reduction of the total reaction time, when compared to conventional heating methodologies described in the literature for the same type of C–P bond formation reactions. Predictably, MWAS afforded the expected organic molecules in high yields and using a fast, easy, clean and safe way. The prepared tetrapodal linkers **H_8btp** and **H_8ptp** were, as predicted, suitable organic PBUs to be employed in the preparation of various structurally distinct porous functional MOFs, together with all the lanthanide cations. Standard liquid-state NMR spectroscopy used in tandem with mass spectrometry were useful tools to unequivocally unveil and characterize the structure of all prepared organic molecules.

As discussed, molecular directionality and general structural properties of the organic ligands arise, undoubtedly, as crucial factors in the preparation of porous multidimensional MOFs, mainly because of the intrinsic orientation displayed by rigid aromatic-based linkers. The use of the more flexible biphenyl **H_8btp** linker led to the preparation of both 2D and 3D MOF materials. These results agree well with several reports published in the literature, in which a certain degree of flexibility will lead to a larger structural diversity of materials, due to the possibility of more spacial conformations of the organic linker in the final framework (hence the seven different structures identified using this PBU). On the other hand, the rigid pyrene-based **H_8ptp** ligand directed the

isolation of only two series of LnOFs, $[Ln_2(H_4ptp)(ox)(H_2O)_6]\cdot 5H_2O$ (**20**-**27**) and $[Ln_2(H_4ptp)(ox)(H_2O)_6]\cdot H_2O$ (**28**-**33**). Nevertheless, these two families of materials were highly porous LnOFs, as expected from the use of rigid organic ligands with several available coordination moieties.

The isolation of all the reported multidimensional MOFs was achieved by employing, mainly, two distinct synthetic approaches: conventional hydro(solvo)thermal synthesis and microwave-assisted synthesis. Predictably, hydro(solvo)thermal synthesis was a good approach to isolate single-crystals suitable for X-ray diffraction studies. However, the preparation of the $[Ln_2(H_4ptp)(ox)(H_2O)_6]\cdot H_2O$ (**28**-**33**) family as large particles was not possible, consequently the crystalline framework of these compounds was not unveiled.

Due to the general harsh reaction conditions (*i.e.* high temperatures under autogenous pressure during long periods of time) needed to prepare MOFs using the conventional hydro(solvo)thermal approach, other easier, faster, cleaner and with low energy-consumption synthetic methodologies were investigated. In this category one finds microwave irradiation emerging as a good alternative to hydrothermal synthesis. The close control of several reaction parameters, such as temperature, time, power, pressure and/or stirring, allowed, for example, the preparation of different MOF architectures using the same organic and inorganic PBUs: the self-assembly between **H_8btp** and Gd^{3+} cations produced the 2D $[Gd_7(H_5btp)_5(H_6btp)_3(H_2O)_{12}]\cdot 23.5H_2O\cdot MeOH$ (**16**) and the 3D $[Gd(H_5btp)]\cdot 2H_2O$ (**8**) materials. While the same reaction mixtures were set up, they led to the preparation of two different phase-pure materials when the heating source and general reaction methodology was changed from hydro(solvo)thermal synthesis to microwave irradiation followed by slow evaporation. For the remaining materials self-assembled using MWAS, this technique also exhibited good reproducibility, and the possibility to prepare MOF materials with homogeneous crystal morphology and particle sizes.

As discussed in Chapter 1, the preparation of phosphonate-based MOFs is usually difficult and the optimization to achieve a phase-pure compound may not be a straightforward process either, due to the various coordination modes exhibited by the phosphonic acid organic group (as demonstrated abundantly in the various MOF structures reported in this thesis), particularly when bonded to lanthanides that also show high coordination numbers and the possibility of various coordination modes. All these factors conjugated lead, in many cases, to the isolation of microcrystalline powders or mixtures of phases due to the so-called supramolecular isomerism. In addition, the final structure of

this type of materials is also less predictable, compared to carboxylate or nitrogen-based organic ligands. The self-assembly using the latter compounds and transition metals allows the isoreticular synthesis of new MOFs; the same concept has not yet been attained or, at least, commonly employed regarding phosphonate-based compounds. Nevertheless, there are a few parameters that could help preventing the occurrence of supramolecular isomerism in phosphonate-based MOFs. For example, using multipodal organic linkers, such as the tetrapodal linkers used in this thesis, promotes supramolecular isomerism due to the large number of possible coordination modes to metal ions; nevertheless, adding aromatic rings to the organic backbone of the linker with a specific shape and size, should enhance both structural robustness and overall structural directionality of the networks, thus not a large number of spacial conformations are expected when a highly rigid linker is used for the self-assembly of new MOFs (which we demonstrated when **H_8ptp**, a more rigid ligand, was used).

Finally, a remarkable family of compounds, formulated as $[Ln(H_5btp)]\cdot 2H_2O$ [where Ln^{3+} = Gd^{3+} (**8**), Tb^{3+} (**9**), Dy^{3+} (**10**), Ho^{3+} (**11**), Er^{3+} (**12**) and Tm^{3+} (**13**)], has been reported whose structures can withstand very high temperatures. An interesting SC-SC transformation triggered inside the porous network between uncoordinated –POH groups (that rearranged into pyrophosphonate moieties) contributed to the registered high decomposition temperature of these materials (*ca.* 800 ºC). This result leaves the door open to new possibilities and new fields of research not considered before for this class of hybrid materials.

Chapter 8

Experimental Section

8.1. General Instrumentation

SEM (scanning electron microscopy) images were acquired using either a Hitachi S4100 field emission gun tungsten filament instrument working at 25 kV or a high-resolution Hitachi SU-70 working at 4 kV. Samples were prepared by deposition on aluminum sample holders followed by carbon coating using an Emitech K950X carbon evaporator. EDS (energy dispersive X-ray spectroscopy) data and SEM mapping images were recorded using the latter microscope, Hitachi SU-70, working at 15 kV and using either a Bruker Quantax 400 or an Esprit 1.9 EDS microanalysis system.

Thermogravimetric analyses (TGA) were carried out using a Shimadzu TGA 50, from ambient temperature to *ca*. 800 ºC (heating rate of 5 ºC/min) under a continuous stream of air at a flow rate of 20 mL min^{-1}. For the thermogravimetric analyses from ambient temperature to *ca.* 1200 ºC, the equipment used was a Setaram Instrumentation SETSYS Evolution (heating rate of 10 ºC/min), under a continuous stream of O_2 at a flow rate of 200 mL min^{-1}.

Fourier Transform Infrared (FT-IR) spectra (in the spectral range of 4000-350 cm^{-1}) were recorded as KBr pellets (typically 2 mg of sample were mixed in a mortar with *ca.* 200 mg of KBr) using a Bruker Tensor 27 spectrometer by averaging 256 scans at a maximum resolution of 2 cm^{-1}.

Elemental analyses for C and H were performed with a Truspec Micro CHNS 630-200-200 elemental analyzer at the Department of Chemistry, University of Aveiro. Analysis parameters: sample amount between 1 and 2 mg; combustion furnace temperature = 1075 ºC; afterburner temperature = 850 ºC. Detection method for carbon and hydrogen - infrared absorption. Analysis time = 4 minutes. Required gasses: carrier – helium; combustion – oxygen; pneumatic – compressed air.

Routine powder X-ray diffraction (PXRD) data for all prepared materials were collected at ambient temperature on a Empyrean PANalytical diffractometer (Cu $K\alpha_{1,2}$ X-radiation, λ_1 = 1.540598 Å; λ_2 = 1.544426 Å), equipped with an PIXcel 1D detector and a flat-plate sample holder in a Bragg-Brentano para-focusing optics configuration (45 kV, 40 mA). Intensity data were collected by the step-counting method (step 0.01º), in continuous mode, in the *ca.* $3.5 \leq 2\theta^{o} \leq 50^{o}$ range.

Variable-temperature powder X-ray diffraction data were collected on a PANalytical X'Pert Powder diffractometer (Cu $K\alpha_{1,2}$ X-radiation, λ_1 = 1.540598 Å; λ_2 =

1.544426 Å) under an air atmosphere, equipped with a PIXcel 1D detector, a flat-plate sample holder in a Bragg-Brentano para-focusing optics configuration (40 kV, 50 mA), and a high-temperature Anton Paar HKL 16 chamber controlled by an Anton Paar 100 TCU unit. Intensity data were collected in the continuous mode (*ca.* 100 s data acquisition) in the angular range *ca.* $5 \leq 2\theta° \leq 35$.

^{1}H and ^{31}P MAS Nuclear Magnetic Resonance (NMR) spectra were recorded at 9.4 T on a Bruker Avance 400 wide-bore spectrometer (DSX model) on a 4 mm magic-angle spinning VTN probe at 161.9 MHz. ^{31}P HPDEC spectra were acquired using a 90° single pulse excitation of 3.0 μs; recycle delay: 60 s; ν_R = 12 kHz. Chemical shifts are quoted in parts per million (ppm) with respect to an 85% H_3PO_4 solution.

^{1}H, ^{13}C and ^{31}P liquid NMR spectra were recorded with a Bruker AVANCE 300 spectrometer at 300.13, 75.47 and 121.49 MHz, respectively. Deuterated chloroform ($CDCl_3$) and dimethylsulfoxide-d_6 (DMSO-d_6) were used as solvents, and tetramethylsilane or H_3PO_4 (85%) were employed as the internal references. Chemical shifts (δ) are quoted in ppm and the coupling constants (J) in Hz.

Mass spectra of octaethyl-[1,1'-biphenyl]-3,3',5,5'-tetrayltetrakis(phosphonate) (***IL*^{1}**) and octaethyl-pyrene-1,3,6,8-tetrayltetrakis(phosphonate) (***IL*^{3}**) were collected using a Micromass Q-TOF2 equipment. Dichloromethane was used as the solvent, with the employed concentration being 1 mg mL^{-1}. Samples were diluted to a concentration of 2 μL (sample)/200 μL (methanol). [1,1'-biphenyl]-3,3',5,5'-tetrayltetrakis(phosphonic acid) (**H_8btp**) and pyrene-1,3,6,8-tetrayltetrakis(phosphonic acid) (**H_8ptp**) were analyzed in a LQT Orbitrap XL mass spectrometer (Thermo Fischer Scientific, Bremen, Germany). Methanol was used as solvent.

8.2. Reagents and solvents

Chemicals, including solvents, were readily available from commercial sources and were used as received, without further purification: lanthanum(III) chloride heptahydrate ($LaCl_3 \cdot 7H_2O$, 99.9%, Sigma-Aldrich); cerium(III) chloride heptahydrate ($CeCl_3 \cdot 7H_2O$, 99.9%, Sigma-Aldrich); praseodymium(III) chloride hydrate ($PrCl_3 \cdot xH_2O$, 99.9%, Sigma-Aldrich); neodymium(III) chloride hexahydrate ($NdCl_3 \cdot 6H_2O$, 99.9%, Sigma-Aldrich); samarium(III) chloride hexahydrate ($SmCl_3 \cdot 6H_2O$, 99.9%, Sigma-Aldrich); europium(III) chloride hexahydrate ($EuCl_3 \cdot 6H_2O$, 99.9%, Sigma-Aldrich); gadolinium chloride

hexahydrate ($GdCl_3 \cdot 6H_2O$, 99.999%, Sigma-Aldrich); terbium(III) chloride hexahydrate ($TbCl_3 \cdot 6H_2O$, 99.9%, Sigma-Aldrich); dysprosium(III) chloride hexahydrate ($DyCl_3 \cdot 6H_2O$, 99.9%, Sigma-Aldrich); holmium(III) chloride hexahydrate ($HoCl_3 \cdot 6H_2O$, 99.9%, Sigma-Aldrich); erbium(III) chloride hexahydrate ($ErCl_3 \cdot 6H_2O$, 99.9%, Sigma-Aldrich); thulium(III) chloride hexahydrate ($TmCl_3 \cdot 6H_2O$, 99.99%, Sigma-Aldrich); ytterbium(III) chloride hexahydrate ($YbCl_3 \cdot 6H_2O$, 99.9%, Sigma-Aldrich); lutetium(III) chloride hexahydrate ($LuCl_3 \cdot 6H_2O$, 99.9%, Sigma-Aldrich); yttrium(III) chloride hexahydrate ($YCl_3 \cdot 6H_2O$, 99.9%, Sigma-Aldrich); copper(II) chloride dihydrate ($CuCl_2 \cdot 2H_2O$, extra pure, Riedel); 3,5-dibromophenylboronic acid ($C_6H_5BBr_2O_2$, containing varying amounts of anhydride, TCI); 1,10-phenanthroline monohydrate ($C_{12}H_{10}N_2O$, >99.0%, TCI); sodium hydroxide (NaOH, ≥98%, Sigma-Aldrich); styrene oxide (C_8H_8O, purum ≥97%, Fluka); benzaldehyde (C_7H_6O, 99%, Sigma-Aldrich); 3,3',5,5'-tetrabromo-1,1'-biphenyl ($C_{12}H_6Br_4$, 100%, Sigma-Aldrich); 1,3,6,8-tetrabromopyrene ($C_{16}H_6Br_4$, 97%, Sigma-Aldrich); oxalic acid ($C_2H_2O_4$, ≥99.0%, Sigma-Aldrich); triethyl phosphite ($C_2H_5PO_3$, 98%, Sigma-Aldrich); tetrakis(triphenylphosphine)palladium(0) ($Pd[(C_6H_5)_3P]_4$, 99%, Sigma-Aldrich); hydrochloric acid (HCl, 37%, José Manuel Gomes dos Santos Lta.); dichloromethane (CH_2Cl_2, pure, Sigma-Aldrich); methanol (CH_4O, >99.8%, Fluka or Chromasolv for HPLC, ≥99.9%, Sigma-Aldrich); *n*-hexane (C_6H_{14}, >99%, Sigma-Aldrich); propan-2-ol (C_3H_8O, 99,7%, Carlo Erba Reagents); deuterated dimethylsulfoxide (DMSO-d_6, 99,99%, Euriso-top); deuterated chloroform ($CDCl_3$, 99,99%, Euriso-top); potassium bromide (KBr for infra-red spectroscopy, > 99%, BDH SpectrosoL).

8.3. Synthesis of [1,1'-biphenyl-3,3',5,5'-tetrayltetrakis(phosphonic acid) (H_8btp)

Tetrakis(triphenylphosphine)palladium(0), [$Pd(PPh_3)_4$], (0.016 g, 0.014 mmol) and triethyl phosphite (2 mL, 12 mmol) were added to a 10 mL IntelliVent microwave reactor containing 3,3',5,5'-tetrabromo-1,1'-biphenyl (0.250 g, 0.532 mmol). The vial was placed inside a CEM Focused Microwave Synthesis System Discover S-Class equipment, pre-stirred for 1 min and then irradiated during 30 min (230 ºC; 120 W; 100 psi). A constant flow of air (*ca.* 20-30 psi of pressure) ensured a close control of the temperature inside the reactor. The resulting mixture was monitored by TLC and purified by flash column chromatography using a mixture of dichloromethane/methanol (95:5). The resulting oily

residue was washed with *n*-hexane (2 × 10 mL). Octaethyl-[1,1'-biphenyl]-3,3',5,5'-tetrayltetrakis(phosphonate) (***IL*^{1}**) was obtained as a colorless oil with a reaction yield of 95%.

A mixture composed of ***IL*^{1}** (1.42 g, 2.03 mmol) and concentrated HCl (50 mL) was refluxed under continuous magnetic stirring for approximately 24 h. After cooling to ambient temperature, distilled water was added and the solvents were evaporated under reduced pressure. The aimed compound [1,1'-biphenyl]-3,3',5,5'-tetrayltetrakis(phosphonic acid) (**H_8btp**) was washed with acetone (5 × 10 mL) and isolated as a white powder in 97% yield.

***IL*^{1}**: **^{1}H NMR** (300.13 MHz, $CDCl_3$): δ 1.37 (t, 24 H, $J(^{1}H\text{-}^{1}H)$ = 6.0 Hz, CH_3), 4.14-4.27 (m, 16 H, CH_2) and 8.18-8.30 (m, 6 H, Ar-H).

^{13}C NMR (75.47 MHz, $CDCl_3$): δ 16.4 (CH_3), 62.7 (CH_2), 130.6 (dd, ^{1}J ($^{13}C\text{-}^{31}P$) = 113.6 Hz, ^{3}J ($^{13}C\text{-}^{31}P$) = 8.7 Hz, 4 C, CPO_3Et_2), 134.1-134.5 (m, 6 C, C1, 1', 2, 2', 6 and 6') and 139.9 (t, ^{2}J ($^{13}C\text{-}^{31}P$) = 8.7 Hz, 2 C, C4 and 4').

^{31}P NMR (121.49 MHz, $CDCl_3$): δ 16.6-17.2 (m, 4 P, PO_3Et_2).

MS (TOF MS ESI^{+}) *m/z* calcd for $C_{28}H_{46}O_{12}P_4$ (M^{+}): 698.19; found: 699.1 $(M + H)^{+}$ and 721.1 $(M + Na)^{+}$.

H_8btp: **^{1}H NMR** (300.13 MHz, DMSO-d_6): δ 8.00-8.08 (m, 6 H, Ar-H).

^{13}C NMR (75.47 MHz, DMSO-d_6): δ 130.1-130.5 (m, 4 C, C2, 2', 6 and 6'), 132.0-132.2 (m, 2 C, C1 and 1'), 135.1 (dd, $^{1}J(^{13}C\text{-}^{31}P)$ = 178.5 Hz, ^{3}J ($^{13}C\text{-}^{31}P$) = 13.2 Hz, 4 C, C3, 3', 5 and 5'), 137.8 (t, ^{2}J ($^{13}C\text{-}^{31}P$) = 12.5 Hz, 2 C, C4 and 4').

^{31}P NMR (121.49 MHz, DMSO-d_6): δ 10.8 (t, 4 P, $J(^{31}P\text{-}^{1}H)$ = 13.4 Hz, PO_3H_2).

HRMS (TOF MS ESI^{-}) *m/z* calcd for $C_{12}H_{13}O_{12}P_4$ $(M - H)^{-}$: 472.93630; found: 472.93745.

8.4. Synthesis of pyrene-1,3,6,8-tetrayltetrakis(phosphonic acid) (H_8ptp)

1,3,6,8-tetrabromopyrene (0.259 g, 0.500 mmol) was transferred to a 10 mL IntelliVent microwave reactor and mixed with 2 mL of triethyl phosphite (12 mmol) and tetrakis(triphenylphosphine)palladium(0), ($[Pd(PPh_3)_4]$, (0.029 g, 0.025 mmol). The reactor was placed inside a CEM Focused Microwave Synthesis System Discover S-Class

equipment, pre-stirred for 1 min and then irradiated during 45 min (230 ºC, 120 W, 100 psi). A constant flow of air (*ca.* 20-30 psi of pressure) ensured a close control of the temperature inside the reactor. The resulting mixture was monitored by TLC and purified by flash column chromatography using a mixture of dichloromethane/methanol (95:5). The resulting yellow oil was washed with hexane (2 × 10 mL). Octaethyl-pyrene-1,3,6,8-tetrayltetrakis(phosphonate) (***IL*^{3}**) was obtained as a yellow oil with a reaction yield of 95%.

A mixture composed of ***IL*^{3}** (0.100 g, 0.134 mmol) and 6 M HCl (50 mL) was heated at 80 ºC under continuous magnetic stirring for approximately 20 h. After cooling to ambient temperature, the mixture was diluted with methanol and the solvents were evaporated under reduced pressure. The resulting yellow color viscous oily solution was washed several times with acetone and precipitated. The precipitate was filtered and dried under high vacuum. The aimed compound pyrene-1,3,6,8-tetrayltetrakis(phosphonic acid) (**H_8ptp**) was isolated as a light green powder in 90% yield.

***IL*^{3}**: **^{1}H NMR** (300.13 MHz, $CDCl_3$): δ 1.39 (t, 24 H, $J(^{1}H\text{-}^{1}H)$ = 7.5 Hz, CH_3), 4.20-4.36 (m, 16 H, CH_2), 9.19 (s, 4 H, Ar-H) and 9.28 (t, ^{3}J ($^{1}H\text{-}^{31}P$) = 15.0 Hz, 2 H, Ar-H).

^{13}C NMR (75.47 MHz, $CDCl_3$): δ 16.4 (s, 8 C, CH_3), 62.9 (s, 8 C, CH_2), 123.8 (dd, ^{1}J ($^{13}C\text{-}^{31}P$) = 186.4 Hz, ^{3}J ($^{13}C\text{-}^{31}P$) = 14.3 Hz, 4 C, CPO_3Et_2), 124.2-124.7 (m, 2 C, Ar-C), 129.2 (s, 4 C, Ar-CH), 134.8-135.2 (m, 4 C, Ar-C) and 137.2 (t, ^{2}J ($^{13}C\text{-}^{31}P$) = 10.2 Hz, 2 C, Ar-CH).

^{31}P NMR (121.49 MHz, $CDCl_3$): δ 16.8-17.2 (m, 4 P, PO_3Et_2).

MS (TOF MS ESI^{+}) *m/z* calcd for $C_{32}H_{46}O_{12}P_4$: 746.19 (M^{+}); found: 746.1 (M^{+}).

H_8ptp: **^{1}H NMR** (300.13 MHz, DMSO-d_6 and D_2O 3:1) δ (in ppm): 9.10-9.20 (m, 6 H, Ar-H).

^{13}C NMR (75.47 MHz, DMSO-d_6 and D_2O 3:1) δ (in ppm): 124.1 (t, 2 C, ^{3}J ($^{13}C\text{-}^{31}P$) = 7.5 Hz, C4), 128.6 (dd, $^{1}J(^{13}C\text{-}^{31}P)$ = 107.9 Hz, ^{3}J ($^{13}C\text{-}^{31}P$) = 7.5 Hz, 4 C, C2), 128.6 (s, 4 C, C5), 133.1-133.4 (m, 4 C, C3), 135.0 (t, ^{2}J ($^{13}C\text{-}^{31}P$) = 5.7 Hz, 2 C, C1).

^{31}P NMR (121.49 MHz, DMSO-d_6 and D_2O 3:1) δ (in ppm): 11.0 (d, 4 P, $J(^{31}P\text{-}^{1}H)$ = 14.6 Hz, PO_3H_2).

HRMS (TOF MS ESI^{-}) *m/z* calcd for $C_{16}H_{13}O_{12}P_4$ $(M - H)^{-}$: 520.94; found: 520.93729 $(M - H)^{-}$.

8.5. Synthesis of 3,3',5,5'-tetrabromobiphenyl (*IL*^{2})

A solution of [{(phen)Cu(μ-OH)}$_2$C·3H$_2$O (**cat-1**, 0.0231 g, 0.0358 mmol) and 3,5-dibromophenylboronic acid (0.500 g, 0.179 mmol) in propan-2-ol (5 mL) was stirred at ambient temperature overnight in air. The resulting grey mixture was monitored by TLC (*n*-hexane) and, once the reaction was complete, the mixture was concentrated *in vacuo*. The residue was purified by silica gel column flash chromatography (*n*-hexane) to afford 3,3',5,5'-tetrabromobiphenyl (***IL***^{2}) (0.325 g, 77%) as a white solid.[1]

IL^2: **^{1}H NMR** (300.13 MHz, $CDCl_3$) δ (in ppm): 7.60 (d, J = 3.0 Hz, 4 H, H2, 2', 6 and 6') and 7.70 (t, J = 3 Hz, 2 H, H4 and 4').

8.6. Single-Crystal X-ray Diffraction Studies

Single crystals of the materials were manually harvested from the crystallization vial and immersed in highly viscous FOMBLIN Y perfluoropolyether vacuum oil (LVAC 140/13, Sigma-Aldrich) to avoid degradation caused by the evaporation of the solvent.[2] Crystals were mounted on Hampton Research CryoLoops with the help of a Stemi 2000 stereomicroscope equipped with Carl Zeiss lenses. X-ray diffraction data were collected at 150(2) or 180(2) K on a Bruker D8 QUEST equipped with Mo Kα sealed tube (λ = 0.71073 Å), a multilayer TRIUMPH X-ray mirror, a PHOTON 100 CMOS detector, controlled by the APEX2 software package,[3] and a Oxford Instruments Cryostrem 700+ Series low temperature device.

Diffraction images were processed using the software package SAINT+,[4] and data were corrected for absorption by the multiscan semi-empirical method implemented in SADABS.[5] The crystal structure of collected compounds was solved according to the description in references [6] and [7].

8.7. Variable-temperature powder X-ray diffraction

Variable-temperature powder X-ray diffraction data were collected on a PANalytical X'Pert diffractometer Cu K$\alpha_{1,2}$ X-radiation (λ_1 = 1.540598 Å; λ_2 = 1.544426 Å) under an air atmosphere, equipped with a PIXcel 1D detector, and a flat-plate sample holder in a Bragg-Brentano para-focusing optics configuration (40 kV, 50 mA), and a

high-temperature Anton Paar HKL 16 chamber controlled by an Anton Paar 100 TCU unit. Intensity data were collected in the continuous mode (*ca.* 100 seconds data acquisition) in the angular range *ca.* $5 \leq 2\theta° \leq 35$.

8.8. Photoluminescence Spectroscopy

The photoluminescence measurements were recorded at 15 K and at ambient temperature (296 K) using a Fluorolog-2® Horiba Scientific (Model FL3-2T) spectroscope, with a modular double grating excitation spectrometer (fitted with a 1200 grooves/mm grating blazed at 330 nm) and a TRIAX 320 single emission monochromator (fitted with a 1200 grooves/mm grating blazed at 500 nm, reciprocal linear density of 2.6 nm mm^{-1}), coupled to a R928 Hamamatsu photomultiplier, using the front face acquisition mode. The excitation source was a 450 W Xe arc lamp. The emission spectra were corrected for detection and optical spectral response of the spectrofluorimeter and the excitation spectra were corrected for the spectral distribution of the lamp intensity using a photodiode reference detector. Time-resolved measurements have been carried out using a 1934D3 phosphorimeter coupled to the Fluorolog®-3, and a Xe-Hg flash lamp (6 μs/pulse half width and 20-30 μs tail) was used as the excitation source. The 15 K measurements were performed using a helium-closed cycle cryostat with vacuum system measuring ~10^{-6} mbar and a Lakeshore 330 auto-tuning temperature controller with a resistance heater.

8.9. Heterogeneous Catalysis

A 5 mL borosilicate batch reactor, equipped with a magnetic stirrer (800 rpm) and a valve for sampling, was charged with 1.5 mL of methanol, 0.4 M substrate, and the MOF catalyst (3.3 or 20 g_{MOF} L^{-1}). Substrates were styrene oxide and benzaldehyde. The catalytic performance of $[Y(H_5btp)]\cdot 2.5H_2O$ (**5**) (3.3 g_{MOF} L^{-1}) was compared to that of the ligand and metal precursors, namely, **H_8btp** and $YCl_3\cdot 6H_2O$, respectively (5.7 mM, corresponding to a molar amount equivalent to the amount of ligand or metal added together with a MOF loading of 3.3 g_{MOF} L^{-1}). Reactions were carried out under atmospheric conditions, and the batch reactors were immersed in a thermostated oil bath at 35 °C.

A leaching test was also carried out for the MOF catalyst. The experiment consisted of carrying out the reaction of styrene oxide (0.4 M) with methanol in the presence of **5** (3.3 g_{MOF} L^{-1}) at 35 °C, during 30 min. Afterward, the solid was separated from the liquid phase using a 0.20 μm PTFE membrane filter. The obtained filtrate was transferred to a preheated (35 °C) batch reactor and left to react at the same temperature under magnetic stirring.

The recyclability of the MOF catalyst was studied by carrying out consecutive batch runs (benzaldehyde as substrate). Between runs the solid catalyst was separated from the reaction mixture by centrifugation (3500 rpm), washed with methanol, and dried under air overnight.

The progress of the catalytic reactions was monitored using a Varian 3800 GC equipped with a capillary column (Bruker, BR-5, 30 m × 0.25 mm × 0.25 μm) and a flame ionization detector, and H_2 was the carrier gas. Reaction products were identified using a GC−MS (Trace GC 2000 series (Thermo Quest CE Instruments), DSQ II (Thermo Scientific)), equipped with a capillary column (DB-1 MS, 30 m × 0.25 mm × 0.25 μm), using He as carrier gas.

8.10. Protonic Conductivity

The proton conductivity (σ) of pelletized samples was determined by electrochemical impedance spectroscopy. Disk shaped samples were obtained after pressing the powders in a uniaxial press at 6.25 MPa, and then isostatically at 200 MPa. The apparent density of these pellets was obtained from measuring their weight and the geometric dimensions. Silver electrodes were applied on both sides of the pellets by painting a commercial paste (Agar Scientific). Samples were placed on ceramic tubular sample-holders inside a climatic chamber (ACS DY110) in order to carry out the measurements under variable temperature (40−94 °C) and relative humidity (RH, 20−98%). One of the pellets, noted as predried, was subjected to a premeasurement thermal treatment at 120 °C overnight. The current collection was ensured by means of platinum wires. The impedance spectra were collected between 20 Hz and 2 MHz with test signal amplitude of 100 mV using an Agilent E4980A LCR meter, and subsequently analyzed with ZView (Version 2.6b, 1990−2002, Scribner Associates). The ohmic resistance (R) of the pellets was normalized to the geometry of the

samples in order to calculate the conductivity through the usual formula $\sigma = L(RA)^{-1}$, where *L* is the thickness of the pellets and A is the surface area of the electrodes.

8.11. Microwave-assisted synthesis of LnOFs

$[Ln_4(H_6btp)_2(H_4btp)_2(H_8btp)(H_2O)_{16}]\cdot 12H_2O$ (1-3): A reactive mixture composed of 0.025 g of [1,1'-biphenyl]-3,3',5,5'-tetrayltetrakis(phosphonic acid) (**H_8btp**) and 0.0783 g of $LaCl_3\cdot 7H_2O$, with an overall molar ratio of approximately 1:4 (H_8btp : La^{3+}), was dissolved at ambient temperature in a mixture of distilled water, HCl (6M) and methanol (2 mL of each solvent), and placed inside a 10 mL IntelliVent microwave reactor. The reaction took place inside a CEM Focused Microwave Synthesis System Discover S-Class equipment, under constant magnetic stirring (controlled by the microwave equipment), at 100 ºC for 60 min (using an irradiation power of 50 W). A constant flow of air (*ca.* 20-30 psi of pressure) ensured a close control of the temperature inside the reactor. After irradiation, the reactor with the homogeneous solution was kept sealed and left motionless for 7 days. This methodology successfully led to the preparation of $[La_4(H_6btp)_2(H_4btp)_2(H_8btp)(H_2O)_{16}]\cdot 12H_2O$ (**1**) as a white microcrystalline powder. The resulting product was recovered by vacuum filtration, washed with copious amounts of distilled water and then air-dried at ambient temperature.

The isotypical materials with 10% of Eu^{3+} (**2**) and Tb^{3+} (**3**) were prepared as described above for compound **1** while adjusting the amounts of the lanthanide chloride salts in the initial reactive mixture to the desired percentages. After irradiation, the reactors with the homogeneous solutions were uncapped and left motionless until *ca.* 2/3 of the reaction mixture volume had evaporated.

Elemental CH composition (%):

Calcd for **1**: C 21.1; H 3.36. Found: C 19.8; H 3.63.

Calcd for **2**: C 21.1; H 3.36. Found: C 20.4; H 3.33.

Calcd for **3**: C 21.0; H 3.35. Found: C 21.1; H 3.57.

Thermogravimetric analysis (TGA) data (weight losses in %) and derivative thermogravimetric peaks (DTG, in italics inside the parentheses):

1: 30-150 ºC -14.9% (*90 ºC*); 150-800 ºC -32.6% (*473 ºC*). Total loss: 47.5%.

2: 30-150 ºC -16.1% (*88 ºC*); 150-800 ºC -29.7% (*487 ºC*). Total loss: 45.8%.

3: 30-150 ºC -14.9% (*85 ºC*); 150-800 ºC -32.8% (*488 ºC*). Total loss: 47.7%.

Selected FT-IR data (in cm^{-1}; from KBr pellets):

1: $\nu(H_2O + POH)$ = 3650-2900*br*; $\nu(C=C) + \delta(H_2O)$ = 1830-1500*m*; $\nu(P=O)$ = 1360-1020*vs*; $\nu(P–O)$ = 1020-800*vs*; $\nu(P–C)$ = 695*m*.

2: $\nu(H_2O + POH)$ = 3650-2940*br*; $\nu(C=C) + \delta(H_2O)$ = 1780-1500*m*; $\nu(P=O)$ = 1260-1020*vs*; $\nu(P–O)$ = 1020-800*vs*; $\nu(P–C)$ = 695*m*.

3: $\nu(H_2O + POH)$ = 3650-2970*br*; $\nu(C=C) + \delta(H_2O)$ = 1790-1530*m*; $\nu(P=O)$ = 1280-1015*vs*; $\nu(P–O)$ = 1015-790*vs*; $\nu(P–C)$ = 695*m*.

$[Ln_7(H_5btp)_5(H_6btp)_3(H_2O)_{12}]\cdot 23.5H_2O\cdot MeOH$ (15 and 16): Reactive mixtures composed of the respective lanthanide(III) chloride hydrates [$LnCl_3\cdot 6H_2O$, where Ln^{3+} = Eu^{3+} (**15**) and Gd^{3+} (**16**)] and 0.025 g of [1,1'-biphenyl]-3,3',5,5'-tetrayltetrakis(phosphonic acid) (**H_8btp**), with an overall molar ratio of approximately 1:4 (H_8btp : Ln^{3+}), were individually prepared at ambient temperature in a mixture of distilled water, HCl (6 M) and methanol (2 mL each solvent), and placed inside a 10 mL IntelliVent microwave reactor. The reaction took place inside a CEM Focused Microwave Synthesis System Discover S-Class equipment, under constant magnetic stirring (controlled by the microwave equipment), at 100 ºC for 60 min (using an irradiation power of 50 W). A constant flow of air (*ca.* 20-30 psi of pressure) ensured a close control of the temperature inside the reactor. After irradiation, the reactors with the homogeneous solutions were uncapped and left motionless until *ca.* 3/4 of the reaction mixture volume had evaporated. This methodology successfully led to the preparation of $[Ln_7(H_5btp)_5(H_6btp)_3(H_2O)_{12}]\cdot 23.5H_2O\cdot MeOH$ (**15** and **16**) materials as a white crystalline needles. The resulting compounds were recovered by vacuum filtration, washed with copious amounts of distilled water and then air-dried at ambient temperature.

Elemental CH composition (%):

Calcd for **15**: C 21.0; H 3.01. Found: C 19.9; H 3.02.

Thermogravimetric analysis (TGA) data (weight losses in %) and derivative thermogravimetric peaks (DTG, in italics inside the parentheses):

16: 25-100 ºC -6.4% (*54 ºC*); 100-250 ºC -7.4% (*144 ºC*); 250-440 ºC -6.4% (*435 ºC*); 440-800 ºC -20.1% (*453 ºC*).

Selected FT-IR data (in cm^{-1}; from KBr pellets):

16: $\nu(H_2O + POH)$ = 3600-2800*br*; $\nu(C=C) + \delta(H_2O)$ = 1745-1560*m*; $\nu(P=O)$ = 1300-1070*vs*; $\nu(P–O)$ = 1070-830*vs*; $\nu(P–C)$ = 695*m*.

8.12. Microwave-assisted synthesis of Yttrium-based MOFs

[Y(H$_5$btp)]·5.5H$_2$O (4): a reactive mixture composed of 0.025 g of [1,1'-biphenyl]-3,3',5,5'-tetrayltetrakis(phosphonic acid) (**H$_8$btp**) and 0.016 g of $YCl_3 \cdot 6H_2O$, with an overall molar ratio of approximately 1 : 1 (H_8btp : Y^{3+}), was dissolved at ambient temperature in a mixture of distilled water, HCl (6M) and methanol (2 mL of each solvent), and placed inside a 10 mL IntelliVent microwave reactor. The reaction took place inside a CEM Focused Microwave Synthesis System Discover S-Class equipment, under constant magnetic stirring (controlled by the microwave equipment), at 100 ºC for 60 min (using an irradiation power of 50 W). A constant flow of air (*ca.* 20-30 psi of pressure) ensured a close control of the temperature inside the reactor. The resulting product, [Y(H_5btp)]·5.5H_2O (**4**), was isolated as a white microcrystalline powder in suspension. Recovery by vacuum filtration was not possible since the material was only stable while in solution.

The optimal synthetic conditions (100 ºC; 60 min) were found by systematically varying the microwave parameters such as temperature (40, 60, 80, 100 and 135 ºC) and irradiation time (1, 5, 15, 30 and 60 min). The irradiation power was maintained constant at 50 W.

[Y(H$_5$btp)]·2.5H$_2$O (5): this material was obtained after filtration of [Y(H_5btp)]·5.5H_2O (**4**) under reduced pressure. The white powder was washed with copious amounts of distilled water and then air-dried at ambient temperature.

Elemental CH composition (%): Calcd: C 23.8; H 2.67. Found: C 23.9; H 2.70.

Thermogravimetric analysis (TGA) data (weight losses in %) and derivative thermogravimetric peaks (DTG, in italics inside the parentheses): 28-100 ºC -4.51% (*59 ºC*); 100-144 ºC -1.52% (*131 ºC*); 144-250 ºC -1.47% (*235 ºC*); 250-310 ºC -1.35% (*293 ºC*); 310-350 ºC -1.36% (*332 ºC*). Total loss: 10.2%.

Selected FT-IR data (in cm^{-1}; from KBr pellets): ν(H_2O_{cryst} + POH + C–H) = 3600-2650*br*; ν(C=C) + δ(H_2O) = 1860-1560*m*; ν(P=O) = 1265-1120*vs*; ν(P–O) = 1120-860*vs*; ν(P–C) = 697*m*.

(H$_3$O)[Y$_2$(H$_5$btp)(H$_4$btp)]·H$_2$O (6): this material was obtained from the dehydration of [Y(H_5btp)]·2.5H_2O (**5**). Compound **5** (0.025 g) was placed into an open crucible inside an

oven, pre-heated at 110 ºC, and dehydrated overnight. The resulting white powder was recovered and cooled to ambient temperature.

Elemental CH composition (%): Calcd: C 24.9; H 2.27. Found: C 24.9; H 2.27.

Thermogravimetric analysis (TGA) data (weight losses in %) and derivative thermogravimetric peaks (DTG, in italics inside the parentheses): 22-190 ºC -3.24% (*135 ºC*); 190-255 ºC -1.68% (*240 ºC*); 255-350 ºC -1.73% (*282 ºC*). Total loss: 6.7%.

Selected FT-IR data (in cm^{-1}; from KBr pellets): $\nu(H_3O^+)$ = 3505*s*; $\nu(H_2O_{cryst})$ = 3375*m*; ν(POH) = 3250*m*; ν(C–H) = 3075*m*; ν(C=C) + $\delta(H_2O)$ = 1810-1575*m*; ν(P=O) = 1280-1120*m-vs*; ν(P–O) = 1120-860*vs*; ν(P–C) = 696*m*.

[Y(H_5btp)]·H_2O·0.5(MeOH) (7): 0.025 g of $(H_3O)[Y_2(H_5btp)(H_4btp)]\cdot H_2O$ (**6**) were placed in a round bottom flask with 1 mL of methanol. The mixture was vigorously stirred during 1 h at ambient temperature. The resulting $[Y(H_5btp)]\cdot H_2O\cdot 0.5$(MeOH) (**7**) compound was recovered by vacuum filtration as a white powder and then air-dried at ambient temperature.

Elemental CH composition (%): Calcd: C 25.3; H 2.55. Found: C 24.7; H 2.02.

Thermogravimetric analysis (TGA) data (weight losses in %) and derivative thermogravimetric peaks (DTG, in italics inside the parentheses): 23-70 ºC -2.57% (*57 ºC*); 70-190 ºC -2.81% (*140 ºC*); 190-255 ºC -1.52% (*242 ºC*); 255-350 ºC -1.77% (*290 ºC*). Total loss: 8.7%.

Selected FT-IR data (in cm^{-1}; from KBr pellets): $\nu(H_2O_{cryst}$ + POH) = 3600-2670*br*; ν(C=C) + $\delta(H_2O)$ = 1705-1580*m*; ν(P=O) = 1265-1120*vs*; ν(P–O) = 1120-870*vs*; ν(P–C) = 697*m*.

8.13. Hydro(solvo)thermal synthesis of LnOFs

[Ln(H_5btp)]·$2H_2O$ (8-13): Reactive mixtures composed of the respective lanthanide(III) chloride hydrates [$LnCl_3\cdot 6H_2O$, where Ln^{3+} = Gd^{3+} (**8**), Tb^{3+} (**9**), Dy^{3+} (**10**), Ho^{3+} (**11**), Er^{3+} (**12**) and Tm^{3+} (**13**)] and 0.025 g of [1,1'-biphenyl]-3,3',5,5'-tetrayltetrakis(phosphonic acid) (H_8btp), with an overall molar ratio of approximately 1:4 (H_8btp : Ln^{3+}), were individually prepared in a mixture of distilled water, HCl (6 M) and methanol (2 mL each solvent). Mixtures were kept under constant magnetic stirring in open air and ambient temperature for approximately 15 min. The resulting homogeneous suspensions were

transferred to Teflon-lined Parr Instrument reaction vessels and placed inside a MMM Venticell oven. The heating program included: i) heating during 48 h up to 140 ºC; ii) 24 h uphold of the temperature (140 ºC); iii) cooling during 48 h until ambient temperature. The resulting materials were isolated as white microcrystalline powders, recovered by vacuum filtration, washed with abundant amounts of distilled water and dried at ambient temperature.

Elemental CH composition (%):

Calcd for **8**: C 21.7; H 2.28. Found: C 22.1; H 2.44.

Calcd for **9**: C 21.6; H 2.27. Found: C 21.2; H 2.36.

Calcd for **10**: C 21.5; H 2.26. Found: C 22.0; H 2.41.

Calcd for **11**: C 21.4; H 2.25. Found: C 21.5; H 2.35.

Calcd for **12**: C 21.4; H 2.24. Found: C 21.5; H 2.37.

Calcd for **13**: C 21.3; H 2.24. Found: C 21.6; H 2.10.

Thermogravimetric analysis (TGA) data (weight losses in %) and derivative thermogravimetric peaks (DTG, in italics inside the parentheses):

8: 25-250 ºC -3.82% (*72 ºC*); 250-670 ºC -4.61% (*355 ºC*); 670-890ºC-6.66% (*835 ºC*); 890-1200 ºC-13.91% (*951ºC*). Total loss: 29.0%.

9: 25-245 ºC -4.83% (*67 ºC*); 245-650 ºC -6.05% (*353 ºC*); 650-867 ºC -7.69% (*838 ºC*); 867-1200 ºC -12.37% (*945ºC*). Total loss: 30.9%.

10: 25-220 ºC -5.11% (*69 ºC*); 220-650 ºC -5.97% (*349 ºC*); 650-865 ºC -5.79% (*841 ºC*); 865-921 ºC -4.76% (*897 ºC*); 921-1200 ºC -15.47% (*948ºC*). Total loss: 37.1%.

11: 25-230 ºC -4.53% (*65 ºC*); 230-650 ºC -6.01% (*354 ºC*); 650-835 ºC -3.77% (*825 ºC*); 835-937 ºC -11.90% (*920 ºC*); 937-1200 ºC -7.68% (*950ºC*). Total loss: 33.9%.

12: 25-245 ºC -5.57% (*70 ºC*); 245-650 ºC -6.32% (*355 ºC*); 650-865ºC-6.11% (*835 ºC*); 865-1200 ºC-17.53% (*951ºC*). Total loss: 35.5%.

Selected FT-IR data (in cm^{-1}; from KBr pellets):

8: $\nu(H_2O_{cryst}$ + POH + C–H) = 3550-2540*br*; ν(C=C) + $\delta(H_2O)$ = 1720-1560*m*; ν(P=O) = 1230-1040*vs*; ν(P–O) = 965-845*vs*; ν(P–C) = 696*m*.

9: $\nu(H_2O_{cryst}$ + POH + C–H) = 3590-2490*br*; ν(C=C) + $\delta(H_2O)$ = 1720-1560*m*; ν(P=O) = 1260-975*vs*; ν(P–O) = 975-860*vs*; ν(P–C) = 697*m*.

10: $\nu(H_2O_{cryst}$ + POH + C–H) = 3565-2500*br*; ν(C=C) + $\delta(H_2O)$ = 1710-1575*m*; ν(P=O) = 1230-975*vs*; ν(P–O) = 975-840*vs*; ν(P–C) = 697*m*.

11: $\nu(H_2O_{cryst}$ + POH) = 3535-2510*br*; ν(C=C) + $\delta(H_2O)$ = 1700-1580*m*; ν(P=O) = 1230-1015*vs*; ν(P–O) = 970-860*vs*; ν(P–C) = 698*m*.

12: $\nu(H_2O_{cryst}$ + POH) = 3580-2500*br*; ν(C=C) + $\delta(H_2O)$ = 1690-1570*m*; ν(P=O) = 1235-1015*vs*; ν(P–O) = 978-865*vs*; ν(P–C) = 698*m*.
13: $\nu(H_2O_{cryst}$ + POH) = 3525-2500*br*; ν(C=C) + $\delta(H_2O)$ = 1710-1570*m*; ν(P=O) = 1270-975*vs*; ν(P–O) = 975-835*vs*; ν(P–C) = 697*m*.

[Tb(L_2)] (14): this material was obtained from the dehydration of [Tb(H_5btp)]·$2H_2O$ (**9**). Compound **9** (5.0 mg) was placed into an open crucible inside an oven, preheated at 400 ºC, and dehydrated overnight. The resulting light-brown powder was recovered and cooled to ambient temperature.
Selected FT-IR data (in cm^{-1}; from KBr pellets): ν(C–H) = 3090-3015*vs*; ν(C=C) = 1625-1570*vs*; ν(P=O) = 1260-1030*vs*; ν(P–O) + ν(P–O–P) = 1055-930*vs*; ν(P–C) = 695*m*.

[Ln_4(H_3btp)(H_4btp)(H_5btp)($H_2O)_8$]·$3H_2O$ (17-19): Reactive mixtures composed of the respective lanthanide(III) chloride hydrates [$LnCl_3$·$6H_2O$, where Ln^{3+} = Ce^{3+} (**17**), Pr^{3+} (**18**), and Nd^{3+} (**19**)] and 0.025 g of [1,1'-biphenyl]-3,3',5,5'-tetrayltetrakis(phosphonic acid) (H_8btp), with an overall molar ratio of approximately 1:4 (H_8btp : Ln^{3+}), were individually prepared in a mixture of distilled water, HCl (6 M) and methanol (2 mL each solvent). Mixtures were kept under constant magnetic stirring in open air and ambient temperature for approximately 15 min. The resulting homogeneous suspensions were transferred to Teflon-lined Parr Instrument reaction vessels and placed inside a MMM Venticell oven. The heating program included: i) heating during 48 h up to 140 ºC; ii) 24 h uphold of the temperature (140 ºC); iii) cooling during 48 h until ambient temperature. The resulting materials were isolated as white microcrystalline powders, recovered by vacuum filtration, washed with abundant amounts of distilled water and dried at ambient temperature.
Elemental CH composition (%):
Calcd for **17**: C 19.9; H 2.42. Found: C 21.0; H 2.47.
Calcd for **18**: C 19.9; H 2.41. Found: C 20.7; H 2.37.
Calcd for **19**: C 19.8; H 2.40. Found: C 20.7; H 2.41.
Thermogravimetric analysis (TGA) data (weight losses in %) and derivative thermogravimetric peaks (DTG, in italics inside the parentheses):
17: 25-200 ºC -18.05% (*110 ºC*); 200-400 ºC -5.98% (*271 ºC*). Total loss: 24.0%.
18: 25-122 ºC -10.13% (*109 ºC*); 122-200 ºC -5.60% (*135 ºC*); 200-294 ºC -6.05% (*270 ºC*); 294-400 ºC -6.51% (*324ºC*). Total loss: 28.3%.

19: 25-133 ºC -12.78% (*108 ºC*); 133-205 ºC -5.92% (*144 ºC*); 205-367 ºC -6.58% (*281 ºC*). Total loss: 25.3%.

Selected FT-IR data (in cm^{-1}; from KBr pellets):

17: $\nu(H_2O + POH)$ = 3600-2550*br*; $\nu(C=C) + \delta(H_2O)$ = 1700-1570*m*; $\nu(P=O)$ = 1270-1060*vs*; $\nu(P–O)$ = 945-840*vs*; $\nu(P–C)$ = 696*m*.

18: $\nu(H_2O + POH)$ = 3610-2570*br*; $\nu(C=C) + \delta(H_2O)$ = 1715-1540*m*; $\nu(P=O)$ = 1245-1070*vs*; $\nu(P–O)$ = 945-850*vs*; $\nu(P–C)$ = 696*m*.

19: $\nu(H_2O + POH)$ = 3625-2565*br*; $\nu(C=C) + \delta(H_2O)$ = 1695-1560*m*; $\nu(P=O)$ = 1245-1070*vs*; $\nu(P–O)$ = 940-850*vs*; $\nu(P–C)$ = 696*m*.

$[Ln_2(H_4ptp)(ox)(H_2O)_6]\cdot 5H_2O$ (20-27): Reactive mixtures composed of the respective lanthanide(III) chloride hydrate [$LnCl_3\cdot 6H_2O$, where Ln^{3+} = Ce^{3+} (**20**), Pr^{3+} (**21**), Nd^{3+} (**22**), Sm^{3+} (**23**), Eu^{3+} (**24**), Gd^{3+} (**25**), Tb^{3+} (**26**) and Dy^{3+} (**27**)], 0.030 g of pyrene-1,3,6,8-tetrayltetrakis(phosphonic acid) (**H_8ptp**) and oxalic acid (H_2ox), with an overall molar ratio of approximately 1:2:2 (**H_8ptp** : H_2ox : Ln^{3+}), were prepared in distilled water (6 mL) at ambient temperature. The mixtures were kept under constant magnetic stirring in open air for approximately 15 min. Then the suspensions were transferred to Teflon-lined Parr Instrument reaction vessels and placed inside a MMM Venticell oven. The selected heating program included: i) heating during 48 h up to 140 ºC; ii) 24 h uphold of the temperature (140 ºC); iii) cooling during 48 h until ambient temperature. The resulting materials were isolated as pale green microcrystalline powders, recovered by vacuum filtration, washed with abundant amounts of distilled water and dried at ambient temperature.

Elemental CH composition (%):

Calcd for **20**: C 20.0; H 2.79. Found: C 20.5; H 2.84.

Calcd for **21**: C 19.9; H 2.79. Found: C 19.8; H 3.08.

Calcd for **22**: C 19.8; H 2.77. Found: C 18.9; H 2.69.

Calcd for **23**: C 19.6; H 2.74. Found: C 19.3; H 2.65.

Calcd for **24**: C 19.5; H 2.73. Found: C 19.7; H 2.63.

Calcd for **25**: C 19.4; H 2.71. Found: C 19.7; H 2.61.

Calcd for **26**: C 19.3; H 2.70. Found: C 19.4; H 2.62.

Calcd for **27**: C 19.2; H 2.68. Found: C 19.6; H 2.39.

Thermogravimetric analysis (TGA) data (weight losses in %) and derivative thermogravimetric peaks (DTG, in italics inside the parentheses):

20: 25-200 ºC -18.05% (*110 ºC*); 200-400 ºC -5.98% (*271 ºC*). Total loss: 24.0%.

21: 25-122 ºC -10.13% (*109 ºC*); 122-200 ºC -5.60% (*135 ºC*); 200-294 ºC -6.05% (*270 ºC*); 294-400 ºC -6.51% (*324 ºC*). Total loss: 28.3%.

22: 25-133 ºC -12.78% (*108 ºC*); 133-205 ºC -5.92% (*144 ºC*); 205-367 ºC -6.58% (*281 ºC*). Total loss: 25.3%.

23: 25-144 ºC -10.30% (*120 ºC*); 144-200 ºC -5.08% (*166 ºC*); 144-370 ºC -7.00% (*279 ºC*). Total loss: 22.4%.

24: 25-55 ºC -1.07% (*43 ºC*); 55-132 ºC -10.35% (*108 ºC*); 132-215 ºC -6.08% (*155 ºC*); 215-400 ºC -6.38% (*282 ºC*). Total loss: 23.9%.

25: 25-140 ºC -11.10% (*111 ºC*); 140-200 ºC -5.41% (*161 ºC*); 200-380 ºC -6.34% (*273 ºC*); 380-608 ºC -8.60% (*509 ºC*). Total loss: 31.5%.

26: 25-128 ºC -11.44% (*111 ºC*); 128-197 ºC -6.35% (*158 ºC*); 197-380 ºC -7.70% (*286 ºC*). Total loss: 25.5%.

27: 25-137 ºC -10.74% (*114 ºC*); 137-220 ºC -5.55% (*157 ºC*); 220-430 ºC -7.06% (*289 ºC*). Total loss: 23.4%.

Selected FT-IR data (in cm^{-1}; from KBr pellets):

20: $\nu(H_2O + POH)$ = 3600-3050*br*; $\nu(C=O) + \nu(C=C) + \delta(H_2O)$ = 1700-1570*s*; $\nu(P=O)$ = 1280-1110*vs*; $\nu(P–O)$ = 1040-880*vs*; $\nu(P–C)$ = 740*m*; $\nu(–CO_2^-)$ = 635-475*m*.

21: $\nu(H_2O + POH)$ = 3635-3020*br*; $\nu(C=O) + \nu(C=C) + \delta(H_2O)$ = 1700-1560*s*; $\nu(P=O)$ = 1280-1040*vs*; $\nu(P–O)$ = 1040-875*vs*; $\nu(P–C)$ = 738*m*; $\nu(–CO_2^-)$ = 645-450*m*.

22: $\nu(H_2O + POH)$ = 3650-3015*br*; $\nu(C=O) + \nu(C=C) + \delta(H_2O)$ = 1705-1560*s*; $\nu(P=O)$ = 1270-1060*vs*; $\nu(P–O)$ = 1060-880*vs*; $\nu(P–C)$ = 742*m*; $\nu(–CO_2^-)$ = 645-455*m*.

23: $\nu(H_2O + POH)$ = 3630-3020*br*; $\nu(C=O) + \nu(C=C) + \delta(H_2O)$ = 1705-1570*s*; $\nu(P=O)$ = 1265-1110*vs*; $\nu(P–O)$ = 1040-860*vs*; $\nu(P–C)$ = 741*m*; $\nu(–CO_2^-)$ = 645-455*m*.

24: $\nu(H_2O + POH)$ = 3650-3015*br*; $\nu(C=O) + \nu(C=C) + \delta(H_2O)$ = 1705-1565*s*; $\nu(P=O)$ = 1285-1065*vs*; $\nu(P–O)$ = 1045-875*vs*; $\nu(P–C)$ = 739*m*; $\nu(–CO_2^-)$ = 650-450*m*.

25: $\nu(H_2O + POH)$ = 3660-3015*br*; $\nu(C=O) + \nu(C=C) + \delta(H_2O)$ = 1710-1575*s*; $\nu(P=O)$ = 1280-1110*vs*; $\nu(P–O)$ = 1035-875*vs*; $\nu(P–C)$ = 742*m*; $\nu(–CO_2^-)$ = 645-455*m*.

26: $\nu(H_2O + POH)$ = 3640-3020*br*; $\nu(C=O) + \nu(C=C) + \delta(H_2O)$ = 1705-1575*s*; $\nu(P=O)$ = 1275-1115*vs*; $\nu(P–O)$ = 1040-885*vs*; $\nu(P–C)$ = 742*m*; $\nu(–CO_2^-)$ = 645-455*m*.

27: $\nu(H_2O + POH)$ = 3630-3040*br*; $\nu(C=O) + \nu(C=C) + \delta(H_2O)$ = 1705-1570*s*; $\nu(P=O)$ = 1280-1110*vs*; $\nu(P–O)$ = 1040-875*vs*; $\nu(P–C)$ = 741*m*; $\nu(–CO_2^-)$ = 640-455*m*.

$[Ln_2(H_4ptp)(ox)(H_2O)_6]\cdot H_2O$ (28-33): Reactive mixtures composed of the respective lanthanide(III) chloride hydrate [$LnCl_3\cdot 6H_2O$, where Ln^{3+} = Ho^{3+} (**28**), Er^{3+} (**29**), Tm^{3+}

(**30**), Yb^{3+} (**31**), Lu^{3+} (**32**) and Y^{3+} (**33**)], 0.030 g of pyrene-1,3,6,8-tetrayltetrakis(phosphonic acid) (**H_8ptp**) and oxalic acid (H_2ox), with an overall molar ratio of approximately 1:2:2 (**H_8ptp** : H_2ox : Ln^{3+}), were prepared in distilled water (6 mL) at ambient temperature. The mixtures were kept under constant magnetic stirring in open air for approximately 15 min. Then the suspensions were transferred to Teflon-lined Parr Instrument reaction vessels and placed inside a MMM Venticell oven pre-heated at 140ºC. The vessels were heated during 5 days at 140 ºC, under autogenous pressure, then removed from the oven and allowed to cool until room temperature (≈ 30 ºC). The resulting materials were isolated as pale green microcrystalline powders, recovered by vacuum filtration, washed with abundant amounts of distilled water and dried at ambient temperature.

Elemental CH composition (%):

Calcd for **28**: C 20.4; H 2.09. Found: C 20.6; H 2.07.

Calcd for **29**: C 20.3; H 2.08. Found: C 20.7; H 2.50.

Calcd for **30**: C 20.2; H 2.08. Found: C 20.5; H 2.42.

Calcd for **31**: C 20.1; H 2.06. Found: C 20.1; H 2.30.

Calcd for **32**: C 20.0; H 2.05. Found: C 18.1; H 2.35.

Calcd for **33**: C 23.8; H 2.44. Found: C 23.0; H 2.72.

Thermogravimetric analysis (TGA) data (weight losses in %) and derivative thermogravimetric peaks (DTG, in italics inside the parentheses):

28: 25-200 ºC -10.98% (*115 ºC*); 200-800 ºC -16.02% (*382 ºC*). Total loss: 27.0%.

29: 25-255 ºC -10.66% (*111 ºC*); 255-800 ºC -17.26% (*397 ºC*). Total loss: 27.9%.

30: 25-250 ºC -11.36% (*113 ºC*); 250-800 ºC -16.03% (*414 ºC*). Total loss: 27.4%.

31: 25-260 ºC -10.71% (*106 ºC*); 260-800 ºC -12.92% (*417 ºC*). Total loss: 23.6%.

32: 25-230 ºC -11.47% (*106ºC*); 230-452 ºC -6.80% (*400 ºC*); 452-800 ºC -8.11% (*510 ºC*). Total loss: 26.4%.

33: 25-240 ºC -12.40% (*123 ºC*); 240-422 ºC -6.39% (*380 ºC*); 422-800 ºC -14.80% (*503 ºC*). Total loss: 33.6%.

Selected FT-IR data (in cm^{-1}; from KBr pellets):

28: ν(H_2O + POH) = 3620-3025*br*; ν(C=O) + ν(C=C) + δ(H_2O) = 1700-1570*s*; ν(P=O) = 1240-1110*vs*; ν(P–O) = 1110-890*vs*; ν(P–C) = 746*m*; ν($–CO_2^-$) = 645-455*m*.

29: ν(H_2O + POH) = 3615-3035*br*; ν(C=O) + ν(C=C) + δ(H_2O) = 1700-1575*s*; ν(P=O) = 1230-1110*vs*; ν(P–O) = 1110-885*vs*; ν(P–C) = 747*m*; ν($–CO_2^-$) = 645-460*m*.

30: $\nu(H_2O + POH)$ = 3615-2990*br*; $\nu(C=O) + \nu(C=C) + \delta(H_2O)$ = 1700-1570*s*; $\nu(P=O)$ = 1230-1110*vs*; $\nu(P–O)$ = 1110-895*vs*; $\nu(P–C)$ = 747*m*; $\nu(–CO_2^-)$ = 640-470*m*.

31: $\nu(H_2O + POH)$ = 3610-3015*br*; $\nu(C=O) + \nu(C=C) + \delta(H_2O)$ = 1695-1575*s*; $\nu(P=O)$ = 1220-1115*vs*; $\nu(P–O)$ = 1115-905*vs*; $\nu(P–C)$ = 748*m*; $\nu(–CO_2^-)$ = 640-460*m*.

32: $\nu(H_2O + POH)$ = 3615-3020*br*; $\nu(C=O) + \nu(C=C) + \delta(H_2O)$ = 1700-1570*s*; $\nu(P=O)$ = 1235-1115*vs*; $\nu(P–O)$ = 1115-895*vs*; $\nu(P–C)$ = 749*m*; $\nu(–CO_2^-)$ = 640-460*m*.

33: $\nu(H_2O + POH)$ = 3615-3010*br*; $\nu(C=O) + \nu(C=C) + \delta(H_2O)$ = 1700-1570*s*; $\nu(P=O)$ = 1230-1115*vs*; $\nu(P–O)$ = 1115-895*vs*; $\nu(P–C)$ = 747*m*; $\nu(–CO_2^-)$ = 640-460*m*.

8.14. References

(1) Kirai, N.; Yamamoto, Y.; *Eur. J. Org. Chem.*, **2009**, 1864.

(2) Kottke, T.; Stalke, D.; *J. Appl. Crystallogr.*, **1993**, *26*, 615.

(3) APEX2; *Data Collection Software Version 2.1-RC13, Bruker AXS, Delft, The Netherlands*, **2006**.

(4) SAINT+; *Data Integration Engine v. 8.27b*©, **1997-2012**, Bruker AXS.

(5) Sheldrick, G. M.; *SADABS 2012/1, Bruker AXS Area Detector Scaling and Absorption Correction* **2012**, Bruker AXS.

(6) Firmino, A. D. G.; Mendes, R. F.; Ananias, D.; Vilela, S. M. F.; Carlos, L. D.; Tome, J. P. C.; Rocha, J.; Paz, F. A. A.; *Inorg. Chim. Acta*, **2017**, *455*, 584.

(7) Firmino, A. D. G.; Mendes, R. F.; Antunes, M. M.; Barbosa, P. C.; Vilela, S. M. F.; Valente, A. A.; Figueiredo, F. M. L.; Tome, J. P. C.; Paz, F. A. A.; *Inorg. Chem.*, **2017**, *56*, 1193.

Appendices

Appendix A

A. Chapter 2: Synthesis of Tetrapodal Phosphonate Organic Ligands

A.1. NMR Spectroscopy and Mass Spectrometry

1. Octaethyl-[1,1'-biphenyl]-3,3',5,5'-tetrayltetrakis(phosphonate) (***IL*^{1}**)

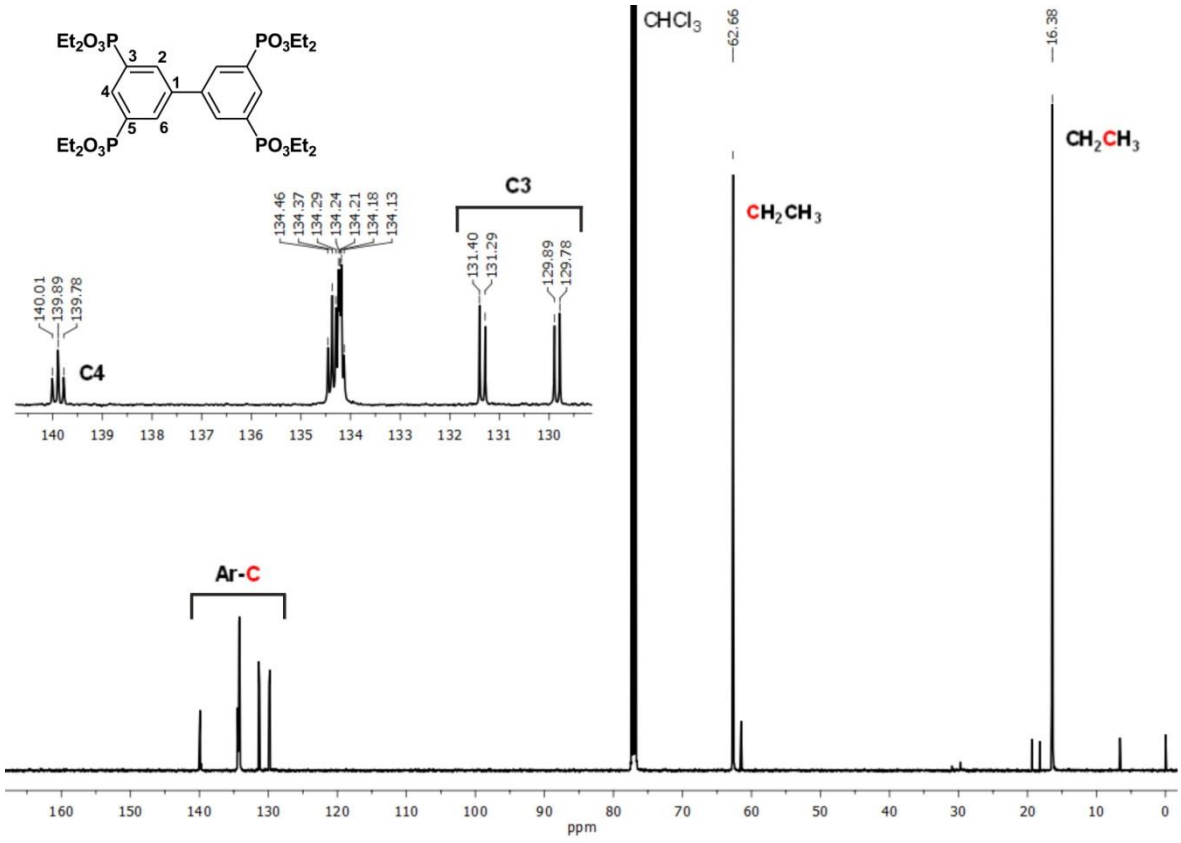

Figure A.1.1. ^{13}C NMR spectrum of the intermediate compound octaethyl-[1,1'-biphenyl]-3,3',5,5'-tetrayltetrakis(phosphonate) (*IL*^{1}) in $CDCl_3$.

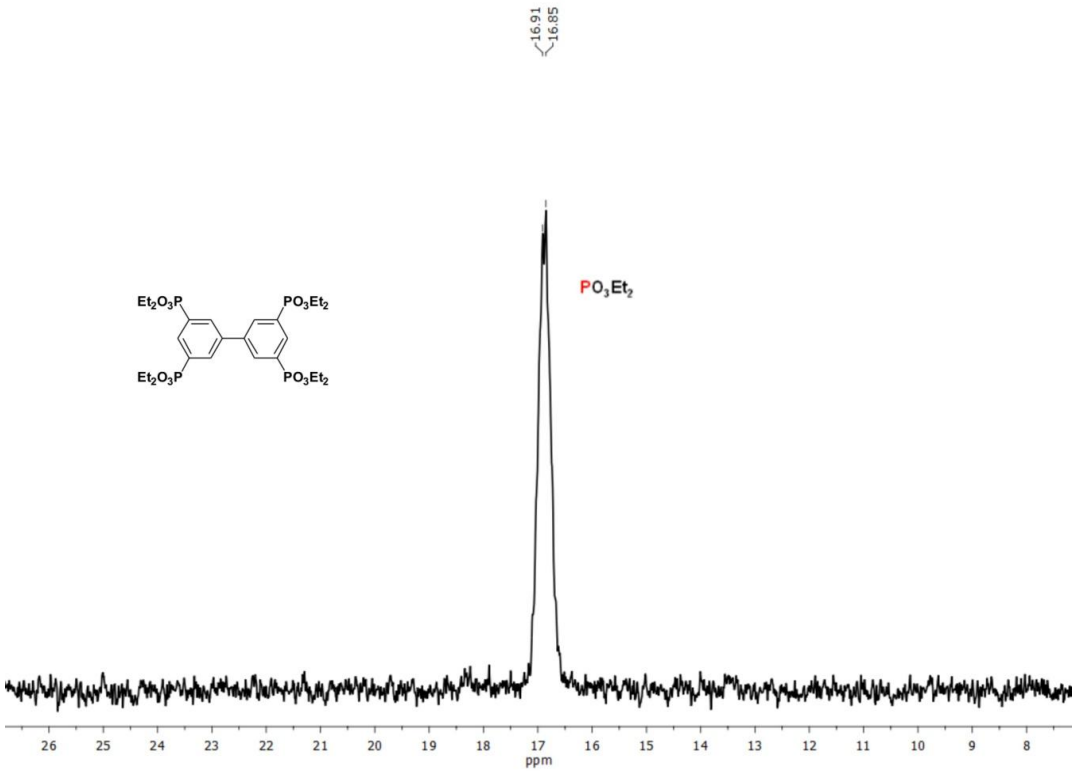

Figure A.1.2. ^{31}P NMR spectrum of the intermediate compound octaethyl-[1,1'-biphenyl]-3,3',5,5'-tetrayltetrakis(phosphonate) (***IL*^{1}**) in $CDCl_3$.

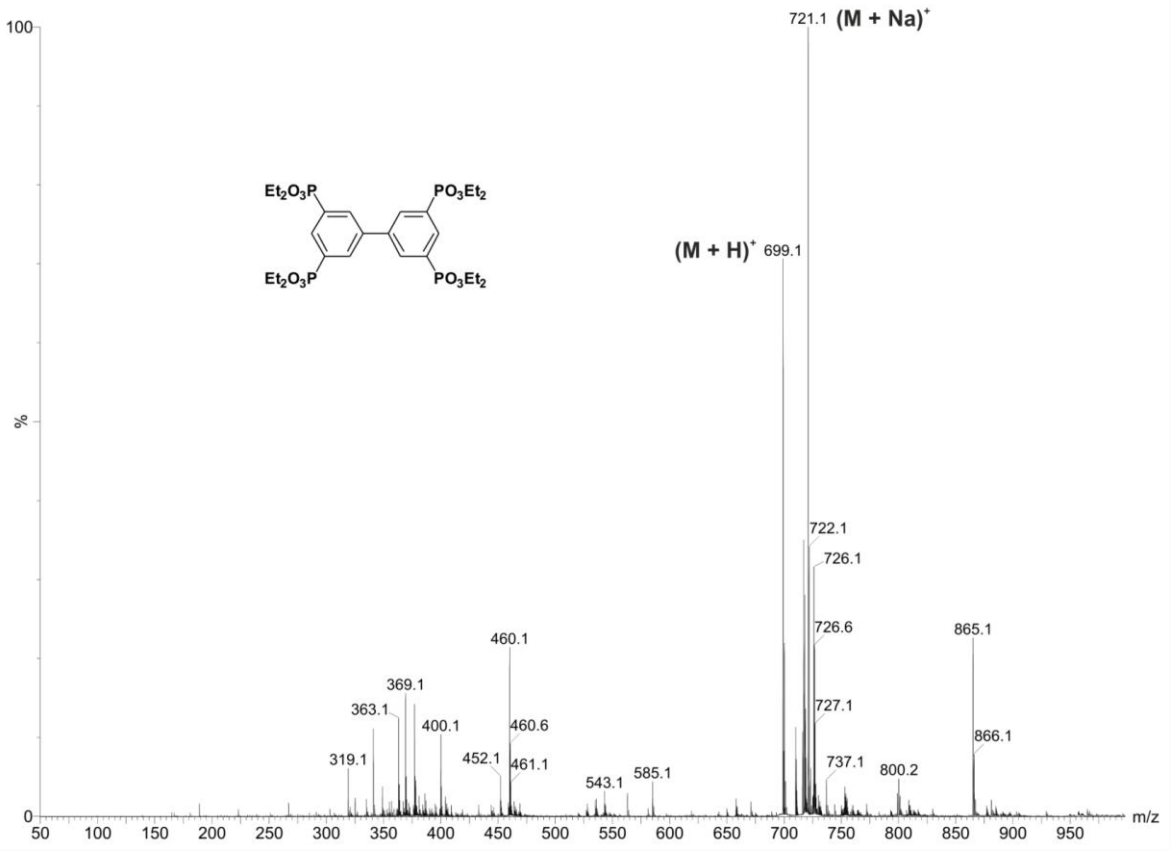

Figure A.1.3. Mass spectrum of the intermediate compound octaethyl-[1,1'-biphenyl]-3,3',5,5'-tetrayltetrakis(phosphonate) (***IL*^{1}**).

2. [1,1'-biphenyl]-3,3',5,5'-tetrayltetrakis(phosphonic acid) (**H_8btp**)

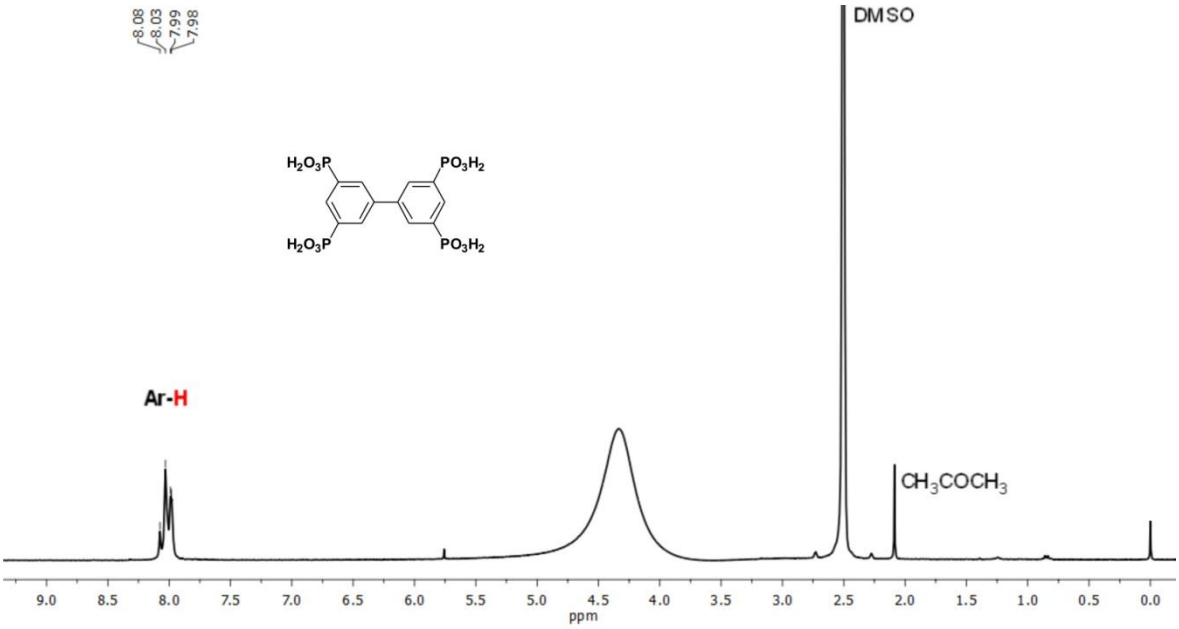

Figure A.1.4. ^{1}HNMR spectrum of the target molecule [1,1'-biphenyl]-3-3',5,5'-tetrayltetrakis(phosphonic acid) (**H_8btp**) in DMSO-d_6.

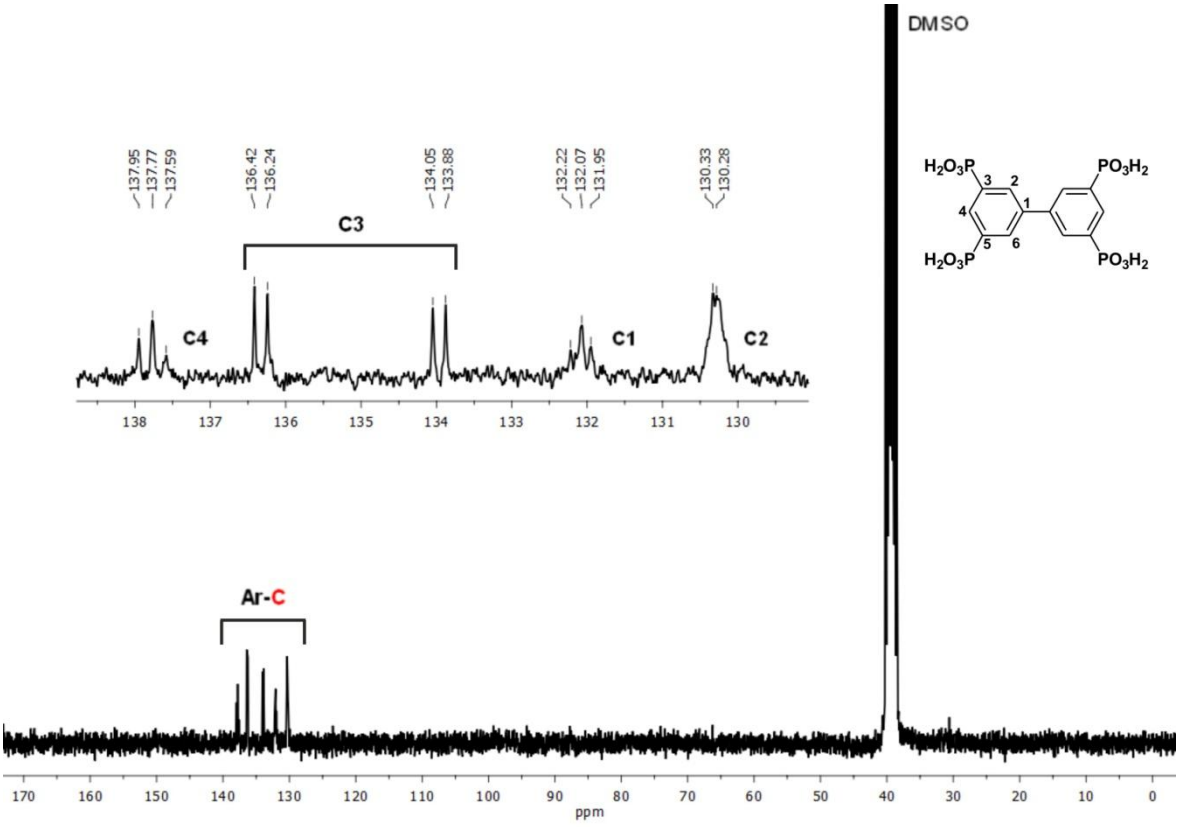

Figure A.1.5. ^{13}C NMR spectrum of the target molecule [1,1'-biphenyl]-3,3',5,5'-tetrayltetrakis(phosphonic acid) (**H_8btp**) in DMSO-d_6.

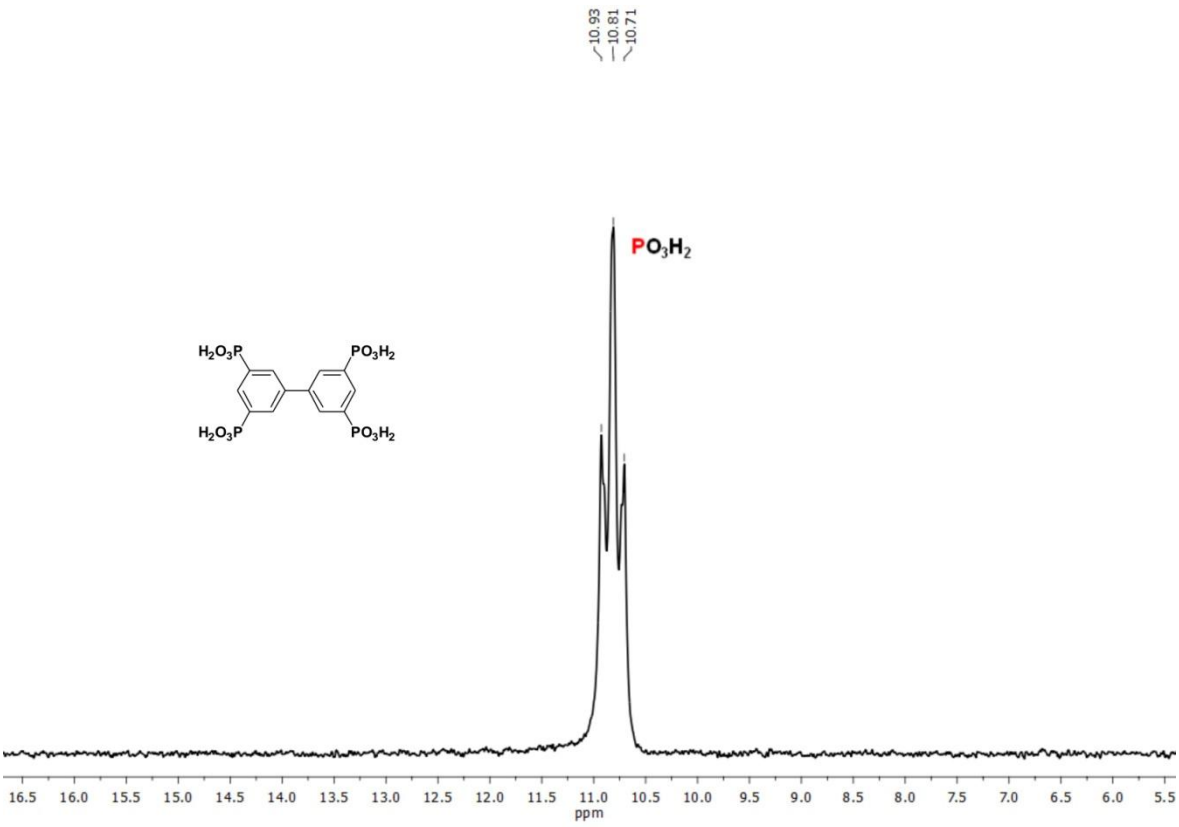

Figure A.1.6. ^{31}P NMR spectrum of the target molecule [1,1'-biphenyl]-3,3',5,5'-tetrayltetrakis(phosphonic acid) (**H_8btp**) in DMSO-d_6.

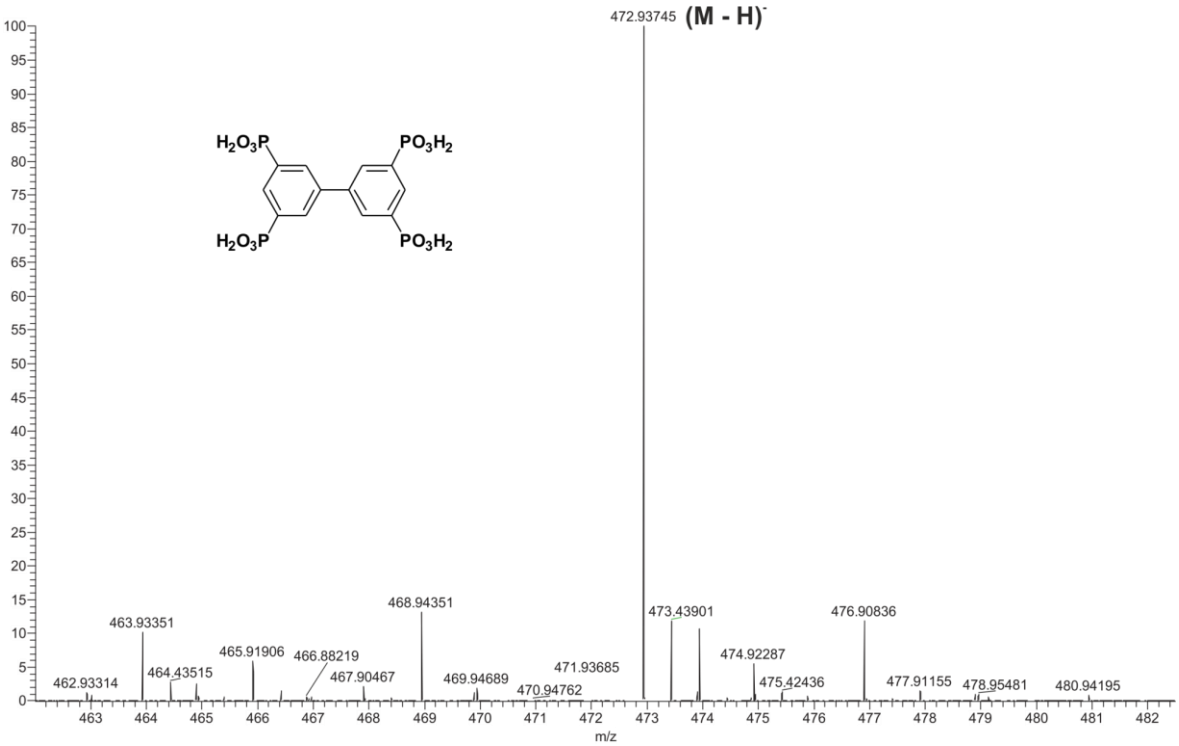

Figure A.1.7. Mass spectrum of the target molecule [1,1'-biphenyl]-3,3',5,5'-tetrayltetrakis(phosphonic acid) (**H_8btp**).

3. Octaethyl-pyrene-1,3,6,8-tetrayltetrakis(phosphonate) (***IL***^{3})

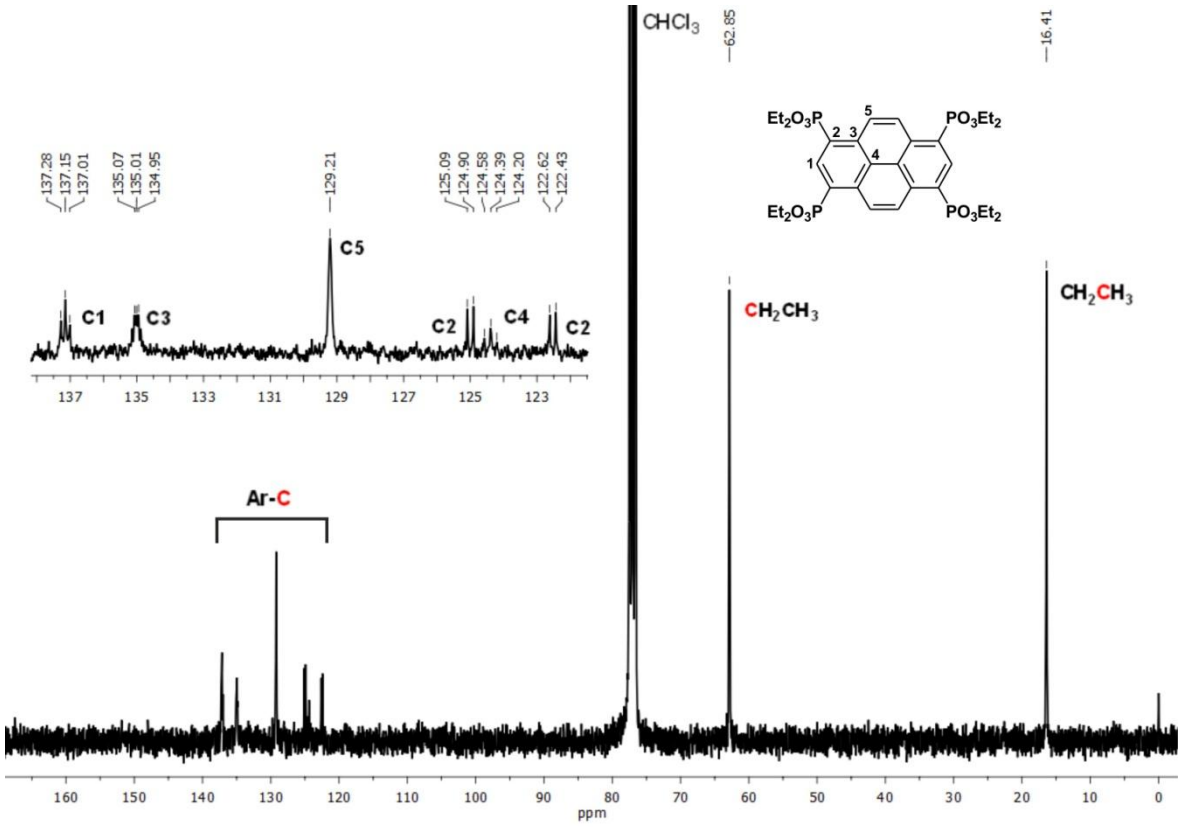

Figure A.1.8. ^{13}C NMR spectrum of the intermediate compound octaethyl-pyrene-1,3,6,8-tetrayltetrakis(phosphonate) (***IL***^{3}) in $CDCl_3$.

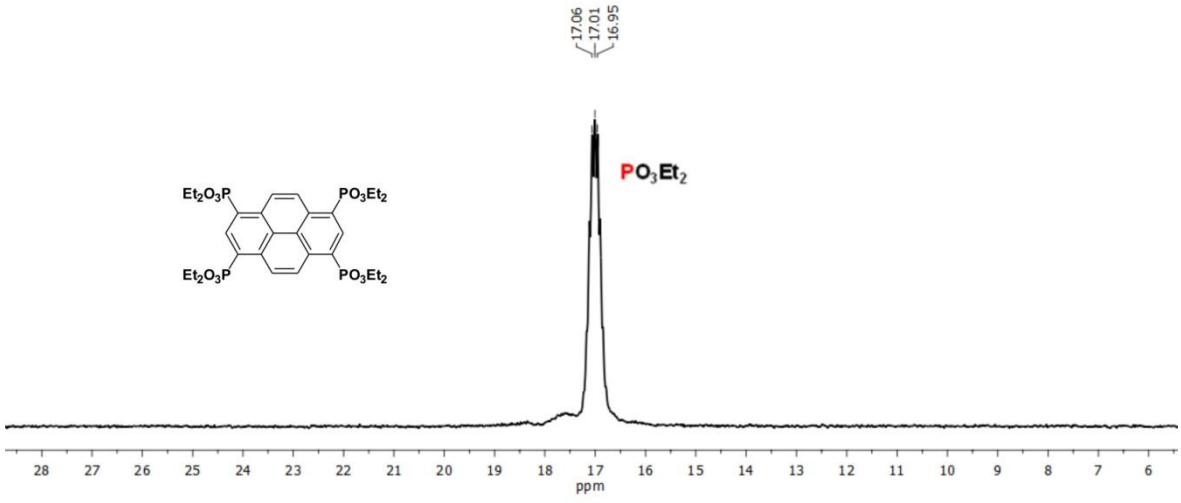

Figure A.1.9. ^{31}P NMR spectrum of the intermediate compound octaethyl-pyrene-1,3,6,8-tetrayltetrakis(phosphonate) (***IL***^{3}) in $CDCl_3$.

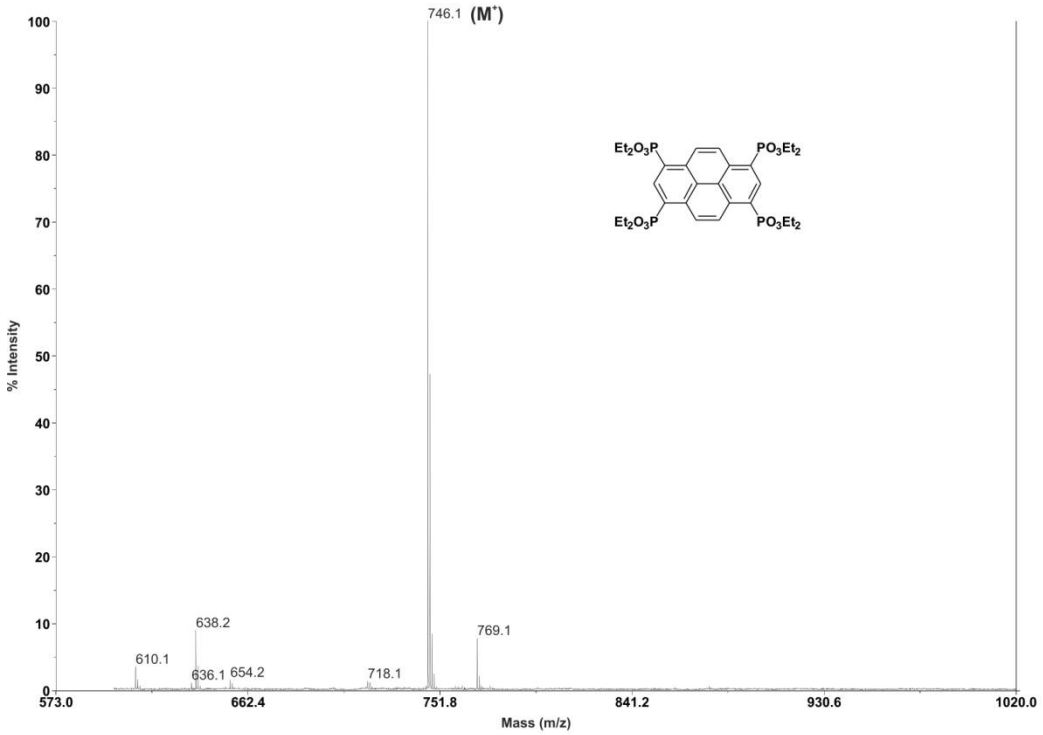

Figure A.1.10. Mass spectrum of the intermediate compound octaethyl-pyrene-1,3,6,8-tetrayltetrakis(phosphonate) (***IL*^{3}**).

4. Pyrene-1,3,6,8-tetrayltetrakis(phosphonic acid) (**H_8ptp**)

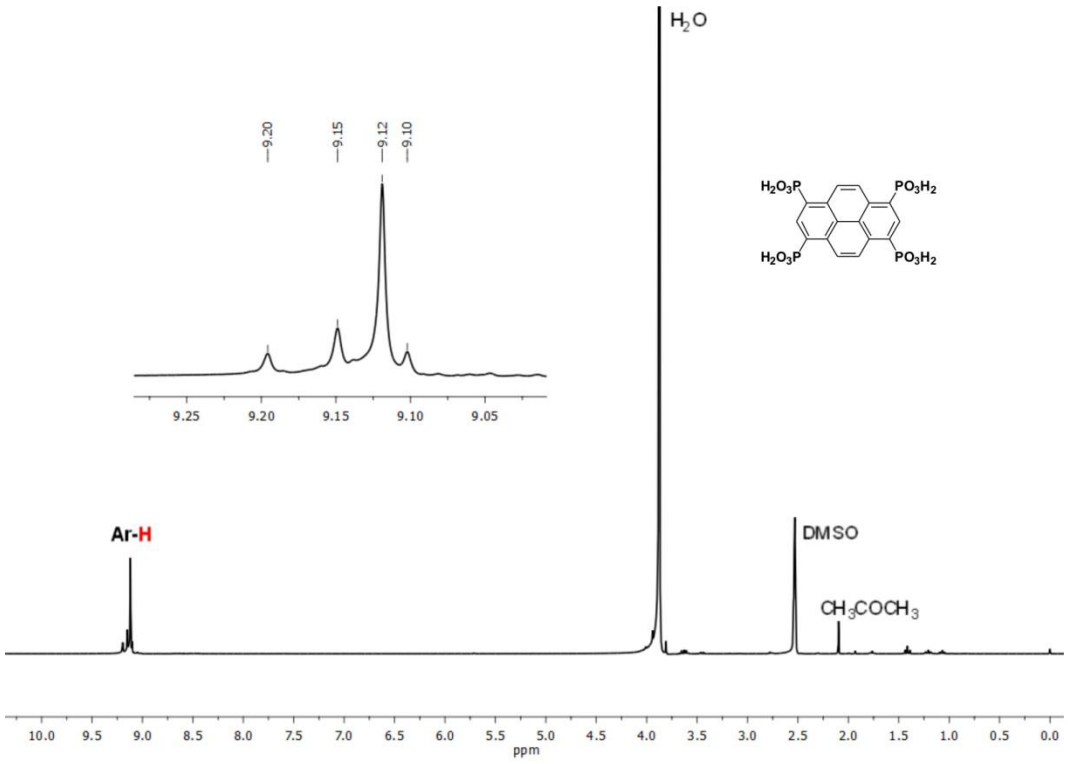

Figure A.1.11. ^{1}HNMR spectrum of the target molecule pyrene-1,3,6,8-tetrayltetrakis(phosphonic acid) (**H_8ptp**) in DMSO-d_6 and D_2O.

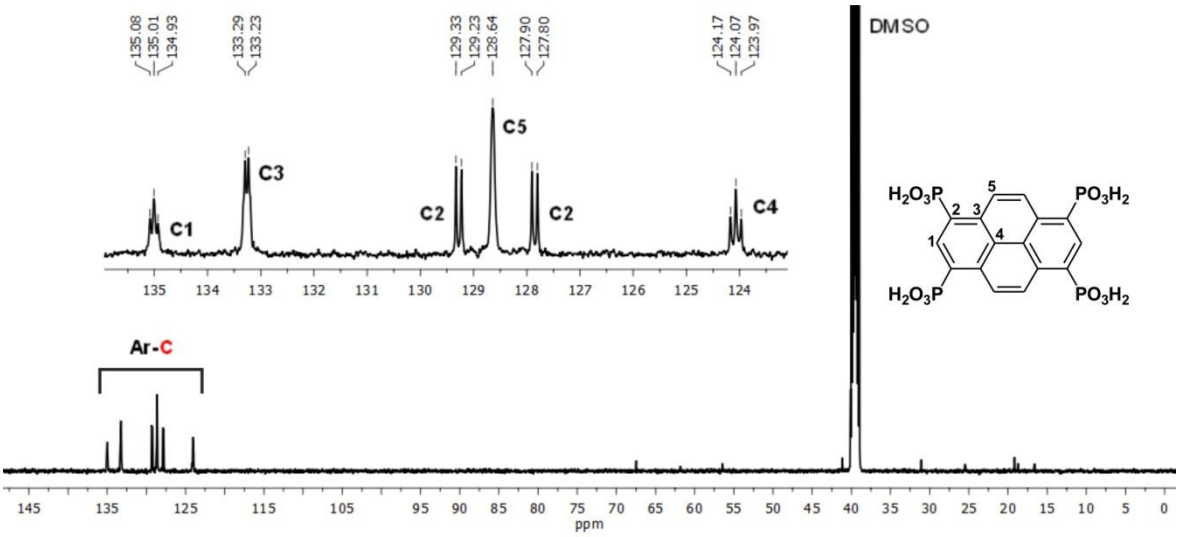

Figure A.1.12. ^{13}C NMR spectrum of the target molecule pyrene-1,3,6,8-tetrayltetrakis(phosphonic acid) (**H_8ptp**) in DMSO-d_6 and D_2O.

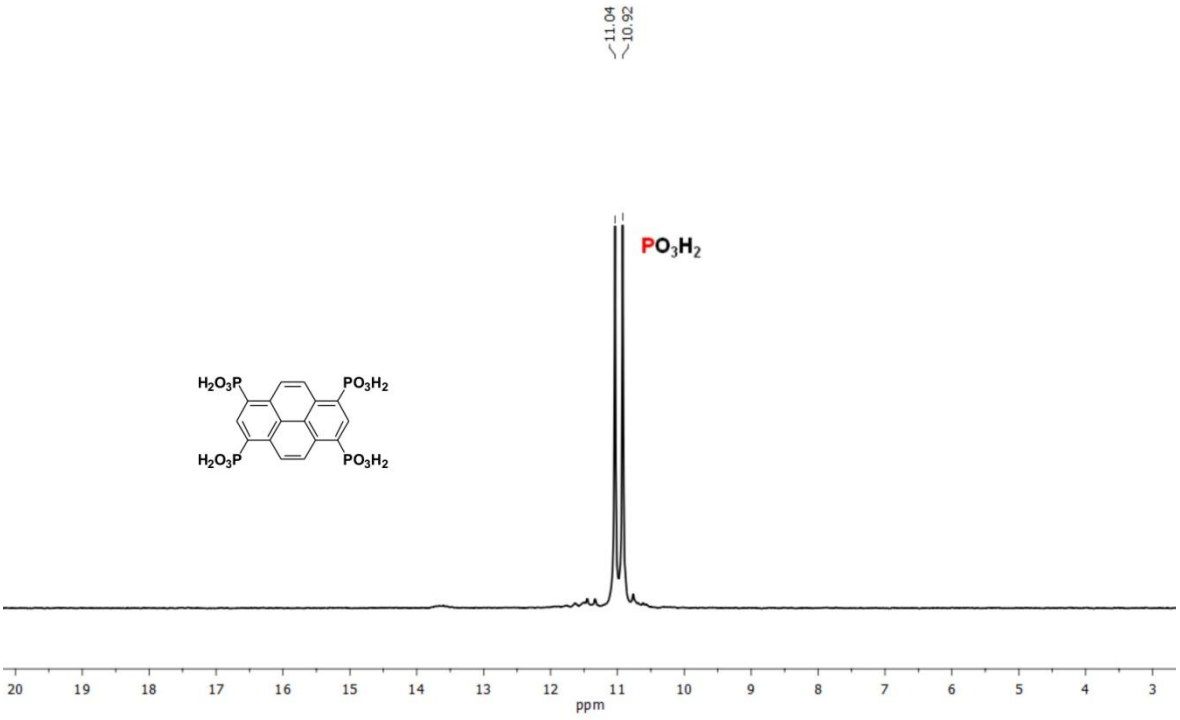

Figure A.1.13. ^{31}P NMR spectrum of the target molecule pyrene-1,3,6,8-tetrayltetrakis(phosphonic acid) (**H_8ptp**) in DMSO-d_6 and D_2O.

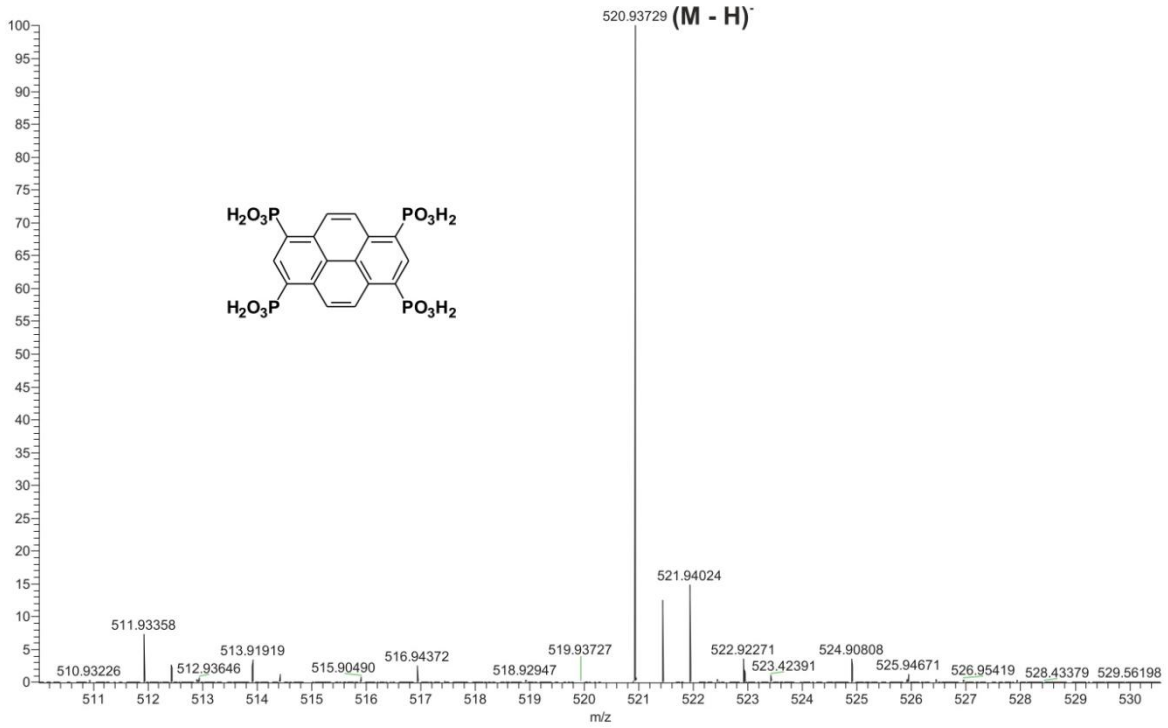

Figure A.1.14. Mass spectrum of the target molecule pyrene-1,3,6,8-tetrayltetrakis(phosphonic acid) (**H_8ptp**).

Appendix B

B. Chapter 3: Microwave Synthesis of a photoluminescent Metal-Organic Framework based on a rigid tetraphosphonate linker

B.1. Electron Microscopy Studies: EDS Mapping

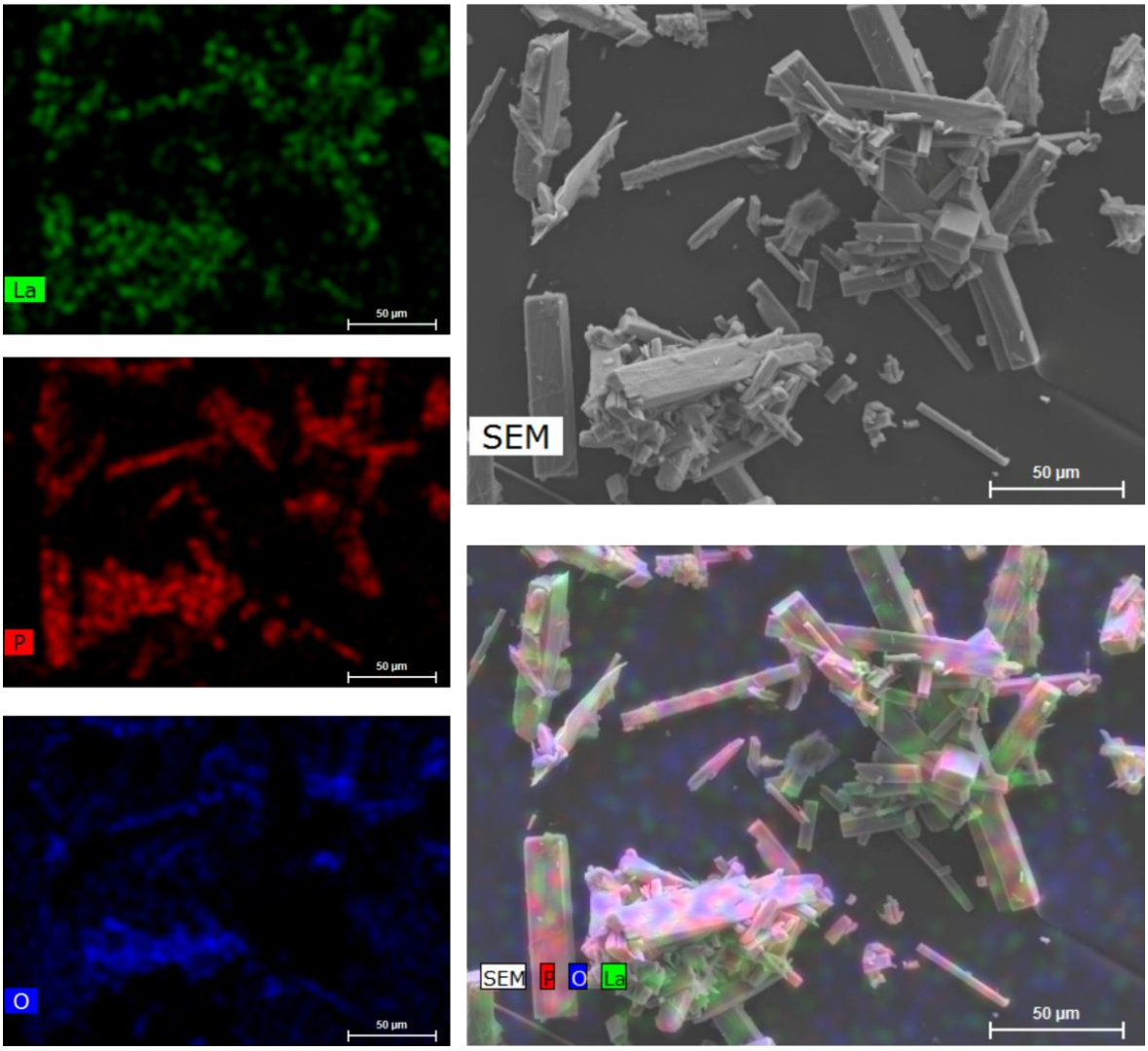

Figure B.1.1. Electron microscopy EDS mapping studies of a portion of the $[La_4(H_6btp)_2(H_4btp)_2(H_8btp)(H_2O)_{16}]\cdot 12H_2O$ (**1**) material. Images show a uniform distribution of the heaviest elements present in **1**, thus confirming a homogeneous dispersion of both the La^{3+} cations and the organic ligand in the materials. Ratio of *ca.* 1:4.1 La : P.

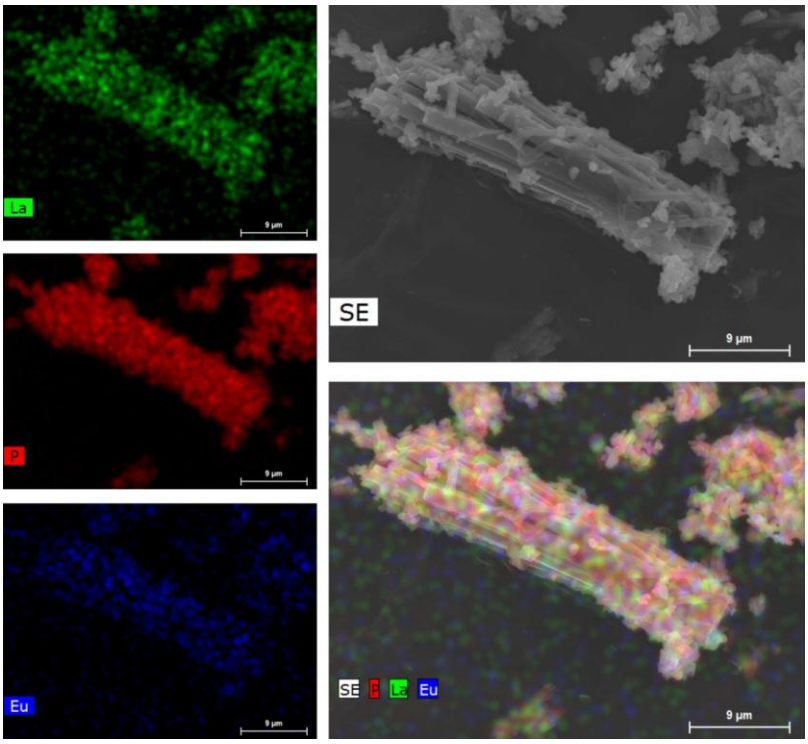

Figure B.1.2. Electron microscopy EDS mapping studies of a portion of the $[(La_{3.6}Eu_{0.4})(H_6btp)_2(H_4btp)_2(H_8btp)(H_2O)_{16}]\cdot 12H_2O$ (**2**) material unequivocally showing an uniform distribution throughout the crystallites of the La^{3+} and Eu^{3+} metallic centers.

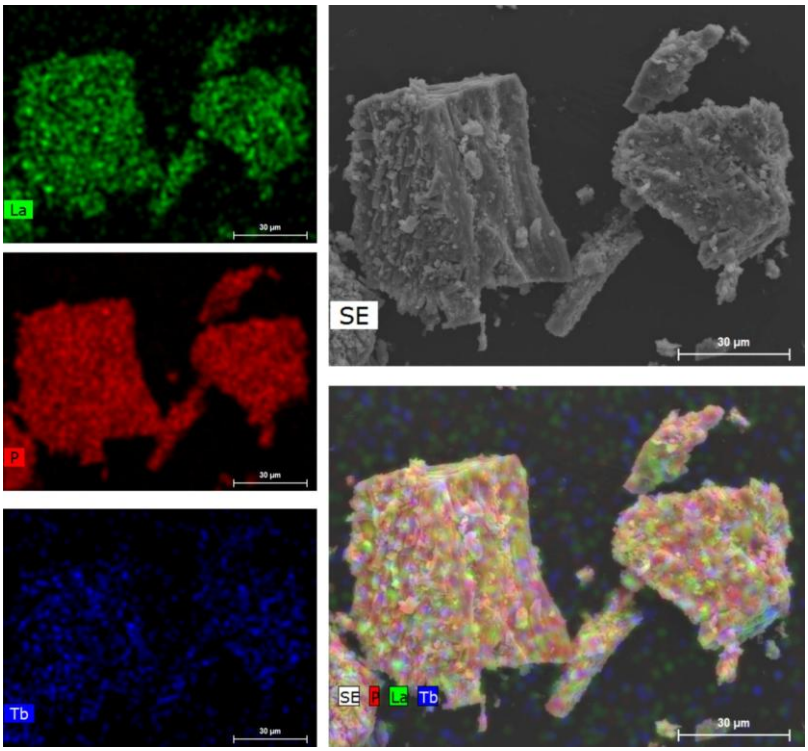

Figure B.1.3. Electron microscopy EDS mapping studies of a portion of the $[(La_{3.6}Tb_{0.4})(H_6btp)_2(H_4btp)_2(H_8btp)(H_2O)_{16}]\cdot 12H_2O$ (**3**) material unequivocally showing an uniform distribution throughout the crystallites of the La^{3+} and Tb^{3+} metallic centers.

B.2. Powder X-ray diffraction of $[Ln_4(H_6btp)_2(H_4btp)_2(H_8btp)(H_2O)_{16}]\cdot 12H_2O$ materials

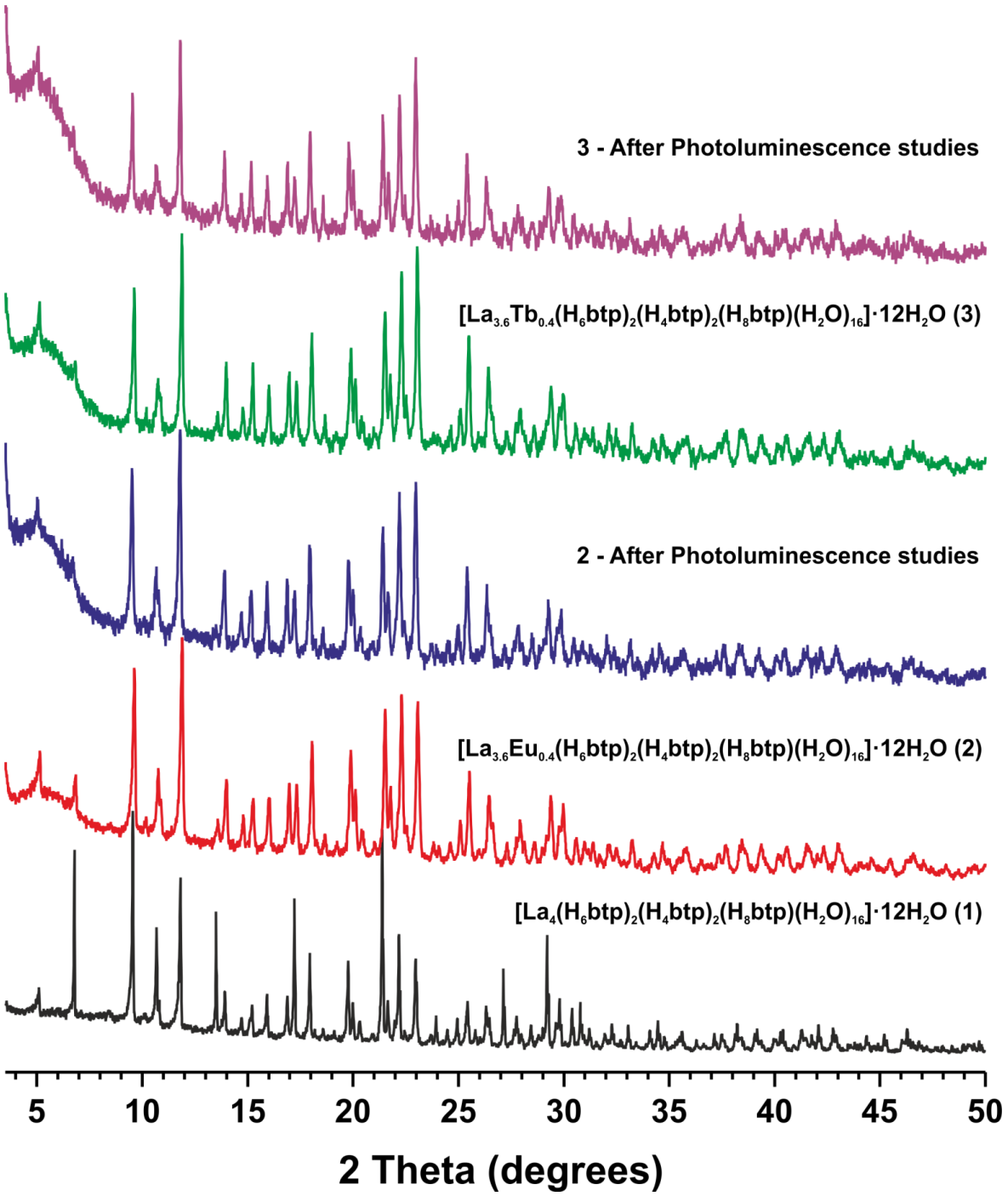

Figure B.2.1. Powder X-ray diffraction patterns of the 2D layered $[Ln_4(H_6btp)_2(H_4btp)_2(H_8btp)(H_2O)_{16}]\cdot 12H_2O$ materials [where $Ln^{3+} = La^{3+}$ (**1**), $(La_{0.9}Eu_{0.1})^{3+}$ (**2**) and $(La_{0.9}Tb_{0.1})^{3+}$ (**3**)].

B.3. Vibrational Spectroscopy: FT-IR studies

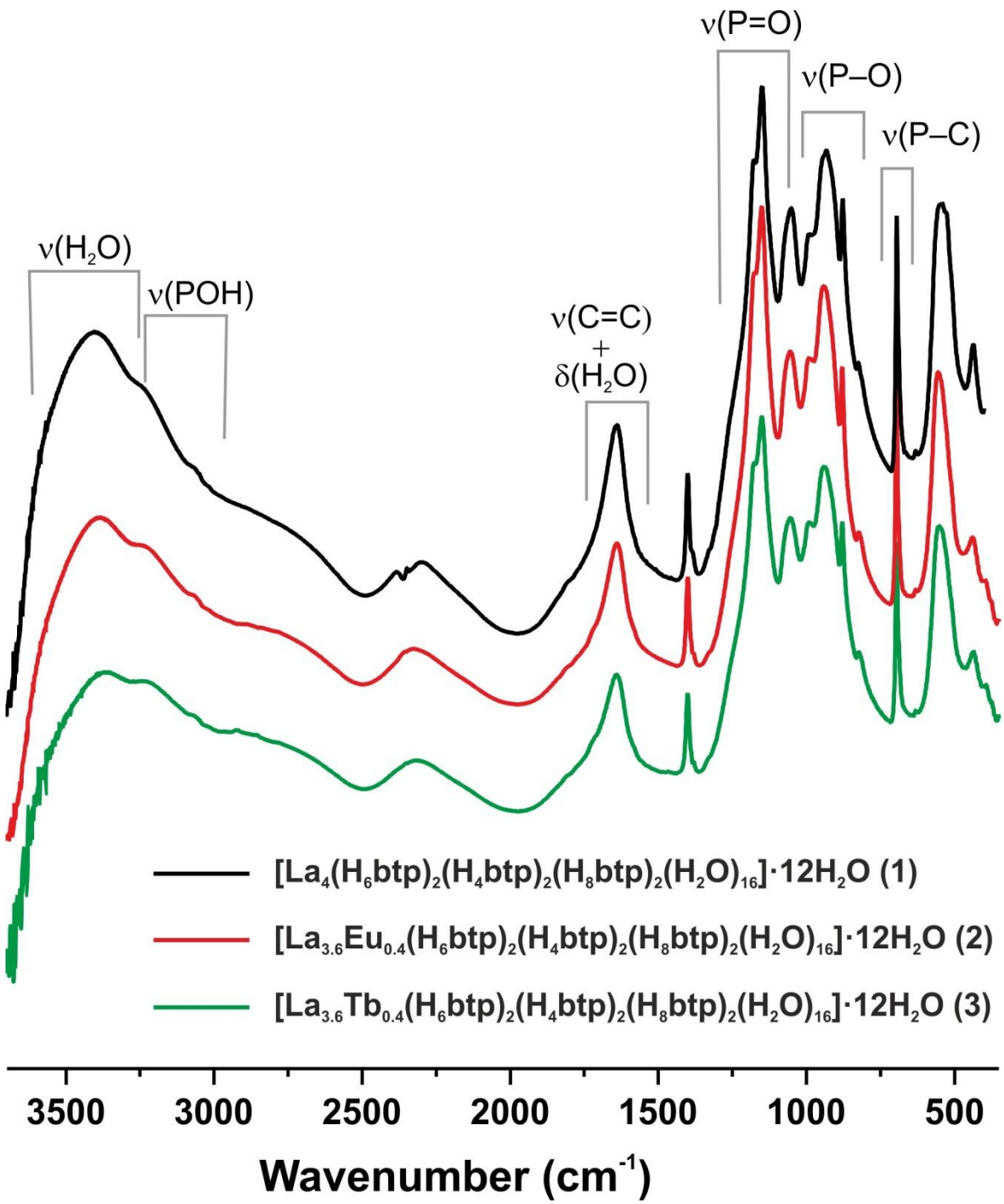

Figure B.3.1. FT-IR spectra (in absorbance, arbitrary units) of the isotypical series of $[Ln_4(H_6btp)_2(H_4btp)_2(H_8btp)(H_2O)_{16}]\cdot 12H_2O$ materials [where Ln^{3+} = La^{3+} (**1**), $(La_{0.9}Eu_{0.1})^{3+}$ (**2**) and $(La_{0.9}Tb_{0.1})^{3+}$ (**3**)].

B.4. Crystallographic Details

Table B.4.1. Crystal data collection and structure refinement details for $[La_4(H_6btp)_2(H_4btp)_2(H_8btp)(H_2O)_{16}]\cdot 12H_2O$ (**1**).

Formula	$C_{30}H_{57}La_2O_{44}P_{10}$
Formula weight	1709.27
Temperature / K	150(2)
Crystal system	Tetragonal
Space group	*P*-4b2
a / Å	18.599(3)
b / Å	18.599(3)
c / Å	17.362(3)
α / º	90
β / º	90
γ / º	90
Volume / Å^3	6006.2(18)
Z	4
ρ_{calc} / g cm^{-3}	1.890
μ(Mo Kα)/mm^{-1}	1.779
Crystal type	Colourless needle
Crystal size / mm	0.03×0.04×0.12
θ range (°)	2.19 – 25.35
Index ranges	$-22 \le h \le 22$
	$-22 \le k \le 22$
	$-19 \le l \le 20$
Collected Reflections	38748
Independent Reflections	5515 (R_{int} = 0.0515)
Completeness to θ = 25.24	99.9%
Final *R* indices [$I > 2\sigma(I)$]	*R*1 = 0.0394
	*wR*2 = 0.0976
Final *R* indices (all data)	*R*1 = 0.0531
	*wR*2 = 0.1049
Absolute structure parameter	-0.0029(6)
Largest diff. peak and hole /eÅ^{-3}	0.937 and -0.852

[a] $R1 = \sum \| |F_o| - |F_c| \| / \sum |F_o|$

[b] $wR2 = \sqrt{\sum \left[w\left(F_o^2 - F_c^2\right)^2 \right] / \sum \left[w\left(F_o^2\right)^2 \right]}$

[c] $w = 1/\left[\sigma^2\left(F_o^2\right) + \left(mP\right)^2 + nP \right]$ where $P = \left(F_o^2 + 2F_c^2\right)/3$

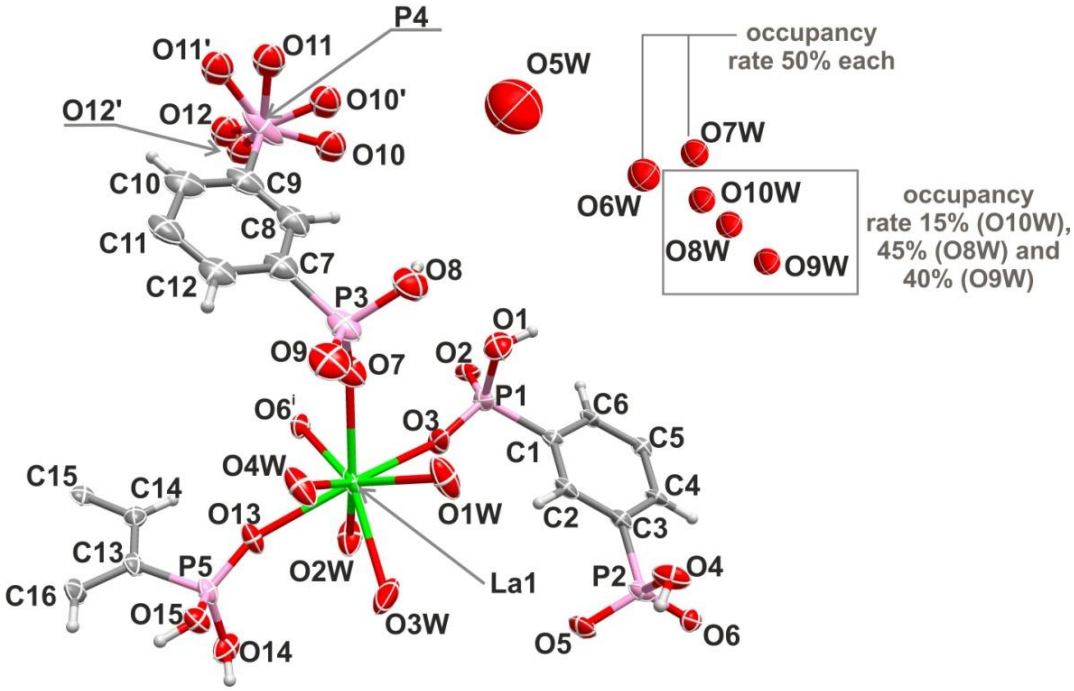

Figure B.4.1. Schematic representation of the asymmetric unit of $[La_4(H_6btp)_2(H_4btp)_2(H_8btp)(H_2O)_{16}]\cdot 12H_2O$ (**1**) showing all non-hydrogen atoms represented as thermal ellipsoids drawn at 50% probability level and hydrogen atoms as small spheres with arbitrary radii. The coordination sphere of the crystallographically independent metallic center was completed while generating (using symmetry) the remaining oxygen atoms. Symmetry code used to generate equivalent atoms: (i) $-x+1/2$, $y-1/2$, z.

Table B.4.2. Selected bond lengths (in Å) and angles (in degrees) for the crystallographically independent La^{3+} coordination environment present in $[La_4(H_6btp)_2(H_4btp)_2(H_8btp)(H_2O)_{16}]\cdot 12H_2O$ (**1**).

La1–O3	2.411(6)	La1–O1W	2.610(8)
La1–O6^{i}	2.420(6)	La1–O2W	2.578(8)
La1–O7	2.521(8)	La1–O3W	2.562(9)
La1–O13	2.467(6)	La1–O4W	2.559(7)
O3–La1–O6^{i}	83.1(2)	O7–La1–O2W	139.8(3)
O3–La1–O7	79.3(2)	O7–La1–O3W	144.1(3)
O3–La1–O13	151.3(2)	O7–La1–O4W	72.5(2)
O3–La1–O1W	73.3(2)	O13–La1–O7	116.4(3)
O3–La1–O2W	79.6(3)	O13–La1–O1W	132.2(2)
O3–La1–O3W	103.4(3)	O13–La1–O2W	73.3(2)
O3–La1–O4W	138.4(2)	O13–La1–O3W	78.3(3)
O6^{i}–La1–O7	74.0(2)	O13–La1–O4W	70.3(2)
O6^{i} –La1–O13	79.1(2)	O2W–La1–O1W	129.4(3)
O6^{i}–La1–O1W	143.9(2)	O3W–La1–O1W	71.7(3)
O6^{i}–La1–O2W	69.9(2)	O3W–La1–O2W	74.4(3)
O6^{i}–La1–O3W	141.8(3)	O4W–La1–O1W	70.3(3)
O6^{i}–La1–O4W	116.4(2)	O4W–La1–O2W	140.5(3)
O7–La1–O1W	75.1(3)	O4W–La1–O3W	83.8(3)

[a] Symmetry transformation used to generate equivalent atoms: (i) -*x*+1/2, *y*-1/2, *z*.

B.5. Thermogravimetry and Thermodiffractometry

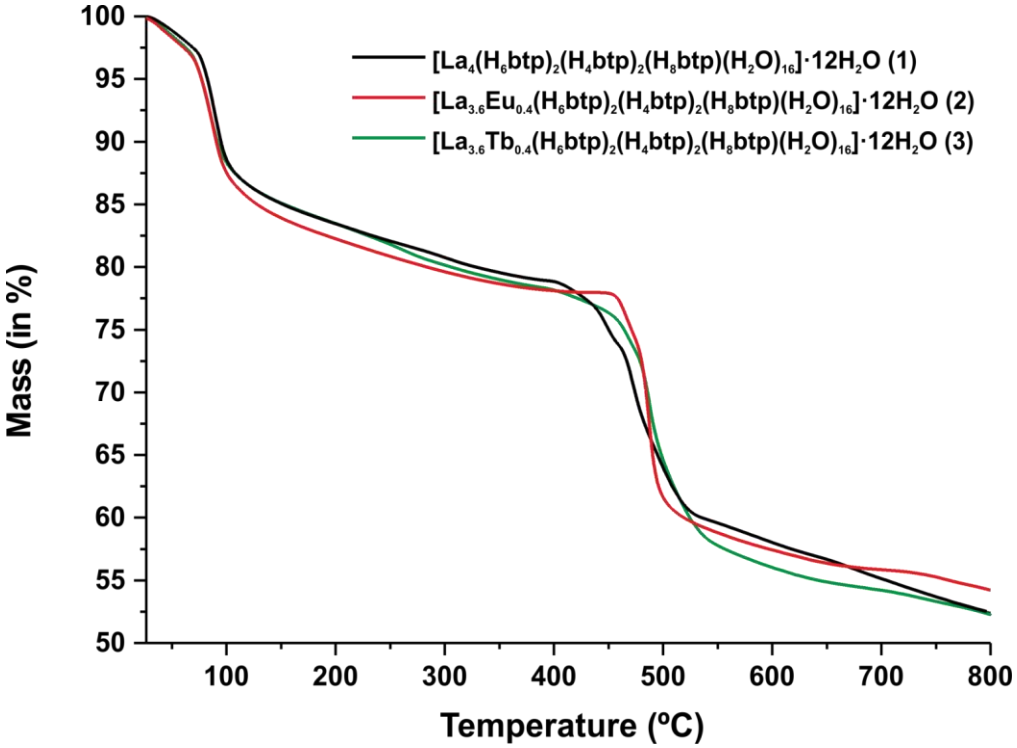

Figure B.5.1. Thermograms of the isotypical series of $[Ln_4(H_6btp)_2(H_4btp)_2(H_8btp)(H_2O)_{16}]\cdot 12H_2O$ materials [where Ln^{3+} = La^{3+} (**1**), $(La_{0.9}Eu_{0.1})^{3+}$ (**2**) and $(La_{0.9}Tb_{0.1})^{3+}$ (**3**)] collected between ambient temperature and 800 ºC.

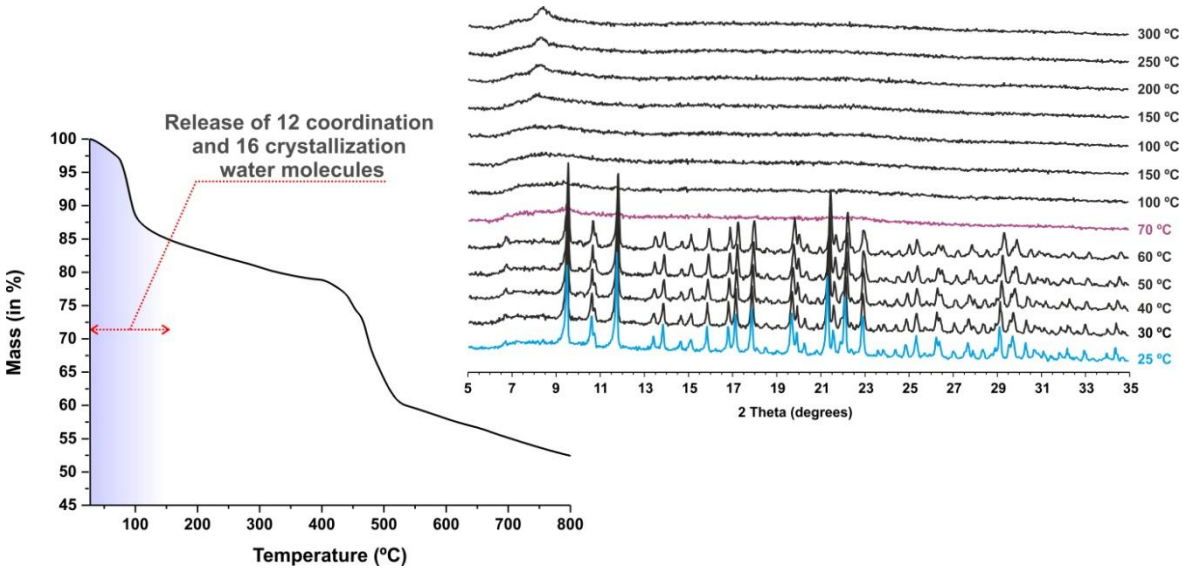

Figure B.5.2. (*left*) Thermogram of $[La_4(H_6btp)_2(H_4btp)_2(H_8btp)(H_2O)_{16}]\cdot 12H_2O$ (**1**) collected between ambient temperature and *ca.* 800 ºC. (*right*) Variable-temperature powder X-ray diffraction studies of 1 registered between ambient temperature and *ca.* 300 ºC, evidencing the transformation of the crystalline material into an amorphous phase at just *ca.* 70 ºC.

Appendix C

C. Chapter 4: Robust Multifunctional Yttrium-Based Metal-Organic Frameworks with Breathing Effect

C.1. Powder X-ray Diffraction Studies

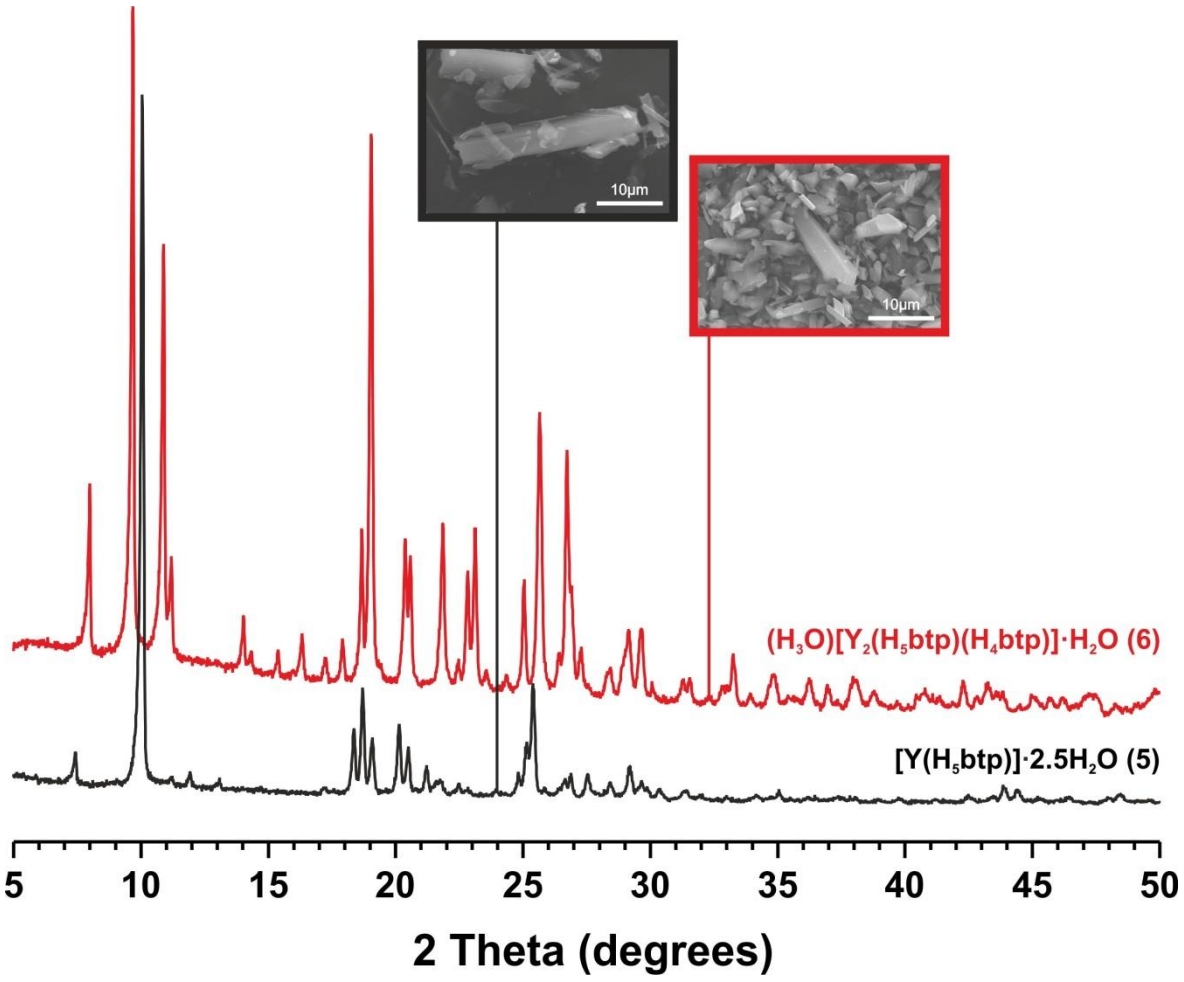

Figure C.1.1. Powder X-ray diffraction patterns and SEM images of bulk materials $[Y(H_5btp)]\cdot 2.5H_2O$ (**5**) and $(H_3O)[Y_2(H_5btp)(H_4btp)]\cdot H_2O$ (**6**).

C.2. Electron Microscopy Studies: EDS Mapping

EDS mapping studies show a uniform distribution of the heaviest elements among the bulk materials, ultimately evidencing the presence of pure phases, as further revealed from the performed X-ray diffraction (sub-section C.1) and solid-state NMR studies (sub-section C.3).

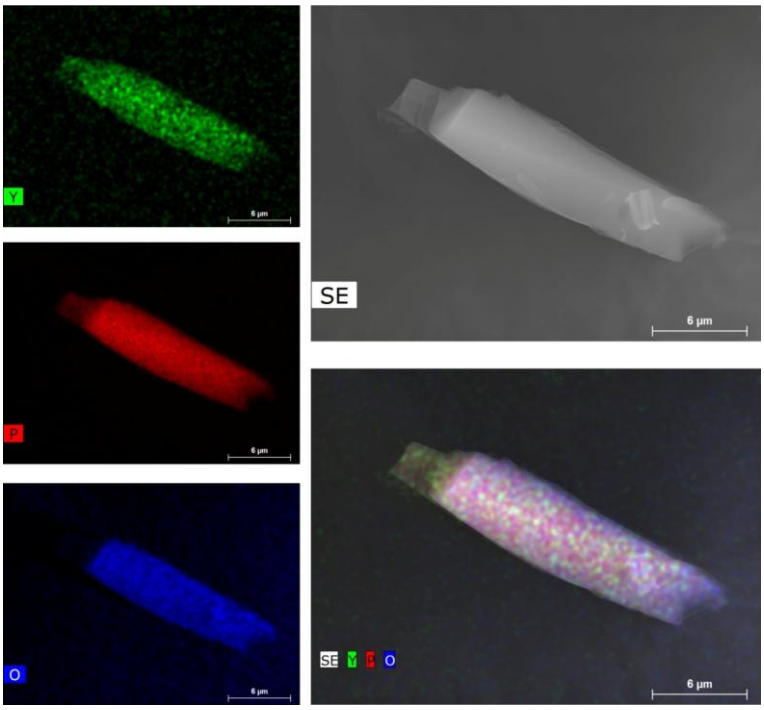

Figure C.2.1. EDS mapping of a representative portion of the $[Y(H_5btp)]\cdot 2.5H_2O$ (**5**) bulk material. Y : P ratio of about 1.0 : 4.1. *Please note*: the Y and P signals are overlapped in the EDS spectrum, leading to a slight increase in the P ratio when the semi-quantification to determine the chemical composition of elements is calculated.

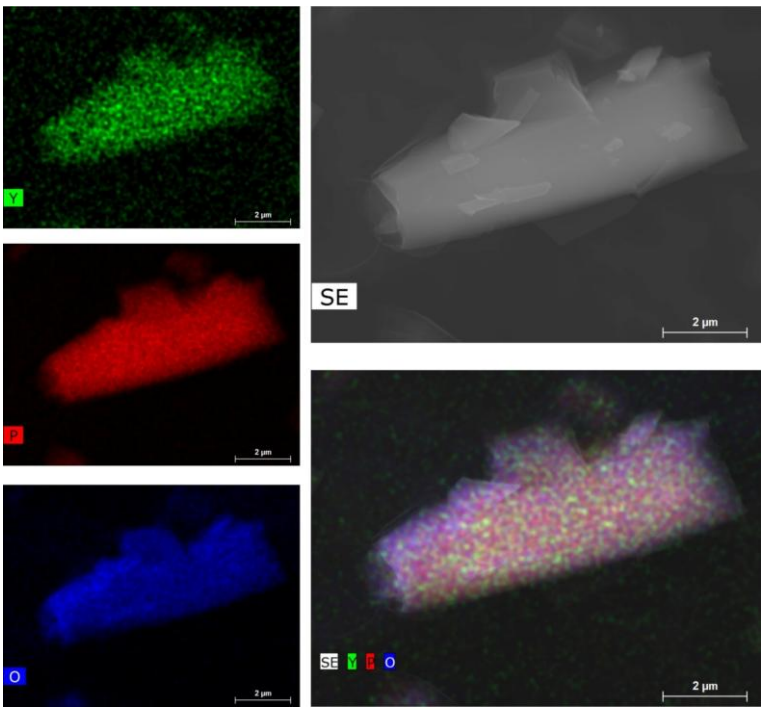

Figure C.2.2. EDS mapping of a representative portion of the $(H_3O)[Y_2(H_5btp)(H_4btp)]\cdot H_2O$ (**6**) bulk material. Y : P ratio of about 1.0 : 4.4. *Please note*: the Y and P signals are overlapped in the EDS spectrum, leading to a slight increase in the P ratio when the semi-quantification to determine the chemical composition of elements is calculated.

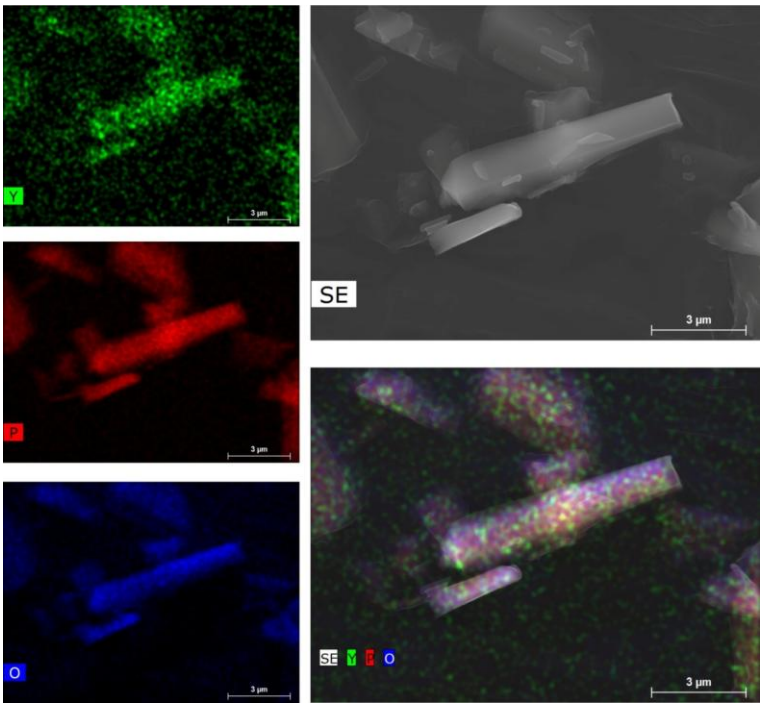

Figure C.2.3. EDS mapping of a representative portion of the [Y(H_5btp)]·H_2O·0.5MeOH (**7**) bulk material. Y : P ratio of 1.0 : 4.6. *Please note*: the Y and P signals are overlapped in the EDS spectrum, leading to a slight increase in the P ratio when the semi-quantification to determine the chemical composition of elements is calculated.

C.3. ^{31}P Solid-State Nuclear Magnetic Resonance

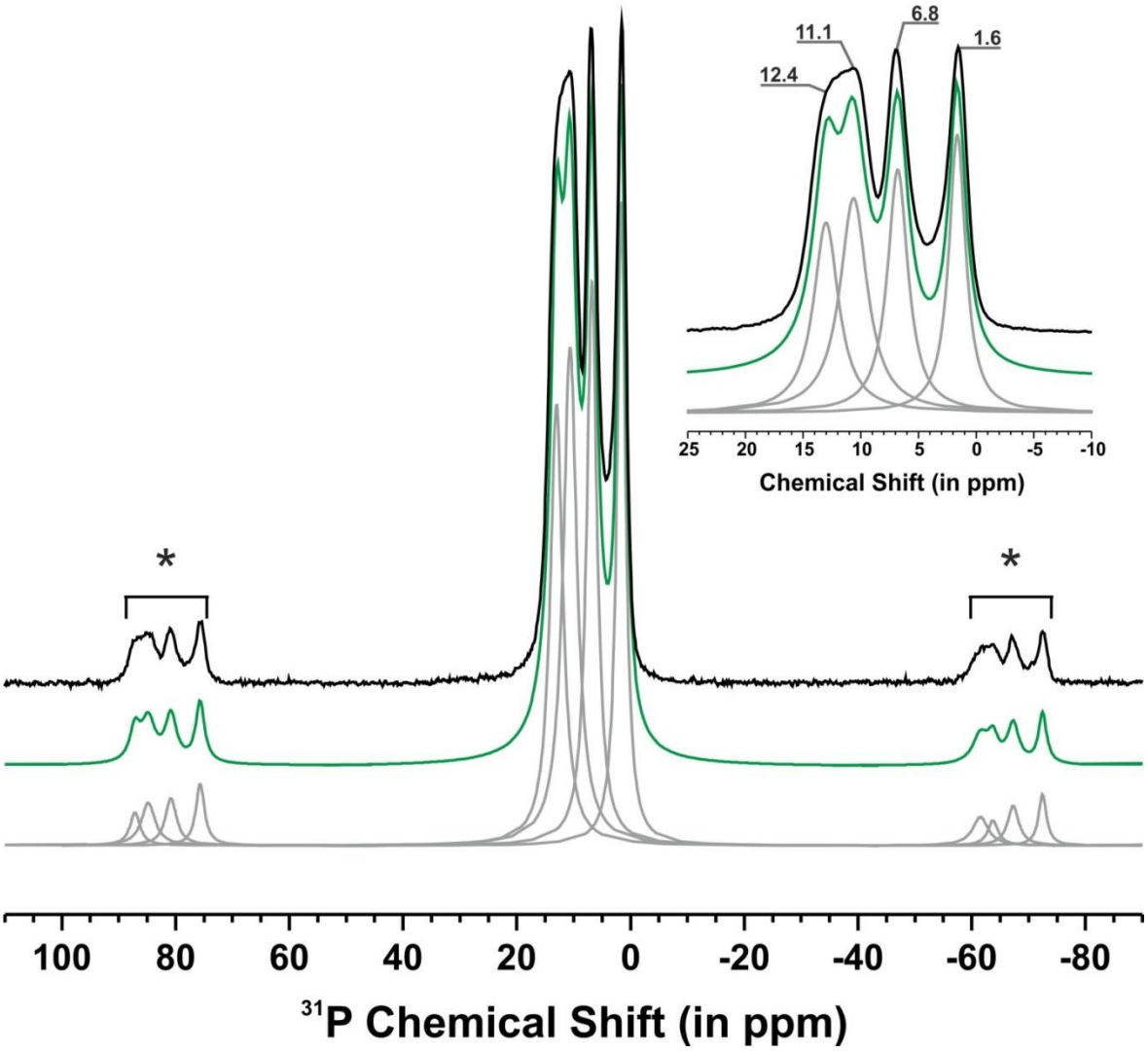

Figure C.3.1. ^{31}P HPDEC MAS spectrum of [Y(H_5btp)]·2.5H_2O (**5**) (black line). Spinning sidebands are denoted using an asterisk. Peak deconvolution and integration throughout the entire spectral range (*i.e.*, including the spinning sidebands) gives a ratio of *ca.* 1.0 : 1.1 : 1.2 : 1.0 for the isotropic resonances centered at *ca.* 1.6, 6.8, 11.1 and 12.4 ppm respectively. The green line depicts the overall (*i.e.*, sum) data fit, while the individual light grey lines correspond to the fits of each single peak.

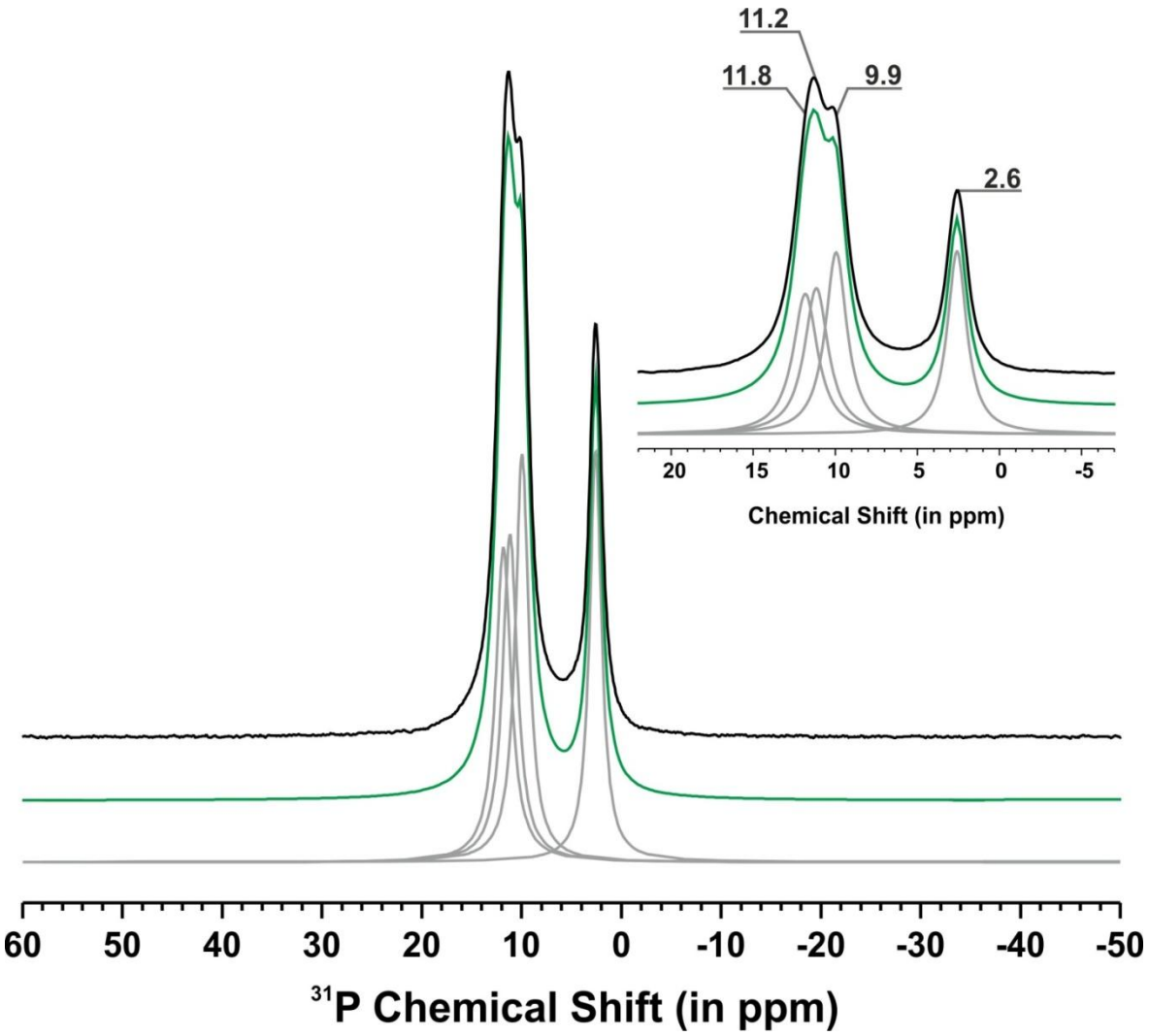

Figure C.3.2. ^{31}P HPDEC MAS spectrum of $(H_3O)[Y_2(H_5btp)(H_4btp)]\cdot H_2O$ (**6**) (black line). Peak deconvolution and integration throughout the spectral range gives a ratio of *ca.* 1.0 : 1.0 : 1.1 : 1.0 for the isotropic resonances at *ca.* 2.6, 9.9, 11.2 and 11.8 ppm respectively. The green line depicts the overall (*i.e.*, sum) data fit, while the individual light grey lines correspond to the fits of each single peak. Spinning sidebands are not included due to lack of resolution (peak deconvolution was not possible).

C.4. Vibrational Spectroscopy: FT-IR studies

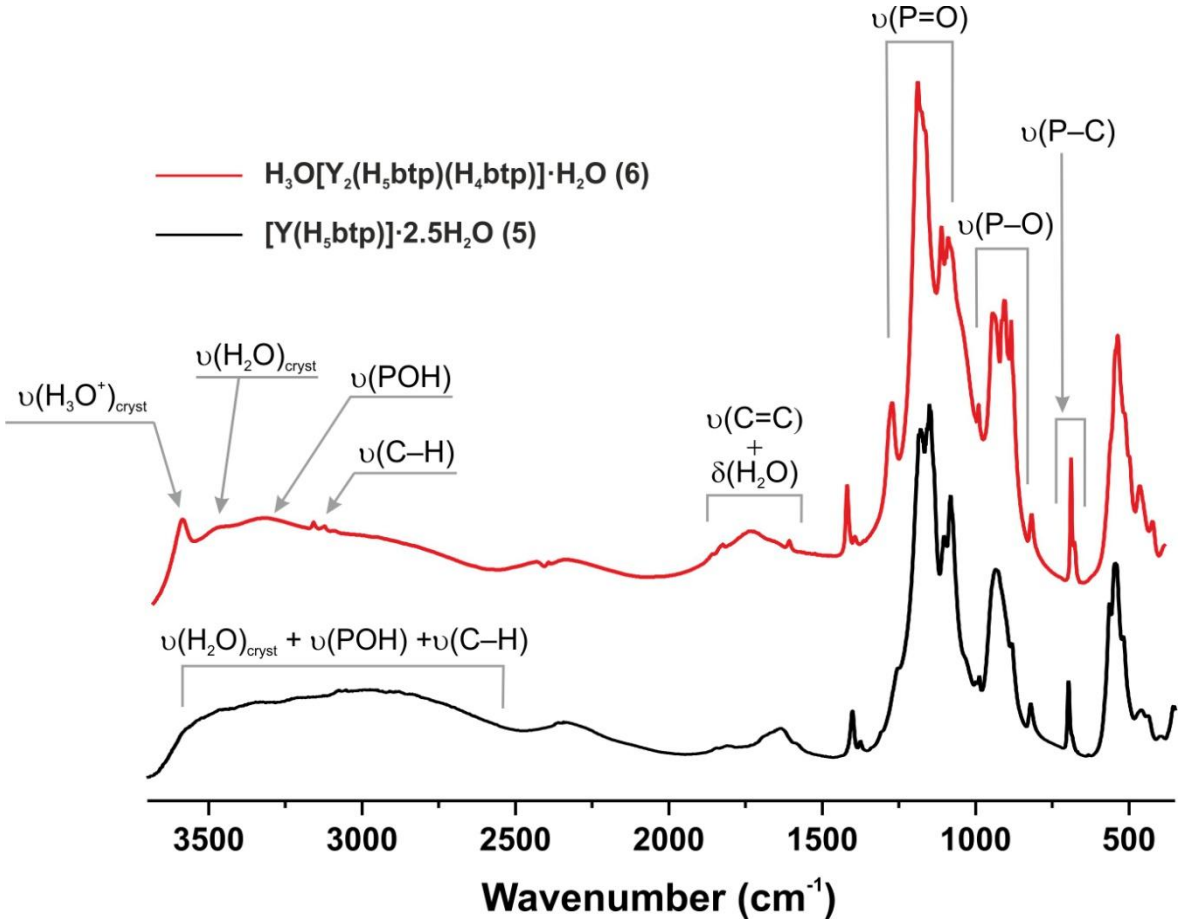

Figure C.4.1. FT-IR spectra (in absorbance, arbitrary units) of the bulk $[Y(H_5btp)]\cdot 2.5H_2O$ (**5**) and $(H_3O)[Y_2(H_5btp)(H_4btp)]\cdot H_2O$ (**6**) materials.

C.5. Crystallographic Studies

Table C.5.1. Crystal data collection and structure refinement details for $[Y(H_5btp)]\cdot 5.5H_2O$ (**4**), $[Y(H_5btp)]\cdot 2.5H_2O$ (**5**) and $(H_3O)[Y_2(H_5btp)(H_4btp)]\cdot H_2O$ (**6**).

	4	**5**	**6**
Formula	$C_{24}H_{44}O_{35}P_8Y_2$	$C_{24}H_{32}O_{29}P_8Y_2$	$C_{12}H_{13}O_{13}P_4Y$
Formula weight	1318.17	1210.07	578.01
Temperature / K	180(2)	180(2)	100(2)
Crystal system	Monoclinic	Monoclinic	Triclinic
Space group	$P2_1/n$	$P2_1/c$	$P\text{-}1$
a / Å	9.3435(11)	9.2274(9)	9.2453(7)
b / Å	22.187(3)	23.952(2)	10.0930(8)
c / Å	13.8761(17)	10.4430(10)	11.7780(9)
α / º	90	90	97.803(3)
β / º	109.571(4)	114.979(3)°.	104.205(4)
γ / º	90	90	111.348(4)
Volume / Å^3	2710.3(6)	2092.2(4)	961.00(13)
Z	2	2	2
ρ_{calc} / g cm^{-3}	1.615	1.921	1.998
μ(Mo Kα) / mm^{-1}	2.459	3.166	3.436
Crystal type	Colorless needle	Colorless needle	Colorless needle
Crystal size / mm	0.08×0.01×0.01	0.08×0.02×0.01	0.16×0.03×0.03
θ range (°)	2.316 – 25.342	3.528 – 29.128	3.545 – 29.131
Index ranges	$-11 \le h \le 11$	$-12 \le h \le 12$	$-12 \le h \le 12$
	$-26 \le k \le 26$	$-32 \le k \le 32$	$-13 \le k \le 13$
	$-16 \le l \le 16$	$-14 \le l \le 13$	$-16 \le l \le 16$
Collected Reflections	34782	53036	45517
Independent Reflections	4962 (R_{int} = 0.0579)	5631 (R_{int} = 0.1348)	5152 (R_{int} = 0.0472)
Completeness (to θ = 25.24°)	100.0%	99.7%	99.7%
Final R indices [I>2σ(I)]	$R1$ = 0.0630	$R1$ = 0.0640	$R1$ = 0.0278
	$wR2$ = 0.1713	$wR2$ = 0.0969	$wR2$ = 0.0634
Final R indices (all data)	$R1$ = 0.0918	$R1$ = 0.1227	$R1$ = 0.0357
	$wR2$ = 0.1911	$wR2$ = 0.1141	$wR2$ = 0.0662
Largest diff. peak and hole /eÅ^{-3}	1.507 and –1.067	1.511 and –0.863	0.568 and –0.399

$^a R1 = \sum \| F_0 \| - \| F_c \| / \sum \| F_0 \|$

$^b wR2 = \sqrt{\sum \left[w(F_0^2 - F_c^2)^2 \right] / \sum \left[w(F_0^2)^2 \right]}$

$^c w = 1/\left[\sigma^2 (F_0^2 + (mP)^2 + nP \right]$ where $P = \left(F_0^2 + 2F_c^2 \right) / 3$

Table C.5.2. Hydrogen bonding geometry (distances in Å and angles in degrees) of $[Y(H_5btp)]\cdot 5.5H_2O$ (**4**), $[Y(H_5btp)]\cdot 2.5H_2O$ (**5**) and $(H_3O)[Y_2(H_5btp)(H_4btp)]\cdot H_2O$ (**6**).

	D–H···A	$d_{D\cdots A}$	**<(DHA)**
4	O2–H2···O1W^{v}	2.627(13)	166
	O2–H2···O2W^{v}	2.52(3)	152
	O8–H8···O8W^{xiv}	2.76(2)	124
	O8–H8···O12W	2.565(15)	162
5	O2–H2···O11^{ix}	2.598(5)	156
	O3–H3···O11^{vi}	2.681(6)	164
	O6–H6···O1W^{xvi}	2.593(6)	174
	O8–H8···O2W^{xvii}	2.598(7)	151
	O12–H12···O2^{xv}	2.688(6)	160
	O1W–H1X···O7	2.718(5)	164
	O1W–H1Y···O5W^{xvii}	2.62(2)	160
	O1W–H1Y···O4W^{xvii}	2.476(15)	132
6	O3–H3···O11	2.785(2)	153
	O5–H5···O12^{xix}	2.703(2)	164
	O8–H8···O3^{xx}	2.911(2)	146
	O11–H11···O4^{xxi}	2.479(2)	169
	O12–H12···O12^{xxii}	2.469(3)	171
	O1W–H1X···O4^{xxi}	2.635(3)	171
	O1W–H1Y···O1^{xx}	2.663(2)	176
	O1W–H1Z···O1W^{xx}	2.477(4)	170

[a]Symmetry transformations used to generate equivalent atoms: (v) -*x*+1/2, *y*-1/2, -*z*+1/2; (vi) *x*-1, *y*, *z*; (ix) *x*-1, -*y*+1/2, *z*+1/2; (xiv) *x*-1, *y*+1, *z*; (xv) *x*+1, *y*, *z*; (xvi) *x*, -*y*+1/2, *z*-1/2; (xvii) –*x*+1, -*y*+1, -*z*+1; (xvii) *x*, *y*, *z*+1. (xix) *x*, *y*, *z*-1; (xx) -*x*+1, -*y*+1, -*z*; (xxi) -*x*+2, -*y*+1, -*z*; (xxii) –*x*+2, -*y*+1, -*z*+1.

Table C.5.3. Selected bond lengths (in Å) and angles (in degrees) for the coordination environment present in $[Y(H_5btp)]\cdot 5.5H_2O$ (**4**), $[Y(H_5btp)]\cdot 2.5H_2O$ (**5**) and $(H_3O)[Y_2(H_5btp)(H_4btp)]\cdot H_2O$ (**6**).

4		**5**		**6**	
Y1-O1	2.210(4)	Y1-O1	2.228(3)	Y1-O1	2.2845(15)
Y1-O3^{iv}	2.236(5)	Y1-O4^{vii}	2.209(3)	Y1-O2^{xii}	2.2159(15)
Y1-O4^{ii}	2.211(9)	Y1-O5^{vi}	2.200(3)	Y1-O6	2.2251(14)
Y1-O6'^{ii}	2.255(12)	Y1-O7^{x}	2.270(3)	Y1-O7^{xiii}	2.2211(14)
Y1-O7^{v}	2.260(5)	Y1-O9^{viii}	2.212(3)	Y1-O9^{xi}	2.1899(16)
Y1-O9^{iii}	2.213(4)	Y1-O10^{ix}	2.217(3)	Y1-O10^{xii}	2.2282(14)
Y1-O11^{i}	2.246(8)				
Y1-O12'^{i}	2.190(12)				
O1-Y1-O3^{iv}	93.58(16)	O1-Y1-O7^{x}	83.12(12)	O2^{xii}-Y1-O1	87.87(5)
O1-Y1-O4^{ii}	170.6(3)	O4^{vii}-Y1-O1	170.76(12)	O2^{xii}-Y1-O6	93.01(5)
O1-Y1-O6'^{ii}	173.1(3)	O4^{vii}-Y1-O7^{x}	87.88(12)	O2^{xii}-Y1-O7^{xiii}	171.14(6)
O1-Y1-O7^{v}	87.33(16)	O4^{vii}-Y1-O9^{viii}	87.77(12)	O2^{xii}-Y1-O10^{xii}	87.74(5)
O1-Y1-O9^{iii}	86.40(17)	O4^{vii}-Y1-O10^{ix}	88.77(12)	O6-Y1-O1	84.49(5)
O1-Y1-O11^{i}	86.1(2)	O5^{vi}-Y1-O1	89.42(12)	O6-Y1-O10^{xii}	174.19(6)
O3^{iv}-Y1-O6'^{ii}	86.1(3)	O5^{vi}-Y1-O4^{vii}	99.82(13)	O7^{xiii}-Y1-O1	85.36(5)
O3^{iv}-Y1-O7^{v}	175.94(16)	O5^{vi}-Y1-O7^{x}	164.39(12)	O7^{xiii}-Y1-O6	92.03(5)
O3^{iv}-Y1-O11^{i}	91.0(3)	O5^{vi}-Y1-O9^{viii}	92.33(13)	O7^{xiii}-Y1-O10^{xii}	86.53(5)
O4^{ii}-Y1-O3^{iv}	95.8(3)	O5^{vi}-Y1-O10^{ix}	85.16(13)	O9^{xi}-Y1-O1	174.27(5)
O4^{ii}-Y1-O7^{v}	83.4(3)	O9^{viii}-Y1-O1	91.99(12)	O9^{xi}-Y1-O2^{xii}	88.48(6)
O4^{ii}-Y1-O9^{iii}	92.7(3)	O9^{viii}-Y1-O7^{x}	101.58(11)	O9^{xi}-Y1-O6	91.29(6)
O6'^{ii}-Y1-O7^{v}	93.5(4)	O9^{viii}-Y1-O10^{iv}	175.31(12)	O9^{xi}-Y1-O7^{xiii}	98.70(6)
O9^{iii}-Y1-O3^{iv}	88.19(17)	O10^{ix}-Y1-O1	91.94(12)	O9^{xi}-Y1-O10^{xii}	94.49(6)
O9^{iii}-Y1-O6'^{ii}	86.7(3)	O10^{ix}-Y1-O7^{x}	81.43(12)	O10^{xii}-Y1-O1	89.78(5)
O9^{iii}-Y1-O7^{v}	95.82(16)			O7^{xiii}-Y1-O10^{xii}	86.53(5)
O9^{iii}-Y1-O11^{i}	172.4(2)				
O11^{i}-Y1-O7^{v}	85.1(3)				
O12'^{i}-Y1-O1	92.3(4)				
O12'^{i}-Y1-O3^{iv}	81.6(4)				
O12'^{i}-Y1-O7^{v}	94.4(4)				
O12'^{i}-Y1-O9^{iii}	169.7(4)				

[a]Symmetry transformations used to generate equivalent atoms: (i) –*x*-1/2, *y*-1/2, *z*+1/2*;* (ii) -*x*+1, -*y*, -*z*+1*;* (iii) *x*+1/2, -*y*+1/2, *z*+1/2*;* (iv) -*x*, -*y*, *z*-1/2; (v) -*x*+1/2, *y*-1/2, -*z*+1/2; (vi) *x*-1, *y*, *z;* (vii) -*x*+1, -*y*, -*z*+2*;* (viii) –*x*-1, *y*-1/2,- *z*+3/2*;* (ix) *x*-1, -*y*+1/2, *z*+1/2; (x) *x*, -*y*+1/2, *z*+1/2; (xi) 1-*x*, -*y*,- *z;* (xii) -*x*+1, -*y*, -*z;* (xiii) *x*-1, *y*,- *z.*

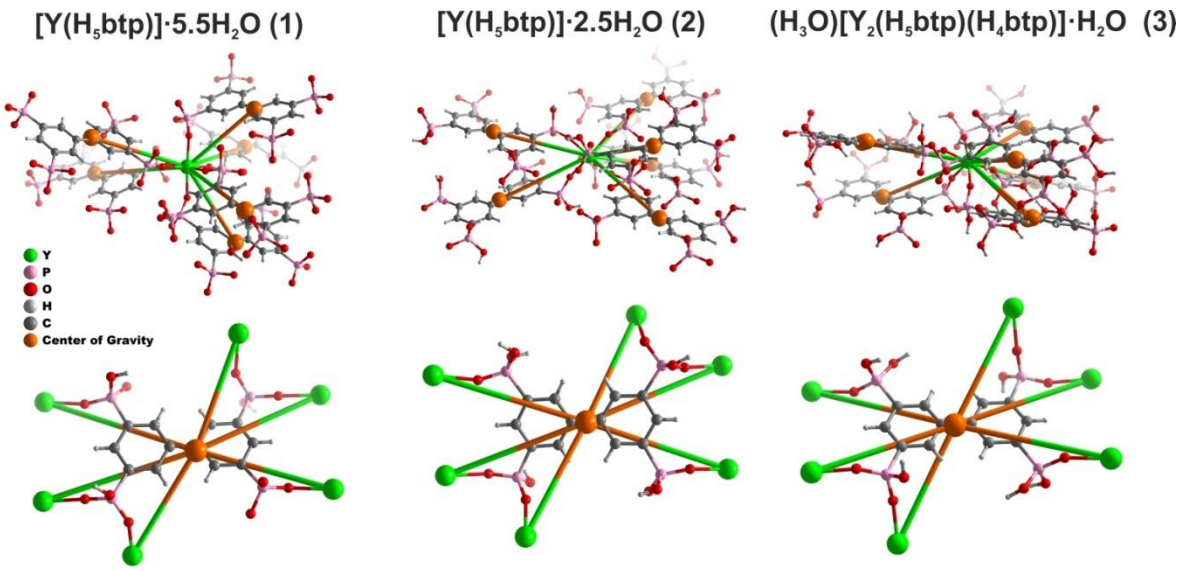

Figure C.5.1. Schematic representation of the connectivity of each individual node composing the binodal networks representative of the compounds **4**-**6**.

C.6. Thermogravimetry and Thermodiffractometry

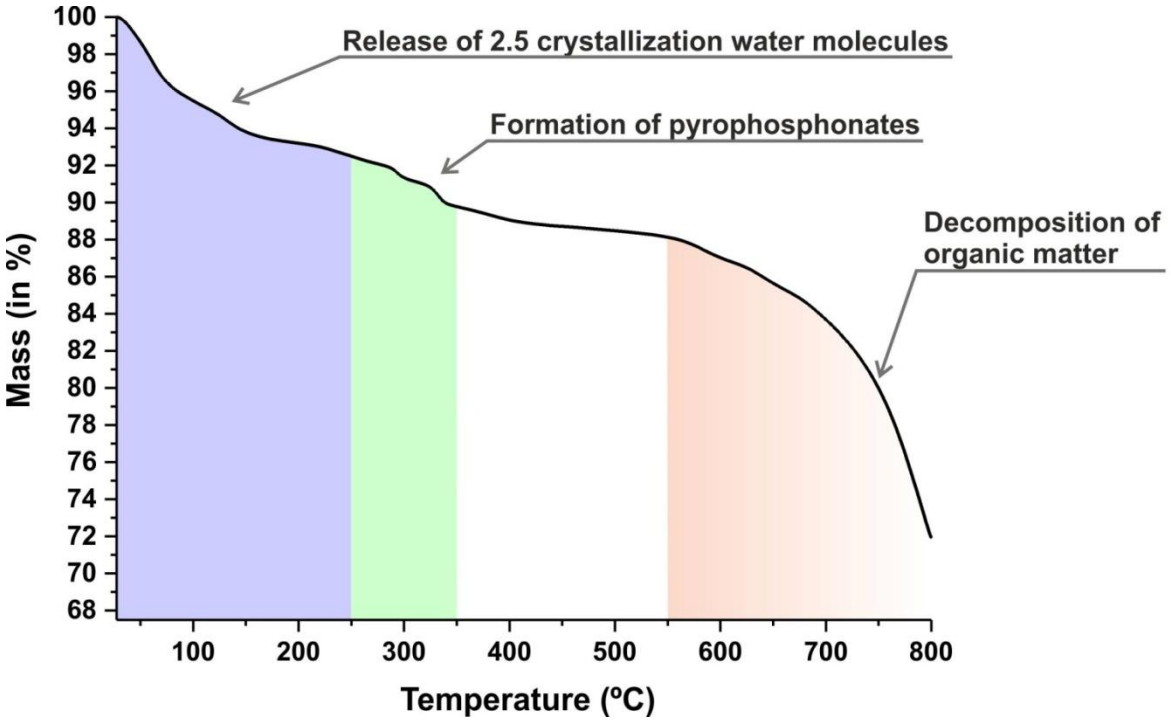

Figure C.6.1. Thermogram of $[Y(H_5btp)]\cdot 2.5H_2O$ (**5**) collected between ambient temperature and *ca*. 800 ºC.

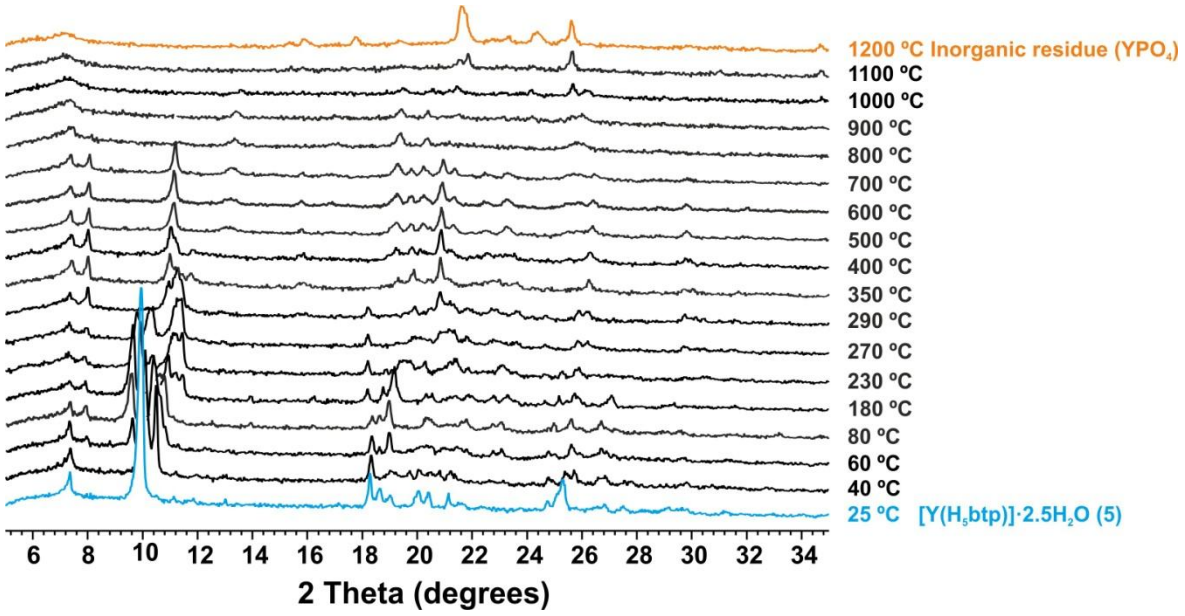

Figure C.6.2. Variable-temperature powder X-ray diffraction study of [Y(H_5btp)]·2.5H_2O (**5**) collected between ambient temperature and *ca.* 1200 ºC.

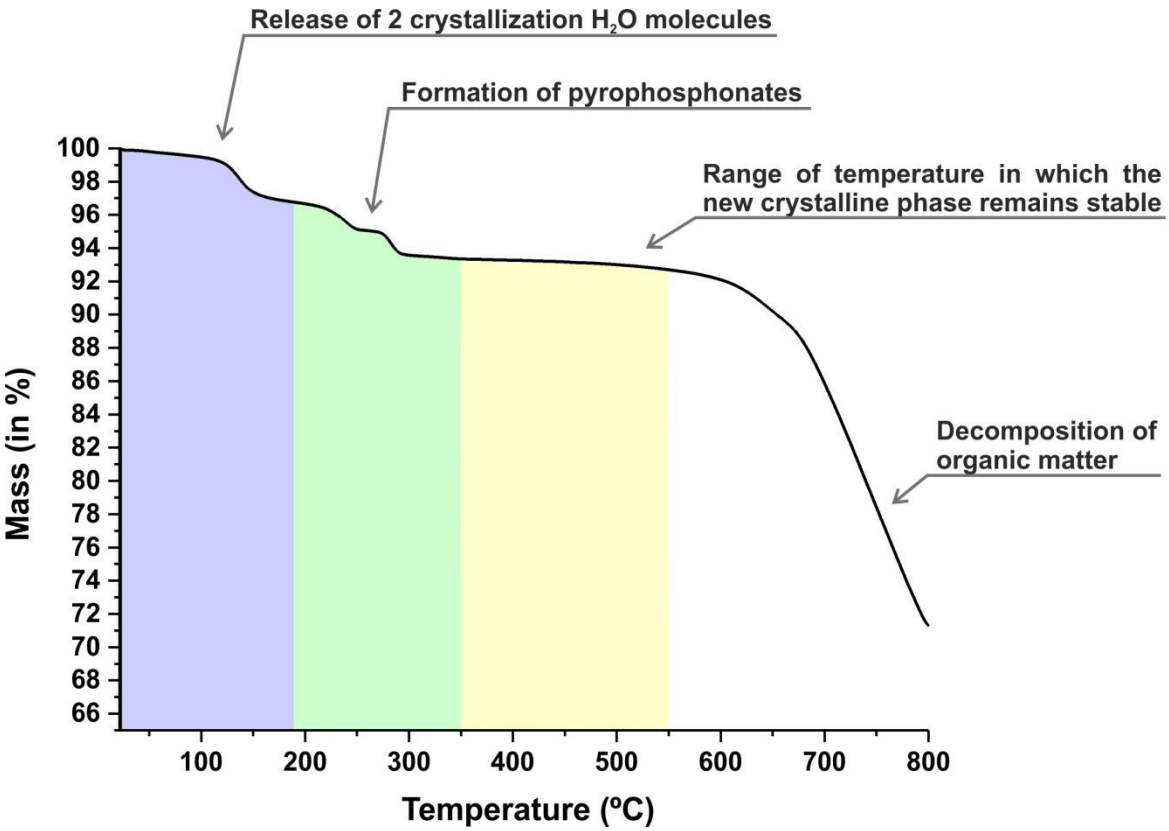

Figure C.6.3. Thermogram of (H_3O)[Y_2(H_5btp)(H_4btp)]·H_2O (**6**) collected between ambient temperature and *ca.* 800 ºC.

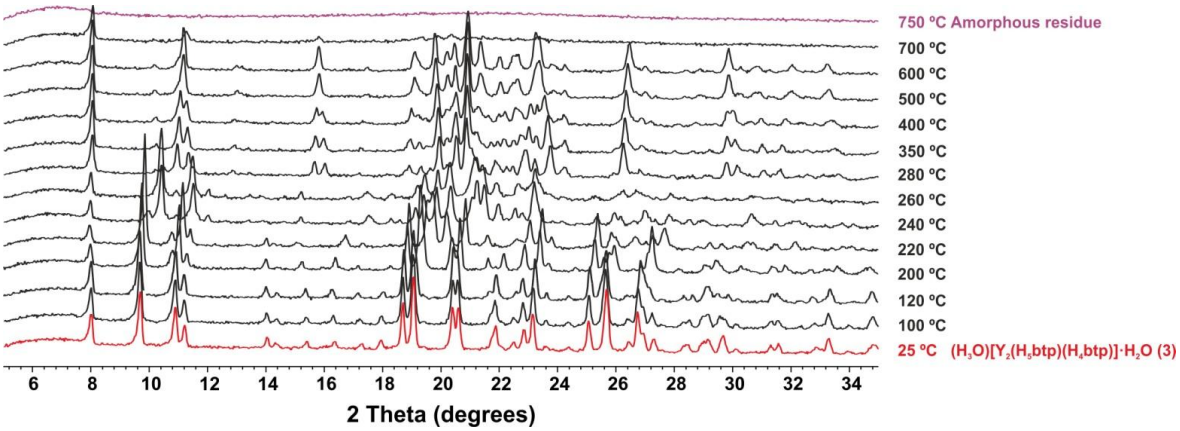

Figure C.6.4. Variable-temperature powder X-ray diffraction study of $(H_3O)[Y_2(H_5btp)(H_4btp)]\cdot H_2O$ (**6**) collected between ambient temperature and *ca.* 800 ºC.

C.7. Heterogeneous catalysis

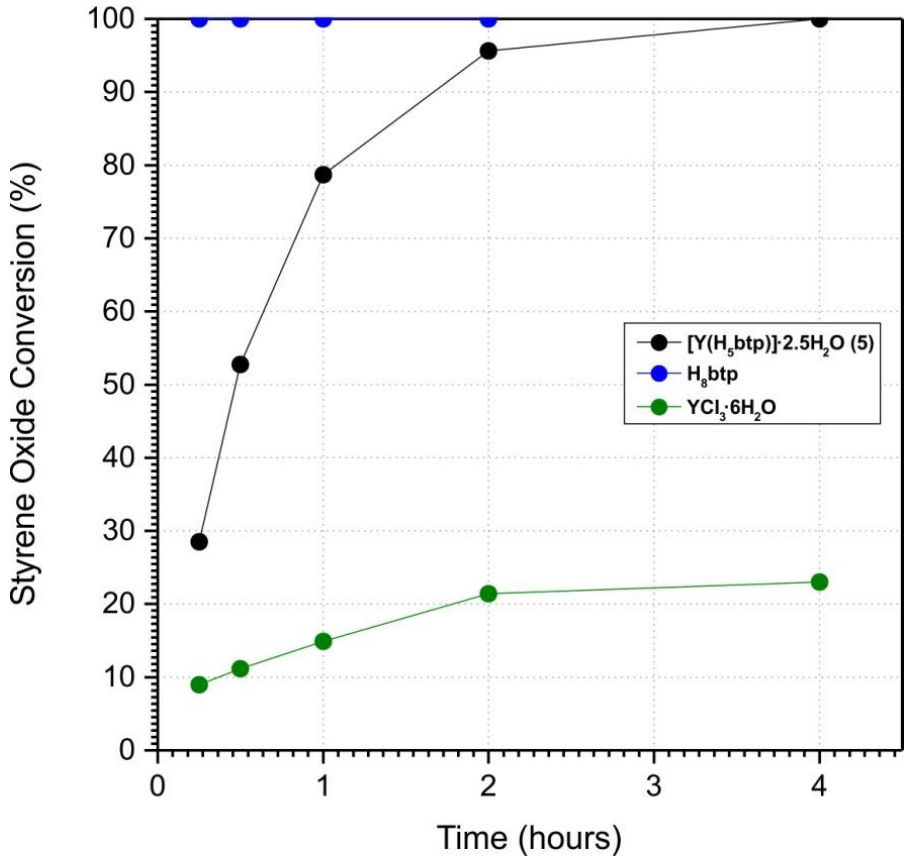

Figure C.7.1. Conversion of styrene oxide with methanol in the presence of $[Y(H_5btp)]\cdot 2.5H_2O$ (**5**), H_8btp or $YCl_3\cdot 6H_2O$ at 35 ºC (catalyst load = 3.3 g_{MOF} L^{-1}). The organic and metal precursors were used in equivalent molar amounts to those corresponding to 3.3 $g_{MOF}L^{-1}$. 2-Methoxy-2-phenylethanol was formed with 100% selectivity. *Please note*: lines connecting experimental points are only for illustrative purposes and do not intend to indicate any experimental trend.

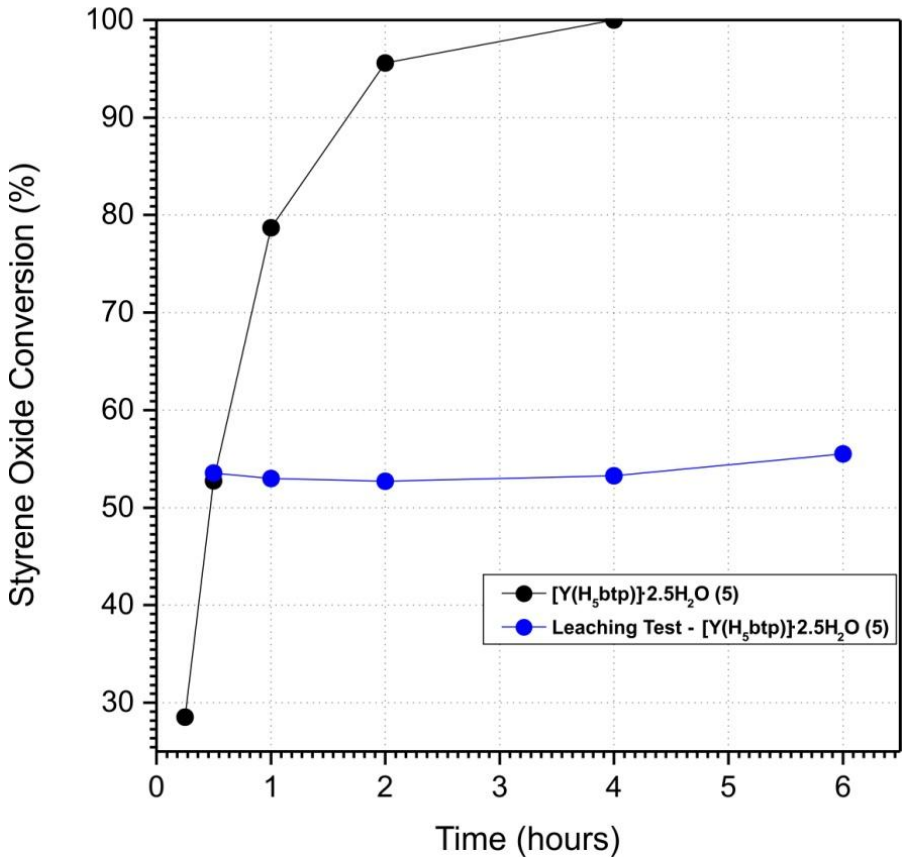

Figure C.7.2. Leaching test carried out for $[Y(H_5btp)]\cdot 2.5H_2O$ (**5**) in the methanolysis of styrene oxide at 35 ºC, and comparison to the typical conditions without removal of the catalyst (catalyst load = 3.3 g_{MOF} L^{-1}). 2-Methoxy-2-phenylethanol was formed with 100% selectivity. *Please note*: lines connecting experimental points are only for illustrative purposes and do not intend to indicate any experimental trend.

Table C.7.1. Comparison between the catalytic performance of compound **5** with other MOF catalysts, reported in the literature in the ring-opening of styrene oxide.[a]

Catalysts[b]	T (ºC)	PhEtO [M]	Cat. (g_{cat} L^{-1})	Time	Conv. (%)	Sel. (%)	Ref.
$[La_2(H_3nmp)_2(H_2O)_4]\cdot 4.5H_2O$	**35**	**0.4**	**3.3**	**30 min / 2 h**	**69 / 97**	**100**	1
5	**35**	**0.4**	**3.3**	**30 min / 2 h**	**53 / 96**	**100**	2
$[Gd(H_4nmp)(H_2O)_2]Cl\cdot 2H_2O$	35	0.4	3.3	30 min / 2h	36/92	100	3
$[La(H_4bmt)(H_5bmt)(H_2O)_2]\cdot 3H_2O$	35	0.4	3.3	1 h / 6 h	40 / 100	100	4
$[La(H_3nmp)]$	40	0.4	17.4	24 h	40	100	5
$[La_2(H_3bmt)_2(H_2O)_2]\cdot H_2O$	55	0.4	20	24 h	80	100	6
$[Ce_2(pydc)_3(H_2O)_2]$	55	0.4	3.3	24 h	49	100	7
$Cu_3(BTC)_2]$ (HKUST-1)	40	0.2	6.7	2.5 h	90	100	8
$Cu_3(BTC)_2]$ (HKUST-1)	40	0.4	10	1 h	93	95	9
[Fe(BTC)]	40	0.4	10	1 h	99	94	10
[Fe(BTC)]	40	0.4	9.4	1 h	99	100	11
$[Al_2(BDC)_3]$	40	0.4	10	1 h	67	96	10
MIL-101(HPW)	40	0.1	5	20 min	99	99	9
MIL-101(HF)	40	0.4	10	24 h	62	100	11
MIL-101(SO_3H)	rt	0.1	[c]	10 min	99	100	12
$[Cu(bpy)(H_2O)_2(BF_4)_2(bpy)]$	25	0.3	12.9	2 h	93	100	13
$[Cu(bpy)(H_2O)_2(BF_4)_2(bpy)]$	25	0.3	13	3 h	99	95	14
$[Eu(Hpdm)(H_2O]$	55	0.4	17.4	24 h	93	100	15
Chiral porous MOF R-3	60	0.9	35.9	24 h	71	93	16
Co-BTT	50	0.2	3.9	29 h	67	100	11
HKUST-1/MG2 composite	60	0.2	6.7	20 min	75	100	17

[a] Experimental conditions: T = reaction temperature (*please note:* rt = ambient temperature); PhEtO = initial molar concentration of styrene oxide; Cat. = catalyst load; Time = reaction time; The catalytic results are reported as conversion of styrene oxide (Conv.) and selectivity the β-alkoxy alcohol (Sel.).

[b] The abbreviations of the names of the MOFs are the same as those used in the original publications.

[c] The amount of catalyst was 0.004 mM.

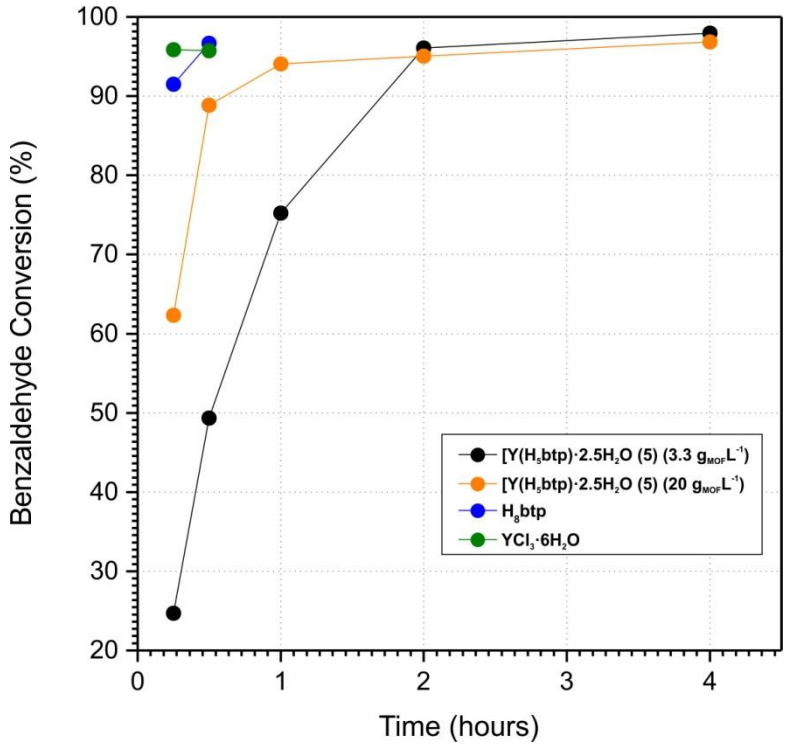

Figure C.7.3. Conversion of benzaldehyde with methanol in the presence of $[Y(H_5btp)]\cdot 2.5H_2O$ (**5**), H_8btp or $YCl_3\cdot 6H_2O$ at 35 ºC, using a catalyst load of 3.3 g_{MOF} L^{-1} or 20 g_{MOF} L^{-1}. The organic and metal precursors were used in equivalent molar amounts to those corresponding to 3.3 $g_{MOF}L^{-1}$. The corresponding acetal product, (dimethoxymethyl)benzene, was formed with 100% selectivity. *Please note*: lines connecting experimental points are only for illustrative purposes and do not intend to indicate any experimental trend.

Table C.7.2. Comparison between the catalytic performance of material **2** with other MOF catalysts, found in the literature, in the acetalization of benzaldehyde.[a]

Catalyst[b]	T (ºC)	BA [M]	Cat. (g_{cat} L^{-1})	Time	Conv. (%)	Sel. (%)	Ref.
5	**35**	**0.4**	**3.3**	**30 min / 2h**	**49 / 96**	**100**	**2**
5	**35**	**0.4**	**20**	**30 min / 1h**	**89 / 94**	**100**	**2**
[Gd(H_4nmp)(H_2O)$_2$]Cl·2H_2O	**35**	**0.4**	**20**	**30 min / 1h**	**84 / 92**	**100**	**3**
[Gd(H_4nmp)(H_2O)$_2$]Cl·2H_2O	**35**	**0.4**	**3.3**	**30 min. / 2h**	**30 / 94**	**100**	**2**
[La_2(H_3nmp)$_2$(H_2O)$_4$]4.5H_2O	**35**	**0.4**	**20**	**30 min / 2h / 20h**	**40 / 62 / 94**	**100**	**1**
MIL-101-Cr	rt	0.5	1.5	1.5 h	73	100	18
MIL-101-Cr-NO_2d	rt	0.5	1.5	1.5 h	99	100	18
MIL-101-Cr-NH_2ps	rt	0.5	1.5	1.5 h	77	100	18
MIL-101(PTA)	25	0.5	1.5	1.5 h	93	100	19
MIL-101	25	0.5	1.5	24 h	80	100	19
MIL-101(Fe)	40	0.6	2	21 h	84	100	11
UIO-66-NO_2	30	0.3	16.7	4 h	100	100	20
UIO-66-NH_2	30	0.3	16.7	18 h	81	100	20
Cu_3(BTC)$_2$	25	0.3	16.7	24 h	88	100	21
Cu_3(BTC)$_2$	25	3.1	16.7	48 h	66	100	21
Cu_3(BTC)$_2$	25	0.3	33.3	7 h	90	100	21
Al_2(BDC)$_3$	25	0.3	16.7	24 h	66	100	21
Fe(BTC)	25	0.3	16.7	24 h	71	100	21
Fe(BTC)	40	0.6	1.8	21 h	84	100	11
MIL-53	25	0.2	10	12 h	50	100	12
BNNS/MIL-53	25	0.2	10	12 h	70	100	12
[Tb_2(dpa)$_3$]	25	0.3	33	10 h	78	100	22

[a] Experimental conditions: T = reaction temperature (*please note:* rt = ambient temperature); BA = initial molar concentration of benzaldehyde; Cat. = catalyst load; Time = reaction time; The catalytic results are reported as conversion of benzaldehyde (Conv.) and selectivity towards (dimethoxymethyl)benzene (Sel.).

[b] The abbreviations of the names of the solid catalysts are the same as those used in the original publications.

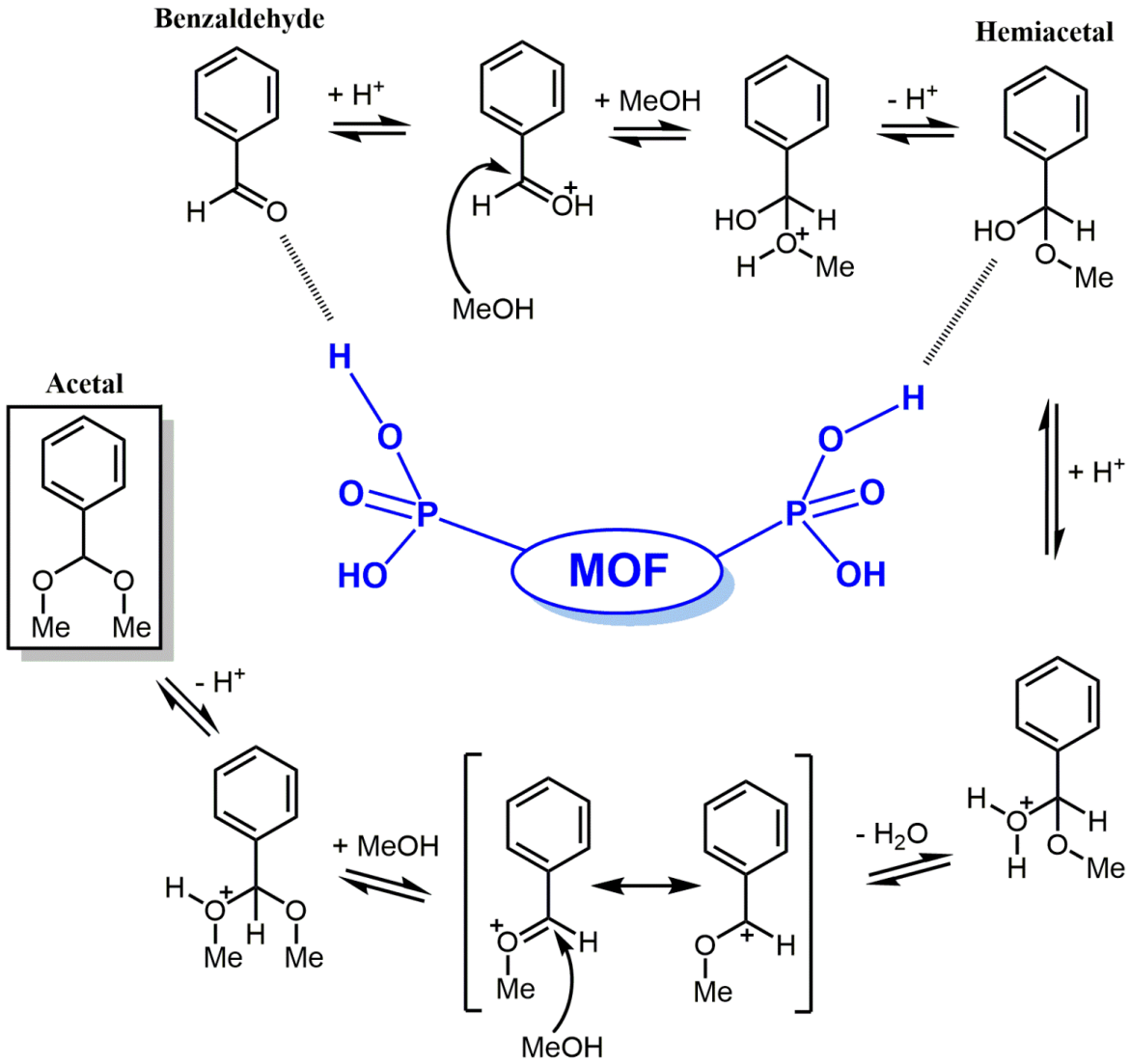

Scheme C.7.1. Mechanistic proposal for the acetalization of benzaldehyde with methanol by Brönsted acid sites (*e.g.* associated with PO_3H_2 groups) [adapted from ref [18]].

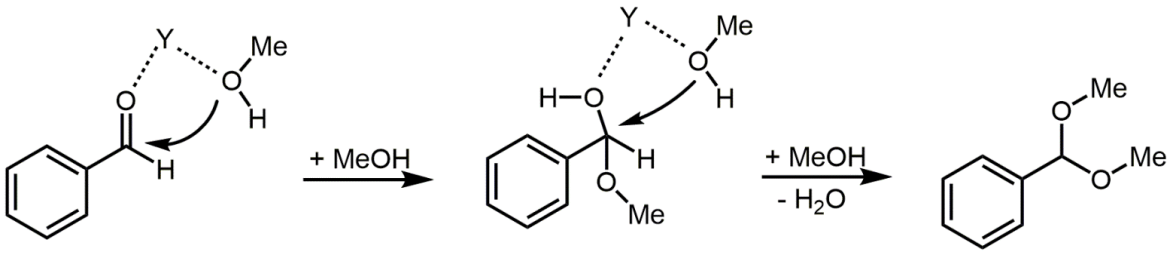

Scheme C.7.2. Mechanistic proposal for the acetalization of benzaldehyde with methanol by Lewis acid sites (*e.g.* associated with $YCl_3 \cdot 6H_2O$) [adapted from ref. [18, 23]].

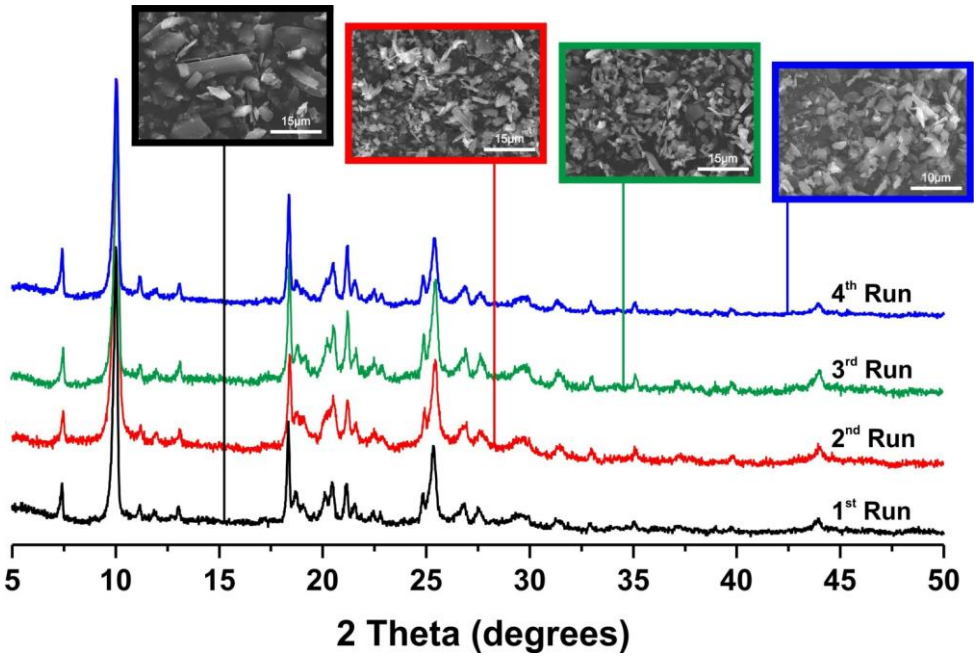

Figure C.7.4. Powder X-ray diffraction patterns and SEM images of the bulk $[Y(H_5btp)]\cdot 2.5H_2O$ (**5**) catalyst used in four consecutive batch runs for benzaldehyde acetalization.

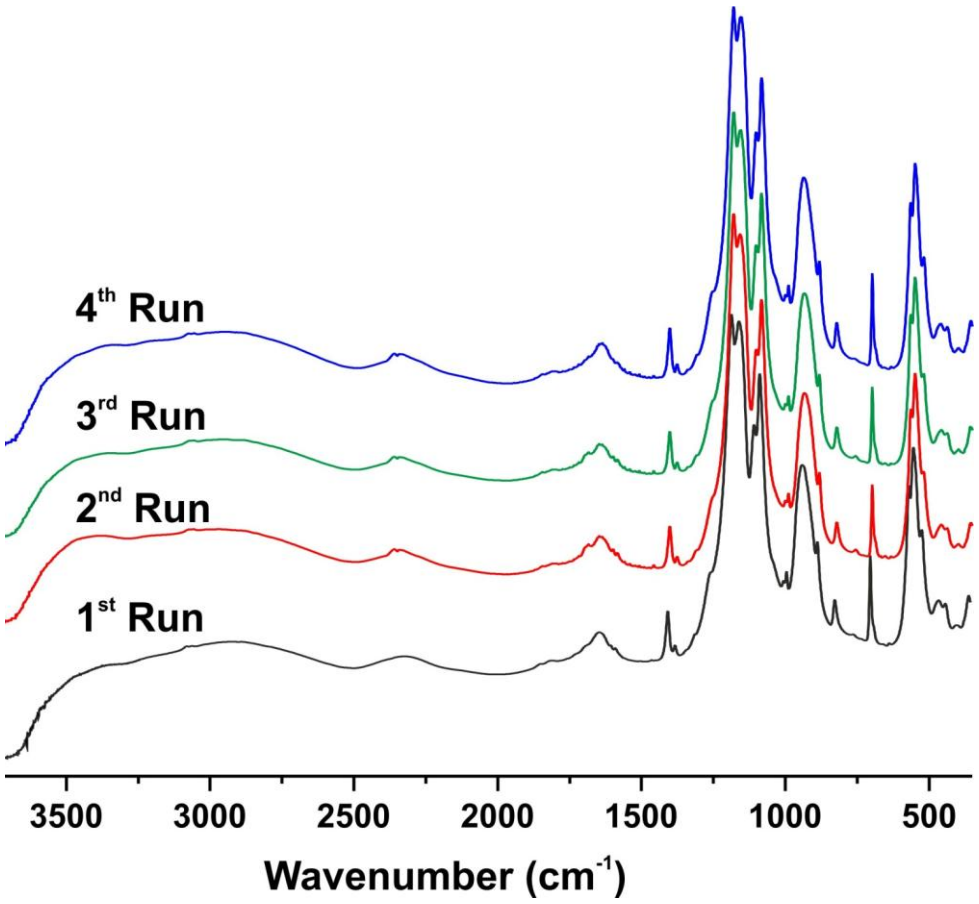

Figure C.7.5. FT-IR spectra (in absorbance, arbitrary units) of the bulk $[Y(H_5btp)]\cdot 2.5H_2O$ (**5**) catalyst used in four consecutive batch runs for benzaldehyde acetalization.

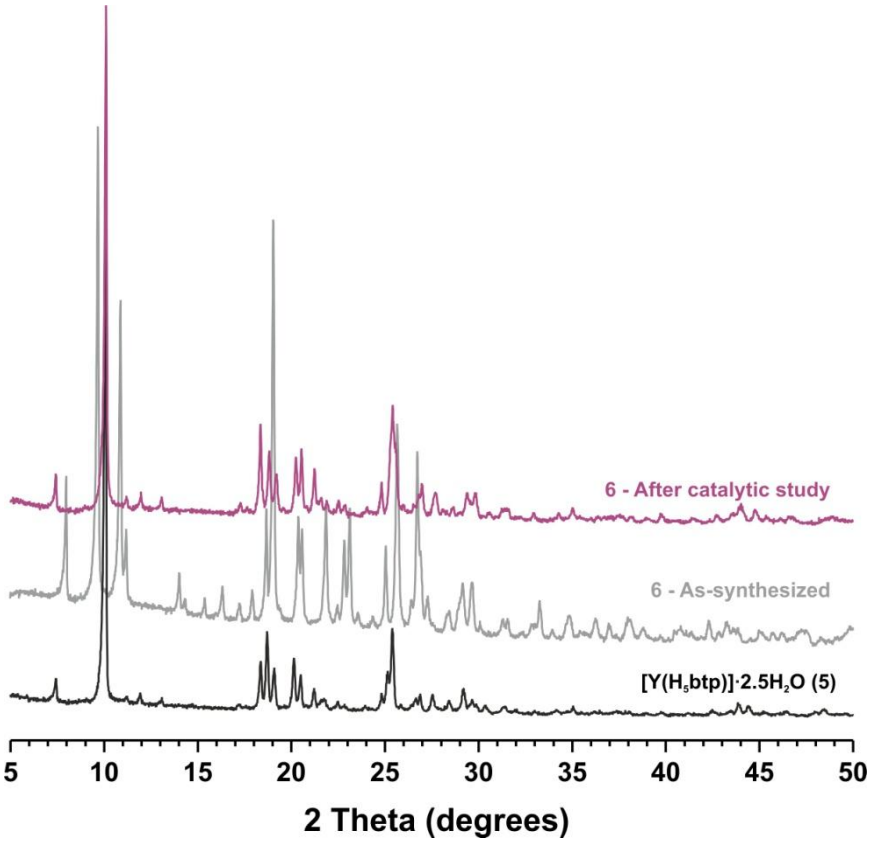

Figure C.7.6. Powder X-ray diffraction patterns of materials (*bottom*) $[Y(H_5btp)]\cdot 2.5H_2O$ (**5**) and (*top*) $(H_3O)[Y_2(H_5btp)(H_4btp)]\cdot H_2O$ (**6**) before and after the catalytic reaction.

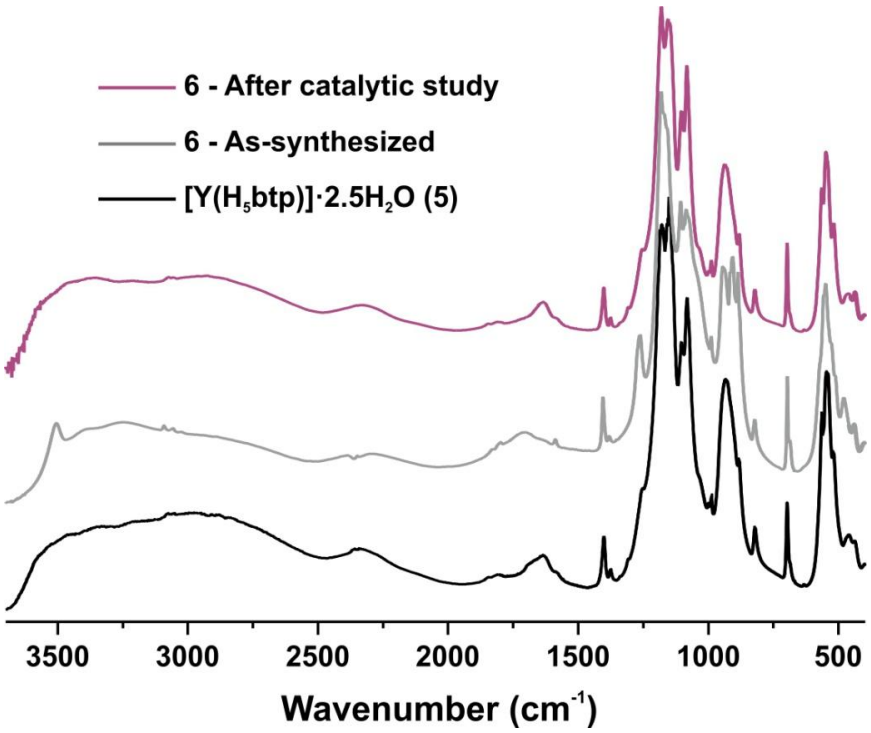

Figure C.7.7. FT-IR spectra (in absorbance, arbitrary units) of the bulk $[Y(H_5btp)]\cdot 2.5H_2O$ (**5**) and $(H_3O)[Y_2(H_5btp)(H_4btp)]\cdot H_2O$ (**6**) before and after the catalytic reaction.

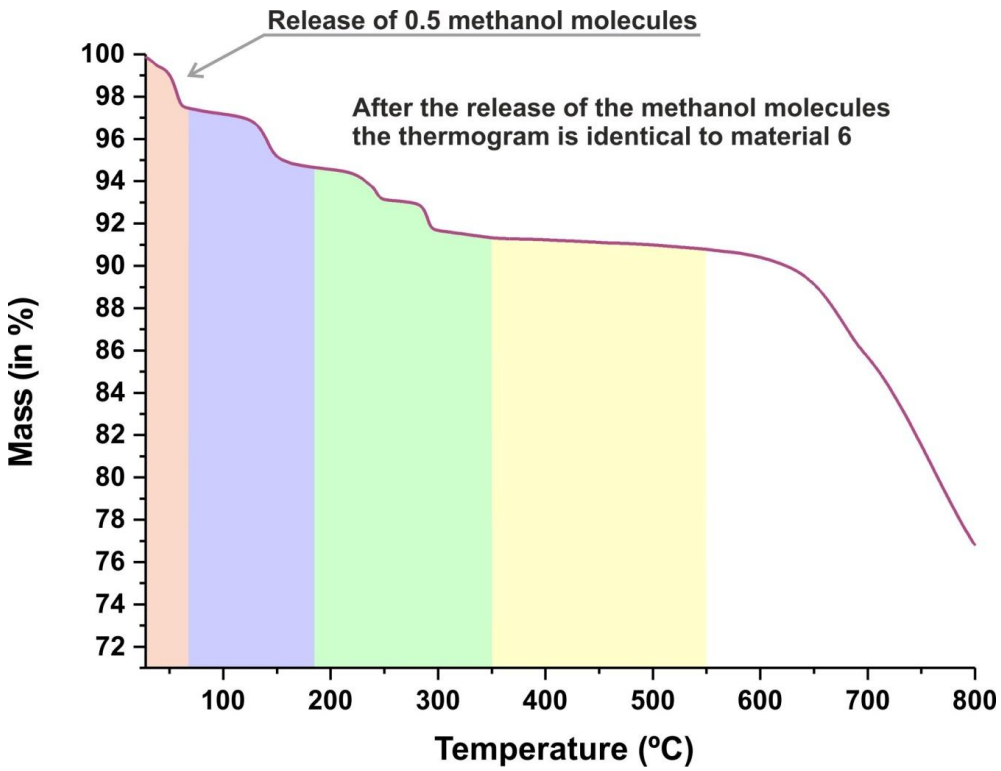

Figure C**.7.8.** Thermogram of [Y(H_5btp)]·H_2O·0.5(MeOH) (**7**) collected between ambient temperature and *ca.* 800 ºC.

C.8. Protonic Conductivity

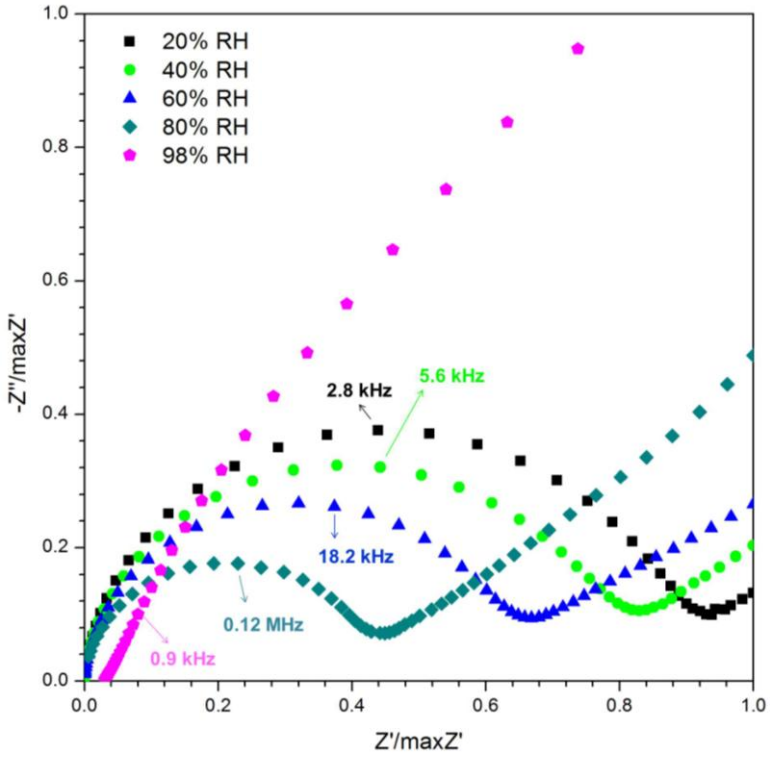

Figure C.8.1. Nyquist plots of the as-prepared (H_3O)[Y_2(H_5btp)(H_4btp)]·H_2O (**6**) sample collected at 80 ºC under variable relative humidities (RH).

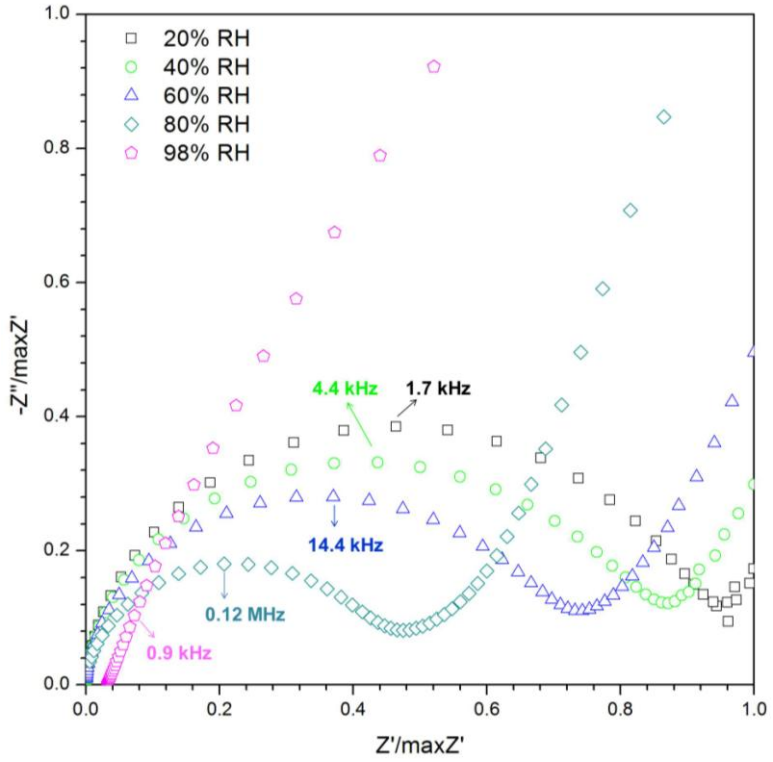

Figure C.8.2. Nyquist plots of the predried $(H_3O)[Y_2(H_5btp)(H_4btp)]\cdot H_2O$ (**6**) sample collected at 80 ºC under variable relative humidities (RH).

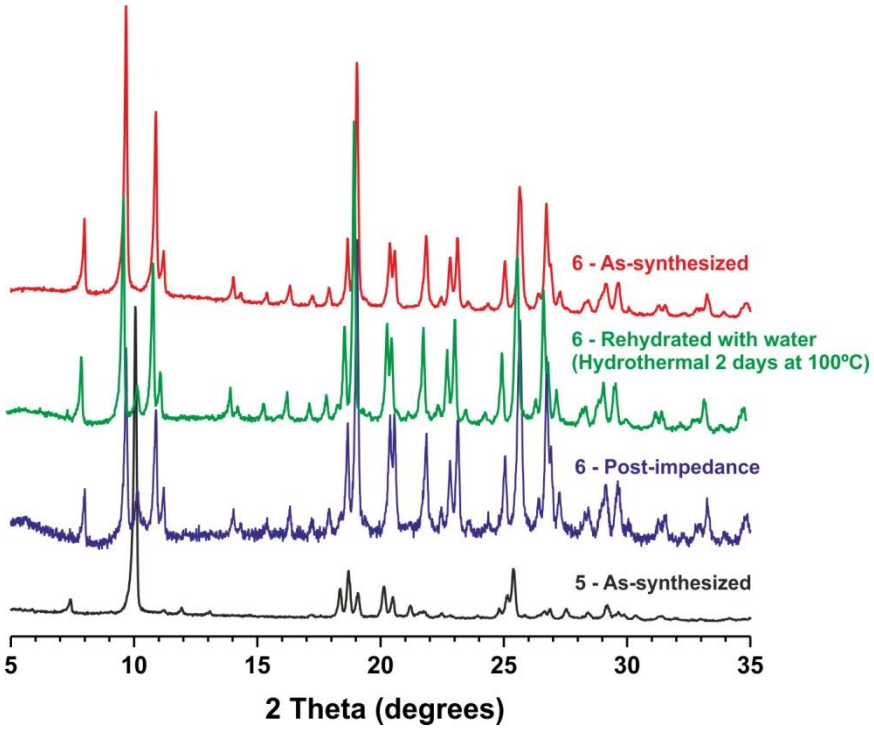

Figure C.8.3. Comparison of the powder X-ray diffraction patterns of $[Y(H_5btp)]\cdot 2.5H_2O$ (**5**) (black line); $(H_3O)[Y_2(H_5btp)(H_4btp)]\cdot H_2O$ (**6**) (red line); **6** exposed to water environment (green line) and **6** after impedance measurements at 94 ºC and 98% RH (blue line). Note that **6** partially transforms into **5** after exposure to wet atmospheres (hydrothermal conditions and after impedance measurements at 98% RH).

Appendix D

D. Chapter 5: Exceptional Thermal Stability of a New Series of Isotypical Lanthanide-Organic Frameworks

D.1. Electron Microscopy Studies: EDS Mapping

EDS mapping studies show a uniform distribution of the heaviest elements among the bulk materials, ultimately evidencing the presence of pure phase, as revealed from the performed powder X-ray diffraction.

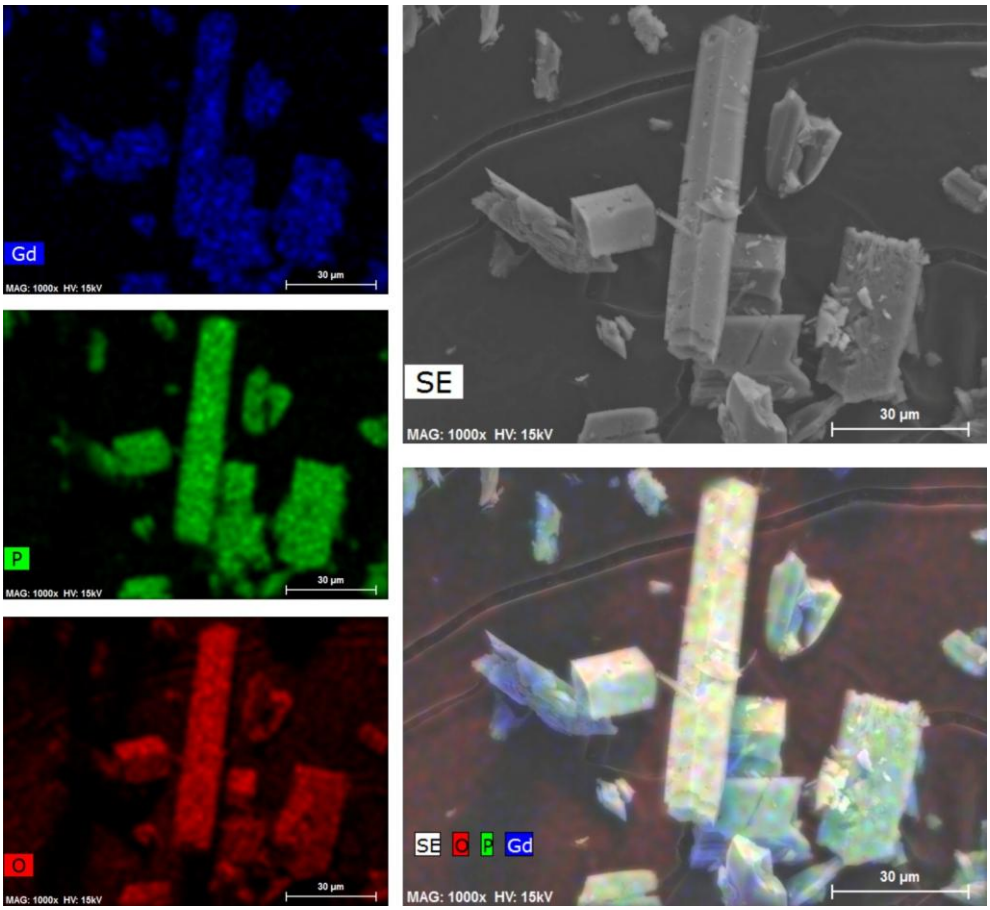

Figure D.1.1. EDS mapping of a representative portion of the $[Gd(H_5btp)]\cdot 2H_2O$ (**8**) bulk material. Gd : P ratio of 1.0 : 3.6.

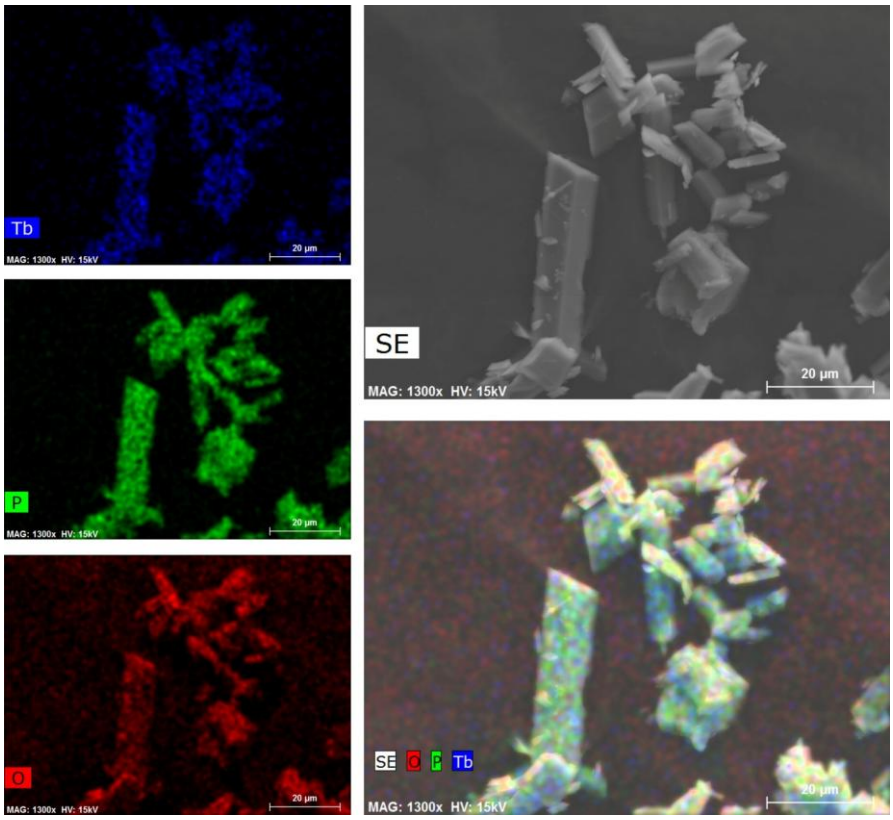

Figure D.1.2. EDS mapping of a representative portion of the $[Tb(H_5btp)]\cdot 2H_2O$ (**9**) bulk material. Tb : P ratio of 1.0 : 3.6.

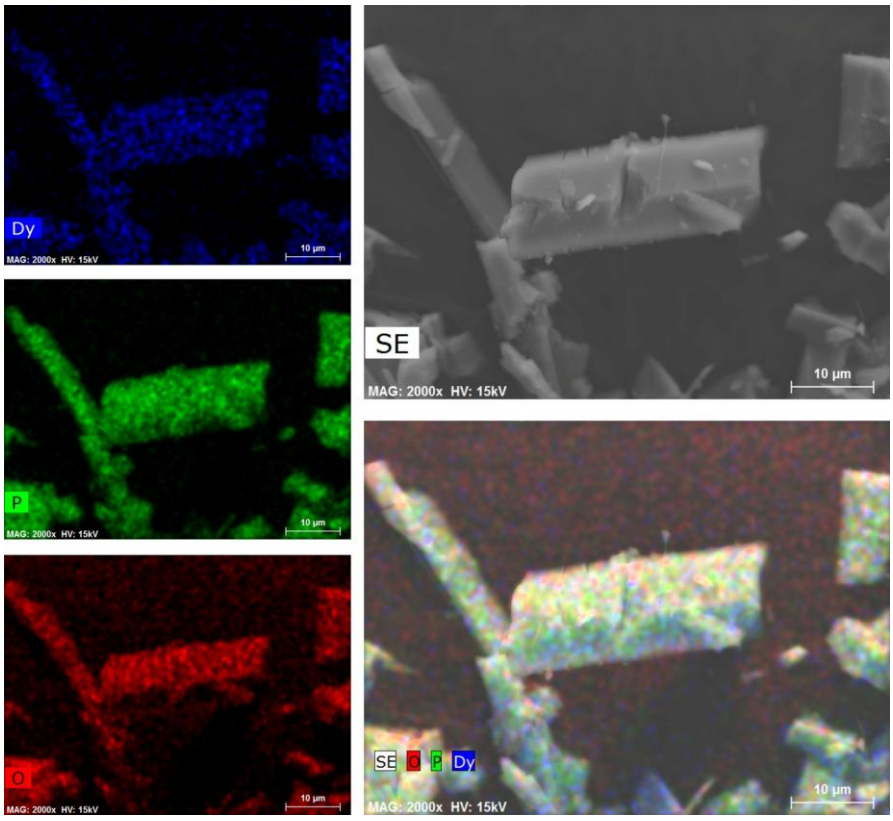

Figure D.1.3. EDS mapping of a representative portion of the $[Dy(H_5btp)]\cdot 2H_2O$ (**10**) bulk material. Dy : P ratio of 1.0 : 3.7.

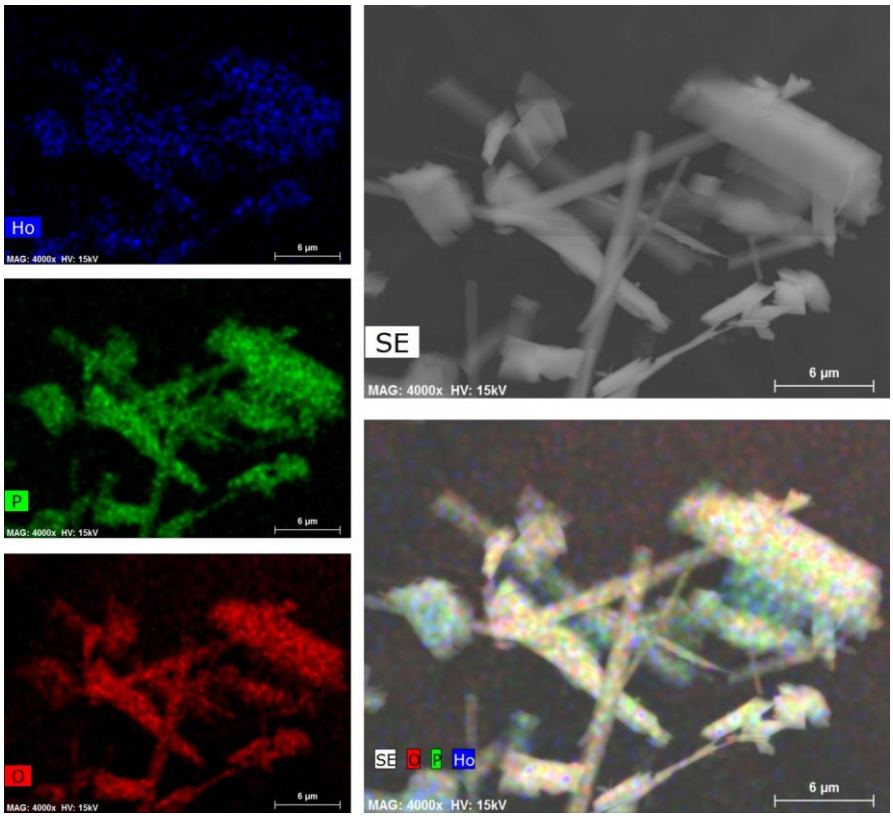

Figure D.1.4. EDS mapping of a representative portion of the $[Ho(H_5btp)]\cdot 2H_2O$ (**11**) bulk material. Ho : P ratio of 1.0 : 3.7.

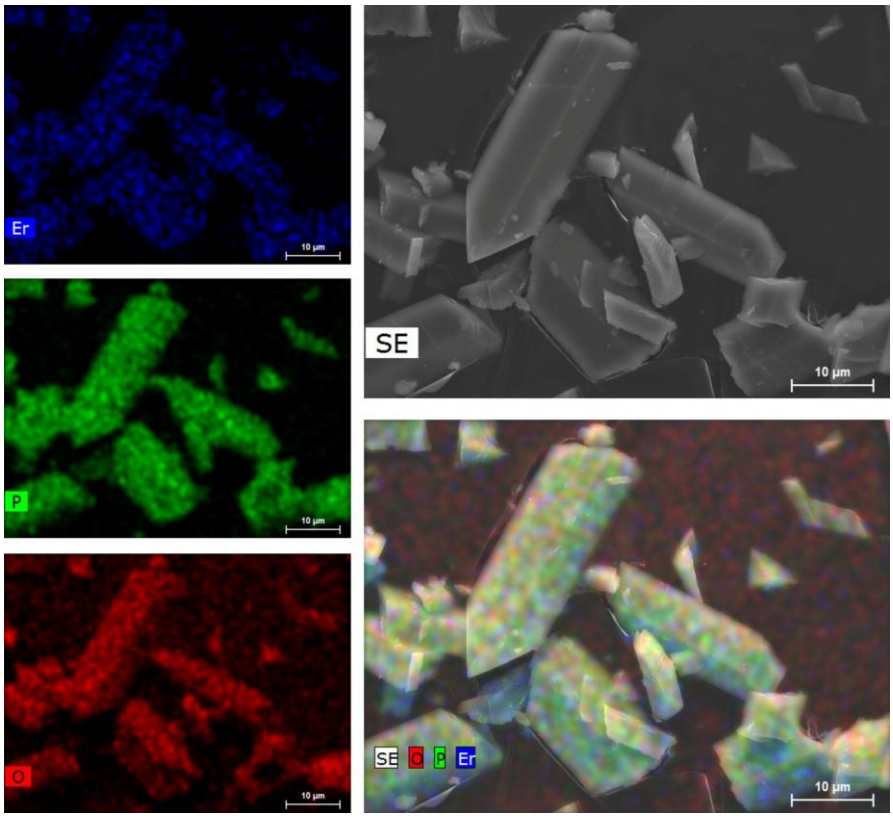

Figure D.1.5. EDS mapping of a representative portion of the $[Er(H_5btp)]\cdot 2H_2O$ (**12**) bulk material. Er : P ratio of 1.0 : 3.6.

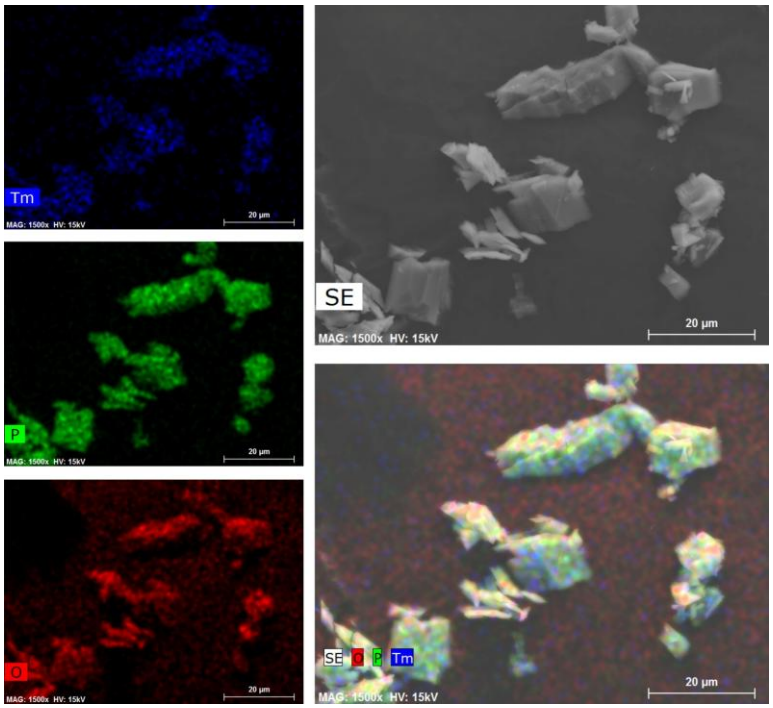

Figure D.1.6. EDS mapping of a representative portion of the [Tm(H_5btp)]·2H_2O (**13**) bulk material. Tm : P ratio of 1.0 : 3.7.

D.2. Vibrational Spectroscopy: FT-IR studies

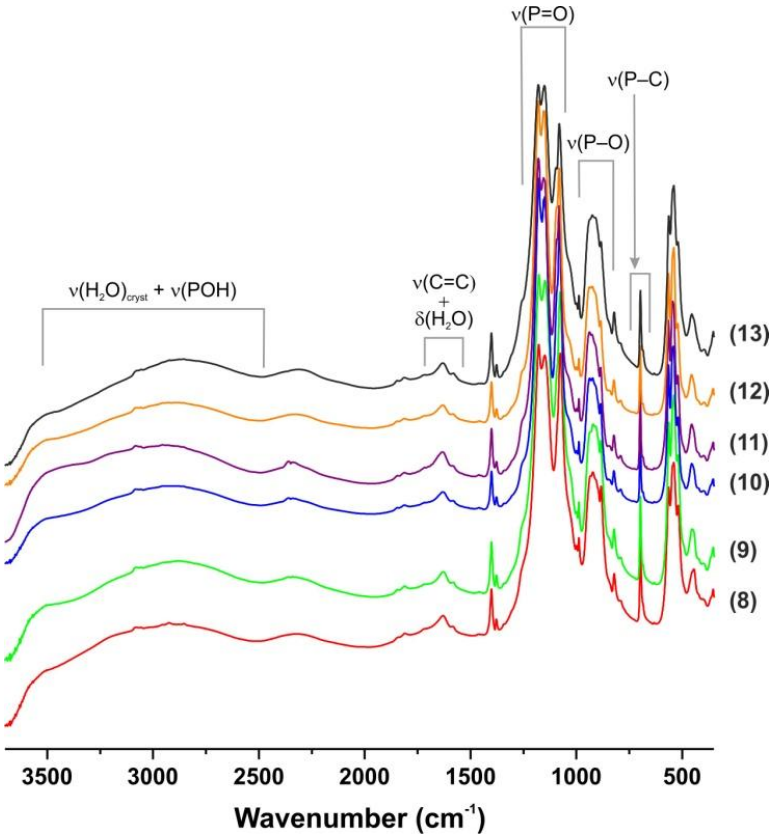

Figure D.2.1. FT-IR spectra (in absorbance, arbitrary units) of the isotypical series of [Ln(H_5btp)]·2H_2O materials [where Ln^{3+} = Gd^{3+} (**8**), Tb^{3+} (**9**), Dy^{3+} (**10**), Ho^{3+} (**11**), Er^{3+} (**12**) and Tm^{3+} (**13**)].

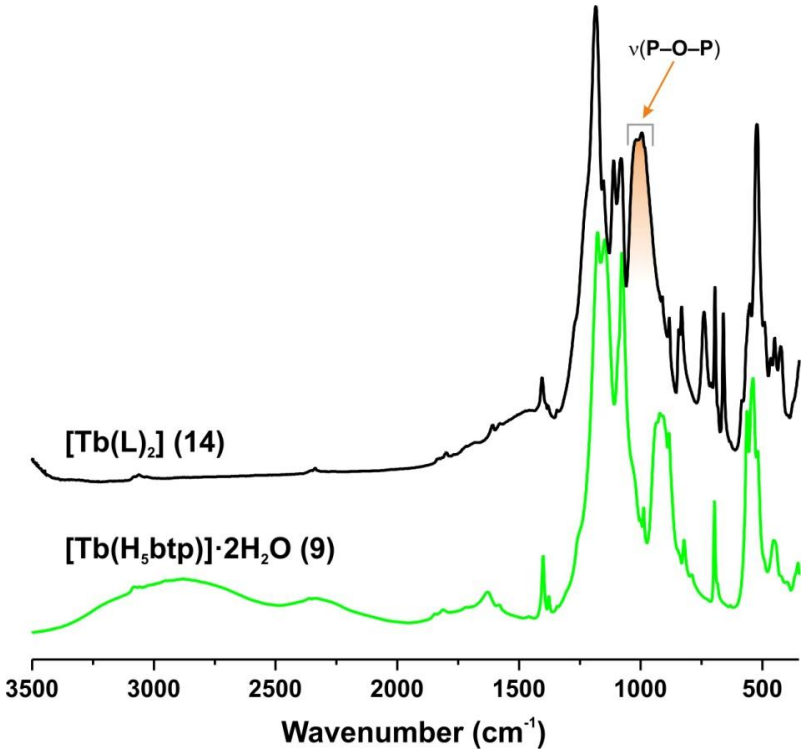

Figure D.2.2. Comparison between the FT-IR spectral features of $[Tb(H_5btp)]\cdot 2H_2O$ (**9**) with $[Tb(L)_2]$ (**14**).

D.3. Thermogravimetry and Thermodiffractometry

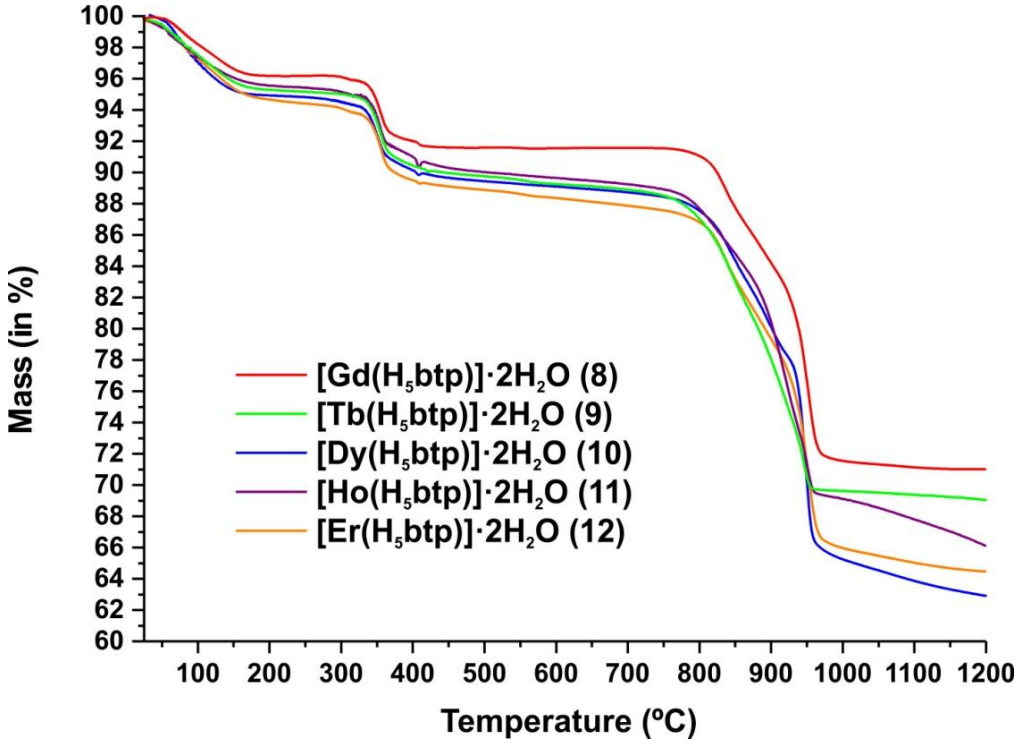

Figure D.3.1. Thermograms of the isotypical series of $[Ln(H_5btp)]\cdot 2H_2O$ materials [where Ln^{3+} = Gd^{3+} (**8**), Tb^{3+} (**9**), Dy^{3+} (**10**), Ho^{3+} (**11**) and Er^{3+} (**12**)] collected between ambient temperature and *ca.* 1200 ºC.

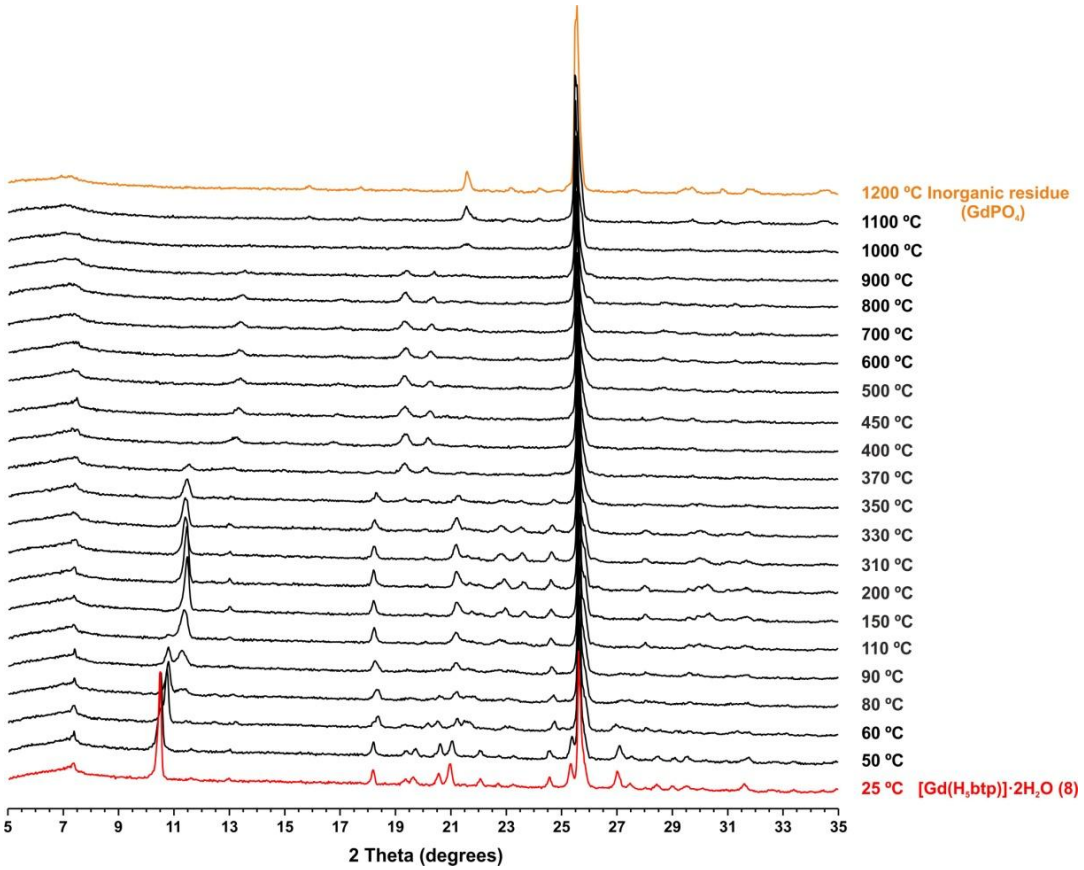

Figure D.3.2. Variable-temperature powder X-ray diffraction study of $[Gd(H_5btp)]\cdot 2H_2O$ (**8**) collected between ambient temperature and *ca.* 1200 ºC.

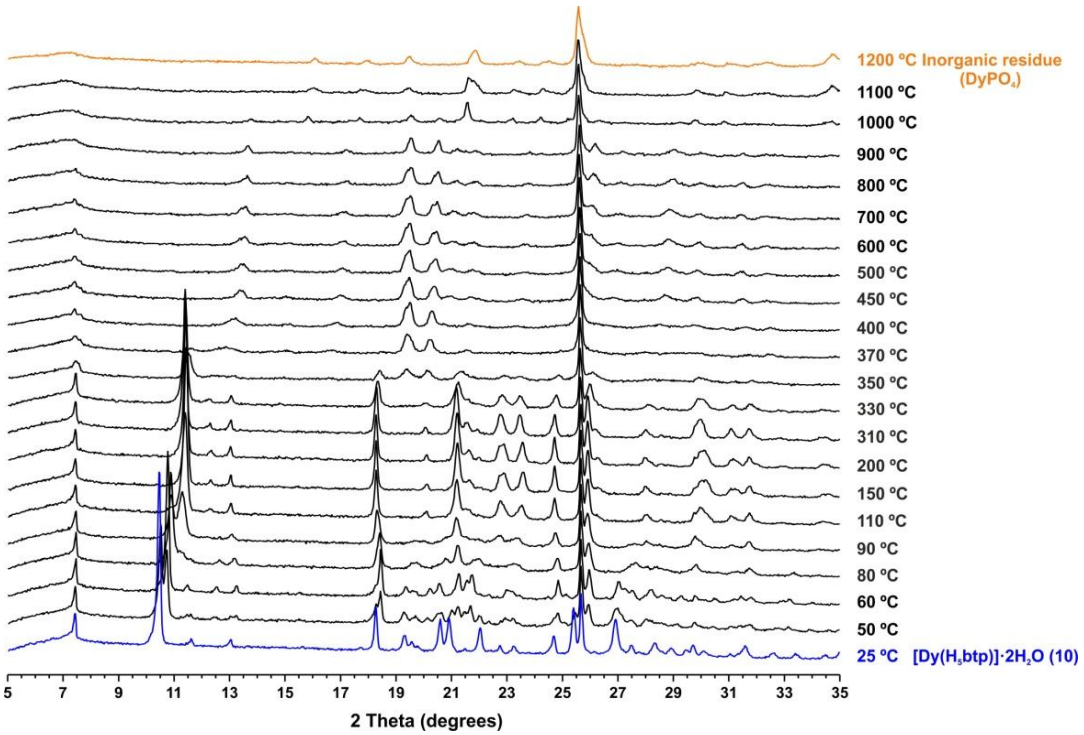

Figure D.3.3. Variable-temperature powder X-ray diffraction study of $[Dy(H_5btp)]\cdot 2H_2O$ (**10**) collected between ambient temperature and *ca.* 1200 ºC.

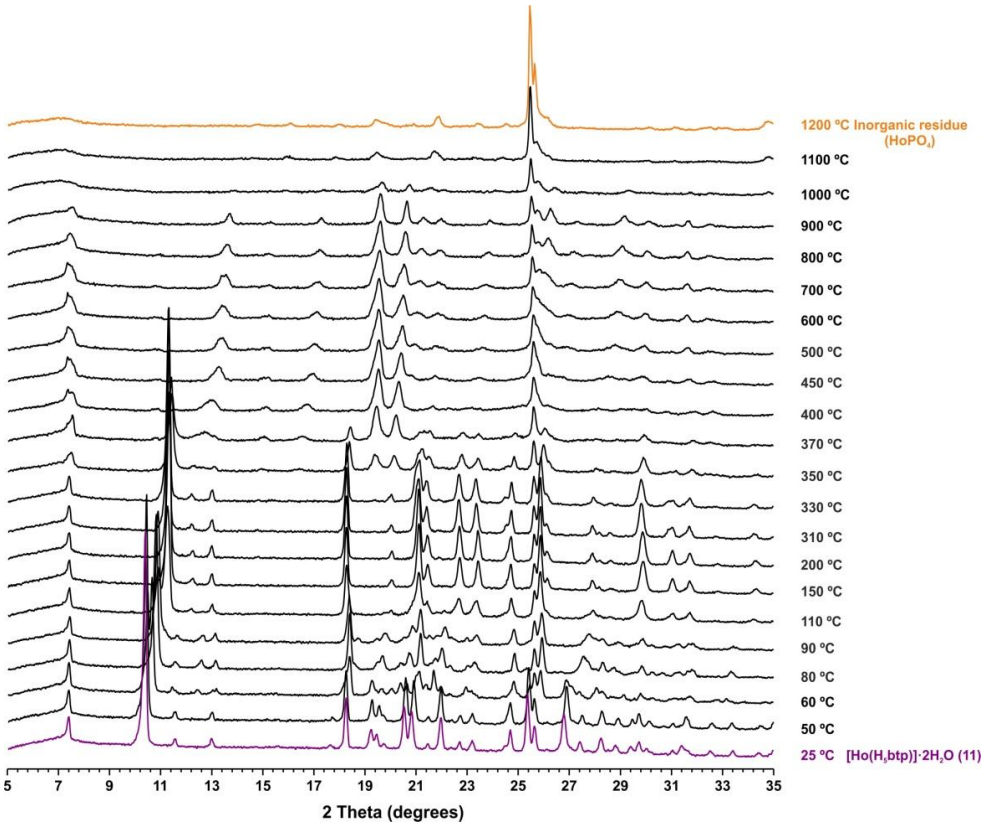

Figure D.3.4. Variable-temperature powder X-ray diffraction study of $[Ho(H_5btp)]\cdot 2H_2O$ (**11**) collected between ambient temperature and *ca.* 1200 ºC.

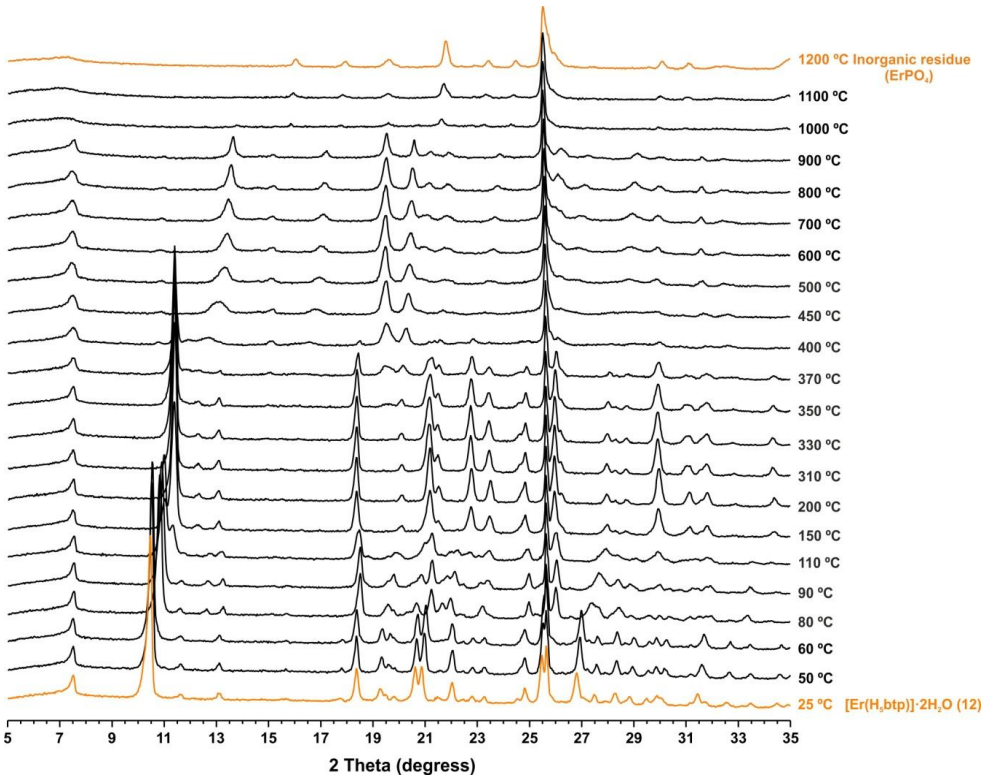

Figure D.3.5. Variable-temperature powder X-ray diffraction study of $[Er(H_5btp)]\cdot 2H_2O$ (**12**) collected between ambient temperature and *ca.* 1200 ºC.

D.4. Crystallographic Details

Table D.4.1. Crystal data collection and structure refinement details for $[Tb(H_5btp)]\cdot 2H_2O$ (**9**).

Formula	$C_{12}H_{15}O_{14}P_4Tb$
Formula weight	666.04
Temperature / K	180(2)
Crystal system	Monoclinic
Space group	*C*2/*c*
a / Å	10.045(4)
b / Å	24.099(8)
c / Å	9.159(3)
α / º	90
β / º	115.052(9)
γ / º	90
Volume / Å^3	2008.5(11)
Z	4
ρ_{calc} / g cm^{-3}	2.203
μ(Mo Kα)/mm^{-1}	3.912
Crystal type	Colourless needle
Crystal size / mm	0.06×0.02×0.10
θ range (°)	3.58 – 25.35
Index ranges	$-12 \le h \le 12$
	$-28 \le k \le 28$
	$-10 \le l \le 11$
Collected Reflections	13966
Independent Reflections	1836 (R_{int} = 0.0625)
Completeness to θ = 25.24	99.7%
Final *R* indices [$I > 2\sigma(I)$]	*R*1 = 0.0393
	*wR*2 = 0.0784
Final *R* indices (all data)	*R*1 = 0.0568
	*wR*2 = 0.0844
Largest diff. peak and hole /eÅ^{-3}	1.500 and -0.749

[a] $R1 = \sum \| |F_o| - |F_c| \| / \sum |F_o|$

[b] $wR2 = \sqrt{\sum \left[w\left(F_o^2 - F_c^2\right)^2 \right] / \sum \left[w\left(F_o^2\right)^2 \right]}$

[c] $w = 1/\left[\sigma^2\left(F_o^2\right) + \left(mP\right)^2 + nP \right]$ where $P = \left(F_o^2 + 2F_c^2\right)/3$

Table D.4.2. Hydrogen bonding geometry (distances in Å and angles in degrees) of $[Tb(H_5btp)]\cdot 2H_2O$ (**9**).

D-H···A	$d_{D\cdots A}$	<(DHA)
O3–H3···O1W^{vi}	2.86(2)	162
O3–H3···O2W^{vi}	2.97(2)	141
O5–H5···O5^{iii}	2.637(9)	174
O6–H6···O1W^{vii}	2.83(2)	161
O6–H6···O2W^{vii}	2.814(19)	146

[a] Symmetry transformations used to generate equivalent atoms:(iii) -*x*+1, *y*, -*z*+3/2 (vi) -*x*+2, -*y*+1, -*z*+3; (vii) –*x*+*2*, *y*, -*z*+5/2.

Table D.4.3. Selected bond lengths (in Å) and angles (in degrees) for the coordination environment present in $[Tb(H_5btp)]\cdot 2H_2O$ (**9**).

Tb1-O1^{i}	2.225(4)	Tb1-O2^{v}	2.301(5)
Tb1-O1^{ii}	2.225(4)	Tb1-O4	2.234(4)
Tb1-O2^{iv}	2.301(5)	Tb1-O4^{iii}	2.233(4)
O1^{i}-Tb1-O1^{ii}	87.5(3)	O1^{ii}-Tb1-O4^{iii}	172.7(2)
O1^{i}-Tb1-O2^{iv}	102.79(18)	O2^{iv}-Tb1-O2^{v}	163.3(2)
O1^{ii}-Tb1-O2^{iv}	89.32(19)	O4^{iii}-Tb1-O4	90.4(3)
O1^{i}-Tb1-O2^{v}	89.32(19)	O4^{iii}-Tb1-O2^{iv}	83.87(19)
O1^{ii}-Tb1-O2^{v}	102.79(19)	O4-Tb1-O2^{iv}	84.41(18)
O1^{i}-Tb1-O4^{iii}	91.50(18)	O4^{iii}-Tb1-O2^{v}	84.41(18)
O1^{i}-Tb1-O4	172.7(2)	O4-Tb1-O2^{v}	83.87(19)
O1^{ii}-Tb1-O4	91.50(18)		

[a] Symmetry transformations used to generate equivalent atoms: (i) –*x*+1, -*y*+*1*,- *z*+2*;* (ii) *x*, -*y*+1, *z*-1/2*;* (iii) -*x*+1, *y*, -*z*+3/2*;* (iv) *x*, *y*, *z*-1; (v) -*x*+1, *y*, -*z*+5/2.

Appendix E

E. Chapter 6: Recently Synthesized Lanthanide-Organic Frameworks: New isotypical families of compounds

E.1. Electron Microscopy Studies: EDS Mapping

EDS mapping studies show a uniform distribution of the heaviest elements among the bulk materials, ultimately evidencing the presence of pure phase, as revealed from the performed powder X-ray diffraction.

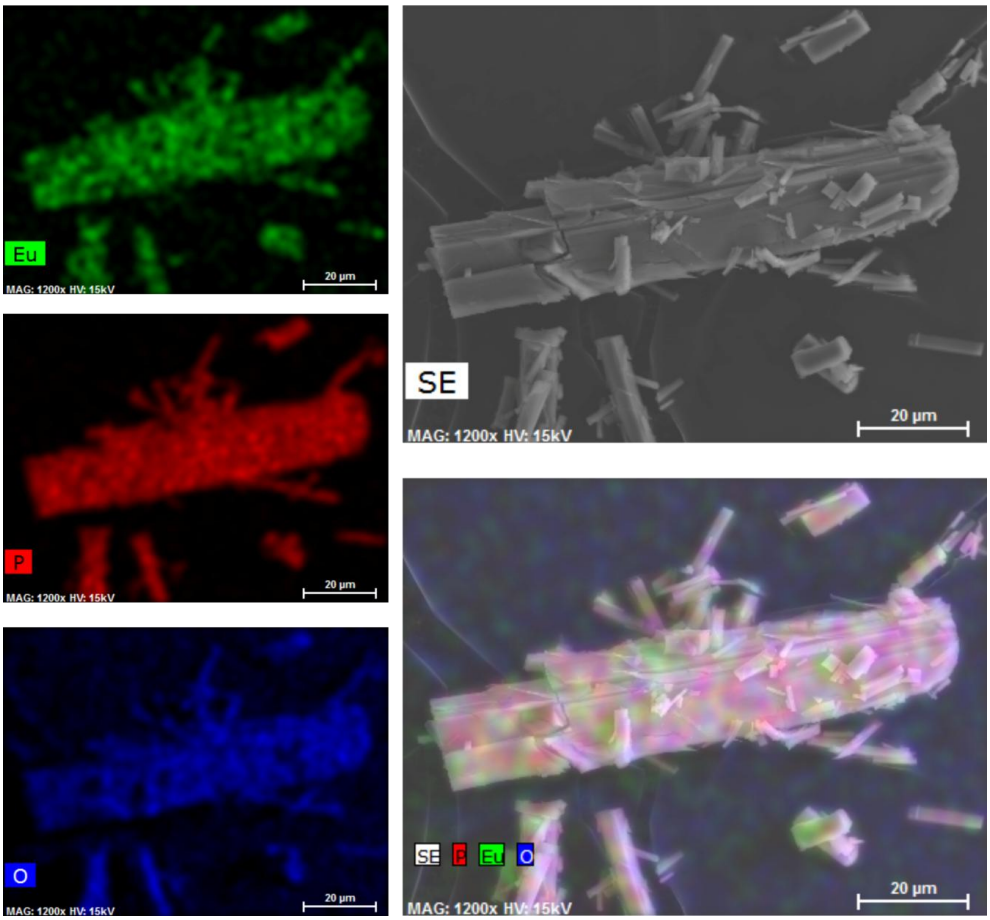

Figure E.1.1. EDS mapping of a representative portion of the $[Eu_7(H_5btp)_5(H_6btp)_3(H_2O)_{12}]\cdot 23.5H_2O\cdot MeOH$ (**15**) bulk material. Eu : P ratio of 1.0 : 4.6.

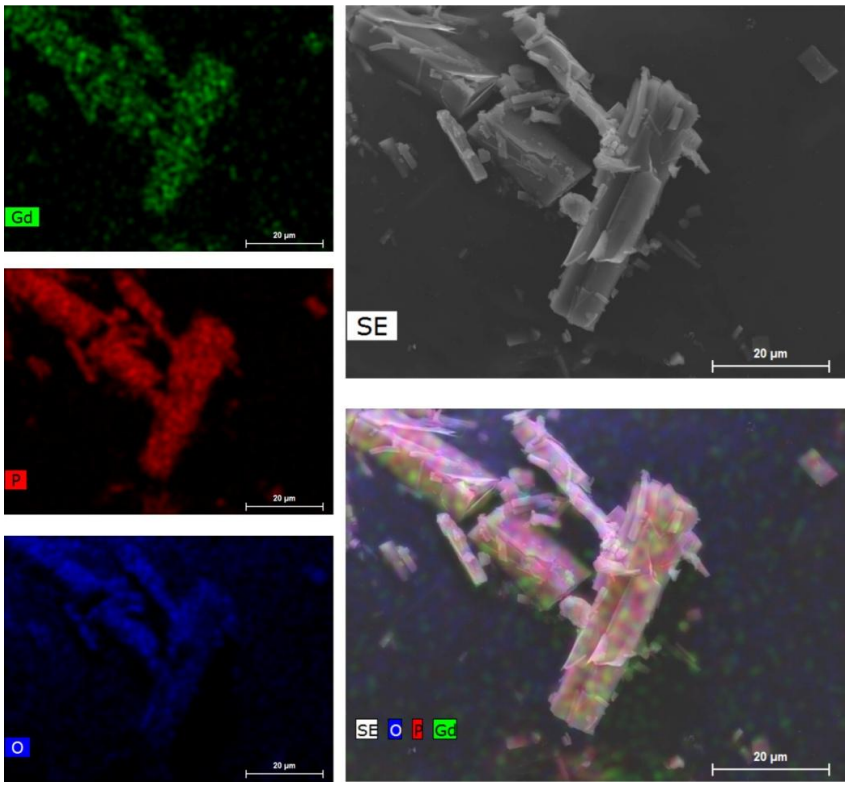

Figure E.1.2. EDS mapping of a representative portion of the $[Gd_7(H_5btp)_5(H_6btp)_3(H_2O)_{12}]\cdot 23.5H_2O\cdot MeOH$ (**16**) bulk material. Gd : P ratio of 1.0 : 4.2.

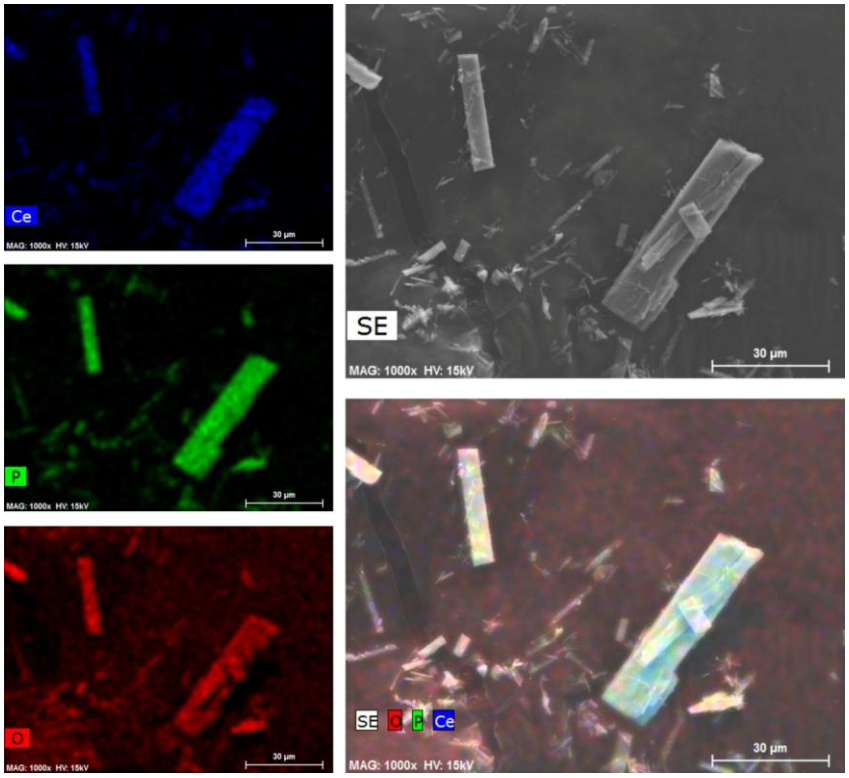

Figure E.1.3. EDS mapping of a representative portion of the $[Ce_4(H_3btp)(H_4btp)(H_5btp)(H_2O)_8]\cdot 3H_2O$ (**17**) bulk material. Ce : P ratio of 1.0 : 2.6.

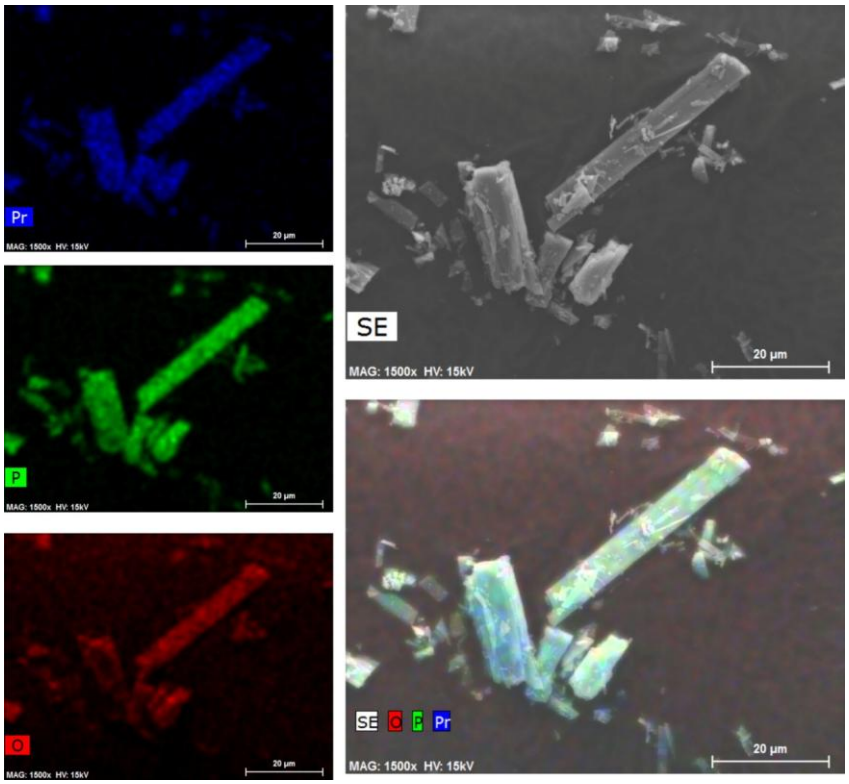

Figure E.1.4. EDS mapping of a representative portion of the $[Pr_4(H_3btp)(H_4btp)(H_5btp)(H_2O)_8]\cdot 3H_2O$ (**18**) bulk material. Pr : P ratio of 1.0 : 2.7.

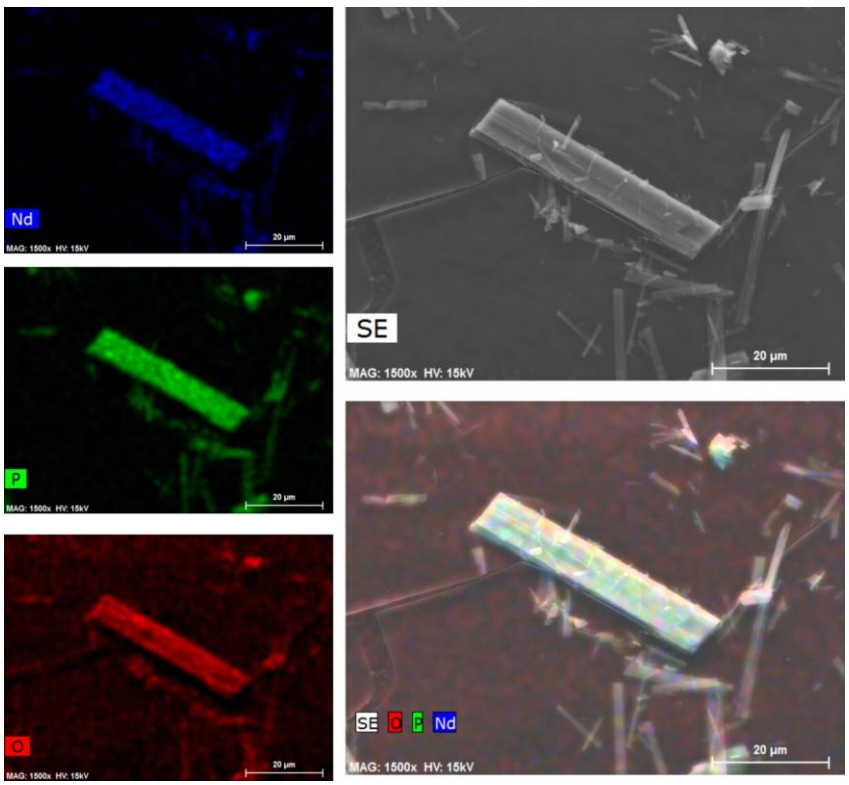

Figure E.1.5. EDS mapping of a representative portion of the $[Nd_4(H_3btp)(H_4btp)(H_5btp)(H_2O)_8]\cdot 3H_2O$ (**19**) bulk material. Nd : P ratio of 1.0 : 2.7.

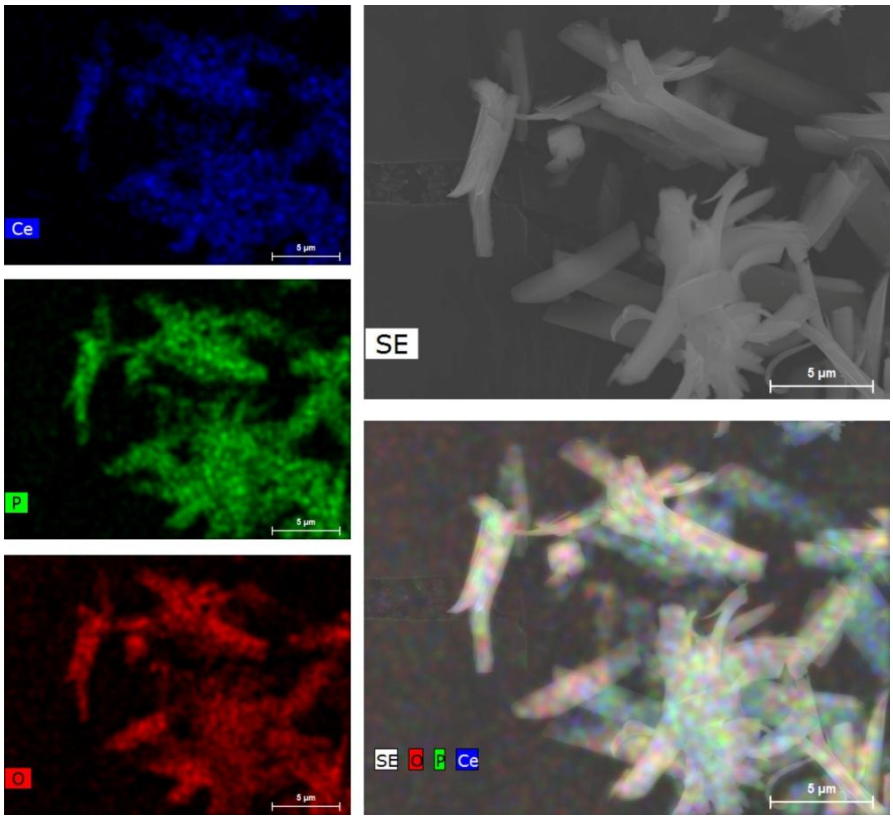

Figure E.1.6. EDS mapping of a representative portion of the $[Ce_2(H_4ptp)(ox)(H_2O)_6]\cdot 5H_2O$ (**20**) bulk material. Ce : P ratio of 1.0 : 1.6.

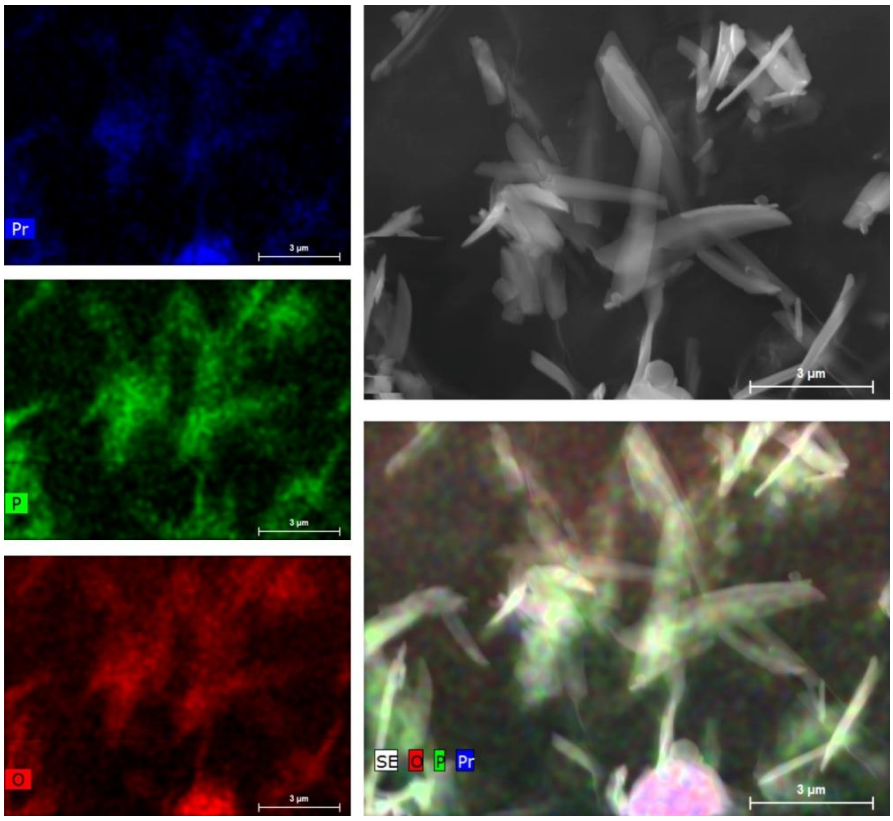

Figure E.1.7. EDS mapping of a representative portion of the $[Pr_2(H_4ptp)(ox)(H_2O)_6]\cdot 5H_2O$ (**21**) bulk material. Pr : P ratio of 1.0 : 1.6.

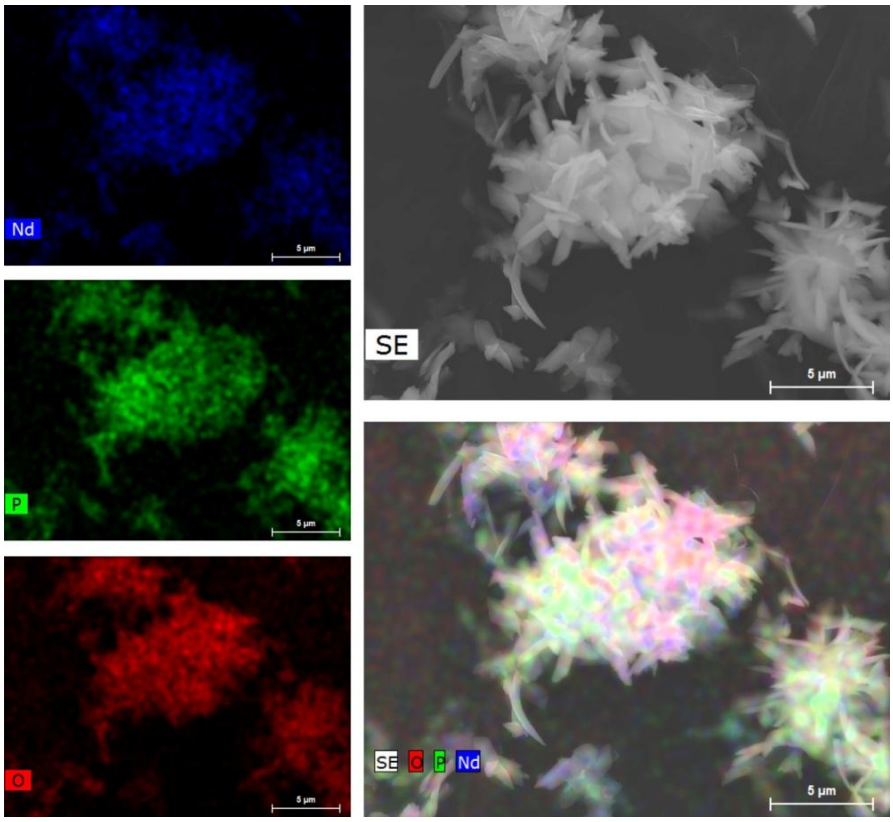

Figure E.1.8. EDS mapping of a representative portion of the $[Nd_2(H_4ptp)(ox)(H_2O)_6]\cdot 5H_2O$ (**22**) bulk material. Nd : P ratio of 1.0 : 1.7.

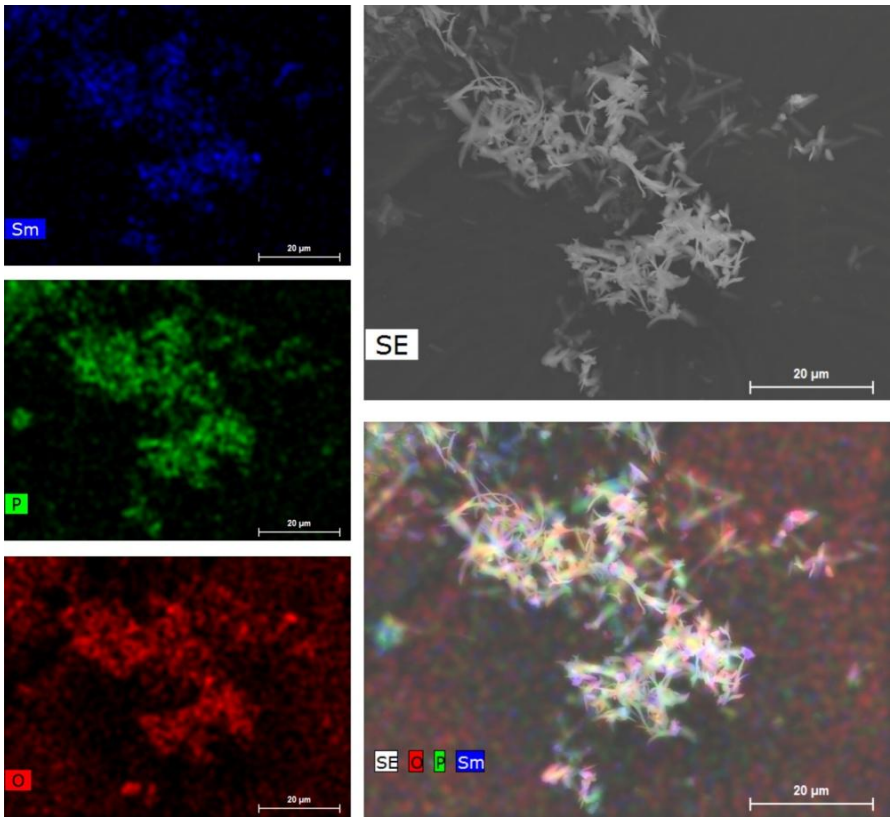

Figure E.1.9. EDS mapping of a representative portion of the $[Sm_2(H_4ptp)(ox)(H_2O)_6]\cdot 5H_2O$ (**23**) bulk material. Sm : P ratio of 1.0 : 1.7.

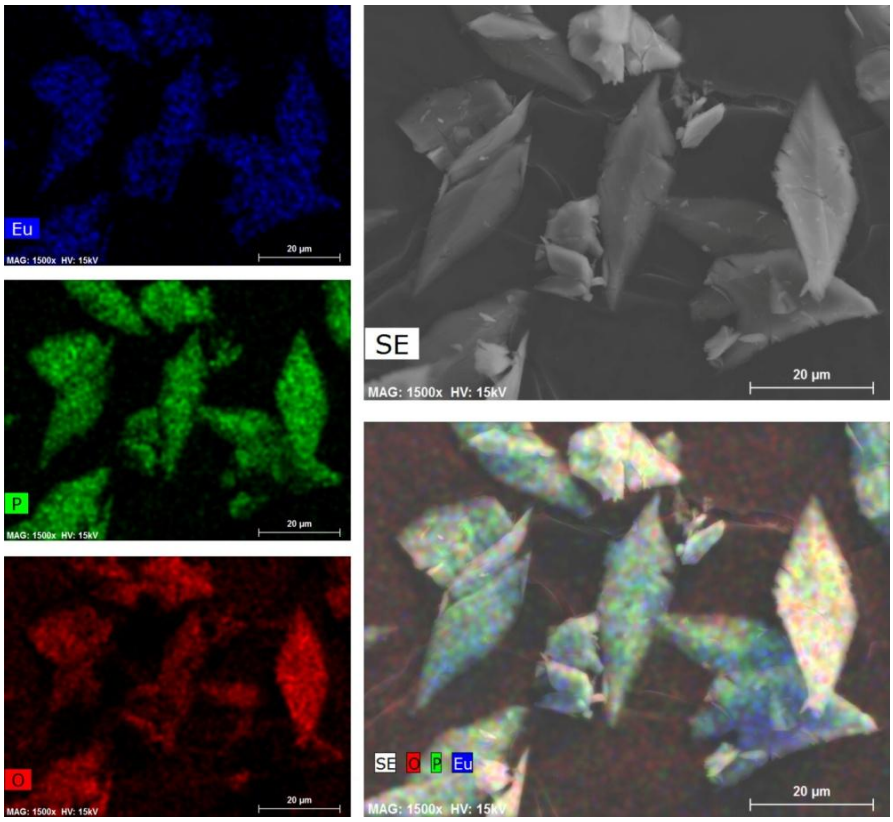

Figure E.1.10. EDS mapping of a representative portion of the $[Eu_2(H_4ptp)(ox)(H_2O)_6]\cdot 5H_2O$ (**24**) bulk material. Eu : P ratio of 1.0 : 1.9.

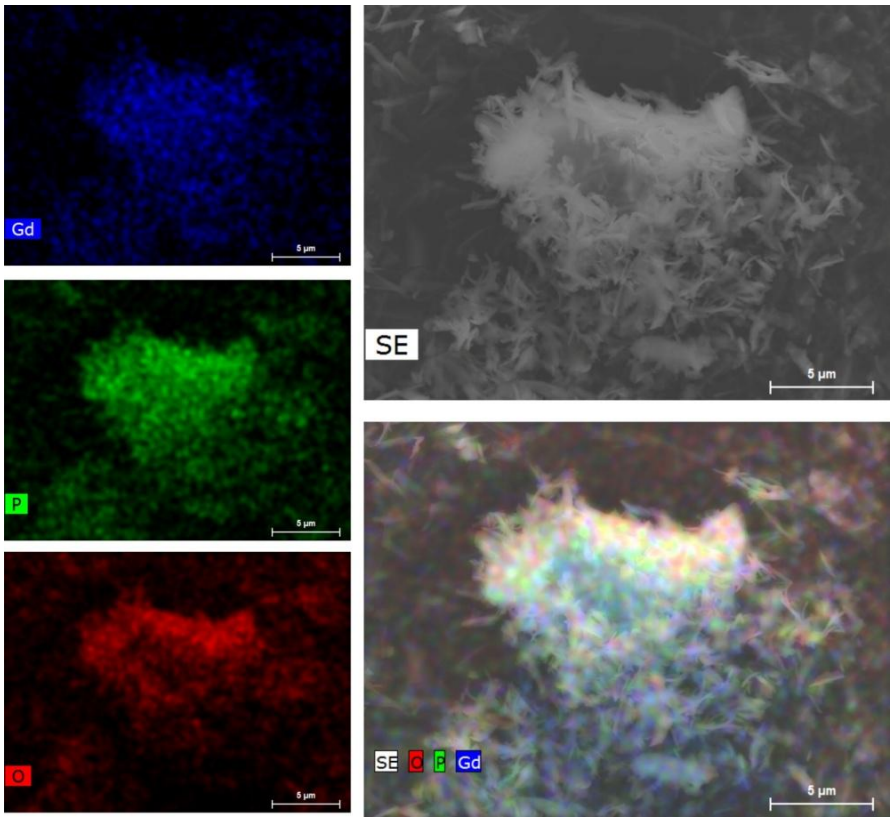

Figure E.1.11. EDS mapping of a representative portion of the $[Gd_2(H_4ptp)(ox)(H_2O)_6]\cdot 5H_2O$ (**25**) bulk material. Gd : P ratio of 1.0 : 1.8.

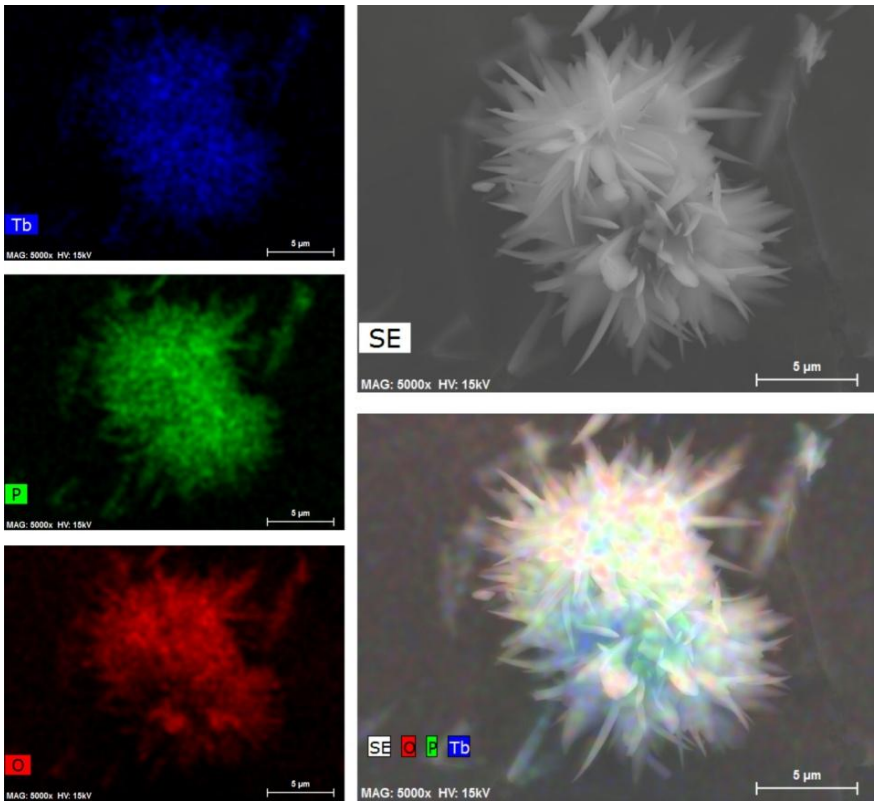

Figure E.1.12. EDS mapping of a representative portion of the $[Tb_2(H_4ptp)(ox)(H_2O)_6]\cdot 5H_2O$ (**26**) bulk material. Tb : P ratio of 1.0 : 1.8.

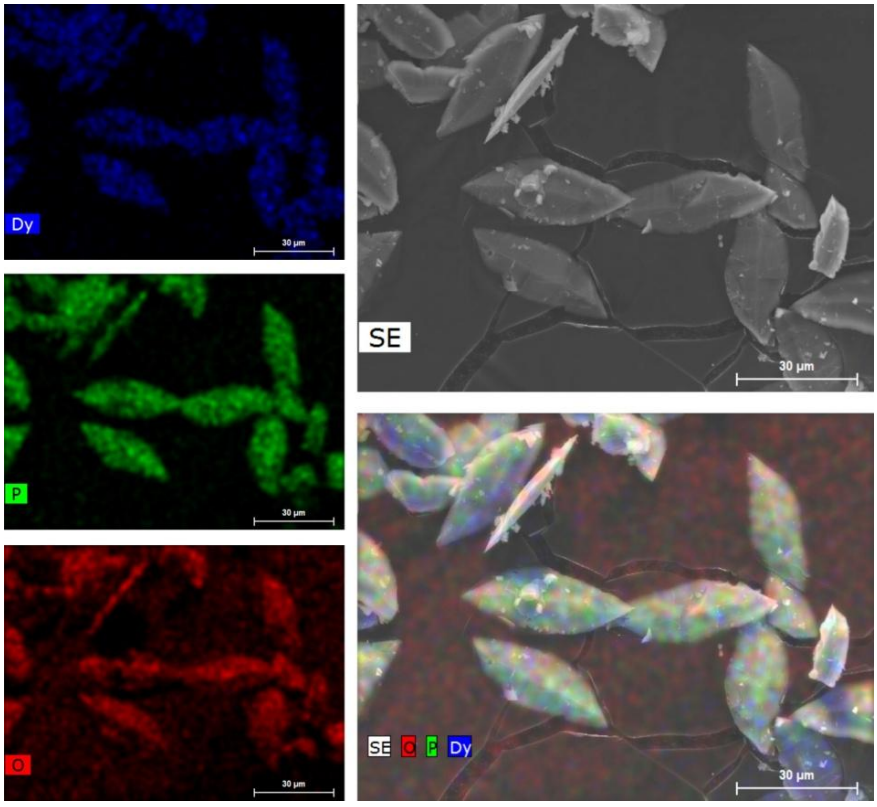

Figure E.1.13. EDS mapping of a representative portion of the $[Dy_4(H_3btp)(H_4btp)(H_5btp)(H_2O)_8]\cdot 3H_2O$ (**27**) bulk material. Dy : P ratio of 1.0 : 1.7.

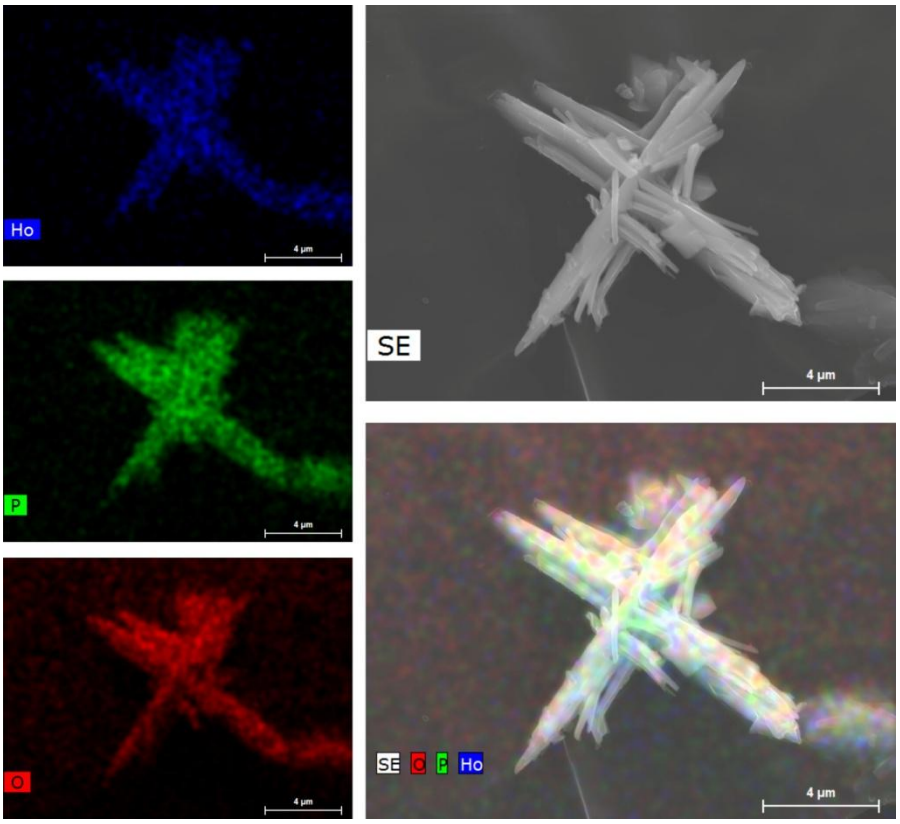

Figure E.1.14. EDS mapping of a representative portion of the $[Ho_2(H_4ptp)(ox)(H_2O)_6]\cdot H_2O$ (**28**) bulk material. Ho : P ratio of 1.0 : 1.8.

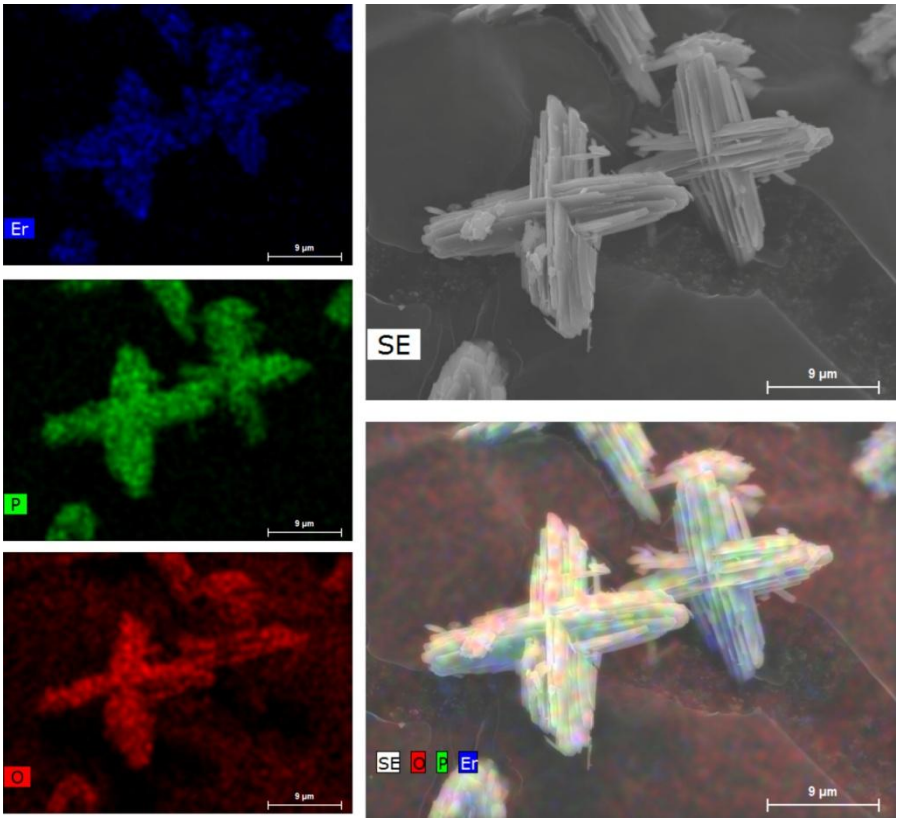

Figure E.1.15. EDS mapping of a representative portion of the $[Er_2(H_4ptp)(ox)(H_2O)_6]\cdot H_2O$ (**29**) bulk material. Er : P ratio of 1.0 : 1.7.

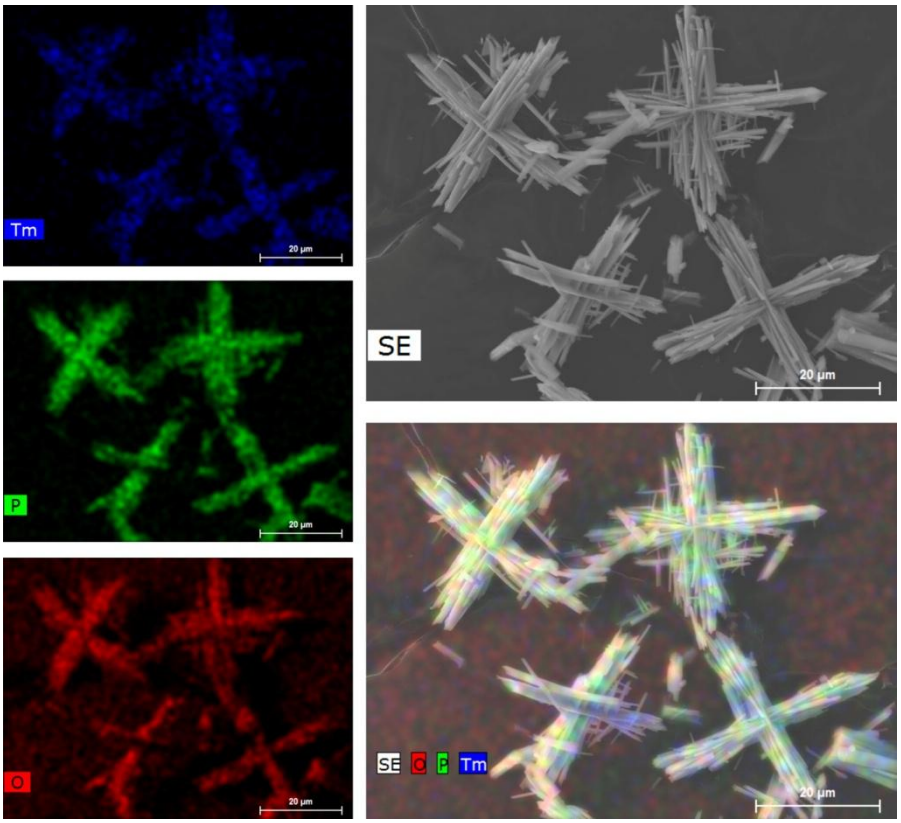

Figure E.1.16. EDS mapping of a representative portion of the $[Tm_2(H_4ptp)(ox)(H_2O)_6]\cdot H_2O$ (**30**) bulk material. Tm : P ratio of 1.0 : 1.8.

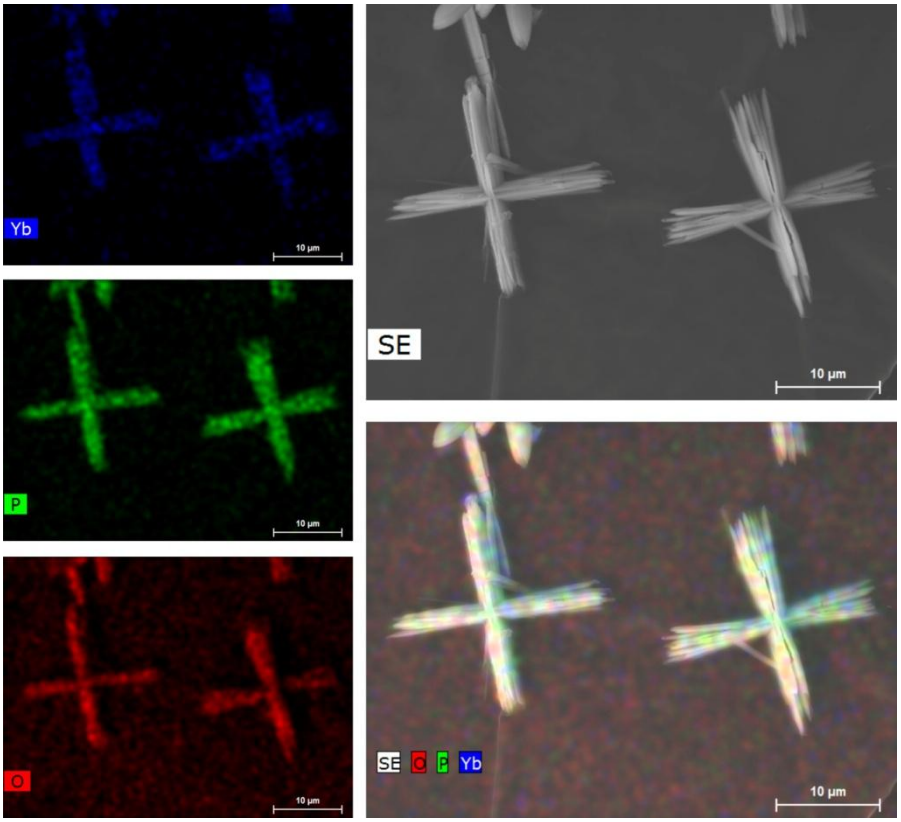

Figure E.1.17. EDS mapping of a representative portion of the $[Yb_2(H_4ptp)(ox)(H_2O)_6]\cdot H_2O$ (**31**) bulk material. Yb : P ratio of 1.0 : 1.8.

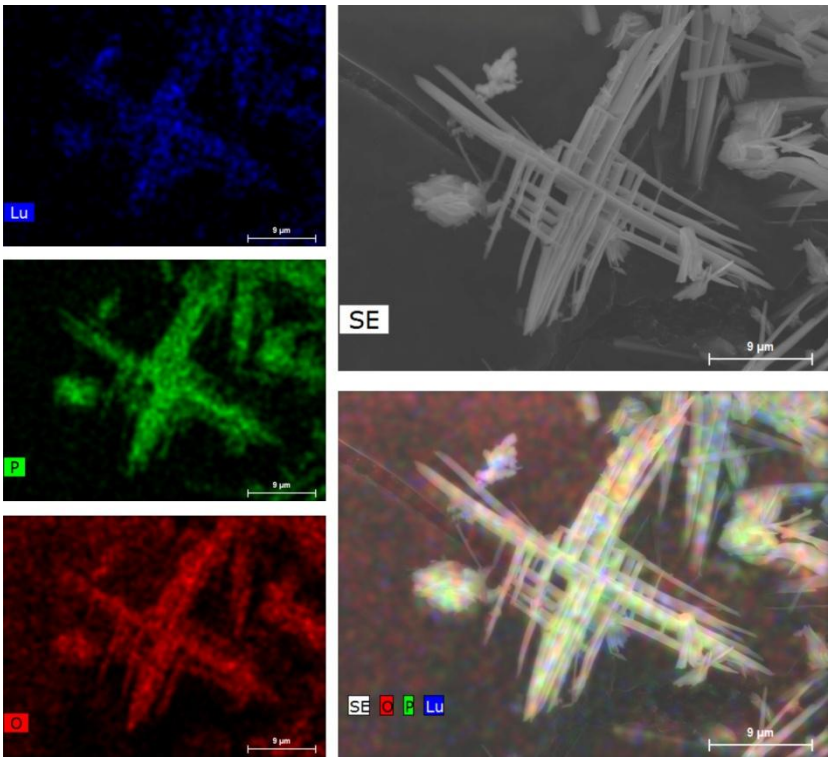

Figure E.1.18. EDS mapping of a representative portion of the $[Lu_2(H_4ptp)(ox)(H_2O)_6]\cdot H_2O$ (**32**) bulk material. Lu : P ratio of 1.0 : 2.0.

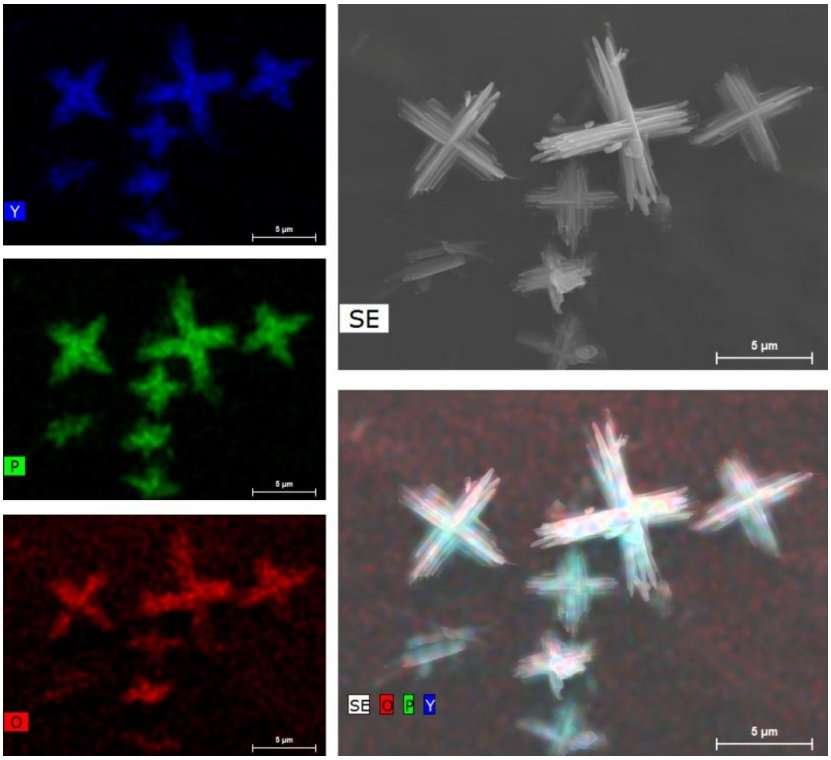

Figure E.1.19. EDS mapping of a representative portion of the $[Y_2(H_4ptp)(ox)(H_2O)_6]\cdot H_2O$ (**33**) bulk material. *Please note*: Y and P signals are overlapped in the EDS spectrum, thus semi-quantification to determine the chemical composition of elements was not possible to perform for this material.

E.2. Crystallographic Details

Table E.2.1. Crystal data collection and structure refinement details for $[Eu_7(H_5btp)_5(H_5btp)_5(H_2O)_{12}]\cdot 23.5H_2O\cdot MeOH$ (**15**).

Formula	$C_{97}H_{166}Eu_7O_{132.5}P_{32}$
Formula weight	5507.05
Temperature / K	150(2)
Crystal system	Monoclinic
Space group	$P2_1/c$
a / Å	13.6342(19)
b / Å	34.172(5)
c / Å	19.049(3)
α / º	90
β / º	93.213(5)
γ / º	90
Volume / Å^3	8861(2)
Z	2
ρ_{calc} / g cm^{-3}	2.064
μ(Mo Kα) / mm^{-1}	2.854
Crystal type	Colorless plate
Crystal size / mm	0.20×0.10×0.02
θ range (°)	3.519 – 25.350
Index ranges	$-16 \le h \le 16$
	$-41 \le k \le 41$
	$-22 \le l \le 22$
Collected Reflections	243730
Independent Reflections	16181 (R_{int} = 0.1633)
Completeness to θ=27.48	99.7%
Final R indices [I>2σ(I)]	$R1$ = 0.0639
	$wR2$ = 0.1327
Final R indices (all data)	$R1$ = 0.1088
	$wR2$ = 0.1507
Absolute Structure Parameter	n/a
Largest diff. peak and hole /eÅ^{-3}	2.005 and –2.1008

[a] $R1 = \sum \| |F_o| - |F_c| \| / \sum |F_o|$;

[b] $wR2 = \sqrt{\sum \left[w\left(F_o^2 - F_c^2\right)^2 \right] / \sum \left[w\left(F_o^2\right)^2 \right]}$

[c] $w = 1/\left[\sigma^2\left(F_o^2\right) + \left(mP\right)^2 + nP \right]$ where $P = \left(F_o^2 + 2F_c^2\right)/3$

Table E.2.2. Hydrogen bonding geometry (distances in Å and angles in degrees) of $[Eu_7(H_5btp)_5(H_5btp)_5(H_2O)_{12}]\cdot 23.5H_2O\cdot MeOH$ (**15**).

D-H···A	$d_{D\cdots A}$	<(DHA)
O2-H2···O48^{v}	2.496(13)	128
O4-H4···O4^{vi}	3.20(2)	152
O8-H8···O10W	3.007(8)	152
O9-H9···O11W^{vii}	2.677(16)	154
O11-H11···O39^{v}	2.648(13)	143
O14-H14···O9	2.544(11)	138
O16-H16···O26	2.897(17)	158
O16-H16···O8W^{viii}	3.067(18)	128
O17-H17···O10	2.499(12)	149
O20-H20···O6	2.557(11)	152
O23-H23···O30	3.263(13)	176
O23-H23···O13W^{vi}	2.97(2)	112
O24-H24···O5^{vi}	2.569(11)	150
O26-H26···O8W^{viii}	2.745(16)	155
O27-H27···O22W^{ix}	2.51(4)	111
O27-H27···O23W^{ix}	2.46(4)	143
O30-H30···O23	3.263(13)	162
O30-H30···O13W^{vi}	2.90(2)	117
O33-H33···O38	2.749(11)	146
O33-H33···O49^{ii}	3.24(3)	134
O36-H36···O40	2.584(10)	155
O38-H38···O33	2.749(11)	171
O42-H42···O6^{x}	3.061(15)	159
O44-H44···O24^{i}	2.916(13)	162
O45-H45···O30	2.661(12)	125
O48-H48···O2^{x}	2.496(13)	157
O49-H49···O38^{ii}	2.94(3)	142
O49-H49···O3W	3.04(3)	120

[a] Symmetry transformations used to generate equivalent atoms: (i) -*x*, -*y*+1, -*z*+1, (ii) -*x*, -*y*+1, -*z*, (v) *x*+1, *y*, *z*, (vi) -*x*+1, -*y*+1, -*z*+1, (vii) -*x*+1, -*y*+1, -*z*, (viii) -*x*+1, *y*+1/2, -*z*+1/2 (ix) -*x*, *y*+1/2, -*z*+1/2, (x) *x*-1, *y*, *z*.

Table E.2.3. Crystal data collection and structure refinement details for $[Ce_4(H_3btp)(H_4btp)(H_5btp)(H_2O)_8]\cdot 3H_2O$ (**17**).

Formula	$C_{36}H_{52}O_{47}P_{12}Ce_4$
Formula weight	2164.05
Temperature / K	150(2)
Crystal system	Monoclinic
Space group	$P2_1/c$
a / Å	12.5332(16)
b / Å	24.147(3)
c / Å	20.852(3)
α / º	90
β / º	100.037(3)
γ / º	90
Volume / Å^3	6213.9(14)
Z	4
ρ_{calc} / g cm^{-3}	2.313
μ(Mo Kα)/mm^{-1}	3.122
Crystal type	Colourless needle
Crystal size / mm	0.17×0.06×0.02
θ range (°)	3.52 – 29.13
Index ranges	$-17 \le h \le 17$
	$-33 \le k \le 33$
	$-26 \le l \le 28$
Collected Reflections	167012
Independent Reflections	16687 (R_{int} = 0.0779)
Completeness to θ = 25.24	99.7%
Final R indices [$I > 2\sigma(I)$]	$R1$ = 0.0549
	$wR2$ = 0.1101
Final R indices (all data)	$R1$ = 0.0709
	$wR2$ = 0.1153
Largest diff. peak and hole /eÅ^{-3}	2.468 and -1.888

[a] $R1 = \sum \| |F_o| - |F_c| \| / \sum |F_o|$

[b] $wR2 = \sqrt{\sum \left[w\left(F_o^2 - F_c^2\right)^2 \right] / \sum \left[w\left(F_o^2\right)^2 \right]}$

[c] $w = 1/\left[\sigma^2\left(F_o^2\right) + \left(mP\right)^2 + nP \right]$ where $P = \left(F_o^2 + 2F_c^2\right)/3$

Table E.2.4. Hydrogen bonding geometry (distances in Å and angles in degrees) of $[Ce_4(H_3btp)(H_4btp)(H_5btp)(H_2O)_8]\cdot 3H_2O$ (**17**).

D-H···A	$d_{D\cdots A}$	<(DHA)
O(2)-H(2)···O(25)	2.771(7)	172
O(6)-H(6)···O(25)^{vi}	2.529(8)	155
O(7)-H(7)···O(10W)^{xv}	2.553(9)	161
O(9)-H(9)···O(6W)^{xv}	3.013(8)	157
O(11)-H(11)···O(23)^{v}	2.647(7)	166
O(16)-H(16)···O(5)^{ii}	2.521(7)	170
O(19)-H(19)···O(7)^{xvi}	2.704(7)	163
O(24)-H(24)···O(27)^{xi}	2.842(8)	111
O(27)-H(27)···O(24)^{ix}	2.842(8)	166
O(30)-H(30)···O(23)^{ix}	2.562(7)	140
O(31)-H(31)···O(11)^{ii}	2.734(7)	163
O(35)-H(35)···O(4W)	2.803(7)	131

[a] Symmetry transformations used to generate equivalent atoms:(ii) 2*x*+1, *y*, *z*, (v) -*x*, -*y*+1, -*z*+1, (vi) *x*+1, -*y*+1/2, *z*+1/2, (ix) *x*, -*y*+1/2, *z*+1/2, (xi) *x*, -*y*+1/2, *z*-1/2, (xv) -*x*-1, -*y*+1, -*z*+1, (xvi) *x*+2, *y*, *z*.

E.3. Vibrational Spectroscopy: FT-IR studies

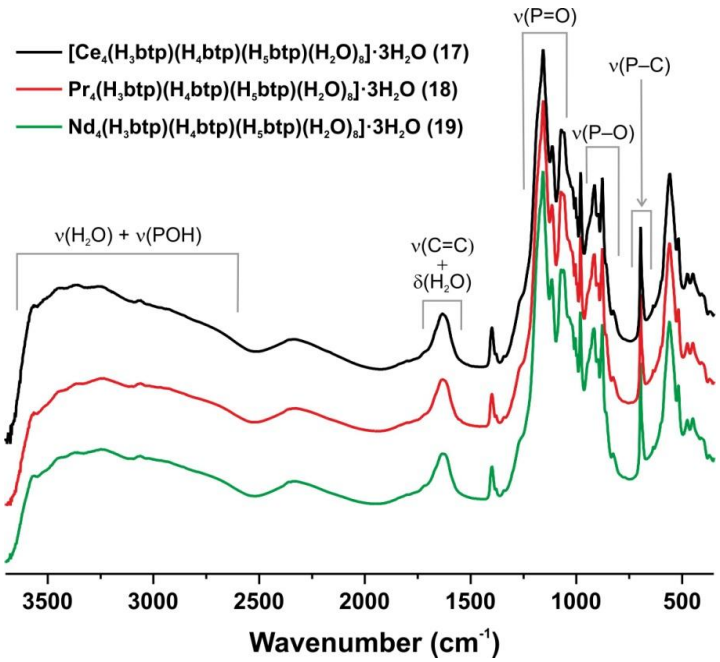

Figure E.3.1. FT-IR spectra (in absorbance, arbitrary units) of the isotypical series of $[Ln_4(H_3btp)(H_4btp)(H_5btp)(H_2O)_8]\cdot 3H_2O$ materials [where Ln^{3+} = Ce^{3+} (**17**), Pr^{3+} (**18**) and Nd^{3+} (**19**)].

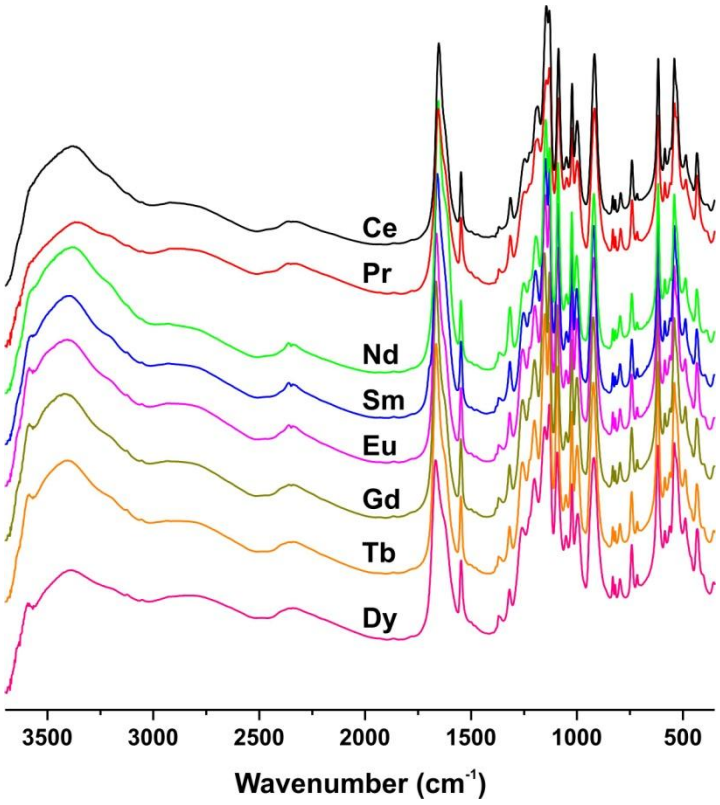

Figure E.3.2. FT-IR spectra (in absorbance, arbitrary units) of the isotypical series of $[Ln_2(H_4ptp)(ox)(H_2O)_6]\cdot 5H_2O$ [where Ln^{3+} = Ce^{3+} (**20**), Pr^{3+} (**21**), Nd^{3+} (**22**), Sm^{3+} (**23**), Eu^{3+} (**24**), Gd^{3+} (**25**), Tb^{3+} (**26**) and Dy^{3+} (**27**)].

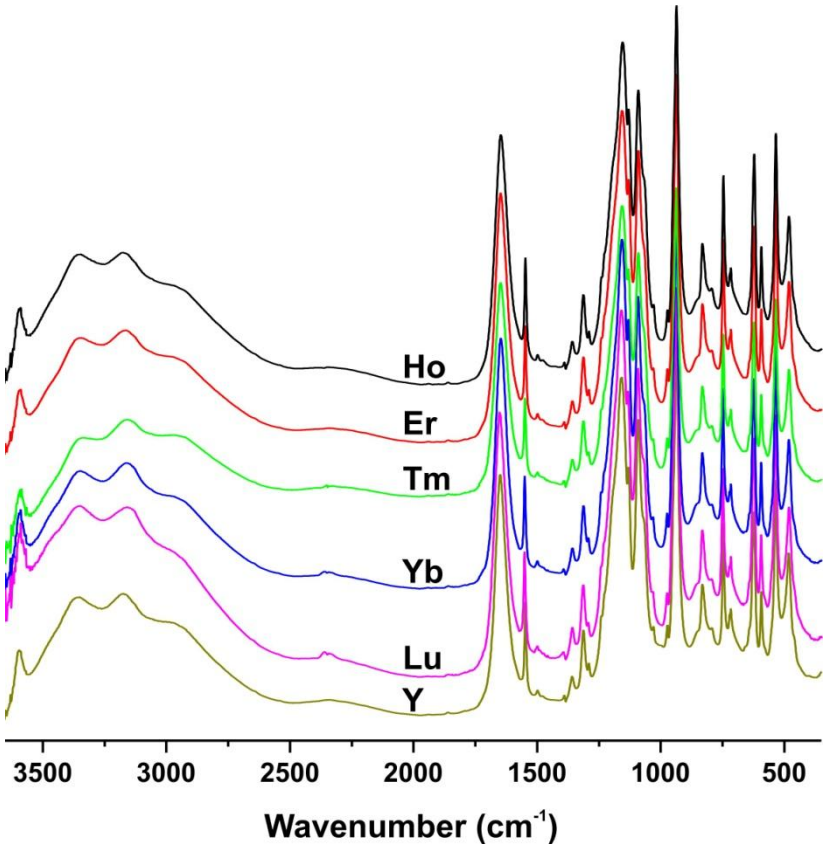

Figure E.3.3. FT-IR spectra (in absorbance, arbitrary units) of the isotypical series of $[Ln_2(H_4ptp)(ox)(H_2O)_6]\cdot H_2O$ [where Ln^{3+} = Ho^{3+} (**28**), Er^{3+} (**29**), Tm^{3+} (**30**), Yb^{3+} (**31**), Lu^{3+} (**32**) and Y^{3+} (**33**)].

E.4. Thermogravimetry

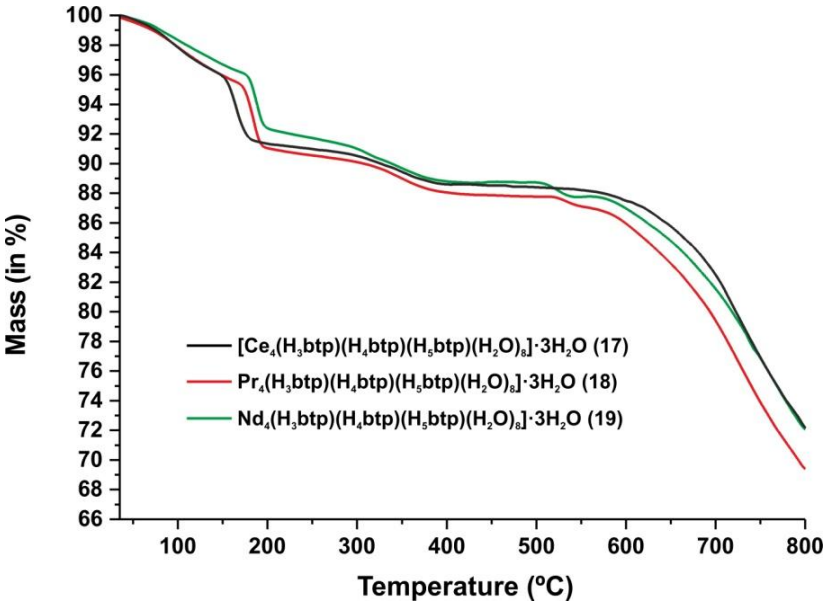

Figure E.4.1. Thermograms of the isotypical series of $[Ln_4(H_3btp)(H_4btp)(H_5btp)(H_2O)_8]\cdot 3H_2O$ materials [where Ln^{3+} = Ce^{3+} (**17**), Pr^{3+} (**18**) and Nd^{3+} (**19**)] collected between ambient temperature and 800 ºC.

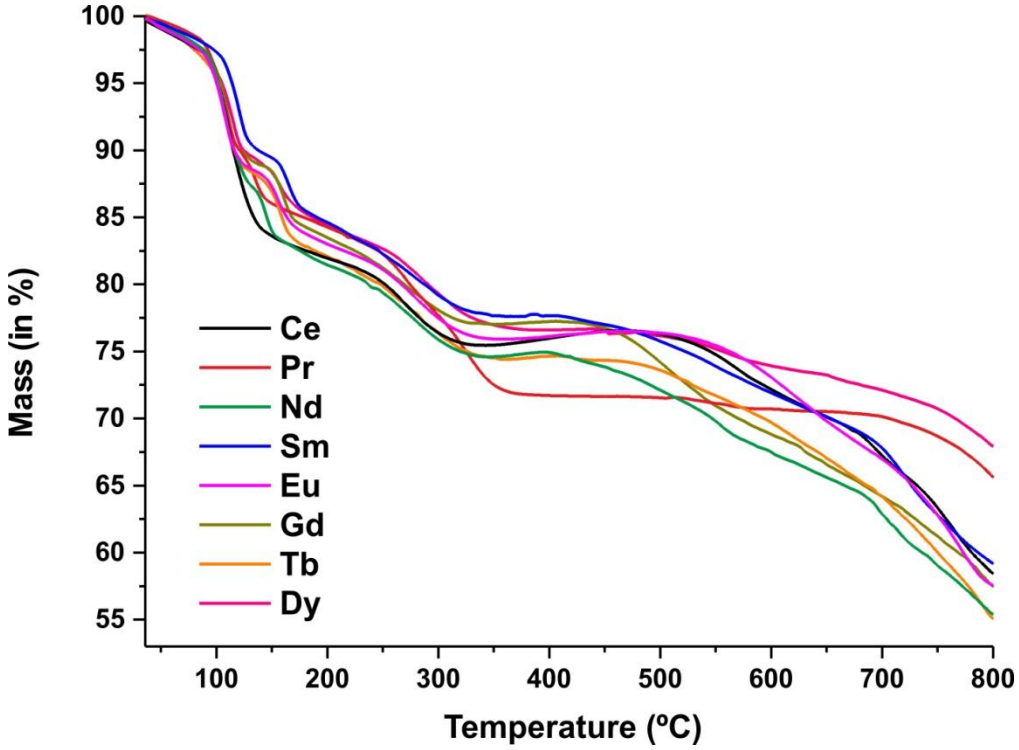

Figure E.4.2. Thermograms of the isotypical series of $[Ln_2(H_4ptp)(ox)(H_2O)_6]\cdot 5H_2O$ [where Ln^{3+} = Ce^{3+} (**20**), Pr^{3+} (**21**), Nd^{3+} (**22**), Sm^{3+} (**23**), Eu^{3+} (**24**), Gd^{3+} (**25**), Tb^{3+} (**26**) and Dy^{3+} (**27**)] collected between ambient temperature and 800 ºC.

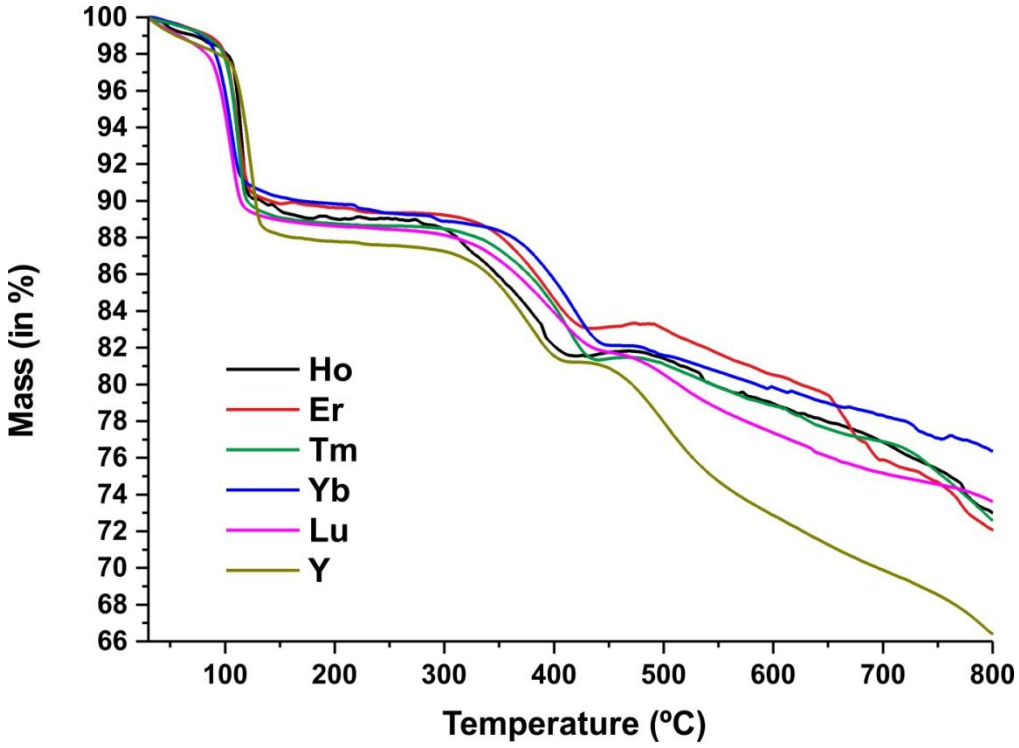

Figure E.4.3. Thermograms of the isotypical series of $[Ln_2(H_4ptp)(ox)(H_2O)_6]\cdot H_2O$ [where Ln^{3+} = Ho^{3+} (**28**), Er^{3+} (**29**), Tm^{3+} (**30**), Yb^{3+} (**31**), Lu^{3+} (**32**) and Y^{3+} (**33**)] collected between ambient temperature and 800 ºC.

References

(1) Mendes, R. F.; Silva, P.; Antunes, M. M.; Valente, A. A.; Paz, F. A. A.; *Chem. Commun.*, **2015**, *51*, 10807.

(2) Firmino, A. D. G.; Mendes, R. F.; Antunes, M. M.; Barbosa, P. C.; Vilela, S. M. F.; Valente, A. A.; Figueiredo, F. M. L.; Tome, J. P. C.; Paz, F. A. A.; *Inorg. Chem.*, **2017**, *56*, 1193.

(3) Mendes, R. F.; Antunes, M. M.; Silva, P.; Barbosa, P.; Figueiredo, F.; Linden, A.; Rocha, J.; Valente, A. A.; Paz, F. A. A.; *Chem.-Eur. J.*, **2016**, *22*, 13136.

(4) Vilela, S. M. F.; Firmino, A. D. G.; Mendes, R. F.; Fernandes, J. A.; Ananias, D.; Valente, A. A.; Ott, H.; Carlos, L. D.; Rocha, J.; Tome, J. P. C.; Almeida Paz, F. A.; *Chem. Commun.*, **2013**, *49*, 6400.

(5) Silva, P.; Vieira, F.; Gomes, A. C.; Ananias, D.; Fernandes, J. A.; Bruno, S. M.; Soares, R.; Valente, A. A.; Rocha, J.; Almeida Paz, F. A.; *J. Am. Chem. Soc.*, **2011**, *133*, 15120.

(6) Vilela, S. M. F.; Ananias, D.; Gomes, A. C.; Valente, A. A.; Carlos, L. D.; Cavaleiro, J. A. S.; Rocha, J.; Tome, J. P. C.; Almeida Paz, F. A.; *J. Mater. Chem.*, **2012**, *22*, 18354.

(7) Silva, P.; Ananias, D.; Bruno, S. M.; Valente, A. A.; Carlos, L. D.; Rocha, J.; Almeida Paz, F. A.; *Eur. J. Inorg. Chem.*, **2013**, *2013*, 5576.

(8) Wee, L. H.; Lohe, M. R.; Janssens, N.; Kaskel, S.; Martens, J. A.; *J. Mater. Chem.*, **2012**, *22*, 13742.

(9) Wee, L. H.; Bonino, F.; Lamberti, C.; Bordiga, S.; Martens, J. A.; *Green Chem.*, **2014**, *16*, 1351.

(10) Dhakshinamoorthy, A.; Alvaro, M.; Garcia, H.; *Chem. Eur. J.*, **2010**, *16*, 8530.

(11) Biswas, S.; Maes, M.; Dhakshinamoorthy, A.; Feyand, M.; De Vos, D. E.; Garcia, H.; Stock, N.; *J. Mater. Chem.*, **2012**, *22*, 10200.

(12) Wang, P.; Li, H.; Gao, Q.; Li, P.-Z.; Yao, X.; Bai, L.; Nguyen, K. T.; Zou, R.-Q.; Zhao, Y.; *J. Mater. Chem. A*, **2014**, *2*, 18731.

(13) Jiang, D.; Urakawa, A.; Yulikov, M.; Mallat, T.; Jeschke, G.; Baiker, A.; *Chem. Eur. J.*, **2009**, *15*, 12255.

(14) Jiang, D.; Mallat, T.; Krumeich, F.; Baiker, A.; *J. Catal.*, **2008**, *257*, 390.

(15) Vilela, S. M. F.; Ananias, D.; Fernandes, J. A.; Silva, P.; Gomes, A. C.; Silva, N. J. O.; Rodrigues, M. O.; Tome, J. P. C.; Valente, A. A.; Ribeiro-Claro, P.; Carlos, L. D.; Rocha, J.; Almeida Paz, F. A.; *J. Mater. Chem. C*, **2014**, *2*, 3311.

(16) Tanaka, K.; Otani, K.-i.; *New J. Chem.*, **2010**, *34*, 2389.

(17) Zu, D.-D.; Lu, L.; Liu, X.-Q.; Zhang, D.-Y.; Sun, L.-B.; *J. Phys. Chem.: C*, **2014**, *118*, 19910.

(18) Herbst, A.; Khutia, A.; Janiak, C.; *Inorg. Chem.*, **2014**, *53*, 7319.

(19) Bromberg, L.; Hatton, T. A.; *ACS Appl. Mater. Interfaces*, **2011**, *3*, 4756.

(20) Timofeeva, M. N.; Panchenko, V. N.; Jun, J. W.; Hasan, Z.; Matrosova, M. M.; Jhung, S. H.; *Appl. Catal., A*, **2014**, *471*, 91.

(21) Dhakshinamoorthy, A.; Alvaro, M.; Garcia, H.; *Adv. Synth. Catal.*, **2010**, *352*, 3022.

(22) Ren, Y.-w.; Liang, J.-x.; Lu, J.-x.; Cai, B.-w.; Shi, D.-b.; Qi, C.-r.; Jiang, H.-f.; Chen, J.; Zheng, D.; *Eur. J. Inorg. Chem.*, **2011**, *2011*, 4369.

(23) Clerici, A.; Pastori, N.; Porta, O.; *Tetrahedron*, **1998**, *54*, 15679.